Universidad Autónoma de Madrid
Facultad de Ciencias
Departamento de Física Teórica

Lepton flavour violation in supersymmetric models with seesaw mechanism

Memoria de Tesis Doctoral realizada por
Ernesto Arganda Carreras
presentada ante el Departamento de Física Teórica
de la Universidad Autónoma de Madrid
para la obtención del Título de Doctor en Ciencias

Trabajo dirigido por la
Dra. María José Herrero Solans,
Profesora Titular del Departamento de Física Teórica

Madrid, mayo de 2008

A Carmen, Justo,
Sara, Ignacio y Andrea.

Contents

Introducción

El Modelo Estándar (SM) [1–5] de las interacciones fundamentales está basado en la simetría gauge $SU(3)_C \times SU(2)_L \times U(1)_Y$ y proporciona el marco indiscutible de la Física de Partículas. Este modelo describe con gran éxito la mayoría de los fenómenos conocidos y, de hecho, el acuerdo entre sus predicciones y los datos experimentales es excelente, en algunas casos con una precisión mayor del 1%. Una de las predicciones que necesita aún ser verificada es la existencia del llamado bosón de Higgs [6–9]. Esta partícula aparece como una consecuencia del mecanismo de ruptura espontánea de la simetría electrodébil, necesaria para explicar el origen de las masas de los fermiones y de los bosones gauge. El valor de la masa del bosón de Higgs no se predice dentro del SM y, en consecuencia, la búsqueda experimental se realiza sobre un rango de valores posibles. Dada la ausencia actual de señales significativas del bosón de Higgs, los experimentos fijan un límite inferior a su masa de $m_{H_{\rm SM}} > 114.4$ GeV al 95% C.L. [10]. Aunque la última confirmación del SM sería el descubrimiento experimental del bosón de Higgs, este modelo todavía tiene algunos problemas, tanto teóricos como experimentales, que requieren la introducción de nueva física para ser resueltos.

En primer de lugar, hay una importante evidencia experimental que sugiere que el SM debería extenderse de alguna manera. El SM se construyó bajo la hipótesis de que los neutrinos de las tres generaciones eran partículas sin masa. En los últimos años, la observación experimental de oscilaciones de neutrinos, descubiertas por primera vez por la colaboración Super-Kamiokande y confirmadas después por otros experimentos [11–19], indica que los neutrinos tienen masa. Estas oscilaciones también aportan información importante sobre los ángulos de mezcla de los neutrinos de la matriz Maki-Nakagawa-Sakata ($U_{\rm PMNS}$) [20–22]. Este hecho representa la primera señal experimental clara de existencia de física más allá del SM. Como hemos dicho, el SM no incluye masas para los neutrinos en su formulación usual, por lo que es necesario modificarlo para tener en cuenta estas masas.

Las pequeñas masas de los neutrinos, sugeridas por los experimentos, pueden explicarse por el mecanismo de seesaw de generación de masas de neutrinos [23–37]. En su versión más simple (llamada seesaw Tipo I), este mecanismo asume la existencia de neutrinos dextrógiros ν_R con una masa de Majorana muy grande en comparación con la escala electrodébil (EW) $v = 174$

GeV y que se acoplan a los neutrinos levógiros mediante acoplos de Yukawa Y_ν. Por lo tanto, este mecanismo explica de manera simple y elegante las masas pequeñas m_ν en términos de dos escalas de masa muy distantes, m_M y la masa de Dirac, m_D, que se relaciona con v por $m_D = vY_\nu$. Las propiedades de los autoestados de masa de los neutrinos dentro del mecanismo de seesaw pueden derivarse fácilmente considerando el límite $m_D \ll m_M$. Por ejemplo, en el caso de una única generación, obtenemos dos autoestados de masa de Majorana, uno muy ligero compuesto predominantemente de ν_L y con una masa alrededor de m_D^2/m_M, y otro muy pesado, formado en su mayoría por ν_R y con una masa cercana a m_M. En consecuencia, para obtener una masa de neutrinos ligera en el rango de $0.1 - 1$ eV con acoplamientos de Yukawa de orden 1, la masa de Majorana m_M debe ser del orden de 10^{14} GeV o incluso mayor. La componente ν_R del autoestado ligero y, correspondientemente, la componente ν_L del autoestado pesado están suprimidas por los factores m_D/m_M, y pueden por tanto despreciarse. Estos argumentos pueden generalizarse al caso de tres generaciones con tres neutrinos dextrógiros, y dentro de este modelo de seesaw los datos experimentales de las masas y mezclas de los neutrinos se pueden acomodar satisfactoriamente. Nótese que también es posible conseguir compatibilidad con los datos experimentales con tan sólo dos ν_R, sin embargo, en esta tesis consideraremos tres ν_R por similitud con el resto de fermiones.

Otra característica llamativa del mecanismo de seesaw con tres neutrinos dextrógiros es que la masa de Majorana produce violación del número leptónico, necesaria para una bariogénesis satisfactoria via leptogénesis [38]. Dentro del contexto de leptogénesis, la asimetría bariónica del universo (BAU) que se observa experimentalmente puede explicarse mediante las desintegraciones fuera del equilibrio de los mismos neutrinos dextrógiros pesados.

A pesar de todo, la existencia de estas dos escalas de masa tan separadas, la escala electrodébil y la escala m_M que, como se ha dicho previamente, explican elegantemente las masas ligeras de los neutrinos y que también pueden proporcionar una BAU satisfactoria, pueden inducir un serio problema de jerarquías, similar al que ocurre en el SM. El llamado problema de la jerarquía del SM se debe a la inestabilidad del sector de Higgs bajo correcciones radiativas al introducir una nueva escala grande de energía asociada a nueva física, como por ejemplo la escala de Planck, M_P, donde los efectos cuánticos gravitacionales llegan a ser importantes. Esta inestabilidad se puede ver claramente en las correcciones radiativas a la masa del bosón de Higgs, m_H. Argumentos de naturalidad sugieren que esta masa debería encontrarse cerca del valor de $v = 174$ GeV que fija la escala de energía de la física electrodébil. No obstante, se sabe que la masa del Higgs recibe correcciones cuánticas enormes de los efectos virtuales de cada partícula a la que se acopla, que desplazan los valores iniciales del orden de 100 GeV a valores del orden de la nueva escala física. Esto ocurre porque las funciones a dos puntos del campo de Higgs del SM son sensibles cuadráticamente al cut-off usado para regular la integral de loop. Cuando el SM es considerado no como una teoría fundamental sino como una teoría

efectiva, este cut-off se interpreta como la escala de energía a la cual la nueva física comienza a alterar el comportamiento a altas energías de la teoría. Por consiguiente, si esta escala es del orden de M_P, donde necesariamente hay nueva física implicada, las correcciones cuánticas a la masa del Higgs mencionadas son aproximadamente 30 órdenes de magnitud más grandes que el valor inicial de $\mathcal{O}(100)$ GeV.

En el caso de los modelos de seesaw, los neutrinos dextrógiros pesados, que se acoplan al campo de Higgs, son los responsables de producir las correcciones radiativas peligrosas a la masa del Higgs. Por lo tanto, una simple extensión del SM con tres neutrinos ν_R y el mecanismo de seesaw para generar masas ligeras de neutrinos (llamada aquí SM-seesaw) no es completamente satisfactoria.

La introducción de una nueva simetría, llamada supersimetría (SUSY) [39–41], suele ser la solución favorita a este problema de la jerarquía. SUSY relaciona fermiones y bosones de tal manera que las nuevas partículas compensan exactamente todas las contribuciones cuadráticas no deseadas a las masas escalares, solucionando el problema de la jerarquía del SM. Por otro lado, esta extensión supersimétrica del SM puede incorporar también el mecanismo de seesaw para generar las masas de los neutrinos satisfactoriamente. Estos modelos SUSY-seesaw no presentan entonces el problema de la jerarquía.

El Modelo Estándar Supersimétrico Mínimo (MSSM) es la versión supersimétrica mínima del SM que incorpora un compañero supersimétrico por cada partícula del SM, con la misma masa y mismos números cuánticos pero con una diferencia de spin de media unidad [42–46]. Por tanto, un nuevo compañero bosónico es asignado a cada fermión del SM y, correspondientemente, se añade un nuevo compañero fermiónico a cada bosón del SM. Se llama mínimo porque contiene el mínimo número de supersimetrías posibles ($N = 1$) y, por lo tanto, el mínimo contenido de partículas supersimétricas. Con la introducción de esta simetría que relaciona bosones y fermiones es posible garantizar que todas las divergencias cuadráticas en las autoenergías escalares se cancelan. Para implementar el mecanismo de seesaw dentro del MSSM, introducimos además tres neutrinos dextrógiros y sus tres supercompañeros correspondientes, los sneutrinos. De manera similar al caso SM-seesaw, dentro de esta versión MSSM-seesaw también podemos acomodar satisfactoriamente los datos experimentales de neutrinos. La ventaja del MSSM-seesaw respecto al SM-seesaw es la ausencia del problema de la jerarquía.

Sin embargo, es bien conocido que SUSY no puede ser una simetría exacta del espectro de partículas observado y, por lo tanto, tiene que estar rota en la naturaleza, ya que hasta ahora no se han encontrado partículas supersimétricas en los experimentos [10]. Aunque todavía no se conoce bien el mecanismo de ruptura de SUSY, los términos de ruptura de SUSY que aparecen en el lagrangiano deben preservar las buenas propiedades de supersimetría. En concreto, estos términos de ruptura de SUSY tienen que ser *suaves* [47], de tal manera que la cancelación de

divergencias cuadráticas se dé todavía. Además, deben proporcionar masas apropiadas para las partículas SUSY, para que sean más pesadas que las de sus compañeras del SM. No obstante, debido a la ruptura de SUSY pueden surgir otros problemas. En el escenario más general, uno de los problemas más serios es la existencia de no alineamiento entre las matrices de masa de los fermiones y los sfermiones. En este caso, estas dos matrices no son simultáneamente diagonales en sabor y, en consecuencia, pueden generarse procesos inaceptables que cambian el sabor. Este es el llamado problema supersimétrico del sabor, que ocurre porque el mencionado no alineamiento entre fermiones y sfermiones conduce a nuevas interacciones intergeneracionales a nivel árbol, que puestas en los loops de los procesos que cambian el sabor pueden producir contribuciones grandes, en contradicción con los datos experimentales.

La mejor evidencia de supersimetría sería por supuesto el descubrimiento de partículas SUSY en cualquiera de los colisionadores actuales o futuros. Sin embargo, el hecho de que SUSY tiene que estar rota en la naturaleza indica que las masas de las partículas supersimétricas deben ser más pesadas que sus correspondientes compañeras del SM y, de hecho, podrían ser mucho más grandes que las energías alcanzadas en los experimentos. Por tanto, podría ocurrir que algunas de estas partículas fueran demasiado pesadas para ser producidas directamente incluso en los próximos colisionadores como el Gran Colisionador de Hadrones (LHC) del CERN. En este último caso, señales de la existencia de supersimetría se producirían primero vía búsquedas indirectas. Estas posibles búsquedas indirectas de SUSY consisten en investigar las contribuciones de estas partículas a correcciones radiativas en observables que se miden con gran precisión. Comparando las predicciones de estos observables, incluyendo sus correcciones radiativas, con sus valores experimentales, podríamos obtener una señal indirecta de SUSY. Con esta idea en mente, deberíamos buscar correcciones radiativas de observables que incluyen partículas supersimétricas dentro de los loops y que se incrementan respecto de su valor en el SM.

Una de las implicaciones fenomenológicas más destacables de los modelos SUSY-seesaw es la predicción de tasas de desintegración considerables de procesos que violan el sabor leptónico (LFV) [48]. En estos modelos SUSY-seesaw aparece una nueva fuente de violación del sabor leptónico (LFV) en los elementos de fuera de la diagonal de las matrices de masa de los sleptones y sneutrinos, que pueden generarse radiativamente. Éstos, de hecho, pueden producir un no alineamiento relevante entre las matrices de masa de sleptones y leptones y entre las matrices de masa de sneutrinos y neutrinos, que podría conducir a consecuencias fenomenológicas importantes en procesos que cambian el sabor leptónico. El tamaño de estos elementos de fuera de la diagonal viene gobernado por la fuerza de los acoplamientos de Yukawa de los neutrinos que, como hemos dicho, para neutrinos de Majorana pueden ser grandes, de orden uno. Los efectos LFV en los procesos de leptones cargados son de este modo inducidos por interacciones sleptón-leptón y sneutrino-neutrino que violan el sabor leptónico, que aparecen en diagramas con loops supersimétricos mediados por sleptones y sneutrinos, y que producen tasas LFV que

son muchos órdenes de magnitud más grandes que las predichas por el SM.

De aquí surge una conexión interesante entre la física de neutrinos y la violación del sabor leptónico, ya que los acoplos grandes de Yukawa de los neutrinos, típicos para neutrinos de Majorana, inducen contribuciones importantes en los procesos LFV, que podrían medirse. De hecho, estas contribuciones están ya, en algunos casos, al alcance de sus cotas experimentales actuales. En este sentido, tanto las desintegraciones radiativas del τ y del μ, $l_j \to l_i\,\gamma$ [49–52], las desintegraciones del τ y del μ en tres leptones, $l_j \to 3\,l_i$ $(i \neq j)$[49, 52, 53], y las desintegraciones semileptónicas del τ del tipo $\tau \to \mu\eta$ [54], como la conversión $\mu - e$ en núcleos pesados [49, 52, 55], se encuentran entre los procesos LFV más interesantes. Las desintegraciones LFV de los bosones de Higgs, $H \to l_j\bar{l}_i$ [56], y las desintegraciones LFV del bosón gauge Z, $Z \to l_j\bar{l}_i$ [57], son también de relevancia en este contexto.

Respecto a los procesos $\mu - e$, los más relevantes actualmente son $\mu \to e\gamma$, $\mu \to 3e$ y la conversión $\mu - e$ en núcleos. Las cotas experimentales presentes para las desintegraciones del muón son $\mathrm{BR}(\mu \to e\gamma) < 1.2 \times 10^{-11}$ [58] y $\mathrm{BR}(\mu \to 3e) < 1.0 \times 10^{-12}$ [59]. En relación a la conversión $\mu - e$ en núcleos pesados, las restricciones más severas provienen del Titanio y del Oro, respectivamente con $\mathrm{CR}(\mu - e,\ \mathrm{Ti}) < 4.3 \times 10^{-12}$ [60] y $\mathrm{CR}(\mu - e,\ \mathrm{Au}) < 7 \times 10^{-13}$ [61]. En el futuro, se esperan mejoras significativas en las sensibilidades de estos procesos LFV. Por ejemplo, MEG espera conseguir una sensibilidad para $\mu \to e\gamma$ de 10^{-13} [62] en un futuro próximo, que podría mejorarse aún más hasta 10^{-14} en los próximos 4-5 años [63]. Aunque la situación para $\mathrm{BR}(\mu \to 3e)$ es menos clara, es de esperar que las cotas mejoren a $10^{-13} - 10^{-14}$ [63]. Indudablemente, las perspectivas más prometedoras conciernen a las cotas experimentales de la conversión $\mu - e$ en Titanio. El experimento PRISM/PRIME en J-PARC ha anunciado una mejora destacable, aunque en un futuro lejano, de 10^{-18} [64].

En relación a los tests de LFV en el sector $\tau - \mu$, el canal más competitivo actualmente es $\tau \to \mu\gamma$, cuya cota superior está fijada ahora a 1.6×10^{-8} [65–68]. Además, la sensibilidad de $\tau \to 3\mu$ ha mejorado notablemente en los últimos años. Las cotas superiores actuales de las colaboraciones BELLE y BABAR son 3.2×10^{-8} [69] y 5.3×10^{-8} [70], respectivamente. Este canal leptónico tiene una ventaja sobre la desintegración radiativa del τ, proporciona un test no sólo de SUSY sino también del sector de Higgs. Es reseñable que ambos procesos, la desintegración $\tau \to 3\mu$ [53, 56, 71] y la conversión $\mu - e$ [55] en núcleos, pueden obtener contribuciones importantes de los diagramas mediados por los bosones de Higgs en escenarios SUSY con gran $\tan\beta$ y bosones de Higgs ligeros. Los canales de desintegración semileptónicos LFV del τ son también de interés debido a las recientes cotas aportadas por las colaboraciones BELLE y BABAR [72–75] que son, para algunos canales, competitivas con las leptónicas del τ. Particularmente interesante es el canal semileptónico $\tau \to \mu\,\eta$, que es claramente sensible a las partículas SUSY y a los bosones de Higgs, y cuya cota experimental actual es 5.1×10^{-8} [68].

Además del gran número de parámetros del MSSM, el mecanismo de seesaw introduce 18 parámetros nuevos en el sector de los neutrinos. Para simplificar el análisis de los procesos LFV en un modelo SUSY-seesaw, elegimos trabajar en el llamado MSSM restringido (CMSSM) (para un resumen ver por ejemplo [76]), asumiendo universalidad de los parámetros de ruptura suave de SUSY a la escala de unificación de los acoplos gauge, M_X. Esto permite reducir los parámetros desconocidos del sector SUSY a los cinco parámetros usuales de un contexto de supergravedad mínima (mSUGRA): M_0, $M_{1/2}$, A_0, $\tan\beta$ y $\mathrm{sign}(\mu)$. Una desviación interesante del CMSSM-seesaw puede obtenerse relajando la hipótesis de universalidad para las masas de ruptura suave de SUSY del sector de Higgs. Este MSSM parcialmente restringido es comúnmente llamado escenario Non Universal Higgs Mass (NUHM) [77–89], y su versión extendida (incluyendo neutrinos y sneutrinos dextrógiros) será designada aquí NUHM-seesaw.

La principal motivación de la presente tesis es el estudio de las correcciones radiativas de las partículas SUSY a procesos que violan el sabor leptónico en escenarios SUSY-seesaw. Nuestra elección de canales con cambio de sabor se debe al hecho de que en el SM éstos están extremadamente suprimidos. En particular, centraremos nuestro estudio en las desintegraciones radiativas LFV $l_j \to l_i\,\gamma$, en las desintegraciones LFV de los bosones de Higgs $H \to l_j\,\bar{l}_i$, en las desintegraciones leptónicas LFV en tres leptones de igual sabor $l_j \to 3\,l_i$, en las desintegraciones semileptónicas LFV del τ y en la conversión $\mu - e$ en núcleos. La razón para estudiar estos canales a la vez es que, como veremos más adelante, hay correlaciones interesantes entre ellos en los escenarios SUSY-seesaw en los que trabajamos. Nuestro objetivo final será usar estas correcciones radiativas como un método eficiente para examinar los sectores SUSY y de neutrinos. La posibilidad de obtener información sobre las masas de los neutrinos dextrógiros mediante estos procesos LFV es especialmente interesante, ya que estas partículas son inaccesibles en los colisionadores, y lo seguirán siendo en el futuro.

En esta tesis presentaremos el cálculo completo a un loop de los procesos LFV y veremos que los loops de las partículas supersimétricas contribuyen de manera relevante a estos observables. Analizaremos en detalle el tamaño de los cocientes de ramificación en términos de los parámetros SUSY y seesaw y exploraremos las restricciones que imponen las cotas experimentales a los diferentes procesos LFV. Además, determinaremos cuáles de estos procesos manifiestan un comportamiento no desacoplante de las partículas SUSY en el límite de masas SUSY grandes. Veremos que este comportamiento no desacoplante es particularmente relevante para las contribuciones a los procesos LFV mediadas por los bosones de Higgs. Por lo tanto, también analizaremos la sensibilidad al sector de Higgs mediante los procesos LFV.

Este trabajo está organizado de la siguiente manera. En el Capítulo 1 revisamos los aspectos básicos del marco teórico en el que vamos a desarrollar la tesis. Primero introducimos el mecanismo de seesaw para la generación de masas de neutrinos, mediante neutrinos dextrógiros, y los diferentes escenarios que consideramos a bajas energías. A continuación resumimos las

características más importantes del MSSM para esta tesis, para posteriormente presentar las extensiones de estos modelos supersimétricos, agrandados con tres neutrinos dextrógiros y sus supercompañeros. También revisamos las características principales de los escenarios restringidos considerados en la tesis: el CMSSM-seesaw y el NUHM-seesaw. Después de esto, se estudia la generación de mezcla de sabor en los sleptones, prestando especial atención a la dependencia de esta mezcla con los parámetros del seesaw. También mostramos otras implicaciones fenomenológicas de los modelos SUSY-seesaw restringidos: leptogénesis térmica, los momentos dipolares eléctricos de los leptones cargados (EDMs) y las contribuciones supersimétricas al momento magnético anómalo del muón, a_μ. Y al final del capítulo mostramos las cotas experimentales presentes de las masas de las partículas supersimétricas y de los bosones de Higgs.

En el Capítulo 2 desarrollamos un estudio detallado de las siguientes desintegraciones leptónicas LFV dentro los escenarios SUSY-seesaw restringidos previos: las desintegraciones radiativas $l_j \to l_i\,\gamma$, las desintegraciones de los bosones de Higgs $H \to l_j\,\bar{l}_i$ (donde H representa los bosones de Higgs neutros del MSSM) y las desintegraciones leptónicas en tres leptones de igual sabor $l_j \to 3\,l_i$. Consideramos espectros degenerados y jerárquicos tanto para los neutrinos ligeros como para los pesados. Primero obtenemos los parámetros más relevantes y después analizamos sistemáticamente la interesante relación entre el ángulo de mezcla leptónico θ_{13} y las desintegraciones LFV del muón y del tau. Exigimos compatibilidad con los datos experimentales de los neutrinos a bajas energías y con las cotas actuales de las desintegraciones LFV y de los EDMs, y también estudiamos las restricciones que surgen de requerir bariogénesis vía leptogénesis térmica. Finalmente enfatizamos las implicaciones que podría tener una medida futura de θ_{13} [90–100] sobre nuestro conocimiento acerca del sector de los neutrinos pesados.

En el Capítulo 3 estudiamos detalladamente las desintegraciones semileptónicas LFV del τ. En particular analizamos las siguientes desintegraciones: $\tau \to \mu PP$ con $PP = \pi^+\pi^-$, $\pi^0\pi^0$, K^+K^-, $K^0\bar{K}^0$, $\tau \to \mu P$ con $P = \pi^0$, η^0, η'^0 y $\tau \to \mu V$ con $V = \rho^0$, ϕ. Presentamos el cálculo completo a un loop y analizamos la relevancia de las distintas contribuciones, mediadas por el fotón, el bosón gauge Z y los bosones de Higgs. La hadronización de los bilineares de quarks se desarrolla dentro del contexto quiral. Finalmente presentamos un conjunto de fórmulas aproximadas para todos los canales semileptónicos, que pensamos que pueden ser útiles para la comparación con los datos experimentales presentes y futuros.

En el Capítulo 4 nos centraremos en la conversión $\mu - e$ en núcleos, trabajando en el contexto de los escenarios CMSSM-seesaw y NUHM-seesaw. Presentamos un cálculo completo a un loop de la tasa de conversión para este proceso que incluye los pingüinos del fotón, del bosón gauge Z y de los bosones de Higgs, y los diagramas tipo caja, y comparamos su importancia en los dos escenarios considerados. Asimismo analizamos la relevancia de los distintos parámetros SUSY-seesaw sobre las tasas de conversión. De hecho, en el caso de neutrinos pesados jerárquicos, encontramos una sensibilidad enorme al ángulo θ_{13}. La última parte de este capítulo está

dedicada al estudio de la pérdida de correlación entre la conversión $\mu - e$ y la desintegración $\mu \to e\gamma$ que ocurre en el escenario no universal. En el caso de gran $\tan\beta$ y un bosón de Higgs H^0 ligero, encontramos que el cociente entre $\mu - e$ y $\mu \to e\gamma$ se incrementa respecto al caso universal, lo cual podría comprobarse con las futuras cotas experimentales.

En la última parte resumimos las conclusiones principales de esta tesis.

Esta tesis está basada en los resultados publicados en los artículos [101], [102], [103], [104] y [105] y en los proceedings de conferencias [106], [107], [108], [109], [110], [111] y [112].

Introduction

The Standard Model (SM) [1–5] of fundamental interactions is based on the gauge symmetry $SU(3)_C \times SU(2)_L \times U(1)_Y$ and provides the indisputable framework of Particle Physics. This model describes with amazing success most of the known phenomena and, indeed, the agreement between its predictions and the data is excellent, tested in some cases to a precision of greater than 1%. One of the predictions which still needs to be verified is the existence of the so-called Higgs boson [6–9]. This particle appears as a consequence of the spontaneous electroweak symmetry breaking mechanism, which is needed to explain the origin of fermions and gauge bosons masses. The value of the Higgs boson mass is not predicted within the SM and, therefore, the experimental search is done over a range of posible values. Given the current absence of significant Higgs boson signals, the experiments set a lower bound on its mass of $m_{H_{\rm SM}} > 114.4$ GeV at the 95% C.L. [10]. Even though the last confirmation of the SM would be the experimental evidence of this Higgs boson, this model has still some theoretical and experimental problems which need to be solved by the introduction of new physics.

First of all, there is an important experimental evidence that suggests the SM should be somehow enlarged. The SM was built with the hypothesis that the three generations of neutrinos were massless particles. In the last years, the experimental observation of neutrino oscillations first reported by the Super-Kamiokande collaboration and then confirmed by other experiments [11–19], indicates that neutrinos do have masses. These oscillations also give an important information on the neutrino mixing angles of the Maki-Nakagawa-Sakata matrix ($U_{\rm MNS}$) [20–22]. This fact appears as the first clear experimental evidence of the existence of some physics beyond the SM. As we have said, in its usual formulation, the SM does not include masses for the neutrinos, thus, it has to be necessarily modified to account for these masses.

The experimentally suggested smallness of the neutrino masses m_ν can be explained by the seesaw mechanism of neutrino mass generation [23–37]. In its simplest version (called Type-I seesaw) this mechanism assumes the existence of right-handed neutrinos ν_R with very large Majorana mass m_M as compared to the electroweak (EW) scale $v = 174$ GeV and coupled to the left-handed neutrinos by Yukawa couplings Y_ν. Then it explains simply and elegantly the smallness of m_ν in terms of two very distant mass scales, m_M and the Dirac mass, m_D, which

is retaled to v by $m_D = vY_\nu$. The properties of the neutrino mass eigenstates within the seesaw mechanism can then be easily derived by considering the limit $m_D << m_M$. For instance, in the one generation case, two Majorana mass eigenstates are obtained, one very light predominantly composed of ν_L and with mass around m_D^2/m_M, and the other one very heavy, predominantly composed of ν_R and with mass around m_M. Thus, in order to get the light neutrino mass in the $0.1 - 1$ eV range with large Yukawa couplings of the order of 1, this m_M must be of the order of 10^{14} GeV or even larger. The ν_R component of the light eigenstate and, correspondingly, the ν_L component of the heavy eigenstate are suppressed by very small factors of the order m_D/m_M, and can therefore be neglected. These above arguments can be generalised to the case of three generations with three right-handed neutrinos, and compatibility with neutrino data on masses and mixings can be succesfully accommodated within this seesaw model. Notice that is also possible to acccomodate neutrino data with just two ν_R, but instead we will consider here three ν_R for similarity to the rest of the fermions.

Another appealing feature of the seesaw mechanism with right-handed neutrinos is that a Majorana mass term provides the violation of lepton number which is needed for a succesful baryogenesis via leptogenesis [38]. Within the framework of leptogenesis, the observed baryon asymmetry of the Universe (BAU) is explained by the out-of-equilibrium decays of the same heavy right-handed neutrinos.

Nevertheless, the existence of these two separate mass scales, the electroweak scale and the m_M scale which, as previously said, elegantly explains the observed very light masses for neutrinos and also can provide succesful BAU, can induce a severe hierarchy problem, similarly to what happens in the SM. The so-called hierarchy problem of the SM is due to the unstability of the Higgs sector under radiative corrections if a new large energy scale associated to new physics is introduced, for instance, the Planck scale, M_P, where quantum gravitational effects become important. This unstability can be clearly seen in the radiative corrections to the Higgs mass, m_H. Naturality arguments suggest that this mass should be near the value of $v = 174$ GeV which sets the energy scale of the electroweak physics. However, m_H is known to get enormous quantum corrections from the virtual effects of every particle it couples to, which shift the starting values of the order of 100 GeV to values of the order of the new physics scale. It occurs because the two point function of the SM Higgs field is quadratically sensitive to the cut-off used to regulate the loop integral. When the SM is seen not as a fundamental theory but as an effective theory, this cut-off is interpreted as the energy scale at which new physics enters to alter the high-energy behavior of the theory. Therefore, if this scale is of the order M_P, where there is necessarily new physics involved, the above mentioned quantum correction to the Higgs mass are approximately 30 orders of magnitude larger than the starting $\mathcal{O}(100)$ GeV value.

In the case of seesaw models, the very massive right-handed neutrinos, which couple to the Higgs field, are the ones that produce the previously commented dangerous radiative corrections

to the Higgs mass. Therefore, a simple extension of the SM with three ν_R and the seesaw mechanism to generate light neutrino masses (called here SM-seesaw) is not fully satisfactory.

The favourite solution to this hierarchy problem is provided by the introduction of a new symmetry, called supersymmetry (SUSY) [39–41]. SUSY relates fermions and bosons in such a way that the new particles exactly compensate all the undesired quadratic contributions to scalar squared masses, solving the previously explained hierarchy problem of the SM. On the other hand, this SUSY extension of the SM may also incorporate the seesaw mechanism to succesfully generate the neutrino masses. These SUSY-seesaw models do not present therefore the hierarchy problem.

The Minimal Supersymmetric Standard Model (MSSM) is the minimal supersymmetric version of the SM which incorporates a supersymmetric partner per SM particle with the same mass and quantum numbers but with spin differing in one half unit [42–46]. Thus, a new boson partner is assigned to each SM fermion and, correspondingly, a new fermionic SUSY partner is added to each SM boson particle. It is called minimal because it has the minimal number of possible supersymmetries ($N = 1$) and therefore, the minimal SUSY particle content. With the introduction of this symmetry relating bosons and fermions it is possible to guarantee that all the quadratic divergences in the scalar self-energies do not arise. In order to implement the seesaw mechanism within the MSSM, one introduces in addition three right-handed neutrinos and the three corresponding superpartners, the sneutrinos. Simmilarly to the SM-seesaw case, one can succesfully accomadate the neutrino data within this MSSM-seesaw version as well. The improvement of MSSM-seesaw respect to the SM-seesaw is again the absence of the hierarchy problem.

However, it is well known that supersymmetry can not be an exact symmetry of the observed particle spectrum and, therefore, it must be broken in Nature, since no SUSY particles have been found up to now in the experiments [10]. Althought the SUSY breaking mechanism is not well known yet, the SUSY breaking terms that appear in the lagrangian must preserve the good properties of supersymmetry. In particular, these SUSY breaking terms must be *soft* [47] such that the required cancellation of quadratic divergences still occur. In addition, they must provide proper masses for the SUSY particles in order to make them heavier than their SM partners. But due to SUSY breaking some other problems can arise. In the most general scenario, one of the most serious problems is that there can be a misalignment between the fermion and sfermion mass matrices. In this case, these two matrices are not diagonal in flavour simultaneuosly and thus, unacceptable large flavour changing processes can be generated. This is called the SUSY flavour problem. This occurs because the mentioned fermion-sfermion missalignment leads to new intergenerational interactions at the tree level, which, when put into the loops of flavour changing procceses, can produce large contributions in contradiction with experimental data.

The best evidence of supersymmetry would be of course the discovery of SUSY particles in any of the present or next generation colliders. However, the fact that SUSY must be broken in Nature indicates that the masses of the supersymmetric particles must be heavier than their corresponding SM partners and could indeed be much larger than the present reached energies. Thus, it could happen that some of these particles are too heavy to be directly produced even in the next generation of colliders like the LHC. In this last case, an indication of the existence of supersymmetry will come first via indirect searches. These possible indirect searches of SUSY consist of looking for some relevant sensitivity to the contributions of these particles to radiative corrections in observables that are measured with high precision. By comparing the predictions of these observables including their radiative corrections with their experimental values, one could then obtain an indirect signal of supersymmetry. With this motivation in mind one should look for radiative corrections of observables that include supersymmetric particles inside the loops and that are enhanced with respect to their SM value.

One of the most striking phenomenological implications of SUSY-seesaw models is the prediction of sizable rates for lepton flavour violating (LFV) processes [48]. In these SUSY-seesaw models a new source of lepton flavour violation (LFV) appears in the off-diagonal elements of the slepton and sneutrino mass matrices, which can be radiatively generated. These can in turn produce a relevant missalignment between the slepton and lepton mass matrices and between the sneutrino and neutrino mass matrices, which can lead to important phenomenological consequences in processes that change lepton flavour. The size of these commented off-diagonal elements is governed by the strength of the neutrino Yukawa couplings which, as we have said, for Majorana neutrinos can be large, of the order of one. The LFV effects in the charged lepton processes are then induced by flavour violating slepton-lepton and sneutrino-neutrino interactions, appearing in SUSY-loop diagrams mediated by sleptons and sneutrinos, and can lead to LFV rates which are many orders of magnitude larger than those expected from the SM-seesaw.

An interesting connection between neutrino and LFV physics then follows, because the large neutrino Yukawa couplings, typical for Majorana neutrinos, induce important contributions to the rare LFV processes, which could be measured. In fact, these contributions are, in some cases, already at the reach of their present experimental sensitivity. In this sense, the radiative decays of τ and μ, $l_j \to l_i\,\gamma$ [49–52], the τ and μ decays into three leptons, $l_j \to 3\,l_i$ $(i \neq j)$ [49, 52, 53], and the LFV semileptonic τ decays like $\tau \to \mu\eta$ [54], as well as $\mu - e$ conversion in heavy nuclei [49, 52, 55], are among the most LFV interesting processes. LFV decays of Higgs bosons $H \to l_j\bar{l}_i$ [56] and LFV decays of Z gauge boson $Z \to l_j\bar{l}_i$ [57] are also of relevance in this context.

Concerning $\mu - e$ flavour violating processes, the most relevant, at present, are $\mu \to e\gamma$, $\mu \to 3e$ and $\mu - e$ conversion in nuclei. The current experimental bounds on the muon decays are $\mathrm{BR}(\mu \to e\gamma) < 1.2 \times 10^{-11}$ [58] and $\mathrm{BR}(\mu \to 3e) < 1.0 \times 10^{-12}$ [59]. Regarding $\mu - e$ con-

version in heavy nuclei, the most stringent constraints arise for Titanium and Gold, respectively with CR($\mu - e$, Ti)$< 4.3 \times 10^{-12}$ [60] and CR($\mu - e$, Au)$< 7 \times 10^{-13}$ [61]. In the future, one expects significant improvements in the sentitivies to these LFV rates. For instance, MEG aims at reaching a sensitivity for $\mu \to e\gamma$ of 10^{-13} [62] in the very near future, which could further be improved to 10^{-14} in the next 4-5 years [63]. Although the situation for BR($\mu \to 3e$) is less certain, one does not expect the sensitivities to be better than $10^{-13} - 10^{-14}$ [63]. Undoubtedly, the most challenging prospects concern the experimental sensitivities to $\mu - e$ conversion in Titanium nuclei. The dedicated J-PARC experiment PRISM/PRIME has anounced a remarkable improvement, albeit in a farer future, of 10^{-18} [64].

Regarding the tests of LFV in the $\tau - \mu$ sector, the most competitive one at present is $\tau \to \mu\gamma$, whose upper bound is now set to 1.6×10^{-8} [65–68]. Furthermore, the sensitivity to LFV in $\tau \to 3\mu$ has also improved notably in the last years. The present upper bounds from BELLE and BABAR collaborations are 3.2×10^{-8} [69] and 5.3×10^{-8} [70], respectively. This leptonic channel has the advantage over the radiative τ decay that provides a test not only of SUSY but also of the Higgs sector. It is remarkable that both $\tau \to 3\mu$ decay [53, 56, 71] and $\mu - e$ conversion [55] in nuclei can get important contributions from Higgs mediated diagrams in SUSY scenarios with large $\tan\beta$ and light MSSM Higgs bosons. LFV semileptonic τ decay channels are also of interest because of the recently reported sensitivities by BELLE and BABAR collaborations [72–75] that are, for some channels, already competitive with the LFV tau leptonic ones. Particullarly interesting is the semileptonic channel $\tau \to \mu\,\eta$, which is clearly sensitive to both SUSY and Higgs boson particles, and its present experimental bound is 5.1×10^{-8} [68].

In addition to the large number of parameters of the MSSM, the seesaw mechanism introduces 18 new parameters in the neutrino sector. As a first step to simplify the analysis of the LFV rates in a SUSY-seesaw model, we choose to work in the so-called constrained MSSM (CMSSM) (for a review see for instance [76]), assuming universality of the soft-SUSY breaking parameters at the scale of gauge coupling unification, M_X. This allows to reduce the unknown parameters in the SUSY sector to the five usual parameters of a minimal supergravity (mSUGRA) framework: M_0, $M_{1/2}$, A_0, $\tan\beta$ and sign μ. An interesting departure from the CMSSM-seesaw can be obtained by relaxing the universality hypothesis for the soft SUSY breaking masses of the Higgs sector. This partially constrained MSSM is commonly referred to as the Non Universal Higgs Mass (NUHM) scenario [77–89], and its enlarged version (including right handed neutrinos and sneutrinos) will be here designated NUHM-seesaw.

The main motivation of the present thesis is the study of the radiative corrections from the genuine SUSY particles to lepton flavour violating processes in the SUSY-seesaw scenarios. Our choice of channels with flavour change is due to the fact that in the SM, as stated above, these are extremely suppressed. In particular, we will focus our study on the LFV radiative decays $l_j \to l_i\,\gamma$, LFV Higgs boson decays $H \to l_j\,\bar{l}_i$, LFV leptonic decays into three leptons of equal

flavour $l_j \to 3\, l_i$, LFV semileptonic τ decays and $\mu - e$ conversion in nuclei. The reason to study these channels together is because, as we will see, there are interesting correlations among them in the SUSY-seesaw scenarios we work with. Our final goal will be to use these radiative corrections as an efficient way to test the SUSY and neutrino sectors. The possibility of testing the very large masses of the right-handed neutrinos with these LFV processes is particularly challenging since these particles are not accesible at colliders, nor they will be at future.

We will present here a complete one-loop computation of the LFV rates and will see that the loops from SUSY particles contribute relevantly to these observables. We will fully analyse the size of the branching ratios in terms of the SUSY and seesaw parameters and will explore in detail the restrictions imposed from the experimental bounds on the different LFV processes. In addition, we will determine which of these processes manifest a non-decoupling behaviour of the SUSY particles in the limit of large SUSY masses. We will see that this non-decoupling behaviour is particularly relevant for the Higgs boson mediated contributions to these LFV processes. Therefore, we will also analyse the sensitivity to the Higgs sector via the LFV processes.

The present work is organised as follows. In Chapter 1 the basic aspects of the theoretical framework in which we work are reviewed. First, we introduce the seesaw mechanism for neutrino mass generation, via right-handed neutrinos, and the different scenarios we consider at low energies. Next the most important features of the MSSM for this thesis are summarised and, later, we present the extensions of these SUSY models, enlarged with three right-handed neutrinos and their superpartnes. We also review the main features of the constrained scenarios considered in this thesis: CMSSM-seesaw and NUHM-seesaw. After that, the generation of slepton flavour mixing in SUSY-seesaw models is studied, paying special attention to the dependence of this mixing on seesaw parameters. Other phenomenological implications from constrained SUSY-seesaw models are also indicated, namely, thermal leptogenesis, charged lepton electric dipole moments (EDMs) and the SUSY contributions to the anomalous magnetic moment of the muon, a_μ. And, at the end of this chapter, we summarise the present experimental bounds on SUSY and Higgs boson masses.

In Chapter 2 we thoroughly perform a detailed study of LFV leptonic decays, namely, radiative decays $l_j \to l_i\, \gamma$, Higgs boson decays $H \to l_j\, \bar{l}_i$ (with H being the neutral MSSM Higgs bosons) and leptonic decays into three leptons of equal flavour $l_j \to 3\, l_i$, within the previous constrained SUSY-seesaw scenarios. Degenerate and hierarchical spectra are considered for both heavy and light neutrinos. First we extract the most relevant parameters and then systematically analyse the interesting relation between the leptonic mixing angle θ_{13} and LFV muon and tau decays, namely $l_j \to l_i\, \gamma$ and $l_j \to 3\, l_i$. We require compatibility with low energy neutrino data and with the present bounds on both LFV decays and charged lepton EDMs, and also study the resctrictions from the requirement of a successful baryogenesis via thermal leptogene-

sis. Particular emphasis is given to the implications that a future θ_{13} measurement [90–100] can have on our knowledge of the heavy neutrino sector.

In Chapter 3 we deeply study LFV semileptonic tau decay channels. In particular we analise the following semileptonic tau decays: $\tau \to \mu PP$ with $PP = \pi^+\pi^-, \pi^0\pi^0, K^+K^-, K^0\bar{K}^0$, $\tau \to \mu P$ with $P = \pi^0, \eta^0, \eta'^0$ and $\tau \to \mu V$ with $V = \rho^0, \phi$. The full one-loop computation is presented and the importance of the various contributions, the γ-, Z-, and Higgs bosons mediated ones are analysed. The hadronisation of quark bilinears is performed within the chiral framework. We further present here a set of approximate formulae for all the semileptonic channels which we believe can be useful for further comparison with present and future data.

In Chapter 4 we will focus on $\mu - e$ conversion in nuclei, working in the context of the CMSSM-seesaw and the NUHM-seesaw scenarios. We present a complete one-loop computation of the conversion rate for this process that includes the photon-, Z-boson, and Higgs-boson penguins, as well as box diagrams, and compare their size in the two considered scenarios. In these two scenarios we analyse the relevance of the various SUSY-seesaw parameters on the conversion rates. In the case of hierachical heavy neutrinos, an extremely high sensitivity of the rates to θ_{13} is indeed found. The last part of this work is devoted to the study of the interesting loss of correlation between the $\mu-e$ conversion and $\mu \to e\gamma$ rates that occurs in the non-universal scenario. In the case of large $\tan\beta$ and light H^0 Higgs boson, an enhanced ratio of the $\mu - e$ to $\mu \to e\gamma$ rates, with respect to the universal case is found, and this could be tested with the future experimental sensitivities.

The last part is devoted to summarise the main conclusions of this thesis.

This thesis is based on the results published in the articles [101], [102], [103], [104] and [105] and in the conference proceedings [106], [107], [108], [109], [110], [111] and [112].

Chapter 1

Supersymmetric models with seesaw mechanism

In this introductory chapter the theoretical framework in which we work is reviewed. First, the seesaw mechanism for neutrino mass generation is introduced. Next the most important features of the MSSM for this thesis are summarised and, later, the extension of the MSSM enlarged with three right-handed neutrinos and their superpartnes is presented. Specific constrained SUSY-seesaw scenarios that lead to the MSSM al low energies are considered. After that, the generation of slepton flavour mixing in these constrained SUSY-seesaw scenarios is studied, paying special attention to the dependence on seesaw parameters. Other phenomenological implications of these SUSY-seesaw models are also indicated, namely, thermal leptogenesis, charged lepton EDMs and the SUSY contributions to a_μ. The present experimental bounds on SUSY and Higgs boson masses are also included at the end of this chapter.

1.1 Neutrino masses and mixings generated by seesaw mechanism

The present strong evidence of lepton flavour changing neutrino oscillations [11–19] in solar and atmospheric neutrino data, as well as in reactor experiments, implies the existence of non-zero masses for the light neutrinos, and provides the first experimental clue for physics beyond the Standard Model. The experimentally suggested smallness of the neutrino masses can be explained in a very simple and elegant way by the seesaw mechanism of neutrino mass generation [23–37]. This mechanism can be implemented by the introduction of heavy right-handed Majorana neutrinos which are singlet under the SM gauge symmetry group and whose Majorana masses, m_{M_i}, can therefore be much higher than the SM particle masses. In this context, the

smallness of the light, mainly left-handed, neutrino masses appears naturally due to the induced large suppression by the ratio of the two very distant mass scales that are involved in the seesaw mass matrices, the Majorana matrix m_M and the Dirac matrix m_D. The latter is generated after electroweak symmetry breaking by $m_D = Y_\nu \langle H \rangle$, where Y_ν is the Yukawa matrix for couplings between the right- and left-handed neutrinos, and $\langle H \rangle = v = 174$ GeV is the SM Higgs boson vacuum expectation value (VEV). For the one generation case, and assuming a Yukawa coupling of order one, the suggested small neutrino mass value signals towards a new phyics mass scale of the order of $m_M \sim 10^{14}$ GeV, but the pattern and size of the seesaw mass parameters can vary much respect to this in the most general case of three generations.

The most general lagrangian that is invariant under $SU(2)_L \times U(1)_Y$ and that accounts for the lepton mass generation in presence of both Yukawa couplings and Majorana mass terms, can be written for the case of three generations as

$$-\mathcal{L}_{Y+M} = Y_e \bar{l}_L e_R H + Y_\nu \bar{l}_L \nu_R \tilde{H} + \frac{1}{2} m_M \nu_R^T C \nu_R + h.c.\,, \tag{1.1}$$

where m_M is the 3×3 Majorana mass matrix for right-handed neutrinos, Y_e is the 3×3 Yukawa coupling matrix for charged leptons and Y_ν is the 3×3 Yukawa coupling matrix for neutrinos. $\tilde{H}$ is defined as $\tilde{H} \equiv i\,\tau_2 H^*$, τ_2 being a Pauli matrix, C is the charge conjugation operator, which flips the sign of all the charge-like quantum numbers of a field (like electric charge, baryon number, lepton number, etc), leaving the rest of quantum numbers (e.g. chirality) intact, and i, j are generation indices which will be taken here to vary from one to three. The Yukawa terms will yield, after electroweak symmetry breaking, the charged lepton mass matrix, $m_e = Y^e \langle H \rangle$ and the neutrino Dirac mass matrix $m_D = Y^\nu \langle H \rangle$. Notice that one fundamental modification with respect to the SM that implies the addition of right-handed neutrinos with Majorana mass terms is that, as can be proved by gauge and Lorentz invariance and renormalizability, the lepton number is not a preserved symmetry any more.

A pedagogical way to study the phenomenological implications of right-handed neutrinos with Majorana mass terms is to consider first the one-generation case [113], where m_M and m_D are just numbers instead of 3×3 matrices. In this case, the neutrino mass matrix that is defined in the electroweak basis is a 2×2 matrix of the form

$$\mathcal{M} = \begin{pmatrix} 0 & m_D \\ m_D & m_M \end{pmatrix}, \tag{1.2}$$

whose eigenvalues are

$$m_{1,2} = \frac{m_M}{2} \mp \sqrt{\left(\frac{m_M}{2}\right)^2 + m_D^2}\,, \tag{1.3}$$

and the angle that defines the rotation to the physical basis is given by

$$\tan 2\theta = \frac{2 m_D}{m_M}\,. \tag{1.4}$$

We introduce the fields χ_L through

$$\begin{pmatrix} \nu_L \\ \nu_L^c \end{pmatrix} = \begin{pmatrix} \cos\theta & \sin\theta \\ -\sin\theta & \cos\theta \end{pmatrix} \begin{pmatrix} \chi_{1L} \\ \chi_{2L} \end{pmatrix}, \tag{1.5}$$

and therefore, the corresponding mass eigenstates can be written as

$$\chi_1 = \chi_{1L} + \eta_1 (\chi_{1L})^c\,, \qquad \chi_2 = \chi_{2L} + \eta_2 (\chi_{2L})^c\,, \tag{1.6}$$

with $\eta_{1,2} = 1$ or -1 for $m_{1,2} > 0$ or < 0 respectively, $\chi_{1,2\,L}$ are the left-handed projections, $\chi_{iL} = \frac{1}{2}(1-\gamma_5)\chi_i$, and $(\chi_{1,2\,L})^c$ are their corresponding transformed fields under particle-antiparticle conjugation operation $\hat{C}$. Notice that the two mass eigenstates behave as Majorana fermions since under $\hat{C}$ they transform as $\chi^c_{1,2} = \eta_{1,2}\chi_{1,2}$, that is, they are $\hat{C}$-eigenstates with eigenvalues $\eta_{1,2}$ respectively, that determine the relative CP parities of χ_1 and χ_2. As for the counting of degrees of freedom, one starts in the electroweak basis with a total of four, ν_L, ν_R, $(\nu_L)^c = \nu_R^c$ and $(\nu_R)^c = \nu_L^c$, and ends up with two mass eigenstates, χ_1 and χ_2, with two degrees of freedom each, as corresponds to massive Majorana fermions. The generalisation of this counting to n generations will lead to $2n$ massive Majorana neutrinos. In the case that will be considered here with three generations, the number of physical Majorana neutrinos will be therefore six.

Once we have introduced non-zero masses for the neutrinos, one may also wonder why these are so particularly small with respect to the masses of other fundamental fermions. The seesaw mechanism provides a very simple and elegant explanation of this smallness. More specifically, it relates the smallness of the neutrino masses with the existence of very large mass scales, given by m_M, as compared to m_D, which are driven by the electroweak scale, $v = \langle H \rangle = 174$ GeV. The violation of the total lepton number being introduced by the right-handed Majorana mass term is therefore assumed to occur at these large m_M scale.

The properties of the neutrino mass eigenstates generated by the seesaw mechanism can be easily deduced in the one generation case by taking the limit $m_D \ll m_M$ in the previous formulae (1.2)-(1.6). This leads to the simple expresions [113]:

$$\theta \approx \frac{m_D}{m_M} << 1,\ m_1 \approx -\frac{m_D^2}{m_M},\ m_2 \approx m_M\,, \tag{1.7}$$

$$\chi_1 \approx \nu_L + \eta_1 (\nu_L)^c,\ \chi_2 \approx (\nu_R)^c + \eta_2 \nu_R\,. \tag{1.8}$$

It is clear that there is one light Majorana mass eigenstate χ_1 composed predominantly of ν_L and one heavy one χ_2 mainly composed of ν_R. The ν_R component in χ_1 and the ν_L component in χ_2 are supressed by a very small factor of the order of $\frac{m_D}{m_M}$.

Next we review the mass parameters and mixings in the neutrino sector of the seesaw models with three right-handed neutrinos, and relate them to the physical light neutrino masses and neutrino mixing angles which are extracted from neutrino data.

We start with the Yukawa-sector of the SM-seesaw that contains the three left-handed SM neutrinos $\nu^0_{L,i}$ and the three extra right-handed massive neutrinos $\nu^0_{R,i}$, whose Yukawa interactions provide, after spontaneous electroweak symmetry breaking, together with the right-handed neutrino masses, the following mass Lagrangian containing the Dirac and Majorana mass terms,

$$-L^{\nu}_{mass} = \frac{1}{2}(\overline{\nu^0_L}, (\overline{\nu^0_R})^C) M^{\nu} \begin{pmatrix} (\nu^0_L)^C \\ \nu^0_R \end{pmatrix} + h.c.\,, \tag{1.9}$$

where

$$M^{\nu} \;=\; \begin{pmatrix} 0 & m_D \\ m_D^T & m_M \end{pmatrix}. \tag{1.10}$$

Here m_D is the 3×3 Dirac mass matrix that is related to the 3×3 Yukawa coupling matrix Y_ν and the SM Higgs vacum expectation value by $m_D = Y_\nu \langle H\rangle$; and m_M is the 3×3 Majorana mass matrix for the right-handed massive neutrinos that is real, non singular and symmetric.

The mass matrix M^ν is a 6×6 complex symmetric matrix that can be diagonalised by a 6×6 unitary matrix U^ν in the following way:

$$U^{\nu T} M^{\nu} U^{\nu} = \hat{M}^{\nu} = \mathrm{diag}\,(m_{\nu_1}, m_{\nu_2}, m_{\nu_3}, m_{N_1}, m_{N_2}, m_{N_3})\,. \tag{1.11}$$

This gives three light Majorana neutrino mass eigenstates ν_i, with masses m_{ν_i} $(i = 1,2,3)$, and three heavy ones N_i, with masses m_{N_i} $(i = 1,2,3)$, which are related to the electroweak eigenstates via

$$\begin{pmatrix} \nu^0_L \\ (\nu^0_R)^C \end{pmatrix} \;=\; U^{\nu *} \begin{pmatrix} \nu_L \\ N_L \end{pmatrix} \quad \text{and} \quad \begin{pmatrix} (\nu^0_L)^C \\ \nu^0_R \end{pmatrix} \;=\; U^{\nu} \begin{pmatrix} \nu_R \\ N_R \end{pmatrix}. \tag{1.12}$$

The seesaw mechanism for neutrino mass generation assumes a large separation between the two mass scales involved in m_D and m_M matrices. More specifically, we shall assume here that all matrix elements of m_D are much smaller than those of m_M, $m_D << m_M$, and we will perform an analytical expansion of all relevant interaction parameters and observables in power series of a matrix defined as

$$\xi \;\equiv\; m_D m_M^{-1}\,. \tag{1.13}$$

In particular, the diagonalisation of the mass matrix M^ν can be solved in power series of ξ. For simplicity, we choose to work here and in the rest of this thesis, in a basis where the right-handed Majorana mass matrix, m_M, and the charged lepton mass matrix, M^l, are flavour diagonal. By working to the lowest order of these power series expansions, M^ν is first diagonalised by blocks leading to the following neutrino 3×3 matrices:

$$\begin{aligned} m_\nu &= -m_D \xi^T + \mathcal{O}(m_D \xi^3) \simeq -m_D m_M^{-1} m_D^T\,, \\ m_N &= m_M + \mathcal{O}(m_D \xi) \simeq m_M\,. \end{aligned} \tag{1.14}$$

Here, m_N is already diagonal, but m_ν is not yet diagonal. The rotation from this flavour basis to the mass eigenstate basis is finally given by the Pontecorvo-Maki-Nakagawa-Sakata (PMNS) unitary matrix [20–22], $U_{\rm PMNS}$. Thus,

$$\begin{aligned} m_\nu^{\rm diag} &= U_{\rm PMNS}^T m_\nu U_{\rm PMNS} = {\rm diag}\,(m_{\nu_1}, m_{\nu_2}, m_{\nu_3})\,, \\ m_N^{\rm diag} &= m_N = {\rm diag}\,(m_{N_1}, m_{N_2}, m_{N_3})\,, \end{aligned} \tag{1.15}$$

and correspondingly the diagonalisation of M^ν in eqs. (1.10) and (1.11) can be performed by the following unitary 6×6 matrix,

$$U^\nu \;=\; \begin{pmatrix} (1 - \frac{1}{2}\xi^*\xi^T) U_{\rm PMNS} & \xi^* (1 - \frac{1}{2}\xi^T\xi^*) \\ -\xi^T (1 - \frac{1}{2}\xi^*\xi^T) U_{\rm PMNS} & (1 - \frac{1}{2}\xi^T\xi^*) \end{pmatrix} + \mathcal{O}(\xi^4)\,. \tag{1.16}$$

We use the standard parameterisation for the $U_{\rm PMNS}$ matrix given by

$$U_{\rm PMNS} = \begin{pmatrix} c_{12}\, c_{13} & s_{12}\, c_{13} & s_{13}\, e^{-i\delta} \\ -s_{12}\, c_{23} \,-\, c_{12}\, s_{23}\, s_{13}\, e^{i\delta} & c_{12}\, c_{23} \,-\, s_{12}\, s_{23}\, s_{13}\, e^{i\delta} & s_{23}\, c_{13} \\ s_{12}\, s_{23} \,-\, c_{12}\, c_{23}\, s_{13}\, e^{i\delta} & -c_{12}\, s_{23} \,-\, s_{12}\, c_{23}\, s_{13}\, e^{i\delta} & c_{23}\, c_{13} \end{pmatrix} \times V\,, \tag{1.17}$$

with

$$V \;=\; {\rm diag}\,(e^{-i\frac{\phi_1}{2}}, e^{-i\frac{\phi_2}{2}}, 1)\,, \tag{1.18}$$

and $c_{ij} \equiv \cos\theta_{ij}$, $s_{ij} \equiv \sin\theta_{ij}$. θ_{ij} are the light neutrino flavour mixing angles, δ is the Dirac phase and $\phi_{1,2}$ are the Majorana phases.

Now, in order to make contact with the experimental data, we use the method proposed in [114]. It provides a simple way to reconstruct the Dirac mass matrix by using as inputs the physical light and heavy neutrino masses, the $U_{\rm PMNS}$ matrix, and a general complex and orthogonal matrix R. With our signs and matrix conventions this relation can be written as

$$m_D = i \sqrt{m_N^{\rm diag}}\, R\, \sqrt{m_\nu^{\rm diag}}\, U_{\rm PMNS}^\dagger\,, \tag{1.19}$$

where $R^T R = R R^T = \mathbb{1}$.

Thus, instead of proposing directly possible textures for m_D (i.e. for Y^ν), one proposes possible values for $m_{N_1}, m_{N_2}, m_{N_3}$ and R, and sets $m_{\nu_1}, m_{\nu_2}, m_{\nu_3}$ and $U_{\rm PMNS}$ to their suggested values from the experimental data. Notice that for $R = \mathbb{1}$, the lepton flavour mixing in $U_{\rm PMNS}$ is the unique source of lepton flavour mixing in m_D. Correspondingly, any hypothesis for R different from the unit matrix will lead to an additional lepton flavour mixing in m_D. Notice also that the previous Eq. (1.19) is established at the right-handed neutrino mass scale m_M, so that the quantities appearing in it are indeed the renormalised ones, namely, $m_\nu^{\rm diag}(m_M)$ and $U_{\rm PMNS}(m_M)$. These latter are obtained here by means of the renormalisation group equations (RGEs) and by starting the running from their corresponding renormalised values at m_Z,

$m_\nu^{\rm diag}\,(m_Z)$ and $U_{\rm PMNS}\,(m_Z)$ which are identified respectively with the physical $m_\nu^{\rm diag}$ and $U_{\rm PMNS}$ from neutrino data.

In this thesis we will consider the following plausible scenarios, for the neutrino sector, being all compatible with present data.

- Light neutrino sector:

$$\begin{aligned} &\text{Quasi-degenerate case:} && m_{\nu_1}\,,\ m_{\nu_2} = m_{\nu_1} + \frac{\Delta m^2_{\rm sol}}{2m_{\nu_1}}\,,\ m_{\nu_3} = m_{\nu_1} + \frac{\Delta m^2_{\rm atm}}{2m_{\nu_1}}\,, \\ &\text{Hierarchical case:} && m_{\nu_1} \ll m_{\nu_2}\,,\ m_{\nu_2} = \sqrt{\Delta m^2_{\rm sol}}\,,\ m_{\nu_3} = \sqrt{\Delta m^2_{\rm atm}}\,. \end{aligned} \tag{1.20}$$

- Heavy neutrino sector:

$$\begin{aligned} &\text{Degenerate case:} && m_{N_1} = m_{N_2} = m_{N_3} = m_N\,, \\ &\text{Hierarchical case:} && m_{N_1} \ll m_{N_2} \ll m_{N_3}\,. \end{aligned} \tag{1.21}$$

For the numerical estimates in this thesis we will use the following input values for the light neutrino mass squared differences and the angles in the $U_{\rm PMNS}$ matrix:

$$\begin{aligned} &\Delta\, m^2_{\rm sol} \,=\, 8\,\times 10^{-5}\ {\rm eV}^2\,, \qquad \Delta\, m^2_{\rm atm} \,=\, 2.5\,\times 10^{-3}\ {\rm eV}^2\,, \\ &\theta_{12} \,=\, 30^\circ\,, \quad \theta_{23} \,=\, 45^\circ\,, \quad \theta_{13} \lesssim 10^\circ\,, \qquad \delta \,=\, \phi_1 \,=\, \phi_2 \,=\, 0\,, \end{aligned} \tag{1.22}$$

which are compatible with present experimental data (see, for instance, the analysis of [115–117]). For quasi-degenerate light neutrinos we will further set $m_{\nu_1} = 0.2$ eV and for hierarchical light neutrinos several choices for the tiny m_{ν_1} will be set. Some results, in this latter case, will be focused on the particular choice $m_{\nu_1} = 0$.

Regarding the R matrix, we will consider the following parameterisation:

$$R = \begin{pmatrix} c_2c_3 & -c_1s_3 - s_1s_2c_3 & s_1s_3 - c_1s_2c_3 \\ c_2s_3 & c_1c_3 - s_1s_2s_3 & -s_1c_3 - c_1s_2s_3 \\ s_2 & s_1c_2 & c_1c_2 \end{pmatrix}\,, \tag{1.23}$$

where $c_i \equiv \cos\theta_i$, $s_i \equiv \sin\theta_i$ and θ_1, θ_2 and θ_3 are arbitrary complex angles. This parametrisation was proposed in [114] for the study of $\mu \to e\gamma$ decays and represents the most general parameterisation of an orthogonal complex matrix in terms of three complex angles. We will choose this parameterisation for most of this work. We will also consider the simplest possibility $R = \mathbb{1}$, as a reference case. Some estimates will be alternatively done, for comparison, with the following parameterisation:

$$R = e^{iA}O\,, \tag{1.24}$$

with $O = 1$, and

$$A = \begin{pmatrix} 0 & a & b \\ -a & 0 & c \\ -b & -c & 0 \end{pmatrix} . \tag{1.25}$$

Here, a, b, and c are three real parameters that are constrained by perturbativity of the Yukawa couplings. In particular, for $a = b = c \equiv k$ and $m_{\nu_{1,2,3}} \simeq 0.2$ eV, it leads to $k < (1.4, 0.9, 0.3)$ for $m_{N_{1,2,3}} \simeq (10^{10}, 10^{12}, 10^{14})$ GeV respectively.

As we have indicated in the introduction, there is, however, one negative aspect in the standard version of the models with seesaw mechanism. It is that the presence of the two distant mass scales can lead to a severe hierarchy problem which requires the introduction of supersymmetry to be solved. In the SUSY-seesaw models the hierarchy between m_M and the electroweak scale is stabilised by the new contributions of the SUSY partners of the right-handed and left-handed neutrinos. Thus, the SUSY-seesaw models, and particularly the simplest version given by the Minimal Supersymmetric Standard Model (MSSM), are becoming more popular.

1.2 The Minimal Supersymmetric Standard Model

This is an introductory section to the Minimal Supersymmetric Standard Model (MSSM), where the most important features of this model for this thesis are summarised. First of all, the MSSM Lagrangian and fields in the interaction eigenstate basis are introduced, with an special discussion about the soft SUSY breaking terms. Then, the mixing between fields with the same quantum numbers and the mass spectrum with the relevant interaction terms are studied in detail, paying special attention to the slepton sector, the gaugino sector and the Higgs sector.

The Minimal Supersymmetric Standard Model is the simplest supersymmetric extension of the Standard Model [42–46], where "minimal" means that it contains the minimal number of superfields and interactions ($N = 1$). The main motivation for introducing low-energy supersymmetry is the cancellation of quadratic divergences (for a full review see [118]), which allows to solve the hierarchy problem. The contribution of fermion loops to the two-point function of the SM Higgs field is quadratically dependent on the cut-off Λ. If this scale Λ is replaced by the Planck mass M_P, the resulting correction to the Higgs mass is 30 orders of magnitud larger than the tree level SM Higgs mass, which should not be in any case higher than 1 TeV in order to preserve unitarity. Here one can see the different consequences between the logarithmic and the quadratic divergences. As a particular example of the first ones, there are the corrections to the electron mass that are small being logarithmic in Λ and proportional to the electron mass. In contrast, the corrections to the scalar masses contain the quadratic dependence on Λ. In particular, the contribution from fermions, with mass m_F and couplings to Higgs δ_F, to the two

point function of the SM Higgs,

$$\delta m_H^2 = \frac{|\delta_F|^2}{16\pi^2}\left(-2\Lambda^2 + 6m_F^2 \log\frac{\Lambda}{m_F}\right), \tag{1.26}$$

does not depend on the Higgs mass, m_H, which is related to the fact that setting $m_H = 0$ does not enlarge the symmetry group of the SM. One can then conclude that there is nothing in the SM that protects the Higgs boson mass of being too large, in a similar way as the photon or the electron masses are protected. This difficulty of getting the Higgs mass stable under the Λ^2-dependent radiative corrections is referred to in the literature as the hierarchy problem of the Standard Model.

One elegant way to sort out this problem is by the introduction of a new symmetry called supersymmetry. In supersymmetry, the problem explained above is solved by the introduction of additional degrees of freedom that provide the needed compensating contributions to the two-point function of the SM Higgs, due to the fact that supersymmetry relates fermions and bosons and requires to have the same total number of bosonic and fermionic degrees of freedom. More specificaly, supersymmetry asigns to each Standard Model particle a new particle, the supersymmetric partner, which has its same quantum numbers and mass but with a difference in spin of one half unit. Thus, each fermion has its corresponding scalar partner, one for the left-handed fermion and another one for the right-handed fermion, each gauge boson has its fermionic partner and each scalar Higgs particle has its fermionic partner. Then, each new scalar particle S with mass m_S which couples to the Higgs with a lagrangian term $-\delta_S|H|^2|S|^2$ gives a correction to the Higgs mass given by

$$\delta m_H^2 = \frac{\delta_S}{16\pi^2}\left(\Lambda^2 - 2m_S^2 \log\frac{\Lambda}{m_S}\right) + \dots . \tag{1.27}$$

Since the couplings are related by SUSY as $\delta_S = |\delta_F|^2$ and there are two scalars per fermion, then the $\mathcal{O}(\Lambda^2)$ terms cancel in the total correction to the Higgs mass. In summary, the fact that the particle content of the SM is doubled [42–46] and that there are precise relations among the couplings of particles and their superpartners imposed by supersymmetry, leads to the interesting result that in SUSY models the Higgs bosons mass corrections are free of quadratic divergences and therefore the hierarchy problem is not present.

One crucial point in the field content of the MSSM is the choice of the Higgs sector. As in the SM, we need to break $SU(2)_L \times U(1)_Y$ invariance by $SU(2)_L$ doublet scalars with hypercharge $|Y| = 1$. Indeed, one needs at least two such scalar fields: H_1 with hypercharge $Y = -1$ and H_2

with hypercharge $Y = 1$, whose notation in this thesis is

$$\begin{aligned} H_1 &\equiv \begin{pmatrix} H_1^0 \\ H_1^- \end{pmatrix} \equiv \begin{pmatrix} (\phi_1^0 - i\chi_1^0)/\sqrt{2} \\ -\phi_1^- \end{pmatrix}, \\ H_2 &\equiv \begin{pmatrix} H_2^+ \\ H_2^0 \end{pmatrix} \equiv \begin{pmatrix} \phi_2^+ \\ (\phi_2^0 + i\chi_2^0)/\sqrt{2} \end{pmatrix}. \end{aligned} \tag{1.28}$$

There are at least two important reasons for this choice:

- A model with one single Higgs doublet superfield has non-vanishing gauge anomalies associated with fermion triangle diagrams. If one adds just one single higgsino doublet, the SUSY partner of the single scalar Higgs doublet, anomalies will be introduced, as it is a new fermion that also contributes. One needs to add a second higgsino doublet, the SUSY partner of the second scalar Higgs doublet, with opposite hypercharge to cancel the contribution of the first one.

- supersymmetry requires that the superpotential be an analytic funcition of the superfields. Therefore it cannot contain the hermitian conjugate of a Higgs superfield and it is then not possible to give masses to both up and down-type quarks without introducing a second Higgs doublet superfield. Here H_1 will be responsible for the masses of the down-type fermions and H_2 the corresponding one for the up-type fermions.

If a theory is invariant under supersymmetric transformations it is required that the particles and their corresponding superpartners have identical masses. This is not realistic since, for instance, no selectron, the scalar partner of the electron, with mass 511 KeV or smuon, the scalar partner of the muon, with mass 106 MeV, have ever been found. Therefore, if supersymmetry exists in nature, it must be broken. Even thought the mechanism of SUSY breaking is still unknown to date, it has to be implemented without introducing new quadratic divergences that could spoil the previously commented solution provided by SUSY to the hierarchy problem. This job is done by a set of specific SUSY breaking terms that are called *soft* supersymmetry breaking terms [47], or soft terms in short. These *soft* terms provide succesfully both the masses of the SUSY particles, in order to get them heavier than their corresponding SM partners, and the required spontaneous electroweak symmetry breaking at low energies, necessary to explain the mass generation of the SM particles.

There is one additional property of the MSSM which makes it to be less constraint than the SM. It is well known that if one imposes the invariance of the interaction lagrangian of the SM particles under the symmetry $SU(3)_C \times SU(2)_L \times U(1)_Y$, one finds that all terms of dimension 4 or less automatically preserve the baryonic number (B) and the leptonic number (L). This is

not the case in the MSSM, and the usual way to get them preserved in this model is by the introduction, *ad hoc*, of a discrete symmetry called R-parity. The R-parity is a multiplicative quantum number defined in terms of the Baryonic and Leptonic numbers, B and L, and the Spin, S, as R= $(-1)^{3(B-L)+2S}$. This leads to R = 1 for SM and Higgs particles and R= −1 for their SUSY partners. Besides, the fact that R-parity must be conserved implies that SUSY particles can only be produced in pairs from SM particles and also that the lightest SUSY particle must be stable. It is important also to notice that any set of states with the same spin, B, L and $SU(3)_C \times U(1)_{EM}$ quantum numbers can mix so one has to diagonalise their mass matrices to obtain the mass eigenstates and the corresponding mass eigenvalues.

We finally present the MSSM spectrum that contains the SM particle content, extended with two Higgs doublets, and all their corresponding SUSY partners. There are the SUSY partners of the quarks, called squarks, the ones of the charged leptons and neutrinos, called charged sleptons and sneutrinos respectivelly, the gluinos being the superpartners of the gluons, and the SUSY partners of the electroweak gauge bosons, called gauginos, that after mixing with the SUSY partners of the Higgs bosons, called Higgsinos, give rise to the mass eigenstates named charginos and neutralinos. In Table 1.1, the full MSSM spectrum is illustrated in both the interaction eigenstate basis and the mass eigenstate basis. Here, the standard notation is used as explained, for instance, in [43, 44].

1.2.1 MSSM Lagrangian

The MSSM Lagrangian can be splitted into two parts: the SUSY-preserving part, $\mathcal{L}_{\rm SUSY}$ and the SUSY breaking part, $\mathcal{L}^{\rm break}_{\rm SUSY}$,

$$\mathcal{L}_{\rm MSSM} = \mathcal{L}_{\rm SUSY} + \mathcal{L}^{\rm break}_{\rm SUSY}\,. \tag{1.29}$$

As usual, the Lagrangian does not contain any interaction term with mass dimension higher than four, in order to preserve the renormalisability of the theory.

$\mathcal{L}_{\rm SUSY}$ is invariant under SUSY and $SU(3)_C \times SU(2)_L \times U(1)_Y$ gauge transformations and contains the MSSM Lagrangian for fermions and gauge bosons and the associated Lagrangian for sfermions and gauginos. It also includes all the renormalisable interactions among supersymmetric particles and among these particles and the SM ones. As the expression for the full supersymmetric version of the SM Lagrangian is rather lengthy (see for instance [45]) we will specify just the interaction terms that are relevant for the present work. Furthermore, we choose to writte these relevant terms in the mass eigenstate basis which is the most convenient one for the purpose of this thesis.

On the other hand, $\mathcal{L}_{\rm SUSY}$ contains as well the Higgs sector Lagrangian and the associated Lagrangian for Higgsinos. The Higgs sector Lagrangian includes the Higgs self-interaction terms and the interactions between these particles and the rest of the MSSM spectrum. In particular,

	SUSY particles			
Extended Standard Model spectrum	$SU(3)_C \times SU(2)_L \times U(1)_Y$ interaction eigenstates		Mass eigenstates	
	Notation	Name	Notation	Name
$q = u, d, s, c, b, t$ $l = e, \mu, \tau$ $\nu = \nu_e, \nu_\mu, \nu_\tau$	$\tilde{q}_L, \tilde{q}_R$ $\tilde{l}_L, \tilde{l}_R$ $\tilde{\nu}$	squarks sleptons sneutrino	$\tilde{q}_1, \tilde{q}_2$ $\tilde{l}_1, \tilde{l}_2$ $\tilde{\nu}$	squarks sleptons sneutrino
g	$\tilde{g}$	gluino	$\tilde{g}$	gluino
$W^\pm$ $H_1^+ \supset H^+$ $H_2^- \supset H^-$	$\tilde{W}^\pm$ $\tilde{H}_1^+$ $\tilde{H}_2^-$	wino higgsino higgsino	$\tilde{\chi}_i^\pm$ (i=1,2)	charginos
γ Z $H_1^o \supset h^0$, H^0, A^0 $H_2^o \supset h^0$, H^0, A^0 W^3 B	$\tilde{\gamma}$ $\tilde{Z}$ $\tilde{H}_1^o$ $\tilde{H}_2^o$ $\tilde{W}^3$ $\tilde{B}$	photino zino higgsino higgsino wino bino	$\tilde{\chi}_j^o$ (j=1,...,4)	neutralinos

Table 1.1: Summary of the MSSM spectrum.

it incorporates the Yukawa interactions between Higgs bosons and fermions and the Higgs potential. The restrictions imposed by SUSY determine the Higgs-bosons self interactions in terms of the $SU(2)_L$ and $U(1)_Y$ gauge couplings, g and g' respectively, such that the SUSY-preserving part of the MSSM Higgs potential is given by

$$V_{\rm SUSY}^{\rm Higgs} = |\mu|^2 \left(|H_1|^2 + |H_2|^2\right) + \frac{1}{8}(g^2 + g'^2)\left(|H_1|^2 - |H_2|^2\right)^2 + \frac{1}{2}g^2|H_1^* H_2|^2 \,. \tag{1.30}$$

Notice that the mass parameter μ is a new mass parameter introduced by SUSY in this potential and that the strength of the self-interactions in the Higgs sector are given in terms of the gauge couplings g and g'. Notice also that the SUSY-preserving potential of Eq. (1.30) is positive

and presents just a trivial minimum; therefore it can not produce the wanted spontaneous electroweak symmetry breaking. This is a common feature in supersymmetric theories and the introduction of the appropriate soft SUSY breaking terms in the Higgs potential, as already mentioned, is mandatory in order to implement the $SU(2)_L \times U(1)_Y \to U(1)_{\rm EM}$ spontaneous symmetry breaking.

The electroweak symmetry breaking will be defined in terms of the two neutral Higgs vacuum expectation values (VEVs)

$$\langle H_1^0 \rangle = v_1 = v \cos\beta, \quad \langle H_2^0 \rangle = v_2 = v \sin\beta \tag{1.31}$$

where v is set by the m_W and m_Z values as in the SM

$$v^2 = \frac{2m_Z^2}{g^2 + g'^2} = \frac{2m_W^2}{g^2}\,. \tag{1.32}$$

The fact that there are two doublets, instead of one, introduces the extra parameter

$$\tan\beta \equiv \frac{v_2}{v_1}\,. \tag{1.33}$$

Regarding the Yukawa interactions between Higgs particles and fermions, they are derived as usual from the superpotential W,

$$W = \hat{U}^c\, Y_u\, \hat{Q}\, \hat{H}_2 + \hat{D}^c\, Y_d\, \hat{Q}\, \hat{H}_1 + \hat{E}^c\, Y_l\, \hat{L}\, \hat{H}_1 + \mu \hat{H}_1 \hat{H}_2\,, \tag{1.34}$$

where Y_u, Y_d and Y_l are the Yukawa couplings of quarks and leptons which are generically 3×3 matrices in the flavour space. After the electroweak symmetry breaking, they are related to the physical masses. For instance, in the one generation case these relations are

$$\begin{aligned} Y_u &= \frac{g m_u}{\sqrt{2} m_W \sin\beta} = \frac{m_u}{v_2} \\ Y_d &= \frac{g m_d}{\sqrt{2} m_W \cos\beta} = \frac{m_d}{v_1} \\ Y_l &= \frac{g m_l}{\sqrt{2} m_W \cos\beta} = \frac{m_l}{v_1} \end{aligned} \tag{1.35}$$

In summary, the set of parameters that appear in this SUSY preserving interaction Lagrangian $\mathcal{L}_{\rm SUSY}$ are:

- the gauge couplings g_s, g and g' corresponding to the $SU(3)_C$, $SU(2)_L$ and $U(1)_Y$ gauge groups, respectively,
- the Yukawa couplings that describe the interaction between fermions and Higgs bosons, and

- the μ mass parameter.

The SUSY breaking Lagrangian $\mathcal{L}_{\rm SUSY}^{\rm break}$ is not completely determined and its explicit form and the set of involved parameters depend on the particular SUSY breaking mechanism. Since this mechanism is not yet known, one usually assumes a set of breaking terms of the most general form, without inquiring into their origins, that are fixed just by demanding $SU(3)_C \times SU(2)_L \times U(1)_Y$ invariance and by requiring them to be soft in order the previously mentioned cancellation of quadratic divergences be maintained.

These soft SUSY breaking terms were classified by Girardello and Grisaru [47] into four different types: Majorana mass terms for gauginos, scalar mass terms for sfermions and Higgs particles, interaction terms among three scalar particles, with corresponding trilinear couplings, and scalar-scalar bilinear terms. In the MSSM, the complete set of soft SUSY breaking terms that preserve the $SU(3)_C \times SU(2)_L \times U(1)_Y$ gauge invariance are

$$
\begin{aligned}
V_{\rm soft} &= m_1^2|H_1|^2 + m_2^2|H_2|^2 - m_{12}^2\left(\epsilon_{ij}H_1^iH_2^j + \text{h.c.}\right) \\
&+ m_{\tilde{Q},q}^2\left[\tilde{q}_L^*\tilde{q}_L\right] + m_{\tilde{L},l}^2\left[\tilde{l}_L^*\tilde{l}_L\right] \\
&+ m_{\tilde{U},u}^2\tilde{u}_R^*\tilde{u}_R + m_{\tilde{U},c}^2\tilde{c}_R^*\tilde{c}_R + m_{\tilde{U},t}^2\tilde{t}_R^*\tilde{t}_R \\
&+ m_{\tilde{D},d}^2\tilde{d}_R^*\tilde{d}_R + m_{\tilde{D},s}^2\tilde{s}_R^*\tilde{s}_R + m_{\tilde{D},b}^2\tilde{b}_R^*\tilde{b}_R \\
&+ m_{\tilde{E},e}^2\tilde{e}_R^*\tilde{e}_R + m_{\tilde{E},\mu}^2\tilde{\mu}_R^*\tilde{\mu}_R + m_{\tilde{E},\tau}^2\tilde{\tau}_R^*\tilde{\tau}_R \\
&+ \frac{g}{\sqrt{2}m_W}\epsilon_{ij}\left[\frac{m_eA_e}{\cos\beta}H_1^i\tilde{l}_L^j\tilde{e}_R^* + \frac{m_\mu A_\mu}{\cos\beta}H_1^i\tilde{l}_L^j\tilde{\mu}_R^* + \frac{m_\tau A_\tau}{\cos\beta}H_1^i\tilde{l}_L^j\tilde{\tau}_R^*\right. \\
&+ \frac{m_dA_d}{\cos\beta}H_1^i\tilde{q}_L^j\tilde{d}_R^* - \frac{m_uA_u}{\sin\beta}H_2^i\tilde{q}_L^j\tilde{u}_R^* + \frac{m_sA_s}{\cos\beta}H_1^i\tilde{q}_L^j\tilde{s}_R^* - \frac{m_cA_c}{\sin\beta}H_2^i\tilde{q}_L^j\tilde{c}_R^* \\
&+ \left.\frac{m_bA_b}{\cos\beta}H_1^i\tilde{q}_L^j\tilde{b}_R^* - \frac{m_tA_t}{\sin\beta}H_2^i\tilde{q}_L^j\tilde{t}_R^* + h.c.\right] \\
&+ \frac{1}{2}\left[M_3\bar{\tilde{g}}^\alpha\tilde{g}^\alpha + M_2\bar{\tilde{W}}^a\tilde{W}^a + M_1\bar{\tilde{B}}\tilde{B}\right], \qquad (1.36)
\end{aligned}
$$

where,

$$
\tilde{q}_L = \begin{pmatrix}\tilde{u}_L\\ \tilde{d}_L\end{pmatrix}, \begin{pmatrix}\tilde{c}_L\\ \tilde{s}_L\end{pmatrix}, \begin{pmatrix}\tilde{t}_L\\ \tilde{b}_L\end{pmatrix}, \qquad (1.37)
$$

and

$$
\tilde{l}_L = \begin{pmatrix}\tilde{\nu}_{L,e}\\ \tilde{e}_L\end{pmatrix}, \begin{pmatrix}\tilde{\nu}_{L,\mu}\\ \tilde{\mu}_L\end{pmatrix}, \begin{pmatrix}\tilde{\nu}_{L,\tau}\\ \tilde{\tau}_L\end{pmatrix}, \qquad (1.38)
$$

for the first, second and third generation terms, respectively; $m_{\tilde{Q},u}^2 = m_{\tilde{Q},d}^2$, $m_{\tilde{Q},c}^2 = m_{\tilde{Q},s}^2$, $m_{\tilde{Q},t}^2 = m_{\tilde{Q},b}^2$, $m_{\tilde{L},\nu_e}^2 = m_{\tilde{L},e}^2$, $m_{\tilde{L},\nu_\mu}^2 = m_{\tilde{L},\mu}^2$, $m_{\tilde{L},\nu_\tau}^2 = m_{\tilde{L},\tau}^2$ due to $SU(2)_L$ invariance; m_f are the fermion masses, and, $\epsilon_{12} = -\epsilon_{21} = 1$, $\epsilon_{ii} = 0$. Notice that the trilinear terms for sneutrinos are absent since, as we have said, we are still assuming in this section the generic MSSM without

right-handed neutrinos and, therefore, vanishing neutrino Yukawa and trilinear couplings and neutrino masses. We will extend this simplest MSSM model to a modified version that includes three right-handed neutrinos, their corresponding superpartners and the associated interactions in the next section.

To sum up, the set of new parameters that appear in the previous soft SUSY breaking potential are the following:

- The soft masses of the Higgs sector, m_1, m_2 and m_{12}, where $m_{12}^2 \equiv B\mu$, μ is the mass parameter introduced in Eqs. (1.30) and (1.34), and B is the soft SUSY breaking parameter.
- The soft masses of squarks and sleptons in each generation: $m_{\tilde{Q},q}$, $m_{\tilde{U},(u,c,t)}$, $m_{\tilde{D},(d,s,b)}$, $m_{\tilde{L},l}$ and $m_{\tilde{E},(e,\mu,\tau)}$.
- The trilinear couplings of squarks and sleptons: A_q and A_l.
- The soft gaugino masses, M_3, M_2 and M_1, associated with the $SU(3)_C$, $SU(2)_L$ and $U(1)_Y$ gauge groups of the SM, respectively.

Notice again that there is a unique mass parameter for the two members of each $SU(2)_L$ sfermion doublet in order to preserve the weak isospin symmetry of the Lagrangian.

As mentioned before, the SUSY breaking terms of the Lagrangian are necessary to implement the electroweak symmetry breaking, $SU(2)_L \times U(1)_Y \rightarrow U(1)_{\rm EM}$. It is because the SUSY invariant Higgs potential is positive and presents a unique minimum at $H_1 = H_2 = 0$. Once the m_1, m_2 and m_{12} mass terms are included in the Higgs potential it becomes

$$\begin{aligned} V_{\rm Higgs} &= m_{1H}^2|H_1|^2 + m_{2H}^2|H_2|^2 - m_{12}^2\left(\epsilon_{ij}H_1^iH_2^j + \text{h.c.}\right) \\ &+ \frac{1}{8}(g^2+g'^2)\left(|H_1|^2-|H_2|^2\right)^2 + \frac{1}{2}g^2|H_1^*H_2|^2\,, \end{aligned} \tag{1.39}$$

where $m_{iH}^2 \equiv |\mu|^2 + m_i^2\,(i=1,2)$, and m_i^2 can be either positive or negative, thus allowing for a non-trivial minimum of the Higgs potential.

By minimizing the scalar potential, that is by setting

$$\frac{\partial V_{\rm Higgs}}{\partial H_1^0} = \frac{\partial V_{\rm Higgs}}{\partial H_2^0} = 0\,, \tag{1.40}$$

and by requiring the proper values of the W and Z gauge boson masses,

$$(v_1^2+v_2^2) = v^2 = \frac{2m_Z^2}{g^2+g'^2} = \frac{2m_W^2}{g^2}\,, \tag{1.41}$$

one obtains the two following equations:

$$\begin{aligned} m_{12}^2 &= \frac{(m_1^2 - m_2^2)\tan 2\beta + m_Z^2 \sin 2\beta}{2} \\ \mu^2 &= \frac{m_2^2 \sin^2\beta - m_1^2 \cos^2\beta}{\cos 2\beta} - \frac{m_Z^2}{2}\,, \end{aligned} \tag{1.42}$$

which relate the previous soft Higgs masses m_1, m_2 and m_{12} to μ, $\tan\beta$ and m_Z.

Once the relevant pieces of the MSSM Lagrangian have been introduced, we next present the MSSM mass eigenvalues and eigenstates, first without flavour mixing in the sfermion sector, which will be our reference point for the rest of this thesis.

1.2.2 Slepton sector

The tree-level 6×6 slepton squared-mass matrix can be written, for the case without intergenerational mixing in the slepton sector, in a three-box-submatrices form as follows

$$M_{\tilde{l}}^2 = \begin{pmatrix} M_{LL}^{ee\,2} & M_{LR}^{ee\,2} & 0 & 0 & 0 & 0 \\ M_{RL}^{ee\,2} & M_{RR}^{ee\,2} & 0 & 0 & 0 & 0 \\ 0 & 0 & M_{LL}^{\mu\mu\,2} & M_{LR}^{\mu\mu\,2} & 0 & 0 \\ 0 & 0 & M_{RL}^{\mu\mu\,2} & M_{RR}^{\mu\mu\,2} & 0 & 0 \\ 0 & 0 & 0 & 0 & M_{LL}^{\tau\tau\,2} & M_{LR}^{\tau\tau\,2} \\ 0 & 0 & 0 & 0 & M_{RL}^{\tau\tau\,2} & M_{RR}^{\tau\tau\,2} \end{pmatrix}, \tag{1.43}$$

where

$$\begin{aligned} M_{LL}^{ll\,2} &= m_{\tilde{L},l}^2 + m_l^2 + m_Z^2 \cos 2\beta \left(-\frac{1}{2} + \sin^2\theta_W\right), \\ M_{RR}^{ll\,2} &= m_{\tilde{E},l}^2 + m_l^2 - m_Z^2 \cos 2\beta \sin^2\theta_W\,, \\ M_{LR}^{ll\,2} &= M_{RL}^{ll\,2*} = m_l(A_l - \mu\tan\beta)\,. \end{aligned} \tag{1.44}$$

Here, m_Z is the Z boson mass, θ_W is the weak mixing angle, m_l is the charged lepton mass, the parameters $m_{\tilde{L},l}$, $m_{\tilde{E},l}$ are the soft-SUSY-breaking masses for the sleptons introduced in Eq. (1.36), and A_l is the corresponding trilinear coupling also given in Eq. (1.36).

The diagonalisation of this 6×6 mass matrices above gives the six slepton mass eigenstates, $\tilde{l}_\alpha$, $(\alpha = 1, .., 6)$, in terms of the interaction eigenstates $\tilde{l}'_\alpha$,

$$\tilde{l}'_\alpha = \begin{pmatrix} \tilde{e}_L \\ \tilde{e}_R \\ \tilde{\mu}_L \\ \tilde{\mu}_R \\ \tilde{\tau}_L \\ \tilde{\tau}_R \end{pmatrix}, \quad \tilde{l}_\alpha = \begin{pmatrix} \tilde{l}_1 \\ \tilde{l}_2 \\ \tilde{l}_3 \\ \tilde{l}_4 \\ \tilde{l}_5 \\ \tilde{l}_6 \end{pmatrix}. \tag{1.45}$$

The rotation matrix, $R^{(l)}$, between these two basis,

$$\tilde{l}'_\alpha = \sum R^{(l)}_{\alpha\beta}\tilde{l}_\beta\,, \tag{1.46}$$

therefore leads to the physical slepton masses:

$$M^2_{\tilde{l}_{\rm diag}} = R^{(l)} M^2_{\tilde{l}} R^{(l)\,\dagger} = {\rm diag}\,(m^2_{\tilde{l}_1},..,m^2_{\tilde{l}_6})\,. \tag{1.47}$$

The fact that there is not any intergenerational mixing yet allows us to diagonalise separately each box submatrix per flavour in Eqs. (1.43), via a 2×2 rotation matrix as follows

$$\begin{pmatrix} \tilde{l}_1 \\ \tilde{l}_2 \end{pmatrix} = (r^{(l)})^{-1} \begin{pmatrix} \tilde{l}_L \\ \tilde{l}_R \end{pmatrix}\,, \tag{1.48}$$

where l here can be any of the three charged leptons $l = e, \mu, \tau$ and the corresponding rotation matrix is

$$r^{(l)} = \begin{pmatrix} \cos\theta_{\tilde{l}} & -\sin\theta_{\tilde{l}} \\ \sin\theta_{\tilde{l}} & \cos\theta_{\tilde{l}} \end{pmatrix}\,. \tag{1.49}$$

Notice that this is the usual notation in the MSSM and these $\tilde{e}_1$, $\tilde{e}_2$, $\tilde{\mu}_1$, $\tilde{\mu}_2$ and $\tilde{\tau}_1$, $\tilde{\tau}_2$ correspond to $\tilde{l}_1$, $\tilde{l}_2$, $\tilde{l}_3$, $\tilde{l}_4$ and $\tilde{l}_5$, $\tilde{l}_6$ respectively of our alternative notation introduced in Eq. (1.45).

The mass eigenvalues in the usual notation are[1]

$$m^2_{\tilde{l}_{1,2}} = \frac{1}{2}\left[M^{ll\,2}_{LL} + M^{ll\,2}_{RR} \pm \sqrt{(M^{ll\,2}_{LL} - M^{ll\,2}_{RR})^2 + 4M^{ll\,4}_{LR}}\right]\,, \tag{1.50}$$

where $l = e, \mu, \tau$ and the corresponding mixing angle $\theta_{\tilde{l}}$ is given by

$$\cos 2\theta_{\tilde{l}} = \frac{M^{ll\,2}_{LL} - M^{ll\,2}_{RR}}{m^2_{\tilde{l}_1} - m^2_{\tilde{l}_2}}\,, \quad \sin 2\theta_{\tilde{l}} = \frac{2M^{ll\,2}_{LR}}{m^2_{\tilde{l}_1} - m^2_{\tilde{l}_2}}\,. \tag{1.51}$$

The sneutrino sector is an exception, since within the MSSM the neutrinos are massless, there are no right-handed neutrinos, ν_R, nor their corresponding SUSY partners $\tilde{\nu}_R$, and consequently there is not LR mixing. The physical sneutrino states, $\tilde{\nu}_L$, are the SUSY partners of the left handed neutrinos ν_L and their squared masses for the three generations are given by

$$m^2_{\tilde{\nu}_l} = m^2_{\tilde{L}\,l} + \frac{1}{2}m^2_Z \cos 2\beta\,, \tag{1.52}$$

where $l = e,\ \mu,\ \tau$, correspondingly.

[1]Note that for the case without intergenerational mixing the convention is $m_{\tilde{l}_1} > m_{\tilde{l}_2}$

1.2.3 Squark sector

In this thesis we work under the hypothesis that there is not intergenerational mixing in the squark sector. Therefore, the tree-level 6×6 squark squared-mass matrices for the up and the down type squarks, referred to the $(\tilde{u}_L, \tilde{u}_R, \tilde{c}_L, \tilde{c}_R, \tilde{t}_L, \tilde{t}_R)$ and $(\tilde{d}_L, \tilde{d}_R, \tilde{s}_L, \tilde{s}_R, \tilde{b}_L, \tilde{b}_R)$ basis respectively, can be written as

$$M^2_{\tilde{u}} = \begin{pmatrix} M^{uu\,2}_{LL} & M^{uu\,2}_{LR} & 0 & 0 & 0 & 0 \\ M^{uu\,2}_{RL} & M^{uu\,2}_{RR} & 0 & 0 & 0 & 0 \\ 0 & 0 & M^{cc\,2}_{LL} & M^{cc\,2}_{LR} & 0 & 0 \\ 0 & 0 & M^{cc\,2}_{RL} & M^{cc\,2}_{RR} & 0 & 0 \\ 0 & 0 & 0 & 0 & M^{tt\,2}_{LL} & M^{tt\,2}_{LR} \\ 0 & 0 & 0 & 0 & M^{tt\,2}_{RL} & M^{tt\,2}_{RR} \end{pmatrix}, \tag{1.53}$$

$$M^2_{\tilde{d}} = \begin{pmatrix} M^{dd\,2}_{LL} & M^{dd\,2}_{LR} & 0 & 0 & 0 & 0 \\ M^{dd\,2}_{RL} & M^{dd\,2}_{RR} & 0 & 0 & 0 & 0 \\ 0 & 0 & M^{ss\,2}_{LL} & M^{ss\,2}_{LR} & 0 & 0 \\ 0 & 0 & M^{ss\,2}_{RL} & M^{ss\,2}_{RR} & 0 & 0 \\ 0 & 0 & 0 & 0 & M^{bb\,2}_{LL} & M^{bb\,2}_{LR} \\ 0 & 0 & 0 & 0 & M^{bb\,2}_{RL} & M^{bb\,2}_{RR} \end{pmatrix}, \tag{1.54}$$

where

$$\begin{aligned} M^{qq\,2}_{LL} &= m^2_{\tilde{Q},q} + m^2_q + m^2_Z \cos 2\beta (T^q_3 - Q_q \sin^2\theta_W)\,, \\ M^{qq\,2}_{RR} &= \begin{cases} m^2_{\tilde{U},q} + m^2_q + m^2_Z \cos 2\beta Q_q \sin^2\theta_W\,, \text{ if } q = u,\, c,\, t, \\ \\ m^2_{\tilde{D},q} + m^2_q + m^2_Z \cos 2\beta Q_q \sin^2\theta_W\,, \text{ if } q = d,\, s,\, b, \end{cases} \\ M^{qq\,2}_{LR} = M^{qq\,2*}_{RL} &= \begin{cases} m_q(A_q - \mu \cot\beta)\,,\ if\ q = u,\, c,\, t, \\ \\ m_q(A_q - \mu \tan\beta)\,,\ if\ q = d,\, s,\, b\,. \end{cases} \end{aligned} \tag{1.55}$$

Here, m_q, T^q_3 and Q_q are the mass, weak isospin and electric charge of the corresponding quark ($T^q_3 = \frac{1}{2}$, $Q_q = \frac{2}{3}$ for q=u, c, t and $T^q_3 = \frac{-1}{2}$, $Q_q = \frac{-1}{3}$ for q=d, s, b), and θ_W is the weak mixing angle. The parameters $m_{\tilde{Q},q}$, $m_{\tilde{D},q}$ and $m_{\tilde{U},q}$ are the soft-SUSY-breaking masses for the squarks introduced in Eq. (1.36), A_q are the trilinear couplings, given also in Eq. (1.36). The rest of parameters are common with the slepton sector. The diagonalisation of the previous 6×6 squark squared-mass matrices is completely analog to the one of the slepton sector, so the corresponding mass eigenstates and physical masses have the corresponding analogous expresions to Eqs. (1.50) and (1.51), respectively.

1.2.4 Gaugino sector

The supersymmetric partners of the gauge bosons, called gauginos, are fermions with spin 1/2. The gluinos $\tilde{g}^\alpha$ ($\alpha = 1, ..., 8$), winos $\tilde{W}^a$ ($a = 1, 2, 3$) and the bino $\tilde{B}$ are the supersymmetric partners of the gluons g^α ($\alpha = 1, ..., 8$), the electroweak gauge bosons W^a ($a = 1, 2, 3$) and B, respectively. Correspondingly, the photino $\tilde{\gamma}$ and the zino $\tilde{Z}$ are the supersymmetric partners of the mass eigenstates of the neutral gauge boson sector, the photon γ and the Z boson, respectively. These SUSY fermions are not the physical states yet, due to their mixing with the SUSY partners of the Higgs bosons, the Higgsinos, which are also fermions. The resulting physical states are the charginos and the neutralinos which will be presented next.

Gluino sector

The gluinos, $\tilde{g}_\alpha (\alpha = 1, ..., 8)$, have a unique characteristic among all of the SUSY partners since they are octet fermions and, therefore, they cannot mix with any other particle in the MSSM. This means that the unique soft-breaking mass parameter that enters in the computation of the gluino masses, at tree level, is M_3. Indeed, one gets at tree level simply $m_{\tilde{g}_\alpha} = M_3$.

Chargino sector

The charginos are four-components Dirac fermions that result from the mixture of charged gauginos, $\tilde{W}^\pm$, i.e., the SUSY partners of the charged gauge bosons $W^\pm$, and charged higgsinos, $\tilde{H}_1^-$ and $\tilde{H}_2^+$, i.e. the SUSY partners of the charged components of the two Higgs doublets, H_1 and H_2, respectively.

In the $\tilde{W}^+ - \tilde{H}^+$ basis, the chargino mass matrix at the tree-level is

$$X = \begin{pmatrix} M_2 & \sqrt{2} m_W \sin\beta \\ \sqrt{2} m_W \cos\beta & \mu \end{pmatrix} . \tag{1.56}$$

Due to the two independent mixings, $(\tilde{W}^-, \tilde{H}_1^-)$ and $(\tilde{W}^+, \tilde{H}_2^+)$, one needs to define two unitary mixing matrices, U and V, in order to obtain the mass eigenstates. The squared mass matrix of the charginos is diagonalised by

$$\mathcal{M}^2_{\tilde{\chi}^+} = \mathrm{diag}(m^2_{\tilde{\chi}_1^+}, m^2_{\tilde{\chi}_2^+}) = V X^\dagger X V^{-1} = U^* X X^\dagger (U^*)^{-1} , \tag{1.57}$$

where the two mass eigenstates are denoted by $\tilde{\chi}_1^+$ and $\tilde{\chi}_2^+$ and the corresponding eigenvalues are given by

$$\begin{aligned} m^2_{\tilde{\chi}^+_{1,2}} &= \frac{1}{2}\Big\{ M_2^2 + \mu^2 + 2m_W^2 \mp \big[(M_2^2 - \mu^2)^2 + 4 m_W^4 \cos^2 2\beta \\ &+ 4 m_W^2 (M_2^2 + \mu^2 + 2 M_2 \mu \sin 2\beta) \big]^{1/2} \Big\} , \end{aligned} \tag{1.58}$$

where by convention, $m_{\tilde{\chi}_1^+} \leq m_{\tilde{\chi}_2^+}$.

Neutralino sector

Finally, the neutralinos, $\tilde{\chi}_j^0$ with $j = 1, ...4$, are mixtures among the photino, the zino and the SUSY partners of the neutral components of the two Higgs doublets, i.e. the neutral higgsinos. In the $\tilde{B} - \tilde{W}^3 - \tilde{H}_1^0 - \tilde{H}_2^0$ basis, the neutralino mass matrix is

$$Y = \begin{pmatrix} M_1 & 0 & -m_Z s_W \cos\beta & m_Z s_W \sin\beta \\ 0 & M_2 & m_Z c_W \cos\beta & -m_Z c_W \sin\beta \\ -m_Z s_W \cos\beta & m_Z c_W \cos\beta & 0 & -\mu \\ m_Z s_W \sin\beta & -m_Z c_W \sin\beta & -\mu & 0 \end{pmatrix} . \tag{1.59}$$

This is in general a complex symmetric matrix, and this symmetry is due to the Majorana nature of the neutralinos. As a consequence, only one unitary matrix, N, is required to diagonalise the neutralino sector, in contrast with the chargino one. The diagonal neutralino mass matrix is given by

$$\mathcal{M}_{\tilde{\chi}^0} = \mathrm{diag}(m_{\tilde{\chi}_1^0}, ..., m_{\tilde{\chi}_4^0}) = N^* Y N^{-1} . \tag{1.60}$$

The matrix N can be chosen in such a way that the elements of the diagonal matrix are real and non-negative. Our convention for the neutralino masses here is $m_{\tilde{\chi}_1^0} \leq ... \leq m_{\tilde{\chi}_4^0}$. The full expressions for $m_{\tilde{\chi}_1^0}, ..., m_{\tilde{\chi}_4^0}$ in terms of M_1, M_2, μ, m_Z, θ_W and $\tan\beta$ are lengthy and are omitted here for brevity. They can be found in [119, 120].

1.2.5 Higgs sector

The Higgs sector of the MSSM contains two Higgs doublet fields which, after electroweak symmetry breaking, lead to five physical Higgs boson particles, h^0, H^0, A^0, and $H^\pm$. In order to obtain the spectrum of the MSSM Higgs sector, one starts with the eight real scalar degrees of freedom, four per Higgs doublet. Three of them are the Goldstone bosons, $G^\pm$ and G^0, that will be transmuted into the longitudinal components of the $W^\pm$ and Z^0, respectively, via the electroweak symmetry breaking mechanism, and will provide the proper gauge boson masses. The remainimg five degrees of freedom constitute the five physical Higgs bosons of the theory, two CP-even neutral scalar particles, h^0, H^0, one CP-odd neutral pseudoscalar particle, A^0, and two charged scalar particles, $H^\pm$.

The peculiarity of the MSSM Higgs boson sector is that the Higgs boson masses and mixing angles are determined, at the tree level and due to supersymmetry, by just two independent parameters usually chosen to be m_{A^0} and $\tan\beta = v_2/v_1$. By taking into account the relation

between m_{A^0} and m_{12},

$$m_{A^0}^2 = \frac{m_{12}^2}{\sin\beta\cos\beta}\,, \tag{1.61}$$

and the fact that $m_W^2 = m_Z^2\cos^2\theta_W = \frac{1}{2}g^2(v_1^2+v_2^2)$ fixes the value $v_1^2+v_2^2 = (174\,\mathrm{GeV})^2$, the remaining tree level Higgs masses and mixing angles are then derived in terms of m_A^0 and $\tan\beta$. In particular, the charged Higgs mass, $H^\pm$ at tree level is given by

$$m_{H^\pm}^2 = m_{A^0}^2 + m_W^2\,, \tag{1.62}$$

and the masses of the CP-even neutral Higgs bosons h^0 and H^0 are obtained by diagonalizing a 2×2 mass-squared matrix, which in the $H_1 - H_2$ basis is given by

$$\mathcal{M}^2 \;=\; \begin{pmatrix} m_{A^0}^2\sin^2\beta + m_Z^2\cos^2\beta & -(m_{A^0}^2+m_Z^2)\sin\beta\cos\beta \\ -(m_{A^0}^2+m_Z^2)\sin\beta\cos\beta & m_{A^0}^2\cos^2\beta + m_Z^2\sin^2\beta \end{pmatrix}. \tag{1.63}$$

Once it is diagonalised, the mass eigenstates are

$$H^0 \;=\; \sqrt{2}\left(\mathrm{Re}\,H_1^0 - v_1\right)\cos\alpha + \sqrt{2}\left(\mathrm{Re}\,H_2^0 - v_2\right)\sin\alpha\,, \tag{1.64}$$

$$h^0 \;=\; -\sqrt{2}\left(\mathrm{Re}\,H_1^0 - v_1\right)\sin\alpha + \sqrt{2}\left(\mathrm{Re}\,H_2^0 - v_2\right)\cos\alpha\,, \tag{1.65}$$

where the mixing angle, at tree level, is given by

$$\tan 2\alpha = \tan 2\beta\,\frac{m_{A^0}^2 + m_Z^2}{m_{A^0}^2 - m_Z^2}\,, \tag{1.66}$$

and the corresponding CP-even Higgs mass eigenvalues are

$$m_{H^0,h^0}^2 = \frac{1}{2}\left[m_{A^0}^2 + m_Z^2 \pm \sqrt{\left(m_{A^0}^2+m_Z^2\right)^2 - 4m_{A^0}^2 m_Z^2\cos^2 2\beta}\right], \tag{1.67}$$

with $m_{h^0} \le m_{H^0}$. In the convention chosen here, the VEVs are positive so that $0 < \beta < \pi/2$ and $-\pi/2 < \alpha < 0$. Notice that it implies an upper bound on the h^0 tree level mass of $m_{h^0} < m_Z|\cos 2\beta|$ and therefore $m_{h^0} < m_Z$.

Similarly one gets a relation between the physical pseudoscalar A^0, the neutral Goldstone boson G^0 and the scalar weak eigenstates, χ_1^0 and χ_2^0 of Eq. (1.28), that is given by

$$\begin{pmatrix} G^0 \\ A^0 \end{pmatrix} \;=\; \begin{pmatrix} \cos\beta & \sin\beta \\ -\sin\beta & \cos\beta \end{pmatrix}\begin{pmatrix} \chi_1^0 \\ \chi_2^0 \end{pmatrix}, \tag{1.68}$$

where now the mixing angle is β, and also between the charged fields in Eq. (1.28) and the charged physical Higgs H^+ and the charged Goldstone boson G^+ that is given by

$$\begin{pmatrix} G^+ \\ H^+ \end{pmatrix} \;=\; \begin{pmatrix} \cos\beta & \sin\beta \\ -\sin\beta & \cos\beta \end{pmatrix}\begin{pmatrix} \phi_1^+ \\ \phi_2^+ \end{pmatrix}. \tag{1.69}$$

All the previous tree level relations and Higgs mass predictions are modified once the radiative corrections are included (see [121–132]). In particular, when electroweak radiative corrections to the Higgs masses are taken into account, the upper bound on m_{h^0} increases substantially from m_Z up to $m_{h^0} \leq 135$ GeV (this is assuming that all supersymmetric particles are not heavier than about 1 TeV). This bound is particularly relevant for the Higgs boson searches at next generation colliders and will be considered in the present work.

1.3 The MSSM extended with three ν_R and their superpartners

In this section the enlarged version of the MSSM with three ν_R and their SUSY partners $\tilde{\nu}_R$ is considered. We define correspondingly the MSSM-seesaw model as the extended MSSM with three ν_R and three $\tilde{\nu}_R$ and where the neutrino masses are generated by the seesaw mechanism. All that has been sumarised in section 1.1 concerning the mass parameters and mixings in the neutrino sector of the SM-seesaw applies to the MSSM-seesaw model as well, so we will not repeat it here.

The previous superpotential of Eq. (1.34) must be modified to include the neutrino Yukawa couplings and neutrino Majorana mass terms. The relevant superpotential for this MSSM-seesaw model is therefore

$$W \,=\, \hat{U}^c\, Y_u\, \hat{Q}\, \hat{H}_2 \,+\, \hat{D}^c\, Y_d\, \hat{Q}\, \hat{H}_1 \,+\, \hat{N}^c\, Y_\nu\, \hat{L}\, \hat{H}_2 \,+\, \hat{E}^c\, Y_l\, \hat{L}\, \hat{H}_1 \,+\, \frac{1}{2}\, \hat{N}^c\, m_M\, \hat{N}^c \,+\, \mu \hat{H}_1 \hat{H}_2\,, \quad (1.70)$$

where $\hat{N}^c$ is the additional superfield that contains the three right-handed neutrinos ν_{R_i} and their scalar partners $\tilde{\nu}_{R_i}$. Here and from now on, the Yukawa couplings Y_u, Y_d, Y_ν, Y_l and the Majorana mass m_M are 3×3 matrices in lepton flavour space. We will further assume that we are in a basis where Y_u, Y_d, Y_l and m_M are diagonal.

After EW symmetry breaking, the charged lepton and Dirac neutrino mass matrices can be written as

$$m_l \,=\, Y_l\, \langle H_1 \rangle\,, \qquad m_D \,=\, Y_\nu\, \langle H_2 \rangle\,, \quad (1.71)$$

where again $\langle H_1 \rangle = v_1$ and $\langle H_2 \rangle = v_2$ are the VEVs of the neutral Higgs scalars, with $v_1 = v\, \cos\beta$, $v_2 = v\, \sin\beta$ and $v = 174$ GeV.

The introduction of right-handed neutrinos and therefore, the corresponding right-handed sneutrinos, change the properties of the sneutrino sector described in Eq. (1.52). Now there are two degrees of freedom $\tilde{\nu}_L$ and $\tilde{\nu}_R$ for each generation and one has to proceed similarly to the charged slepton sector diagonalisation. However, in the sneutrino sector, the "small" matrix $\xi = m_D m_M^{-1}$ appears as in the neutrino sector and gives rise to a natural suppresion of the right-handed sneutrino components in the relevant mass eigenstates, leading to a diagonalisation procedure that is simpler than in the charged slepton case. In order to understand properly this

feature of the MSSM-seesaw model, we will first illustrate this diagonalisation process for the sneutrino sector in the one generation case where this behaviour is already present. We will next extend it to the three generations case, first without considering any intergenerational mixing, and in Section 1.5 we will introduce the intergenerational mixing.

The addition of right-handed neutrinos and sneutrinos to the MSSM leads to new terms in the MSSM lagrangian. In particular the soft SUSY breaking potential of Eq. (1.36) must be modified to include new mass and coupling terms for the right-handed sneutrinos which for the one generation case are the following:

$$V^{\tilde{\nu}}_{soft} = m^2_{\tilde{M}}\tilde{\nu}^*_R\tilde{\nu}_R - \left(\frac{g}{\sqrt{2}m_W}\epsilon_{ij}\frac{m_D A_\nu}{\sin\beta}H_2^i\tilde{l}_L^j\tilde{\nu}^*_R + h.c.\right) + (m_M B_M\tilde{\nu}^*_R\tilde{\nu}_R + h.c.)\ , \qquad (1.72)$$

where $m_{\tilde{M}}$, A_ν and B_M are the new soft breaking parameters. The sneutrino mass terms of the MSSM-seesaw model can then be written in the one generation case [133] as

$$-\mathcal{L}^\nu_{mass} = \left(\begin{array}{cccc}\mathrm{Re}(\tilde{\nu}_L) & \mathrm{Re}(\tilde{\nu}_R) & \mathrm{Im}(\tilde{\nu}_L) & \mathrm{Im}(\tilde{\nu}_R)\end{array}\right)\left(\begin{array}{cc} M^2_+ & 0 \\ 0 & M^2_-\end{array}\right)\left(\begin{array}{c}\mathrm{Re}(\tilde{\nu}_L)\\ \mathrm{Re}(\tilde{\nu}_R)\\ \mathrm{Im}(\tilde{\nu}_L)\\ \mathrm{Im}(\tilde{\nu}_R)\end{array}\right)\ , \qquad (1.73)$$

with

$$M^2_\pm = \left(\begin{array}{cc} m^2_{\tilde{L}} + m^2_D + \frac{1}{2}m^2_Z\cos 2\beta & m_D(A_\nu - \mu\cot\beta \pm m_M) \\ m_D(A_\nu - \mu\cot\beta \pm m_M) & m^2_{\tilde{M}} + m^2_D + m^2_M \pm 2B_M m_M\end{array}\right)\ . \qquad (1.74)$$

Notice that now there are several mass scales involved, the soft SUSY-breaking parameters, $m_{\tilde{L}}$, $m_{\tilde{M}}$, B_M and A_ν, the Dirac mass m_D, the μ-mass parameter, the Z boson mass m_Z and the Majorana neutrino mass m_M. Our basic assumption in all this work is that m_M is much heavier than the other mass scales involved, $m_M >> m_D, m_Z, \mu, m_{\tilde{L}}, m_{\tilde{M}}, A_\nu, B_M$. The size of B_M has been discussed in the literature [133, 134] and seems more controversial. For simplicity, we shall assume here that this is also smaller than m_M. In this large m_M limit, the diagonalisation of the previous sneutrino squared mass matrix is simpler and leads to four mass eigenstates, two of which are light, ξ^l_1, ξ^l_2 and two heavy, ξ^h_1, ξ^h_2. In the leading orders of the series expansion in powers of ξ the mass eigenstates and their corresponding mass eigenvalues are given by

$$\begin{aligned}
\xi^l_1 &= \sqrt{2}\left(\mathrm{Re}(\tilde{\nu}_L) - \xi\mathrm{Re}(\tilde{\nu}_R)\right)\ , \quad \xi^l_2 = \sqrt{2}\left(\mathrm{Im}(\tilde{\nu}_L) + \xi\mathrm{Im}(\tilde{\nu}_R)\right)\ ,\\
\xi^h_1 &= \sqrt{2}\left(\mathrm{Re}(\tilde{\nu}_R) + \xi\mathrm{Re}(\tilde{\nu}_L)\right)\ , \quad \xi^h_2 = \sqrt{2}\left(\mathrm{Im}(\tilde{\nu}_R) - \xi\mathrm{Im}(\tilde{\nu}_L)\right)\ ,\\
m^2_{\xi^l_{1,2}} &= m^2_{\tilde{L}} + \frac{1}{2}m^2_Z\cos 2\beta \mp 2m_D(A_\nu - \mu\cot\beta - B_N)\xi\,,\\
m^2_{\xi^h_{1,2}} &= m^2_M \pm 2B_M m_M + m^2_{\tilde{M}} + 2m^2_D\,.
\end{aligned} \qquad (1.75)$$

Here we can see that the heavy states $\xi^h_{1,2}$ will couple very weakly to the rest of particles of the MSSM via their $\tilde{\nu}_L$ component, which is highly suppresed by the small factor ξ and, therefore,

at the electroweak scale it is a good approximation to ignore them and keep just the light states $\xi^l_{1,2}$, which are made mainly of $\tilde{\nu}_L$ and its complex conjugate $\tilde{\nu}^*_L$. We say then that the heavy sneutrinos decouple from low energy physics.

The previous analysis can be easily generalised to the three generations case. By working in the simplified basis with just the light sneutrinos, referred now to the three generations case, we can see that before introducing any possible intergenerational mixing, the relevant 3×3 sneutrino squared mass matrix is already diagonal, since the LR mixings can be ignored for $\xi \ll 1$, and can be written as follows

$$M^2_{\tilde{\nu}} = \begin{pmatrix} m^2_{\tilde{L},e} + \frac{1}{2}m^2_Z \cos 2\beta & 0 & 0 \\ 0 & m^2_{\tilde{L},\mu} + \frac{1}{2}m^2_Z \cos 2\beta & 0 \\ 0 & 0 & m^2_{\tilde{L},\tau} + \frac{1}{2}m^2_Z \cos 2\beta \end{pmatrix}, \tag{1.76}$$

where $m^2_{\tilde{L},l}$ are the same as in the charged slepton squared mass matrix of Eq. (1.43). Therefore, in the seesaw limit, $\xi \ll 1$, the physical sneutrino eigenstates, $\tilde{\nu}_\beta$ ($\beta = 1, 2, 3$) are made mainly of just the left handed components, that is the $\tilde{\nu}_{L,\,l}$ states with $l = e$, μ, τ respectively, and their corresponding complex conjugates. The situtation described above will change when the intergenerational mixing in the lepton sector is considered, as will be explained in Section 1.5.

1.4 Constrained SUSY-seesaw models

As already mentioned in the introduction, we will work in constrained SUSY scenarios where the number of input parameters is reduced by assuming universality conditions of the soft parameters at the gauge coupling unification scale, $M_X = 2 \times 10^{16}$ GeV, inspired in mSUGRA-like scenarios. Specifically, we will work in two scenarios, one with universal scalar masses, trilinear couplings and gaugino masses which will be named here CMSSM-seesaw, and another one with universal sfermion masses, trilinear couplings and gaugino masses but with non-universal soft masses for the Higgs bosons, that we will call NUHM-seesaw. In these two constrained SUSY-seesaw scenarios the predictions for the low-energy parameters are obtained by solving the full RGEs, which must now include the appropriate equations and extra terms for the extended neutrino and sneutrino sectors. Due to the existence of intermediate scales m_M introduced by the seesaw mechanism, the running must be carried in two steps. The full set of equations is first run down from M_X to m_M. At the seesaw scales, the right-handed neutrinos as well as their SUSY partners decouple, and the new RGEs (without the equations and terms for ν_R and $\tilde{\nu}_R$) are then run down from m_M to the EW scale, where the couplings and mass matrices are finally computed. Notice that the high energy scale M_X is taken here to be the gauge coupling unification scale.

For the numerical implementation of the above procedure we have used the public Fortran code `SPheno2.2.2` [135] which integrates the RGEs to one-loop. The value of M_X is derived from the unification condition of the $SU(2)$ and $U(1)$ gauge couplings (systematically leading to a value of M_X very close to 2×10^{16} GeV throughout all the numerical analysis), while $|\mu|$ is derived from the requirement of obtaining the correct radiative EW symmetry breaking. The code `SPheno2.2.2` has been adapted by us in order to fully incorporate the right-handed neutrino and sneutrino sectors, as well as the full lepton flavour structure.

1.4.1 CMSSM-seesaw scenarios

In these constrained SUSY-seesaw scenarios the universality conditions of the soft-SUSY breaking parameters at the high-energy scale M_X are defined as follows

$$\begin{aligned}
&\left(m_{\tilde{Q}}\right)^2_{ij} = \left(m_{\tilde{U}}\right)^2_{ij} = \left(m_{\tilde{D}}\right)^2_{ij} = \left(m_{\tilde{L}}\right)^2_{ij} = \left(m_{\tilde{E}}\right)^2_{ij} = \left(m_{\tilde{M}}\right)^2_{ij} = M_0^2\,\delta_{ij}\,, \\
&(A_u)_{ij} = A_0\,(Y_u)_{ij}\;,\; (A_d)_{ij} = A_0\,(Y_d)_{ij}\;,\; (A_l)_{ij} = A_0\,(Y_l)_{ij}\;,\; (A_\nu)_{ij} = A_0\,(Y_\nu)_{ij} \\
&M^2_{H_1} = M^2_{H_2} = M_0^2 \\
&M_1 = M_2 = M_3 = M_{1/2}\,,
\end{aligned} \tag{1.77}$$

where M_0 is the universal scalar soft mass, $M_{1/2}$ is the universal gaugino soft mass, A_0 is the universal trilinear coupling and i, j denote lepton flavour indices, with $i, j = 1, 2, 3$. This scenario is further specified by the the ratio of the Higgs VEVs, $\tan\beta$, and the sign of the bilinear μ-parameter, $\text{sign}(\mu)$.

In summary, the CMSSM-seesaw scenario is defined by the following (unknown) input parameters:

- SUSY parameters: M_0, $M_{1/2}$, A_0, $\text{sign}\,(\mu)$ and $\tan\beta$.
- ν-seesaw parameters: m_{N_1}, m_{N_2}, m_{N_3} and R (or equivantly θ_1, θ_2, θ_3).

1.4.2 NUHM-seesaw scenarios

An interesting departure from the previous CMSSM-seesaw scenarios can be obtained by relaxing the universality hypothesis for the soft SUSY breaking masses of the Higgs sector. This partially constrained MSSM is commonly referred to as the Non Universal Higgs Mass (NUHM) scenario [77–89], and its enlarged version (including right-handed neutrinos and sneutrinos) with the seesaw mechanism implemented will be here designated NUHM-seesaw. The universality

conditions at the high energy scale M_X in these NUHM-seesaw scenarios are

$$\begin{aligned}
&\left(m_{\tilde{Q}}\right)^2_{ij} = \left(m_{\tilde{U}}\right)^2_{ij} = \left(m_{\tilde{D}}\right)^2_{ij} = \left(m_{\tilde{L}}\right)^2_{ij} = \left(m_{\tilde{E}}\right)^2_{ij} = \left(m_{\tilde{M}}\right)^2_{ij} = M_0^2\,\delta_{ij}\,, \\
&(A_u)_{ij} = A_0\,(Y_u)_{ij}\;,\; (A_d)_{ij} = A_0\,(Y_d)_{ij}\;,\; (A_l)_{ij} = A_0\,(Y_l)_{ij}\;,\; (A_\nu)_{ij} = A_0\,(Y_\nu)_{ij} \\
&M_1 = M_2 = M_3 = M_{1/2}\,,
\end{aligned} \tag{1.78}$$

Notice that now the soft Higgs mases M_{H_1} and M_{H_2} are not universal. The departure from universality in the soft Higgs masses of the NUHM-seesaw is parameterised here in terms of two non-vanishing parameters, δ_1 and δ_2,

$$M^2_{H_1} = M_0^2(1+\delta_1),\; M^2_{H_2} = M_0^2(1+\delta_2)\,. \tag{1.79}$$

The most important features of these scenarios, for the present work, is that a proper choice of these non-universal parameters, δ_1 and δ_2, can lead us to light Higgs particles, with masses m_{H^0} and m_{A^0} (in addition to m_{h^0}) indeed close to the present lower experimental bound (near the SM bound $m_{H_{SM}} > 114$ GeV [10]), even for very large soft SUSY masses of $\mathcal{O}(1$ TeV).

In summary, the NUHM-seesaw scenarios are specified by the following (unknown) input parameters:

- SUSY parameters: M_0, $M_{1/2}$, A_0, sign (μ) and $\tan\beta$.
- NUHM parameters: δ_1 and δ_2.
- ν-seesaw parameters: m_{N_1}, m_{N_2}, m_{N_3} and R (or equivantly θ_1, θ_2, θ_3).

1.4.3 Parameter space of constrained SUSY-seesaw models

For the forthcoming numerical estimates of LFV rates in this thesis, we will explore the (M_0, $M_{1/2}$, A_0, $\tan\beta$, sign(μ)) parameter space considering the following intervals:

$$\begin{aligned}
250\,\text{GeV} &< M_{1/2} < 2000\,\text{GeV}\,, \\
250\,\text{GeV} &< M_0 < 2000\,\text{GeV}\,, \\
-500\,\text{GeV} &< A_0 < 500\,\text{GeV}\,, \\
3 &< \tan\beta < 60\,,
\end{aligned} \tag{1.80}$$

and we will consider the two possibilities, sign(μ) = ± 1. In addition, for the NUHM-seesaw scenario and in order to further reduce the number of input parameters, we will set $M_0 = M_{1/2} \equiv M_{\text{SUSY}}$. The values for the non-universal parameters δ_1 and δ_2 will be taken to lie within the interval

$$-3 \leq \delta_{1,2} \leq 3\,. \tag{1.81}$$

Regarding the seesaw parameters, we will consider the following intervals for heavy neutrinos:

$$\begin{aligned} &\text{Degenerate case:} \quad 10^8\,\text{GeV} \leq m_N \leq 10^{15}\,\text{GeV} \\ &\text{Hierarchical case:} \quad m_{N_1} \ll m_{N_2} \ll m_{N_3},\ 10^9\,\text{GeV} \leq m_{N_3} \leq 10^{15}\,\text{GeV} \end{aligned} \tag{1.82}$$

Besides, we will explore the values of complex angles θ_i of the R matrix within the following intervals:

$$\begin{aligned} &0 \leq |\theta_1|,\, |\theta_2|,\, |\theta_3| \leq 3\,, \\ &-\pi \leq \arg\theta_1,\, \arg\theta_2,\, \arg\theta_3 \leq \pi\,. \end{aligned} \tag{1.83}$$

1.5 Slepton and sneutrino flavour mixing in SUSY-seesaw models

In this section we study the generation of lepton flavour mixing in the slepton and sneutrino sectors of SUSY-seesaw models. Since we work within constrained scenarios with universal conditions on the mass matrices at M_X which are diagonal in flavour space, all slepton and sneutrino flavour mixing at low energies will solely come from the RGE generated radiative corrections involving Y_ν. Notice that these corrections can be important since, due to the Majorana nature of the neutrinos, the Yukawa couplings may be as large as $\mathcal{O}(1)$. As we will see later, these slepton and sneutrino flavour mixings will produce in turn, via SUSY-loops, sizeable contributions to lepton flavour violating processes, like LFV radiative decays $l_j \to l_i\,\gamma$ and others.

As we have previously said the RGE running from M_X down to the EW scale is performed in two steps. First from M_X to m_M where all equations, including neutrinos and sneutrinos, participate, and next from m_M to the EW scale where the right-handed neutrinos and their superpartners decouple and, therefore, they are not included in the RGEs. The most important flavour mixing in the slepton and sneutrino soft terms is produced in the first step of this running, that is from M_X to m_M. The clearest way to illustrate this RGE-induced intergenerational mixing is by working in the one-loop leading-log (LLog) approximation where the approximate solution for the off-diagonal terms ($i \neq j$, $i,j = 1,2,3$) can be written as [49]

$$\begin{aligned} (\Delta m^2_{\tilde{L}})_{ij} &= -\frac{1}{8\,\pi^2}\,(3\,M_0^2 + A_0^2)\,(Y_\nu^\dagger\,L\,Y_\nu)_{ij}\,, \\ (\Delta A_l)_{ij} &= -\frac{3}{16\,\pi^2}\,A_0\,Y_{l_i}\,(Y_\nu^\dagger\,L\,Y_\nu)_{ij}\,, \\ (\Delta m^2_{\tilde{E}})_{ij} &= 0\ ;\ L_{kl} \equiv \log\left(\frac{M_X}{m_{M_k}}\right)\,\delta_{kl}\,. \end{aligned} \tag{1.84}$$

The previous equations indicate clearly that the size of the off-diagonal matrix elements are driven by the size of the off-diagonal $(Y_\nu)_{ij}$ matrix elements. We also see that, within the LLog approximation, the dominant flavour off-diagonal matrix elements are those of the LL sector since they become enhanced with factors given by squared soft-breaking parameters. The next dominant elements are those of the LR sector (which are suppressed by the small lepton mass) and the smallest ones are those of the RR sector.

The matrix elements $(Y_\nu^\dagger L Y_\nu)_{ij}$ in Eq. (1.84) can be simply written in terms of the parameterisation of Eq. (1.23). In particular, we obtain

$$
\begin{aligned}
& v_2^2 \left(Y_\nu^\dagger\, L\, Y_\nu\right)_{21} = \\
& L_{33}\, m_{N_3} \left[\left(\sqrt{m_{\nu_3}}\, c_1\, c_2\, s_{13} + \sqrt{m_{\nu_2}}\, s_1\, c_2\, s_{12}\, c_{13} + \sqrt{m_{\nu_1}}\, s_2\, c_{12}\, c_{13}\right)\right. \\
& \quad \left.\left(\sqrt{m_{\nu_3}}\, c_1^*\, c_2^*\, c_{13}\, s_{23} + \sqrt{m_{\nu_2}}\, s_1^*\, c_2^*\, (c_{12}\, c_{23} - s_{12}\, s_{13}\, s_{23}) - \sqrt{m_{\nu_1}}\, s_2^*\, (s_{12}\, c_{23} + c_{12}\, s_{13}\, s_{23})\right)\right] \\
& L_{22}\, m_{N_2} \left[\left(-\sqrt{m_{\nu_3}}\, s_{13}\, (s_1\, c_3 + c_1\, s_2\, s_3) + \sqrt{m_{\nu_2}}\, s_{12}\, c_{13}\, (c_1\, c_3 - s_1\, s_2\, s_3) + \sqrt{m_{\nu_1}}\, c_2\, s_3\, c_{12}\, c_{13}\right)\right. \\
& \quad \left(-\sqrt{m_{\nu_3}}\, c_{13}\, s_{23}\, (s_1^*\, c_3^* + c_1^*\, s_2^*\, s_3^*) - \sqrt{m_{\nu_1}}\, c_2^*\, s_3^*\, (s_{12}\, c_{23} + c_{12}\, s_{13}\, s_{23}) + \right. \\
& \quad \left.\left.\sqrt{m_{\nu_2}}\, (c_{12}\, c_{23} - s_{12}\, s_{13}\, s_{23})\, (c_1^*\, c_3^* - s_1^*\, s_2^*\, s_3^*)\right)\right] \\
& L_{11}\, m_{N_1} \left[\left(\sqrt{m_{\nu_3}}\, s_{13}\, (s_1\, s_3 - c_1\, s_2\, c_3) - \sqrt{m_{\nu_2}}\, s_{12}\, c_{13}\, (s_1\, s_2\, c_3 + c_1\, s_3) + \sqrt{m_{\nu_1}}\, c_{12}\, c_{13}\, c_2\, c_3\right)\right. \\
& \quad \left(\sqrt{m_{\nu_3}}\, c_{13}\, s_{23}\, (s_1^*\, s_3^* - c_1^*\, s_2^*\, c_3^*) - \sqrt{m_{\nu_1}}\, c_2^*\, c_3^*\, (s_{12}\, c_{23} + c_{12}\, s_{13}\, s_{23}) - \right. \\
& \quad \left.\left.\sqrt{m_{\nu_2}}\, (c_{12}\, c_{23} - s_{12}\, s_{13}\, s_{23})\, (c_1^*\, s_3^* + s_1^*\, s_2^*\, c_3^*)\right)\right] , \qquad (1.85)
\end{aligned}
$$

where again $s_{ij} \equiv \sin\theta_{ij}$, $c_{ij} \equiv \cos\theta_{ij}$, $s_i \equiv \sin\theta_i$ and $c_i \equiv \cos\theta_i$. This is the relevant matrix element for $\mu - e$ transitions (i.e., intergenerational mixing between the second and first lepton generations). Similarly we get

$$
\begin{aligned}
& v_2^2 \left(Y_\nu^\dagger\, L\, Y_\nu\right)_{32} = \\
& L_{33}\, m_{N_3} \left[\left(\sqrt{m_{\nu_3}}\, c_1\, c_2\, c_{13}\, s_{23} + \sqrt{m_{\nu_2}}\, s_1\, c_2\, (c_{12}\, c_{23} - s_{12}\, s_{13}\, s_{23}) - \sqrt{m_{\nu_1}}\, s_2\, (s_{12}\, c_{23} + c_{12}\, s_{13}\, s_{23})\right)\right. \\
& \quad \left.\left(\sqrt{m_{\nu_3}}\, c_1^*\, c_2^*\, c_{13}\, c_{23} - \sqrt{m_{\nu_2}}\, s_1^*\, c_2^*\, (c_{12}\, s_{23} + s_{12}\, s_{13}\, c_{23}) + \sqrt{m_{\nu_1}}\, s_2^*\, (s_{12}\, s_{23} - c_{12}\, s_{13}\, c_{23})\right)\right] \\
& L_{22}\, m_{N_2} \left[\left(-\sqrt{m_{\nu_3}}\, c_{13}\, s_{23}\, (s_1\, c_3 + c_1\, s_2\, s_3) - \sqrt{m_{\nu_1}}\, c_2\, s_3\, (s_{12}\, c_{23} + c_{12}\, s_{13}\, s_{23}) + \right.\right. \\
& \quad \left.\sqrt{m_{\nu_2}}\, (c_{12}\, c_{13} - s_{12}\, s_{13}\, s_{23})\, (c_1\, c_3 - s_1\, s_2\, s_3)\right) \\
& \quad \left(-\sqrt{m_{\nu_3}}\, c_{13}\, c_{23}\, (s_1^*\, c_3^* + c_1^*\, s_2^*\, s_3^*) + \sqrt{m_{\nu_1}}\, c_2^*\, s_3^*\, (s_{12}\, s_{23} - c_{12}\, s_{13}\, c_{23}) - \right. \\
& \quad \left.\left.\sqrt{m_{\nu_2}}\, (c_{12}\, s_{23} + s_{12}\, s_{13}\, c_{23})\, (c_1^*\, c_3^* - s_1^*\, s_2^*\, s_3^*)\right)\right] \\
& L_{11}\, m_{N_1} \left[\left(\sqrt{m_{\nu_3}}\, c_{13}\, s_{23}\, (s_1\, s_3 - c_1\, s_2\, c_3) - \sqrt{m_{\nu_1}}\, c_2\, c_3\, (s_{12}\, c_{23} + c_{12}\, s_{13}\, s_{23}) - \right.\right. \\
& \quad \left.\sqrt{m_{\nu_2}}\, (c_{12}\, c_{23} - s_{12}\, s_{13}\, s_{23})\, (s_1\, s_2\, c_3 + c_1\, s_3)\right) \\
& \quad \left(\sqrt{m_{\nu_3}}\, c_{13}\, c_{23}\, (s_1^*\, s_3^* - c_1^*\, s_2^*\, c_3^*) + \sqrt{m_{\nu_1}}\, c_2^*\, c_3^*\, (s_{12}\, s_{23} - c_{12}\, s_{13}\, c_{23}) + \right. \\
& \quad \left.\left.\sqrt{m_{\nu_2}}\, (c_{12}\, s_{23} + s_{12}\, s_{13}\, c_{23})\, (c_1^*\, s_3^* + s_1^*\, s_2^*\, c_3^*)\right)\right] . \qquad (1.86)
\end{aligned}
$$

This latter element is the relevant one for LFV $\tau - \mu$ processes. Similarly, the $v_2^2 (Y_\nu^\dagger\, L\, Y_\nu)_{31}$

matrix element, omitted here for brevity, is the relevant one for $\tau - e$ transitions. From the previous expressions, we can already conclude that the most relevant parameters to get large intergenerational mixings are m_{N_3} in the case of hierarchical neutrinos (m_N in the degenerate case) and the complex angles θ_1 and θ_2 (all θ_i for the degenerate case). In the case of $\mu - e$ and $\tau - e$ transitions we will further see that the angle θ_{13} of the U_{PMNS} matrix and the lightest neutrinos mass m_{ν_1} also play an important role (but they are irrelevant for $\tau - \mu$ transitions).

Due to the previously commented RGE running from M_X down to the EW scale, which induces flavour mixing in the low-energy slepton squared mass matrices, these will contain in general non-vanishing off-diagonal entries and one has to proceed to the full diagonalisation of these general matrices. The situation is qualitatively different for charged sleptons and for sneutrinos as we will be seen next.

The most general squared mass matrix for the case of charged sleptons is given by a 6×6 matrix, with all entries being now non-vanishing. Therefore, the corresponding matrix, referred to the $(\tilde{e}_L, \tilde{e}_R, \tilde{\mu}_L, \tilde{\mu}_R, \tilde{\tau}_L, \tilde{\tau}_R)$ basis, can be written as follows

$$M_{\tilde{l}}^2 \;=\; \begin{pmatrix} M_{LL}^{ee\,2} & M_{LR}^{ee\,2} & M_{LL}^{e\mu\,2} & M_{LR}^{e\mu\,2} & M_{LL}^{e\tau\,2} & M_{LR}^{e\tau\,2} \\ M_{RL}^{ee\,2} & M_{RR}^{ee\,2} & M_{RL}^{e\mu\,2} & M_{RR}^{e\mu\,2} & M_{RL}^{e\tau\,2} & M_{RR}^{e\tau\,2} \\ M_{LL}^{\mu e\,2} & M_{LR}^{\mu e\,2} & M_{LL}^{\mu\mu\,2} & M_{LR}^{\mu\mu\,2} & M_{LL}^{\mu\tau\,2} & M_{LR}^{\mu\tau\,2} \\ M_{LR}^{\mu e\,2} & M_{RR}^{\mu e\,2} & M_{RL}^{\mu\mu\,2} & M_{RR}^{\mu\mu\,2} & M_{RL}^{\mu\tau\,2} & M_{RR}^{\mu\tau\,2} \\ M_{LL}^{\tau e\,2} & M_{LR}^{\tau e\,2} & M_{LL}^{\tau\mu\,2} & M_{LR}^{\tau\mu\,2} & M_{LL}^{\tau\tau\,2} & M_{LR}^{\tau\tau\,2} \\ M_{RL}^{\tau e\,2} & M_{RR}^{\tau e\,2} & M_{RL}^{\tau\mu\,2} & M_{RR}^{\tau\mu\,2} & M_{RL}^{\tau\tau\,2} & M_{RR}^{\tau\tau\,2} \end{pmatrix} , \tag{1.87}$$

where

$$\begin{aligned} M_{LL}^{ij\,2} &= m_{\tilde{L},ij}^2 + v_1^2 \left(Y_l^\dagger Y_l\right)_{ij} + m_Z^2 \cos 2\beta \left(-\frac{1}{2} + \sin^2\theta_W\right) \delta_{ij} \,, \\ M_{RR}^{ij\,2} &= m_{\tilde{E},ij}^2 + v_1^2 \left(Y_l^\dagger Y_l\right)_{ij} - m_Z^2 \cos 2\beta \sin^2\theta_W \,\delta_{ij} \,, \\ M_{LR}^{ij\,2} &= v_1 \left(A_l^{ij}\right)^* - \mu\, Y_l^{ij}\, v_2 \,, \\ M_{RL}^{ij\,2} &= \left(M_{LR}^{ji\,2}\right)^* . \end{aligned} \tag{1.88}$$

The off-diagonal entries in flavour space are originated obvioulsy from the soft-SUSY breaking masses and trilinear couplings above, $m_{\tilde{L},ij}$, $m_{\tilde{E},ij}$ and A_l^{ij}, with $i, j = e\,,\, \mu\,,\, \tau$, which here refer to their corresponding values at the electroweak scale. As we have already said, we will get them by solving numerically the RGEs to one loop with the public code `SPheno2.2.2` and by imposing the universality conditions at M_X for the sfermion and gaugino sectors, Eq. (1.77), together with the corresponding ones for the Higgs sector.

Regarding the sneutrino sector, we work in the very good approximation explained previously where at low energies we keep just the light sneutrino states which are made mainly of $\tilde{\nu}_L$'s and

assume that the $\tilde{\nu}_R$'s decouple [133]. Thus, the diagonalisation procedure is simpler than in the charged slepton case since the sneutrino squared mass matrix is 3×3 type. This 3×3 matrix, referred to the $\tilde{\nu}' = (\tilde{\nu}_{e,\,L},\, \tilde{\nu}_{\mu,\,L},\, \tilde{\nu}_{\tau,\,L})$ basis can be written as follows

$$M^2_{\tilde{\nu}} \;=\; \begin{pmatrix} m^2_{\tilde{L},e} + \frac{1}{2} m^2_Z \cos 2\beta & m^2_{\tilde{L},e\mu} & m^2_{\tilde{L},e\tau} \\ m^2_{\tilde{L},\mu e} & m^2_{\tilde{L},\mu} + \frac{1}{2} m^2_Z \cos 2\beta & m^2_{\tilde{L},\mu\tau} \\ m^2_{\tilde{L},\tau e} & m^2_{\tilde{L},\tau\mu} & m^2_{\tilde{L},\tau} + \frac{1}{2} m^2_Z \cos 2\beta \end{pmatrix} , \tag{1.89}$$

where $m^2_{\tilde{L},ij}$ are the same as in the previous charged slepton squared mass matrix.

The physical masses and states are obtained by diagonalising the previous squared mass matrices, leading to

$$\begin{aligned} M^{2\,\mathrm{diag}}_{\tilde{l}} \;&=\; R^l\, M^2_{\tilde{l}}\, R^{l\,\dagger} \;=\; \mathrm{diag}\,(m^2_{\tilde{l}_1}, .., m^2_{\tilde{l}_6})\,, \\ M^{2\,\mathrm{diag}}_{\tilde{\nu}} \;&=\; R^\nu\, M^2_{\tilde{\nu}}\, R^{\nu\,\dagger} \;=\; \mathrm{diag}\,(m^2_{\tilde{\nu}_1},\, m^2_{\tilde{\nu}_2},\, m^2_{\tilde{\nu}_3})\,, \end{aligned} \tag{1.90}$$

where R^l and R^ν are unitary rotation matrices.

Notice that when working in the physical mass eigenstate basis, all the information of flavour mixing is encoded in the previous values of the physical masse $m_{\tilde{l}_i}$ and $m_{\tilde{\nu}_i}$ and the rotation matrices R^l and R^ν. In particular, these physical parameters will transmit the flavour mixing to the relevant couplings for the forthcoming computation of LFV rates, that are summarised in Appendix A.

1.5.1 Dependence of slepton and sneutrino flavour mixing on seesaw parameters

In order to illustrate the size of the flavour mixing in slepton and sneutrino sectors, we define here the following flavour changing dimensionless parameters:

$$\begin{aligned} \delta^{ij}_{LL} &= \frac{M^{ij2}_{LL}}{\tilde{m}^2}\,, \\ \delta^{ij}_{LR} &= \frac{M^{ij2}_{LR}}{\tilde{m}^2}\,, \\ \delta^{ij}_{RR} &= \frac{M^{ij2}_{RR}}{\tilde{m}^2}\,, \end{aligned} \tag{1.91}$$

where $i, j = 1, 2, 3,\ i \neq j$ and

$$\tilde{m}^2 = \left(m^2_{\tilde{l}_1} m^2_{\tilde{l}_2} m^2_{\tilde{l}_3} m^2_{\tilde{l}_4} m^2_{\tilde{l}_5} m^2_{\tilde{l}_6} \right)^{1/6}\,, \tag{1.92}$$

is an average slepton squared mass, which we have set in terms of the physical masses.

One can estimate the previous dimensionless parameters of Eq. (1.91) by using the LLog approximation which leads to the following simple results:

$$\begin{aligned}
\delta^{ij}_{LL}\Big|_{\rm LLog} &= \frac{(\Delta m^2_{\tilde{L}})_{ij}}{M_0^2}\,, \\
\delta^{ij}_{LR}\Big|_{\rm LLog} &= \frac{v_1(\Delta A_l)_{ij}}{M_0^2}\,, \\
\delta^{ij}_{RR}\Big|_{\rm LLog} &= \frac{(\Delta m^2_{\tilde{E}})_{ij}}{M_0^2}\,,
\end{aligned} \tag{1.93}$$

where $(\Delta m^2_{\tilde{L}})_{ij}$, $(\Delta A_l)_{ij}$ and $(\Delta m^2_{\tilde{E}})_{ij}$ are given in Eq. (1.84). Notice that the results in Eq (1.84) imply the following hierarchy in the size of these parameters:

$$\delta^{ij}_{LL}\Big|_{\rm LLog} \gg \delta^{ij}_{LR}\Big|_{\rm LLog} \gg \delta^{ij}_{RR}\Big|_{\rm LLog}\,.$$

Some studies of bounds on these parameters from experimental data can be found in [136–138]. In the following and for illustrative purposes, we will show first some results in the LLog approximation. We will see later that some predictions of the full computation disagree with the LLog results, what indicates that the LLog approximation does not fully work. For the following discussion we choose the CMSSM-seesaw scenario.

We show in Figs. 1.1 and 1.2 the predictions of the $\delta_{ij} \equiv \delta^{ij}_{LL}\Big|_{\rm LLog}$ parameter as a function of the seesaw parameters, and in some selected examples within the scenarios described in Eq. (1.20) and Eq. (1.21). We show in Fig. 1.1a the dependence of $|\delta_{ij}|$ with m_N, for degenerate heavy neutrinos, quasi-degenerate light neutrinos and real R. Notice that in this case, the δ_{ij} turn out to be independent on R. As can be seen, the three $|\delta_{ij}|$ grow with m_N and the largest one, which is $|\delta_{32}|$, reaches values up to 2.4×10^{-3} for $m_N = 10^{14}$ GeV. The size of $|\delta_{21}|$ can reach values up to 3.8×10^{-5} for $m_N = 10^{14}$ GeV, and correspondingly for $|\delta_{31}| \simeq |\delta_{21}|$. The size of the δ_{ij} in this scenario with degenerate heavy neutrinos and quasi-degenerate light neutrinos can obviously be increased if R is assumed instead to be complex. In this case, the δ_{ij} are in general complex numbers. As an example, we show in Fig. 1.1b the dependence of $|\delta_{ij}|$, with $m_N = 10^{14}$ GeV, on the parameter a of Eq. (1.25), for $a = b = c$. The size of $|\delta_{ij}|$ increases clearly with a and, for the studied range, $|\delta_{21}|$ can be as large as 2×10^{-2}. In particular, for values of $|abc| \simeq 10^{-5}$, that is claimed to generate succesfull baryogenesis [139], the generated $|\delta_{ij}|$ are still large, namely, $|\delta_{21}| = 4 \times 10^{-3}$. Notice also that the relative size of the different δ_{ij} changes with respect to Fig. 1.1a. Similar conclusions can be reached if we use instead the R parameterisation with complex θ_1, θ_2 and θ_3.

The case of hierarchical heavy and light neutrinos is shown in Figs. 1.1c and 1.1d for real R and in Fig. 1.2 for complex R. In Fig. 1.1c it is plotted the dependence with real θ_1 with $(m_{N_1}, m_{N_2}, m_{N_3}) = (10^8, 2 \times 10^8, 10^{14})$ GeV and $\theta_2 = \theta_3 = 0$. We see that δ_{32} is the largest one

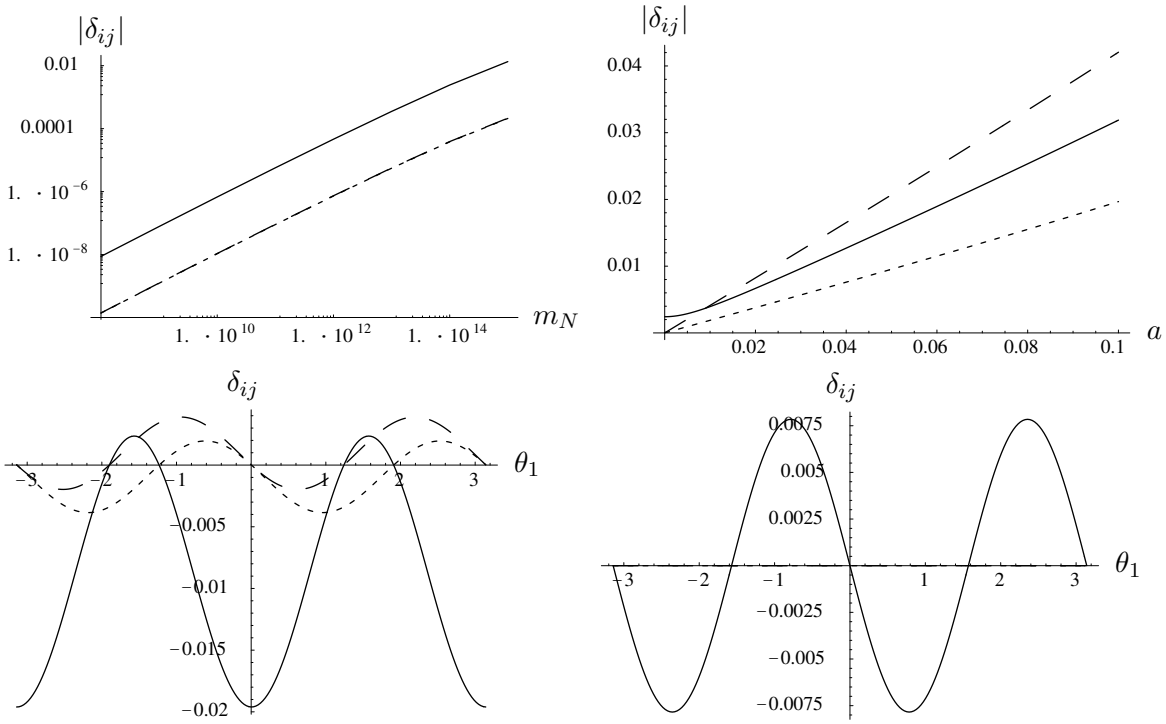

Figure 1.1: Dependence of δ_{ij} with the seesaw parameters. Solid, long-dashed and short-dashed lines are for δ_{32}, δ_{31} and δ_{21} respectively. The two upper plots are for quasi-degenerate light neutrinos and degenerate heavy neutrinos. The two lower plots are for hierarchical light and heavy neutrinos. **(a)** Upper left panel: Dependence with m_N for real R. **(b)** Upper right panel: Dependence with the a parameter with $m_N = 10^{14}$ GeV and complex R, with $a = b = c$. **(c)** Lower left panel: Dependence with real θ_1 for $(m_{N_1}, m_{N_2}, m_{N_3}) = (10^8, 2 \times 10^8, 10^{14})$ GeV and $\theta_2 = \theta_3 = 0$.**(d)** Lower right panel: Same as in (3c) but for $U_{\rm PMNS} = 1$. In all plots here, $\tan\beta = 35$.

and reaches negative values up to -1.96×10^{-2} at the points $\theta_1 = 0, \pm\pi$, precisely where δ_{21} and δ_{31} vanish. Notice that the point $\theta_1 = 0$ in Fig. 1.1c corresponds to the simplest case of $R = \mathbb{1}$ and, therefore, represents the situation where the $U_{\rm PMNS}$ matrix is the only origin for flavour changing. This means that our experimental input for the $U_{\rm PMNS}$ matrix generates by itself sizeable rates for slepton flavour mixing between the second and third generations. The alternative situation where just the R matrix is generating the flavour mixing is illustrated in Fig. 1.1d. Here we show the δ_{ij} dependence with θ_1 for $\theta_2 = \theta_3 = 0$ and $U_{\rm PMNS} = \mathbb{1}$. We see that $|\delta_{32}|$ reaches values up to about 7.8×10^{-3} whereas δ_{21} and δ_{31} vanish for all θ_1. By comparing these two situations we can infere that, for the case of real R with $\theta_1 \neq 0$ and $\theta_2 = \theta_3 = 0$, the induced mixing between the second and third generations from the experimental $U_{\rm PMNS}$ is relevant and can be even larger than the effect from R.

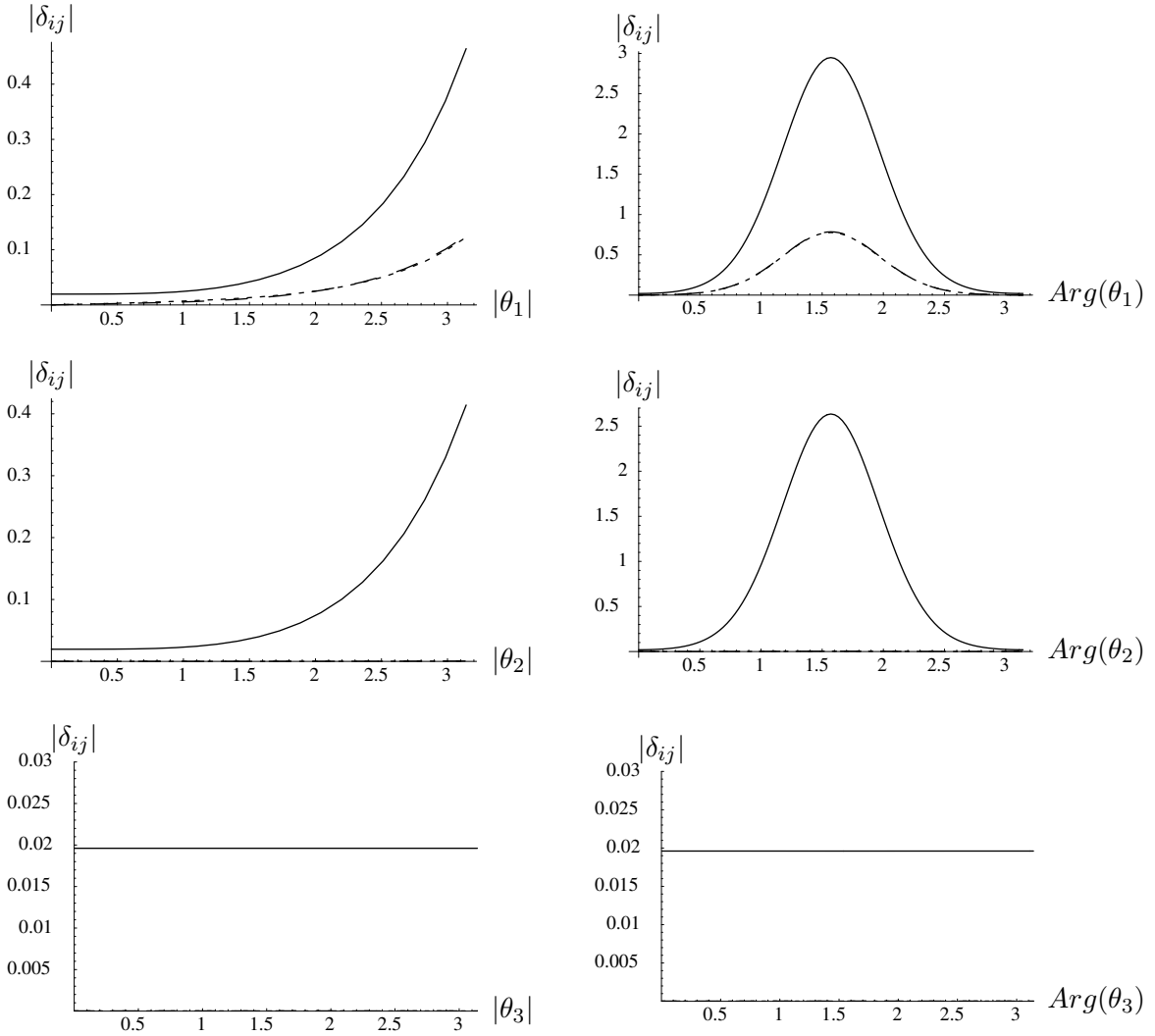

Figure 1.2: Dependence of $|\delta_{ij}|$ on the seesaw parameters for hierarchical neutrinos and complex θ_i. Solid, long-dashed and short-dashed lines (the two later being undistinguishible in the plots) are for $|\delta_{32}|$, $|\delta_{31}|$ and $|\delta_{21}|$ respectively. Left panels: Dependence with $|\theta_1|$, $|\theta_2|$ and $|\theta_3|$ respectively. We take $\arg\theta_i = \pi/4$, correspondingly, and the rest of angles are set to zero. Right panels: Dependence with $\arg\theta_1$, $\arg\theta_2$ and $\arg\theta_3$ respectively. We take $|\theta_i| = \pi$, correspondingly, and the rest of angles are set to zero. In all plots here, $(m_{N_1}, m_{N_2}, m_{N_3}) = (10^8, 2\times10^8, 10^{14})$ GeV and $\tan\beta = 35$.

We have also studied in this hierarchical case the alternative choices for real R with $\theta_2 \neq 0$, $\theta_1 = \theta_3 = 0$ and with $\theta_3 \neq 0$, $\theta_1 = \theta_2 = 0$, although the corresponding plots are not shown here for brevity. We find a δ_{32} dependence on θ_2 very similar to that on θ_1, with maximum negative δ_{32} values at $\theta_2 = 0, \pm\pi$ of -1.96×10^{-2}. In contrast, δ_{21} and δ_{31} now take very small values whose maximum are 2.4×10^{-5}. Regarding the dependence with θ_3 a different situation is found, where the three δ_{21}, δ_{31} and δ_{32} are approximately constant with θ_3 and take the values, $\delta_{32} = -1.96 \times 10^{-2}$, and $\delta_{31} \simeq \delta_{21} = 2.4 \times 10^{-5}$, respectively.

The case of hierarchical neutrinos with complex R produces, in most cases, complex δ_{ij} values and their moduli are in general larger than in the case of real R, as can be clearly seen in Fig. 1.2. The particular choice for the heavy neutrino masses $(m_{N_1}, m_{N_2}, m_{N_3}) = (10^8, 2\times10^8, 10^{14})$ GeV, where the two lightest neutrinos have closer masses and well below the mass of the heaviest one, produces the specific pattern shown in these plots, where the dependence of $|\delta_{32}|$ on θ_1, for $\theta_2 = \theta_3 = 0$, and on θ_2, for $\theta_1 = \theta_3 = 0$ are very similar, and $|\delta_{32}|$ can reach very large values for a large region of the $(|\theta_i|,\arg(\theta_i))$, $i = 1, 2$ parameter space. For instance, for fixed $\arg(\theta_1) = \pi/4$, and $|\theta_1|$ up to π we find $|\delta_{32}|$ values up to 0.46 and similarly for θ_2. Larger values of $\arg\theta_i$, $i = 1, 2$, produce even larger $|\delta_{32}|$ and it reaches its maximum at $\arg(\theta_i) = \pi/2$. In contrast, δ_{21} and δ_{31} reach much smaller values with complex θ_2 than with complex θ_1, being $|\delta_{21}| \simeq |\delta_{31}| < 5 \times 10^{-4}$ for $|\theta_2| < \pi$. On the other hand, they depend strongly on complex θ_1 and $|\delta_{21}|$ can reach too large values, up to $\mathcal{O}(10^{-1})$. Finally, the behaviour with complex θ_3 is very similar to the real case, with the three $|\delta_{21}|$, $|\delta_{31}|$ and $|\delta_{32}|$ being nearly constant with θ_3. Their values are $|\delta_{32}| = 1.96 \times 10^{-2}$ and $|\delta_{21}| \simeq |\delta_{31}| = 2.4 \times 10^{-5}$, respectively.

The correlation between $|\delta_{32}|$ and $|Y_\nu^{32}|$ is clearly shown in Fig. 1.3. Here we have set $M_{\rm SUSY} = M_0 = M_{1/2} = 250$ GeV, $A_0 = 0$, $(m_{N_1}, m_{N_2}, m_{N_3}) = (10^{10}, 10^{11}, 10^{14})$ GeV, and hierarchical light neutrino parameters as in Eq. 1.22. We see that $|\delta_{32}|$ follows the same pattern as $|Y_\nu^{32}|$ (and $|Y_\nu^{33}|$) and can reach large values in the range 0.1-1 for several choices of $|\theta_2|$ and $\arg\theta_2$. The dips are also found at the same $|\theta_2|$ value for both $|\delta_{32}|$ and $|Y_\nu^{32}|$ predictions and occur for real θ_2 and due to the particular parameterisation of R in Eq. (1.23) in terms of $\cos\theta_i$ and $\sin\theta_i$. Notice also that the predictions for $|\delta_{32}|$ corresponding to Yukawa couplings larger than about 4 are not shown, because in this plot and in the following predictions for LFV processes in this work perturbativity in all the gauge and Yukawa couplings are imposed. This is set numerically in the code `SPheno2.2.2` by the requirement $|Y_\nu|^2/(4\pi) < 1.5$ and corresponds to a maximal predicted value of about $|\delta_{32}| < 0.4$. The corresponding predictions with respect to θ_1 are very similar to those of θ_2 and are not shown for brevity.

The numerical predictions for $|\delta_{32}|$ with hierarchical neutrinos as a function of the heaviest neutrino mass, m_{N_3} are shown in Fig.1.4. $|\delta_{32}|$ values within the range 0.1-1 are obtained for large m_{N_3} values, say within the interval $10^{13} - 10^{15}$ GeV. Notice that $|\delta_{32}|$ for $\theta_2 = 2.9\, e^{i\pi/4}$ enters into the above commented non-perturbative region for values larger than $m_{N_3} = 10^{14}$

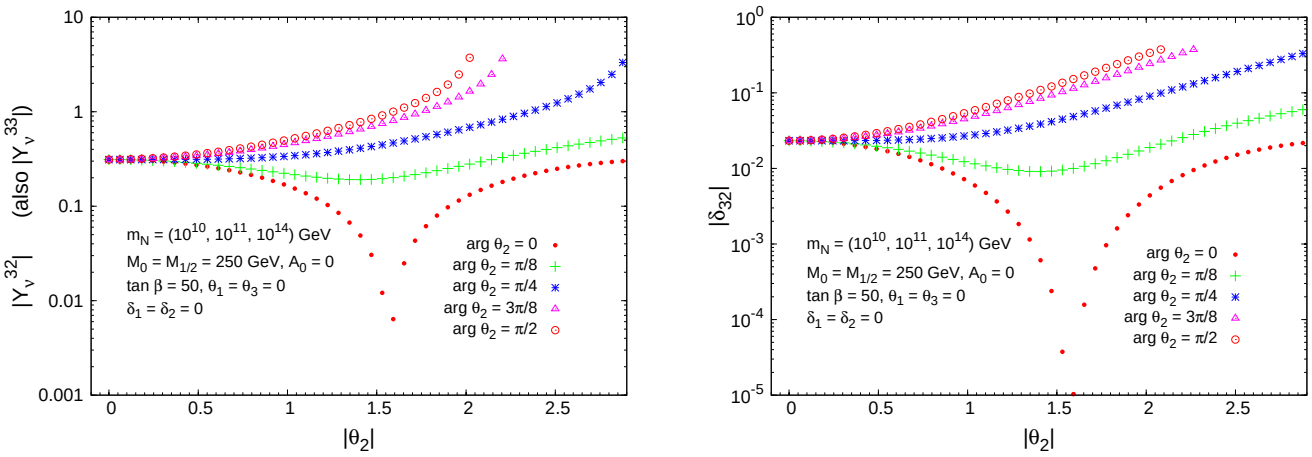

Figure 1.3: Correlation between $|Y_\nu^{32}|$ and $|\delta_{32}|$, in the CMSSM-seesaw scenario, as a function of $|\theta_2|$, for $\arg\theta_2 = \{0, \pi/8, \pi/4, 3\pi/8, \pi/2\}$ (dots, crosses, asterisks, triangles and circles, respectively). Both $|\theta_2|$ and $\arg\theta_2$ are given in radians. The predictions for $|Y_\nu^{33}|$ are practically indistinguishable from those for $|Y_\nu^{32}|$.

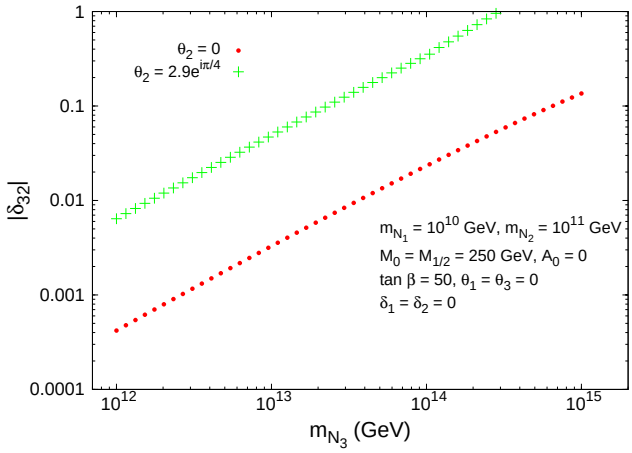

Figure 1.4: $|\delta_{32}|$, in the CMSSM-seesaw scenario, as a function of m_{N_3}.

GeV. Concretely, the value $|\delta_{32}| = 1$, which is interesting for later discussion and comparison with other works, corresponds to $m_{N_3} = 3 \times 10^{14}$ GeV and lies clearly in the non-perturbative region. Finally, we have checked that $|\delta_{32}|$ is not much dependent on $\tan\beta$ nor on $m_{N_{1,2}}$.

In summary, the case of hierarchical heavy neutrinos with complex θ_i leads to larger δ_{ij} values than the degenerate case and, in consequence, larger LFV rates.

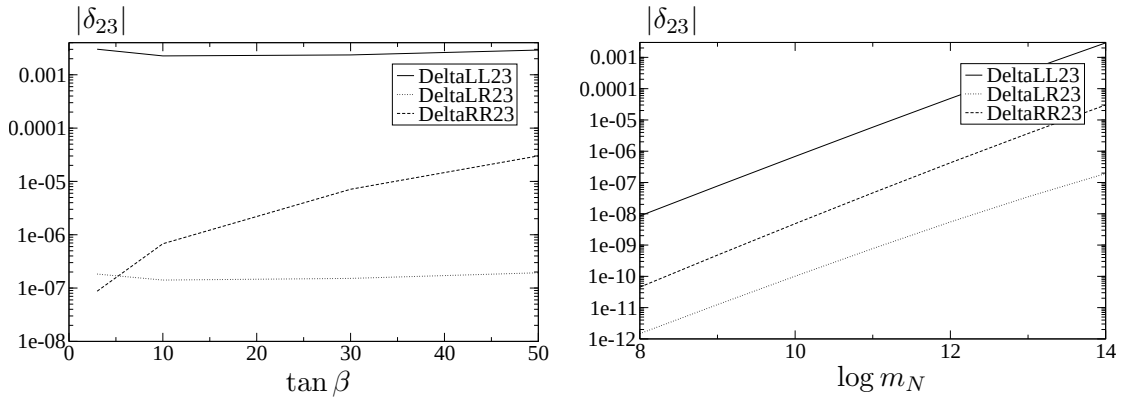

Figure 1.5: Predicitons of the full parameters $|\delta^{32}_{LL,LR,RR}|$ for quasi-degenerate light neutrinos, degenerate heavy neutrinos and real R. (a) Left panel, dependence on $\tan\beta$ for $m_N = 10^{14}$ GeV, (b) right panel, dependence on m_N for $\tan\beta = 50$. The other input parameters are $M_0 = 400$ GeV, $M_{1/2} = 300$ GeV, $A_0 = 0$ and $\text{sign}(\mu) > 0$.

Next we compare the full RGEs predictions with the previous results of the LLog approximation.

In Fig. 1.5 we show the predictions for the full δ^{32}_{LL}, δ^{32}_{LR} and δ^{32}_{RR}, as defined in Eq. (1.91), for the case of quasi-degenerate light neutrinos and degenerate heavy neutrinos as a function of $\tan\beta$ and m_N. These are the flavour changing parameters that are the relevant ones for the $\tau-\mu$ transitions. As expected from the previous results of the LLog approximation, we see in Fig. 1.5 that $|\delta^{32}_{LL}|$ is much larger than $|\delta^{32}_{LR}|$ and $|\delta^{32}_{RR}|$. However, we get $|\delta^{32}_{RR}|$ larger than $|\delta^{32}_{LR}|$ and it can be indeed two orders of magnitude larger than $|\delta^{32}_{LR}|$ at large $\tan\beta$. The parameter $|\delta^{32}_{RR}|$ is clearly the most sensitive to $\tan\beta$. It is clear that, at least for the parameters chosen here, the LLog approximation does not fully work. Indeed, we will see later in the estimates of LFV rates that there are cases (in particular for large negative A_0) where the LLog approximation fails even more, leading to overestimates of those rates in more than a factor 10^4.

We show in fig 1.6 the dependence of the other full parameters $|\delta^{12,13}_{LL,LR,RR}|$ on $\tan\beta$. The main difference is that here $|\delta^{12(13)}_{LR}|$ is larger than $|\delta^{12(13)}_{RR}|$. The maximum reached values are very small in this case, $|\delta^{12(13)}_{LL}| \sim 5\times 10^{-5}$.

The predictions of the full parameters $|\delta^{32}_{LL,LR,RR}|$ as a function of $|\theta_2|$ for hierarchical neutrinos are shown in Fig. 1.7. We see that $|\delta^{32}_{LL}|$ can reach very large values, up to 0.4, for $|\theta_2| = 3$ and $\arg(\theta_2) = \pi/4$. We have checked that this particular choice of $\theta_2 = 3e^{i\pi/4}$ gives rise to large neutrino Yukawa matrix elements $|Y^{33}_\nu|$ and $|Y^{32}_\nu|$ of the order of 1, which are the responsible for this large mixing in the slepton sector. By comparing this figure with Fig. 1.3 we also see that the numerical predictions for the full δ^{32}_{LL} and δ_{32} of the LLog approximation are indeed pretty

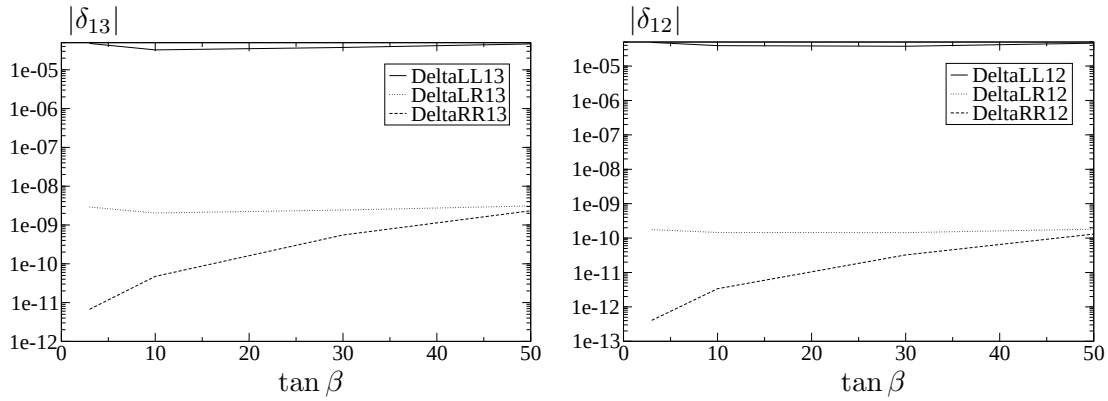

Figure 1.6: Predicitons as a function of $\tan\beta$ of the full parameters $|\delta^{12,13}_{LL,LR,RR}|$ for quasi-degenerate light neutrinos, degenerate heavy neutrinos, real R and for $m_N = 10^{14}$ GeV. (a) left panel, $|\delta^{31}_{LL,LR,RR}|$ and (b) right panel, $|\delta^{21}_{LL,LR,RR}|$. The other input parameters are $M_0 = 400$ GeV, $M_{1/2} = 300$ GeV, $A_0 = 0$ and $\text{sign}(\mu) > 0$.

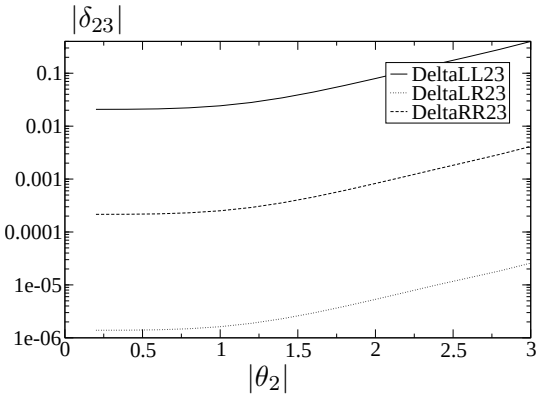

Figure 1.7: Dependence of the full parameters $|\delta^{32}_{LL,LR,RR}|$ on $|\theta_2|$ for hierarchical neutrinos and for $\arg(\theta_2) = \pi/4$, $(m_{N_1}, m_{N_2}, m_{N_3}) = (10^8, 2\times10^8, 10^{14})$ GeV, $\theta_1 = \theta_3 = 0$, $\tan\beta = 50$, $M_0 = 400$ GeV, $M_{1/2} = 300$ GeV, $A_0 = 0$ and $\text{sign}(\mu) > 0$.

close. This so, even that the choices for m_{N_1} and m_{N_2} are different in this two plots, but as we have said the relevant mass for the right-handed neutrinos is the heaviest one, m_{N_3}, which is common in the two plots. Therefore, in this case the LLog approximation works well for the LL parameter, but again fails for the LR and the RR ones.

Finally, we summarise in Fig. 1.8 the predictions of the relevant entries of the Y_ν coupling matrix as a function of $|\theta_1|$ for hierarchical neutrinos. Similar results are obtained for the behaviour of $|Y^{ij}_\nu|$ with $|\theta_2|$, not shown here for brevity.

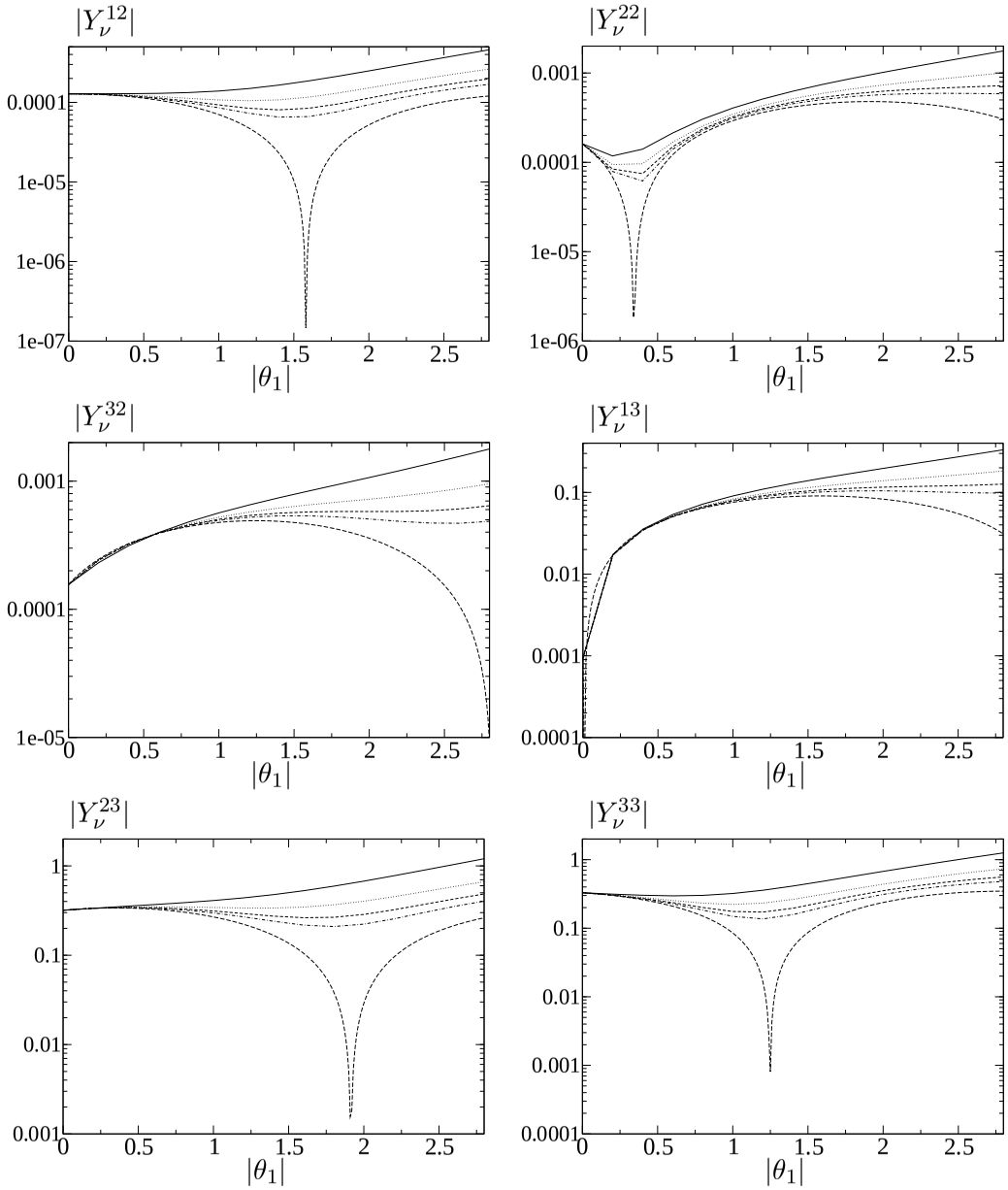

Figure 1.8: Dependence of $|Y_\nu|$ on $|\theta_1|$ with hierarchical heavy neutrinos and complex R, for $\arg(\theta_1) = 0, \pi/10, \pi/8, \pi/6, \pi/4$ in radians (lower to upper lines), $(m_{N_1}, m_{N_2}, m_{N_3}) = (10^8, 2 \times 10^8, 10^{14})$ GeV, $\theta_2 = \theta_3 = 0$, $\tan\beta = 50$, $M_0 = 400$ GeV, $M_{1/2} = 300$ GeV and $A_0 = 0$.

1.6 Examples of spectra of constrained SUSY-seesaw models

The spectrum of the constrained MSSM-seesaw scenarios is very similar to the common CMSSM-like scenarios, but it is slightly modified by the introduction of the seesaw mechanism and the existence of new particles (right-handed neutrinos and sneutrinos) which take part in the RGEs.

SPS	$M_{1/2}$ (GeV)	M_0 (GeV)	A_0 (GeV)	$\tan\beta$	μ
1 a	250	100	-100	10	> 0
1 b	400	200	0	30	> 0
2	300	1450	0	10	> 0
3	400	90	0	10	> 0
4	300	400	0	50	> 0
5	300	150	-1000	5	> 0

Table 1.2: Values of $M_{1/2}$, M_0, A_0, $\tan\beta$, and sign μ for the SPS points considered in the analysis.

Within the CMSSM, instead of scanning over the full ($M_{1/2}$, M_0, A_0, $\tan\beta$, sign μ) parameter space, it is usual in the literature to define specific points, each exhibiting distinct characteristics from the low-energy phenomenology point of view, which are specified by means of the "Snowmass Points and Slopes" (SPS) cases [140] listed in Table 1.2. These points are benchmark scenarios for an mSUGRA SUSY breaking mechanism. Points 1a and 1b are "typical" mSUGRA points (with intermediate and large $\tan\beta$, respectively), lying on the so-called bulk of the cosmological region. The focus-point region for the relic abundance is represented by SPS 2, also characterised by a fairly light gaugino spectrum. SPS 3 is directed towards the coannihilation region, accordingly displaying a very small slepton-neutralino mass difference. Finally, SPS 4 and 5 are extreme $\tan\beta$ cases, with very large and small values, respectively. The corresponding mass spectra of each of these SPS points, which define different CMSSM scenarios, are displayed in Figs. 1.9, 1.10 and 1.11.

As we have said, the introduction of right-handed neutrinos, their SUSY partners and the seesaw mechanism vary the predicted spectrum of the previous CMSSM scenarios. For instance, in the case with input parameters given by the SPS 4 point, assuming degenerate light and heavy neutrinos with $m_N = 10^{14}$ GeV and $\theta_i = 0$, and by using the code `SPheno2.2.2`[2] to solve the full one-loop RGEs we get the following MSSM spectrum (we just specify here the relevant sectors for this thesis):

[2]In this code the predicted masses at the EW scale include in addition the corresponding corrections from one-loop diagrams.

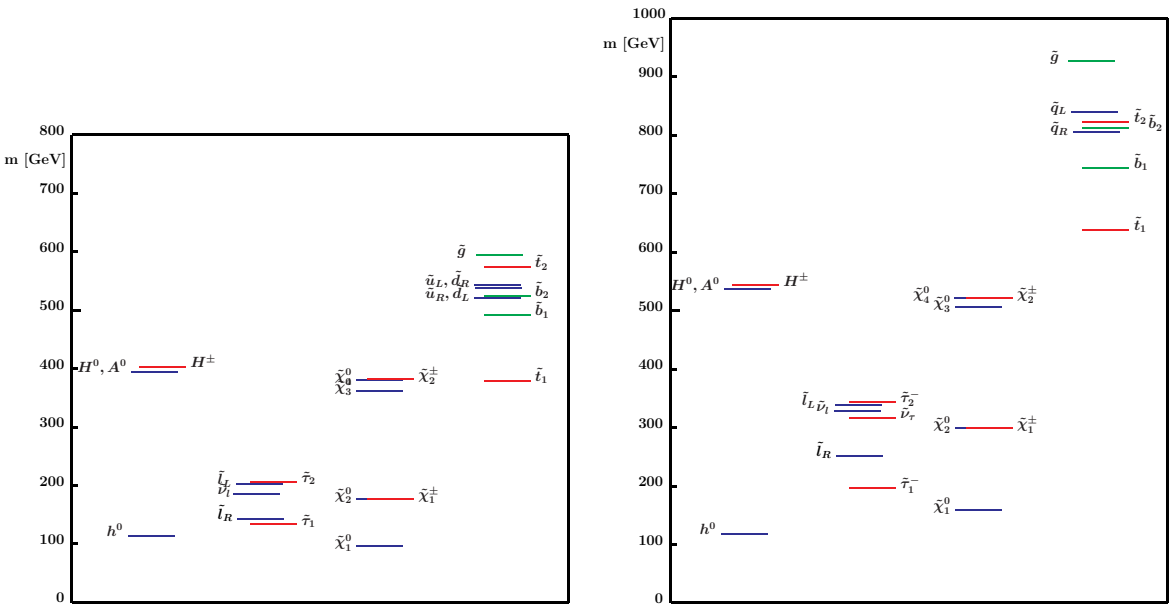

Figure 1.9: Mass spectrum of SPS 1a (left panel) and SPS 1b (right panel).

$$
\begin{array}{lll}
m_{\tilde{l}_1} = 247 \text{ GeV} & m_{\tilde{\chi}_1^0} = 121 \text{ GeV} & m_{h^0} = 114 \text{ GeV} \\
m_{\tilde{l}_2} = 397 \text{ GeV} & m_{\tilde{\chi}_2^0} = 232 \text{ GeV} & m_{H^0} = 457 \text{ GeV} \\
m_{\tilde{l}_3} = 413 \text{ GeV} & m_{\tilde{\chi}_3^0} = 484 \text{ GeV} & m_{A^0} = 457 \text{ GeV} \\
m_{\tilde{l}_4} = 416 \text{ GeV} & m_{\tilde{\chi}_4^0} = 493 \text{ GeV} & m_{\tilde{\nu}_1} = 351 \text{ GeV} \\
m_{\tilde{l}_5} = 417 \text{ GeV} & m_{\tilde{\chi}_1^-} = 232 \text{ GeV} & m_{\tilde{\nu}_2} = 409 \text{ GeV} \\
m_{\tilde{l}_6} = 419 \text{ GeV} & m_{\tilde{\chi}_2^-} = 495 \text{ GeV} & m_{\tilde{\nu}_3} = 410 \text{ GeV}.
\end{array}
$$

We clearly see that the mass spectrum is very similar to that of the SPS 4 point in a CMSSM scenario, shown in Fig. 1.11 (left panel). There are some slight differences like a noticeable spliting between the charge sleptons, and also between the sneutrinos, but it is at the most of 2-3 GeV. The most important difference of this CMSSM-seesaw spectrum is the flavour mixing that as we have said is implicit in the slepton and sneutrinos masses and in their corresponding rotation matrices, which, as we will see in the next chapters, can be sizable and induce large LFV rates, via SUSY-loops.

It is also interesting to compare the spectrum for the hierarchical heavy neutrino case with the previous degenerate case. For instance, for the same input values as above but now with $(m_{N_1}, m_{N_2}, m_{N_3}) = (10^8, 2 \times 10^8, 10^{14})$ GeV, $\theta_1 = \theta_3 = 0$ and θ_2 set to the extreme value $\theta_2 = 2.8 e^{i\frac{\pi}{4}}$ we get the following masses:

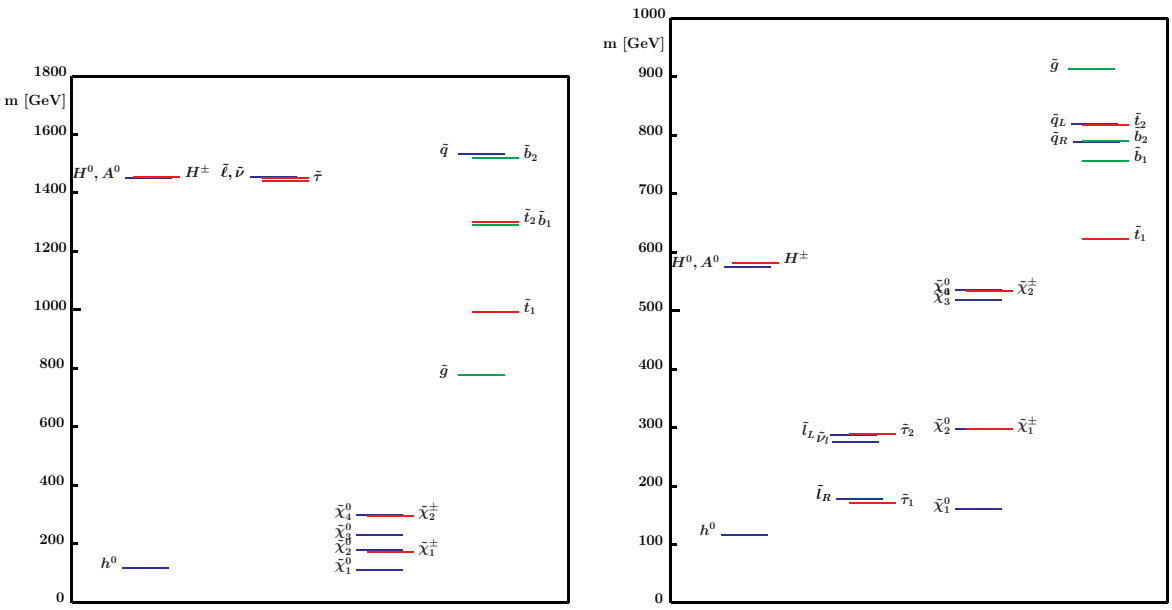

Figure 1.10: Mass spectrum of SPS 2 (left panel) and SPS 3 (right panel).

$$
\begin{array}{lll}
m_{\tilde{l}_1} = 230 \text{ GeV} & m_{\tilde{\chi}_1^0} = 122 \text{ GeV} & m_{h^0} = 114 \text{ GeV} \\
m_{\tilde{l}_2} = 356 \text{ GeV} & m_{\tilde{\chi}_2^0} = 232 \text{ GeV} & m_{H^0} = 455 \text{ GeV} \\
m_{\tilde{l}_3} = 413 \text{ GeV} & m_{\tilde{\chi}_3^0} = 481 \text{ GeV} & m_{A^0} = 455 \text{ GeV} \\
m_{\tilde{l}_4} = 417 \text{ GeV} & m_{\tilde{\chi}_4^0} = 490 \text{ GeV} & m_{\tilde{\nu}_1} = 296 \text{ GeV} \\
m_{\tilde{l}_5} = 436 \text{ GeV} & m_{\tilde{\chi}_1^-} = 232 \text{ GeV} & m_{\tilde{\nu}_2} = 422 \text{ GeV} \\
m_{\tilde{l}_6} = 448 \text{ GeV} & m_{\tilde{\chi}_2^-} = 492 \text{ GeV} & m_{\tilde{\nu}_3} = 441 \text{ GeV}
\end{array}
$$

It is obvious that the complex R affects significantly the predictions of the masses, specially in the slepton sector. For comparison with the previous case of reference, we also include here the predicted masses for lower values of the universal soft parameters, $M_0 = 250$ GeV and $M_{1/2} = 150$ GeV, which lead to a lighter spectrum, and for the particular value $\theta_1 = 2.8e^{i\frac{\pi}{4}}$ ($\theta_2 = \theta_3 = 0$):

$$
\begin{array}{lll}
m_{\tilde{l}_1} = 94 \text{ GeV} & m_{\tilde{\chi}_1^0} = 58 \text{ GeV} & m_{h^0} = 108 \text{ GeV} \\
m_{\tilde{l}_2} = 218 \text{ GeV} & m_{\tilde{\chi}_2^0} = 107 \text{ GeV} & m_{H^0} = 269 \text{ GeV} \\
m_{\tilde{l}_3} = 259 \text{ GeV} & m_{\tilde{\chi}_3^0} = 284 \text{ GeV} & m_{A^0} = 269 \text{ GeV} \\
m_{\tilde{l}_4} = 259 \text{ GeV} & m_{\tilde{\chi}_4^0} = 296 \text{ GeV} & m_{\tilde{\nu}_1} = 143 \text{ GeV} \\
m_{\tilde{l}_5} = 273 \text{ GeV} & m_{\tilde{\chi}_1^-} = 107 \text{ GeV} & m_{\tilde{\nu}_2} = 247 \text{ GeV} \\
m_{\tilde{l}_6} = 273 \text{ GeV} & m_{\tilde{\chi}_2^-} = 300 \text{ GeV} & m_{\tilde{\nu}_3} = 261 \text{ GeV}
\end{array}
$$

Notice that the lightest slepton, neutralino, chargino and Higgs boson have masses close to their

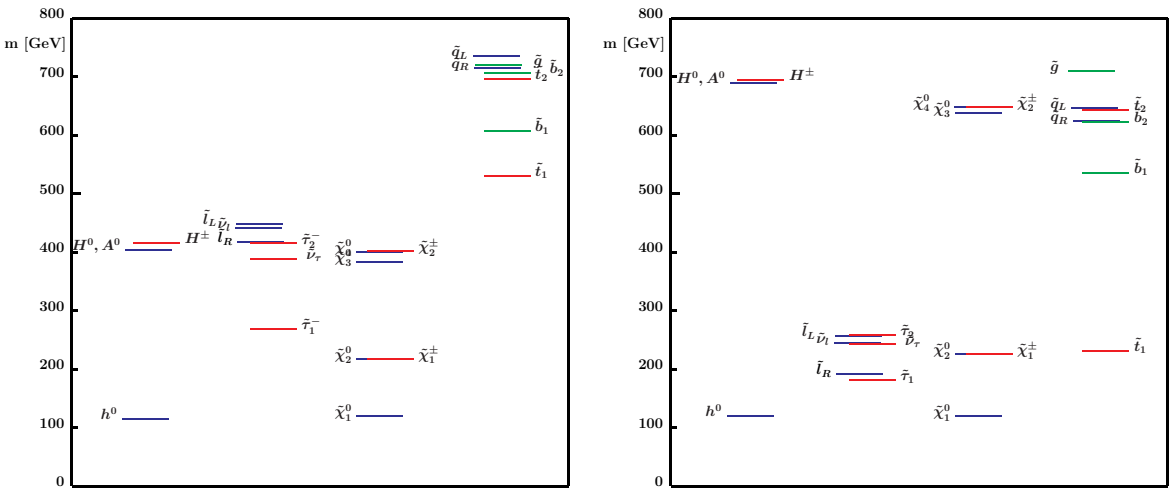

Figure 1.11: Mass spectrum of SPS 4 (left panel) and SPS 5 (right panel).

experimental lower bounds.

Similar patterns of SUSY masses are obtained for the NUHM-seesaw scenario. The main difference is that a proper choice of the non-universality parameters δ_1 and δ_2, within the range $-3 \leq \delta_{1,2} \leq 3$, can lead us to a very different Higgs sector from the previous cases of CMSSM-seesaw scenarios. We present some examples in the following.

The predictions of the Higgs boson masses m_{H^0} and m_{A^0}, since the results for these two masses are indistinguisable, as a function of δ_1 and δ_2 in the NUHM-seesaw scenarios with hierarchical neutrinos are summarised in Fig. 1.12. We have chosen here the largest value of $\tan\beta = 50$ and three representative values of $M_{\rm SUSY} = 250$, 500 and 850 GeV for moderate, heavy and very heavy SUSY spectra, respectively. The other parameters are set to the values of $m_{N_i} = (10^{10}, 10^{11}, 10^{14})$ GeV, $\theta_i = 0$, $A_0 = 0$, $\theta_{13} = 5^\circ$ and sign$(\mu) = +1$.

First, it is important to mention that not all the considered values of the $\delta_{1,2}$ parameters and $M_{\rm SUSY}$ allow for a correct $SU(2) \times U(1)$ breaking. In fact some particular choices for δ_1, δ_2 and $M_{\rm SUSY}$ lead to unacceptable negative values of $B\mu$ (and hence, negative $m^2_{A^0}$). For instance, this is the case when $\delta_{1,2}$ are simultaneously positive or negative. Some other points, despite leading to a proper $SU(2) \times U(1)$ breaking, are nevertheless not acceptable, since they lead to a Higgs boson sector which is too light, with masses below the present experimental lower limits. To ensure that our results are indeed experimentally viable, we have included in this, and in the following, only the solutions where the three neutral Higgs boson masses are above the experimental bound for the lightest MSSM Higgs boson, which at present is 110 GeV for $\tan\beta > 5$ (99.7% CL) [10]. The most interesting solutions with important phenomenological implications are found for negative δ_1 and positive δ_2, the choice selected for Fig. 1.12. In this

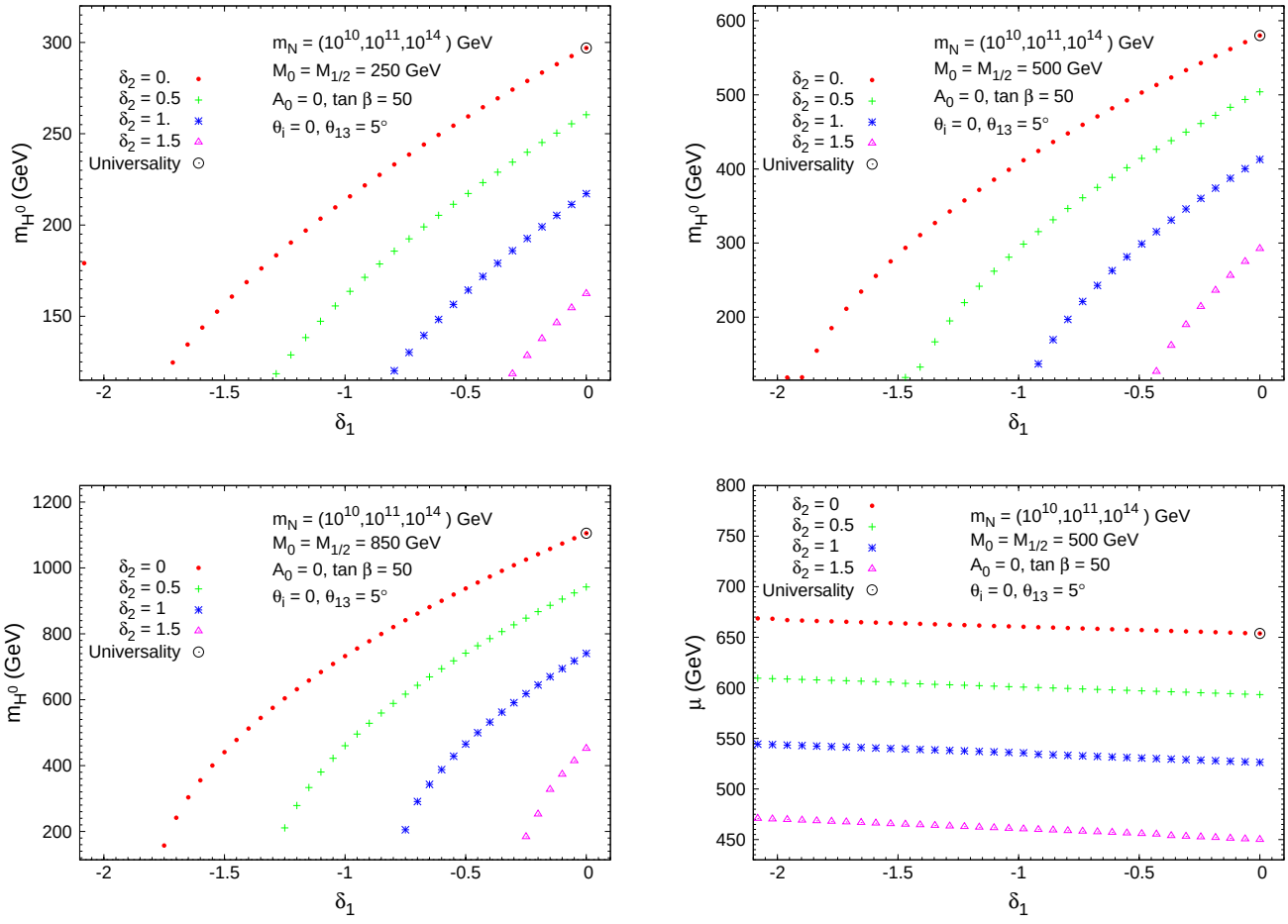

Figure 1.12: Mass of the heaviest Higgs scalar (m_{H^0}) as a function of the non-universality parameter δ_1, for fixed values of $\delta_2 = \{0, 0.5, 1, 1.5\}$ (respectively dots, crosses, asterisks, triangles). The universality case $\delta_{1,2} = 0$ is represented by a large circle. We also take $m_{N_i} = (10^{10}, 10^{11}, 10^{14})$ GeV, set $\theta_i = 0$, $A_0 = 0$, $\tan\beta = 50$ and impose the relation $M_0 = M_{1/2}$. The first three plots correspond to $M_0 = 250$, 500 and 850 GeV, respectively. On the fourth plot, we display the μ parameter as a function of the non-universality parameter δ_1, for fixed values of δ_2, and for $M_0 = M_{1/2} = 500$ GeV. The predictions for m_{A^0} are indistinguisable from those of m_{H^0} in this figure.

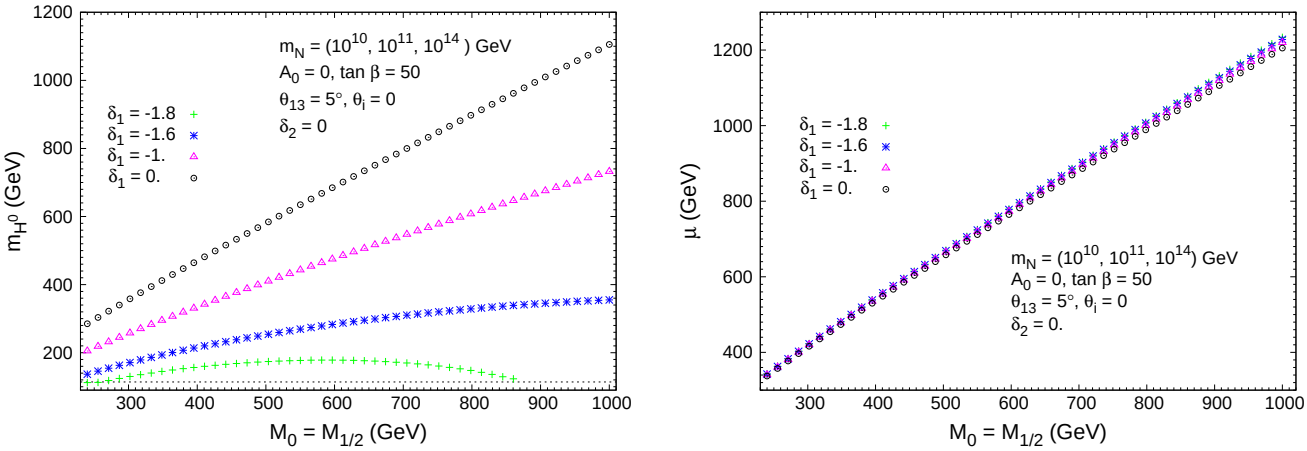

Figure 1.13: On the left, mass of the heaviest Higgs scalar (m_{H^0}) as a function of the SUSY scale ($M_{\rm SUSY} = M_0 = M_{1/2}$), for fixed values of $\delta_1 = \{-1.8, -1.6, -1, 0\}$ (respectively crosses, asterisks, triangles and circles). We take $m_{N_i} = (10^{10}, 10^{11}, 10^{14})$ GeV, and set $\theta_i = 0$, $A_0 = 0$, $\tan\beta = 50$ with $\theta_{13} = 5^\circ$. On the right, the μ-parameter is displayed as a function of $M_{\rm SUSY}$, for the same choices of SUSY-seesaw parameters. The predictions for m_{A^0} are indistinguisable from those of m_{H^0} in this figure.

figure, for all the explored values of δ_1 and δ_2, we find a value of m_{H^0} that is significantly smaller than what one would encounter in the universal case (here represented by the choice $\delta_1 = \delta_2 = 0$). This is truly remarkable in the case of large soft breaking masses, as can be seen, for instance, in the panel with $M_{\rm SUSY} = 850$ GeV, where low values of m_{H^0} are still found, even close to the experimental limit. For completeness we have also shown in Fig. 1.12 the predictions for the μ parameter as a function of δ_1 and δ_2. This parameter turns out to be nearly independent of δ_1, and its largest values are obtained for $\delta_2 = 0$.

The behaviour of the predicted m_{H^0} and μ parameter as a function of $M_{\rm SUSY} = M_0 = M_{1/2}$ is shown in Fig. 1.13. Here the specific values of $\delta_1 = \{-1.8, -1.6, -1, 0\}$ and $\delta_2 = 0$ have been considered. This figure again illustrates the interesting departure from the linear behaviour of m_{H^0} with $M_{\rm SUSY}$, which is generic in the universal case ($\delta_{1,2} = 0$). In contrast, the μ parameter conserves a similar linear behaviour with $M_{\rm SUSY}$ in all the studied scenarios (universal and non-universal).

As a representative example of these interesting non-universal points, we explicitly refer to the case with $\delta_1 = -1.8$ and $\delta_2 = 0$, where the predicted masses are $m_{H^0} = 113$, 174 and 127 GeV for $M_{\rm SUSY} = 250$, 500 and 850 GeV, respectively. For completeness, we have also collected the corresponding masses of the other relevant SUSY particles in Table 1.3. Notice that, in the case of $M_{\rm SUSY} = 850$ GeV, this table illustrates a very heavy SUSY spectrum, even with a

considerably heavy lightest SUSY particle, $m_{\tilde{\chi}_1^0} = 362$ GeV, but where the heavy scalar Higgs boson is still light, $m_{H^0} = 127$ GeV.

MSSM masses	$M_{\rm SUSY}$ (GeV)		
(GeV)	250	500	850
$m_{\tilde{l}_1}$	175	415	734
$m_{\tilde{l}_2}$	258	511	867
$m_{\tilde{l}_3}$	258	511	867
$m_{\tilde{l}_4}$	307	594	985
$m_{\tilde{l}_5}$	309	607	1025
$m_{\tilde{l}_6}$	323	609	1031
$m_{\tilde{\nu}_1}$	281	571	971
$m_{\tilde{\nu}_2}$	297	601	1022
$m_{\tilde{\nu}_3}$	299	605	1028
$m_{\tilde{\chi}_1^-}$	185	395	687
$m_{\tilde{\chi}_2^-}$	379	679	1075
$m_{\tilde{\chi}_1^0}$	99	207	362
$m_{\tilde{\chi}_2^0}$	185	394	687
$m_{\tilde{\chi}_3^0}$	363	668	1067
$m_{\tilde{\chi}_4^0}$	377	678	1074
m_{h^0}	110	119	123
m_{H^0}	113	174	127

Table 1.3: Relevant MSSM spectra for $M_0 = M_{1/2} = M_{\rm SUSY}$, $\tan\beta = 50$, $A_0 = 0$, $\theta_i = 0$, $\theta_{13} = 5^\circ$, $M_{N_i} = (10^{10}, 10^{11}, 10^{14})$ GeV, $\delta_1 = -1.8$ and $\delta_2 = 0$.

If one wants to obtain light Higgs bosons in the $\theta_i \neq 0$ case, one needs to explore first the optimal values of δ_1 and δ_2. We summarise the predictions for the Higgs boson mass m_{A^0} (and m_{H^0}) as a function of δ_1 and δ_2 in Fig. 1.14 for the extreme value of $\theta_2 = 2.9e^{i\pi/4}$. We have chosen here $\tan\beta = 50$ and two representative values of $M_{\rm SUSY} = 250$ and 750 GeV for moderate and heavy SUSY spectra, respectively. The other parameters are set to the values of $m_{N_i} = (10^{10}, 10^{11}, 10^{14})$ GeV, $\theta_1 = \theta_3 = 0$, $A_0 = 0$ and sign$(\mu) = +1$. The most interesting solutions with important phenomenological implications are found for negative δ_1 within the range $(-3, -2)$ and very small and positive δ_2, the choices selected for Fig. 1.14. In this figure, for all the explored values of δ_1 and δ_2, we find a value of m_{A^0} that is significantly smaller than what one would encounter in the universal case (here represented by the choice $\delta_1 = \delta_2 = 0$). This is truly remarkable in the case of large soft breaking masses, as can be seen, for instance,

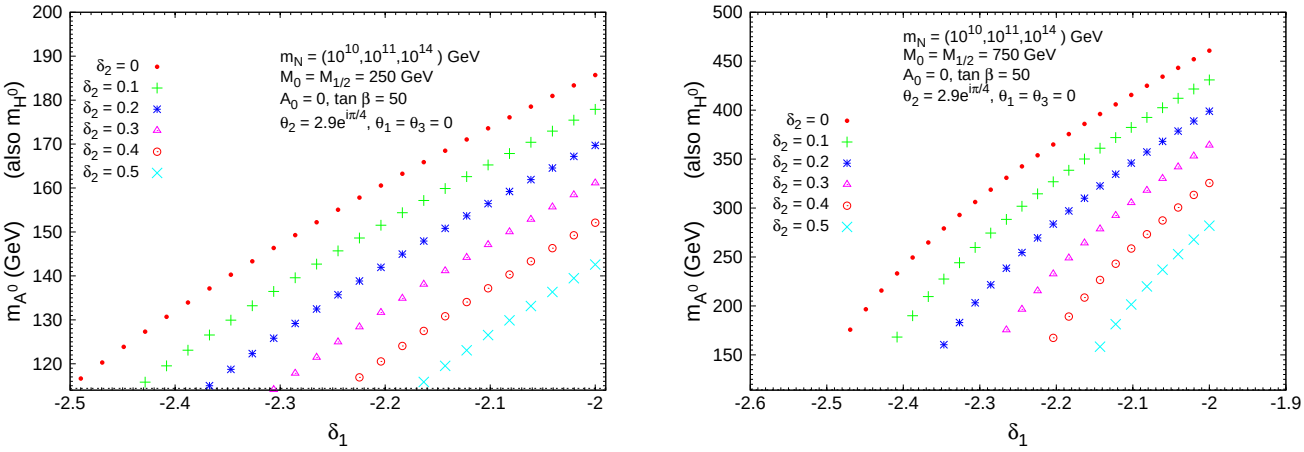

Figure 1.14: Light m_{A^0} predictions as a function of non-universal parameters δ_1 and δ_2 in the NUHM scenario. The predictions for m_{H^0} are indistinguisable from those of m_{A^0} in this figure.

in the panel with $M_{\rm SUSY} = 750$ GeV, where low values of $m_{A^0} \sim 150$ GeV are still found.

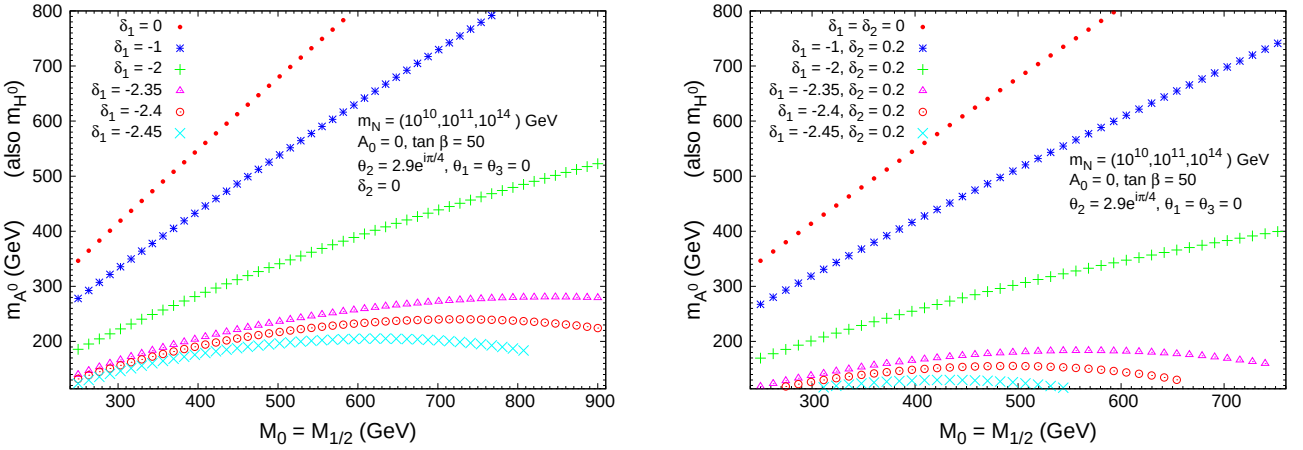

Figure 1.15: Light m_{A^0} predictions as a function of $M_{\rm SUSY} = M_0 = M_{1/2}$ in the NUHM scenario. The predictions for m_{H^0} are indistinguisable from those of m_{A^0} in this figure. The predictions for the CMSSM scenario ($\delta_1 = \delta_2 = 0$) are also included for comparison.

The behaviour of the predicted m_{A^0} as a function of $M_{\rm SUSY}$ is depicted in Fig. 1.15. Here the specific values of $\delta_1 = \{-2.45, -2.4, -2.35, -2, -1, 0\}$ and $\delta_2 = 0, 0.2$ have been considered. This figure illustrates again the interesting departure in NUHM scenarios from the linear behaviour of m_{A^0} with $M_{\rm SUSY}$, which is generic in the universal case ($\delta_1 = \delta_2 = 0$).

1.7 Other phenomenological implications from SUSY-seesaw models

As we have said, our main goal in this thesis is the study of the most important phenomenological implication of constrained SUSY-seesaw models, the production of large rates in LFV processes. Here we will mention some consequences of this models which are also interesting from a phenomenological point of view. On the one hand, the hypothesis of right-handed neutrinos with a Majorana mass term which violates the lepton number offers in addition the possibility of providing succesful baryogenesis via leptogenesis [38]. Within the framework of leptogenesis, the observed baryon asymmetry of the Universe (BAU) is explained by the out-of-equilibrium decays of the same heavy right-handed neutrinos which are responsible for the suppression of the light neutrino masses. On the other hand, the presence of CP violating phases in the neutrino Yukawa couplings has further implications on low-energy phenomenology. In particular, RGE running will also induce, in addition to the LFV decays, contributions to CP violating (and flavour conserving) observables, as is the case of the charged lepton electric dipole moments (EDMs). Finally, the anomalous magnetic moment of the muon, $a_\mu = (g_\mu - 2)/2$, is known to be sensitive to the new particle content of SUSY theories and the pressence of new possible CP violation phases. One interesting possibility is that the corresponding SUSY contributions to a_μ could be the origin of the observed excess in $a_\mu^{\rm exp}$ [141]. It is worth commenting here that there are other proposed quantities which are also sensitive to the presence of new particles in these constrained SUSY-seesaw models. Particularly interesting are the studies of B meson decays like $B_s \to X_s\gamma$ and $B_s \to \mu^+\mu^-$. The present data on the search of these channels put indeed some constraints on the SUSY parameters. However, we do not consider these processes in this thesis since we neglect the mixing in the quark (and squark) sector, what means that we set $U_{\rm CKM} = \mathbb{1}$ and therefore quark-flavour changing processes do not occur.

In these section we have studied BAU, EDMs and a_μ within the constrained SUSY-seesaw scenarios. For the numerical computation we use the code `SPheno2.2.2` that we have been adapted with additional subroutines which estimate the value of the BAU, evaluate the contributions to the charged lepton EDMs and compute the new contributions to a_μ.

1.7.1 Thermal leptogenesis and gravitino constraints

In the class of scenarios considered in this thesis, the requirement of successfully generation of BAU via thermal leptogenesis [38] is usually explained by the out-of-equilibrium decay of the same heavy right-handed neutrinos which are responsible for the suppression of light neutrino masses in the seesaw mechanism. The needed CP asymmetry for BAU is obtained from the CP violating phases in the complex angles θ_i (see Eqs. (1.19), (1.23)), which, as will be seen

in the next chapters, also have a clear impact on the LFV rates. Here we assume that the necessary population of right-handed neutrinos emerges via processes in the thermal bath of the early Universe. We will furthermore consider cosmological constraints on the reheat temperature after inflation associated with thermally produced gravitinos. The reheat temperature, $T_{\rm RH}$, has a strong impact on thermal leptogenesis since the thermal production of right-handed neutrinos N_1 is suppressed if $T_{\rm RH} \ll m_{N_1}$. Notice that although the constrained SUSY-seesaw scenarios we take into account do not make any reference to gravity, they are considered very often in the literature to be inspired in mSUGRA models, where obviously the gravitinos do play a role, as will be commented next.

Gravitino problems and the reheat temperature

Thermally produced gravitinos can lead to two generic constraints on the reheat temperature [142]. Both are associated with the fact that in the scenarios under consideration, and assuming R-parity conservation, the gravitinos will ultimately decay in the lightest supersymmetric particle (LSP). Firstly, they can decay late, after the Big Bang nucleosynthesis (BBN) epoch, and potentially spoil the success of BBN. This leads to upper bounds on the reheat temperature which depend on the specific supersymmetric model as well as on the mass of the gravitino. In particular, with a heavy gravitino (roughly above 100 TeV), the BBN constraints can be nearly avoided. In the context of the present work, the gravitino mass is a free (unknown) parameter, so that we can safely avoid the latter constraints for any given reheat temperature. On the other hand, in mSUGRA the decay of a gravitino produces one LSP, which has an impact on the relic density of the latter. The number of thermally produced gravitinos increases with the reheat temperature, and we can estimate the contribution to the dark matter (DM) relic density arising from non-thermally produced LSPs via gravitino decay as [142]

$$\Omega_{\rm LSP}^{\rm non-th} h^2 \approx 0.054 \left(\frac{m_{\rm LSP}}{100\,{\rm GeV}}\right) \left(\frac{T_{\rm RH}}{10^{10}\,{\rm GeV}}\right), \tag{1.94}$$

which depends on the LSP mass, $m_{\rm LSP}$, as well as on the reheat temperature $T_{\rm RH}$. Taking the bound $\Omega_{\rm LSP}^{\rm non-th} h^2 \leq \Omega_{\rm DM} h^2 \lesssim 0.13$ from the Wilkinson Microwave Anisotropy Probe (WMAP) [143], we are led to an upper bound on the reheat temperature of

$$T_{\rm RH} \lesssim 2.4 \times 10^{10}\,{\rm GeV} \left(\frac{100\,{\rm GeV}}{m_{\rm LSP}}\right). \tag{1.95}$$

For most of the considered SUSY scenarios in this work, the mass of the LSP (which is the lightest neutralino) is in the range 100 GeV - 150 GeV, resulting in an estimated upper bound on the reheat temperature of approximately $T_{\rm RH} \lesssim 2 \times 10^{10}\,{\rm GeV}$. In the following subsection, we will consider the constraints on the R-matrix parameters from the requirement of generating

the BAU via thermal leptogenesis, while taking into account the latter bound on the reheat temperature.

Thermal leptogenesis

In the scenario with hierarchical right-handed neutrinos, which will be the most frequently assumed in this thesis, the baryon asymmetry arises from the out-of-equilibrium decay of the lightest right-handed neutrino N_1. The produced lepton asymmetry is then partially transformed into a baryon asymmetry via sphaleron conversion. In the SUSY-seesaw models, the resulting baryon to photon ratio from thermal leptogenesis can be written as [144]

$$\frac{n_{\rm B}}{n_\gamma} \approx -\,1.04\,\times\,10^{-2}\,\varepsilon_1\,\eta\,, \tag{1.96}$$

where ε_1 is the decay asymmetry of N_1 into Higgs and lepton doublets and η is an efficiency factor for thermal leptogenesis, which can be estimated by solving the Boltzmann equations. The efficiency strongly depends on the ratio $m_{N_1}/T_{\rm RH}$ as well as on the parameter $\widetilde{m}_1$ [145], which is defined as

$$\widetilde{m}_1 = \frac{\sum_f (Y_\nu)_{1f}(Y_\nu^\dagger)_{f1}\,v_2^2}{m_{N_1}}\,. \tag{1.97}$$

In the following, regarding the estimation of the efficiency $\eta(\widetilde{m}_1, m_{N_1}/T_{\rm RH})$, we will use the numerical results of [144] for 10^{-7} eV $\leq \widetilde{m}_1 \leq 1$ eV and $0.1 \leq m_{N_1}/T_{\rm RH} \leq 100$ (under the assumption of a zero initial population of N_1). As presented in [144], the efficiency dramatically drops if either $m_{N_1} \gg T_{\rm RH}$ or if $\widetilde{m}_1$ strongly deviates from its optimal value $\widetilde{m}_1 \approx 10^{-3}$ eV. Thus, the optimisation of this efficiency factor, to obtain a successful BAU, suggests that $m_{N_1} \lesssim T_{\rm RH}$.

With respect to the decay asymmetries we will use the 1-loop results [146]

$$\varepsilon_1 = \frac{1}{8\pi}\frac{\sum_{j\neq 1}{\rm Im}\left\{[(Y_\nu Y_\nu^\dagger)_{1j}]^2\right\}}{\sum_f |(Y_\nu)_{1f}|^2}\,\sqrt{x_j}\,\left[\frac{2}{1-x_j} - \ln\left(\frac{x_j+1}{x_j}\right)\right], \tag{1.98}$$

with $x_j = m_{N_j}^2/m_{N_1}^2$, for $j \neq 1$.

Since in our analysis we use the R-matrix parameterisation of Eq. (1.19), it is convenient to rewrite both the decay asymmetry ε_1 (in the limit of hierarchical right-handed neutrinos) and the washout parameter $\widetilde{m}_1$, in terms of the R-matrix parameters [147],

$$\varepsilon_1 \approx -\frac{3}{8\pi}\frac{m_{N_1}}{v_2^2}\frac{\sum_j m_{\nu_j}^2 {\rm Im}(R_{1j}^2)}{\sum_i m_{\nu_i}|R_{1i}|^2}\,, \quad \widetilde{m}_1 = \sum_j m_{\nu_j}|R_{1j}|^2\,. \tag{1.99}$$

As seen from the previous equation, a successful leptogenesis requires complex values of the R-matrix entries in order to generate a non-zero decay asymmetry.

The BAU estimate in Eq. (1.96) should be compared with the reported WMAP 68% confidence range for the baryon-to-photon ratio [143]

$$\frac{n_{\rm B}}{n_\gamma} = (6.0965 \pm 0.2055) \times 10^{-10}\,. \tag{1.100}$$

Finally, the constraints on the R-matrix parameters from the requirement of a successful BAU compatible with the upper bound $T_{\rm RH} \lesssim 2 \times 10^{10}$ GeV are summarised in Figs. 1.16 and 1.17. Figure 1.16 illustrates the impact of θ_2 (with $\theta_1 = \theta_3 = 0$) on the estimated BAU.

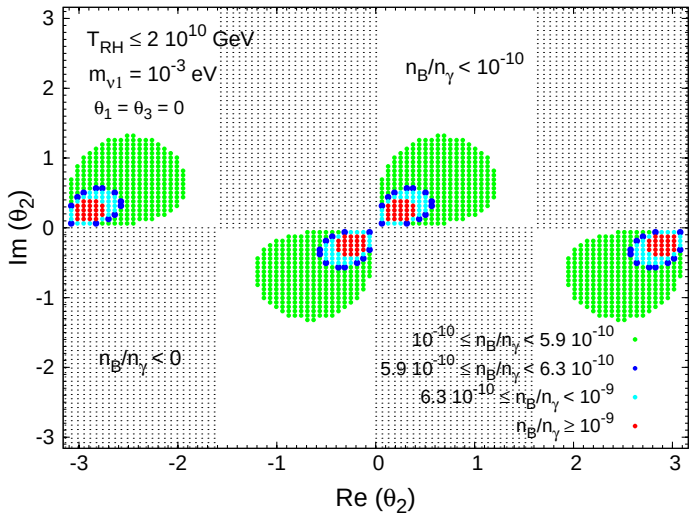

Figure 1.16: Constraints on the R-matrix angle θ_2 (in radians) defined in Eq. (1.23), from the requirement of a successful BAU via thermal leptogenesis (compatible with the constraint on $T_{\rm RH}$ from Eq. (1.95)). From out- to inner-most rings, the regions are associated with the following BAU ranges: $n_{\rm B}/n_\gamma \in [10^{-10}, 5.9 \times 10^{-10}]$, $n_{\rm B}/n_\gamma \in [5.9 \times 10^{-10}, 6.3 \times 10^{-10}]$, $n_{\rm B}/n_\gamma \in [6.3 \times 10^{-10}, 10^{-9}]$ and $n_{\rm B}/n_\gamma \gtrsim 10^{-9}$.

As one can see, the 68% WMAP confidence range of Eq. (1.100) corresponds to a very narrow ring (represented by the darkest region in Fig. 1.16) in the Re(θ_2)-Im(θ_2) plane. Notice also that values of either Re(θ_2) or Im(θ_2) larger than 1.2 radians (mod π) lead to very small values of the BAU,namely $n_{\rm B}/n_\gamma < 10^{-10}$. On the other hand, the analogous study of Fig. 1.17 shows that with just θ_3 ($\theta_1 = \theta_2 = 0$) one cannot accommodate the WMAP range. Similarly, values of Re(θ_3) or Im(θ_3) larger than 1.2 radians (mod π) also lead to excessively small $n_{\rm B}/n_\gamma$ ($< 10^{-10}$). Similar results regarding the constraints on θ_2 and θ_3 from successfull BAU via leptogenesis have been found in [148] and [149]. We also see from Figs. 1.16 and 1.17 that a significant part of the parameter space is excluded since the baryon asymmetry is produced with the wrong sign, $n_{\rm B}/n_\gamma < 0$, which contradicts observation.

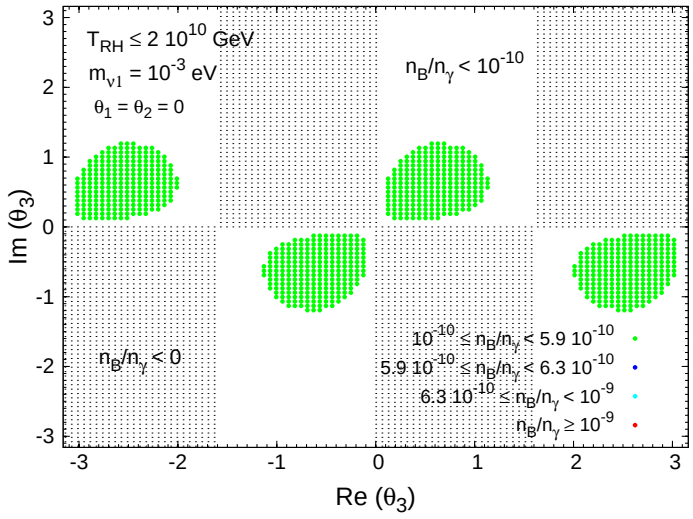

Figure 1.17: Constraints on the R-matrix angle θ_3 defined in Eq. (1.23), from the requirement of successful BAU via thermal leptogenesis with the constraint $T_{\rm RH} \lesssim 2 \times 10^{10}\,\text{GeV}$. Colour code as in Fig. 1.16 (in this case only the region $n_{\rm B}/n_\gamma \in [10^{-10},\, 5.9 \times 10^{-10}]$ is present).

Regarding θ_1, and even though it cannot independently account for a successful BAU, it may have an impact on leptogenesis if θ_2 and/or θ_3 are non-zero, as can be inferred from Eq. (1.99).

One can adopt a conservative approach and only require the estimated baryon-to-photon ratio to be within the range

$$\frac{n_{\rm B}}{n_\gamma} \in \left[10^{-10}, 10^{-9}\right]. \tag{1.101}$$

This broad range for $n_{\rm B}/n_\gamma$ reflects the theoretical uncertainties in our estimate which may come, for instance, from flavour effects in the Boltzmann equations [150–152] and, more generally, from the approximations made in [144] in order to calculate the efficiency factor η. To accommodate the extended range of Eq. (1.101), Figs. 1.16 and 1.17 suggest that one should take values of θ_2 and θ_3 not larger than approximately 1 radian (mod π).

Another possibility, that we do not study in this thesis, is to consider flavour-dependent leptogenesis, which implies that even in the absence of CP violation in the right-handed neutrino sector (which would lead to a zero baryon asymmetry in the flavour-independent case), a non-vanishing baryon asymmetry can in principle be generated from the CP phases in the $U_{\rm PMNS}$ [153].

1.7.2 Charged lepton EDMs

The presence of CP violating phases in the neutrino Yukawa couplings has further implications on low-energy phenomenology. In particular, RGE running will also induce, in addition to the LFV processes, contributions to flavour conserving CP violating observables, as is the case of the charged lepton EDMs. Here, we have also analysed the potential constraints on the SUSY seesaw parameter space arising from the present experimental bounds [10] on the EDMs of the electron, muon and tau, that are given by

$$|d_e| \lesssim (6.9 \pm 7.4) \times 10^{-28} \text{ e.cm}\,, \quad |d_\mu| \lesssim (3.7 \pm 3.4) \times 10^{-19} \text{ e.cm}\,,$$
$$-2.2 \times 10^{-17} \lesssim d_\tau \lesssim 4.5 \times 10^{-17} \text{ e.cm}\,. \tag{1.102}$$

As argued in [154–157], the dominant contributions to the EDMs arise from the renormalisation of the charged lepton soft-breaking parameters. In particular, the EDMs are strongly sensitive to the non-degeneracy of the heavy neutrinos, and to the several CP violating phases of the model (in our case, the complex R-matrix angles). In the present analysis we have estimated the relevant contributions to the charged lepton EDMs, taking into account the associated one-loop diagrams (chargino-sneutrino and neutralino-slepton mediated), working in the mass eigenstate basis, and closely following the computation of [158, 159] and [160].

In the presence of complex θ_i, the EDMs are clearly non-vanishing and we have numerically checked that for all the explored parameter space, the predicted values for the electron, muon and tau EDMs are well below the experimental bounds given in Eq. (1.102). More specifically, for the whole parameter space analysed in this thesis we have obtained values for the EDMs lying in the following ranges (in units of e.cm):

$$10^{-39} \lesssim |d_e| \lesssim 2\times10^{-35}\,,\ 6\times10^{-37} \lesssim |d_\mu| \lesssim 1.5\times10^{-32}\,,\ 10^{-34} \lesssim |d_\tau| \lesssim 4\times 10^{-31}\,. \tag{1.103}$$

1.7.3 SUSY contributions to a_μ

If radiative corrections are ignored, the g factor of the magnetic moment of the muon is 2. A deviation from 2, namely $g-2$, is crucial to investigate quantum corrections. The present world average experimental value of the anomalous magnetic moment of the muon, $a_\mu = (g_\mu - 2)/2$ is given by [161, 162]

$$a_\mu^{\text{exp}} = 116\,592\,080\,(63) \times 10^{-11} \quad [0.54\text{ppm}]\,. \tag{1.104}$$

The SM prediction a_μ^{SM}, which is usually split into three parts (QED, electroweak and hadronic), is calculated with very high precision [141],

$$a_\mu^{\text{SM}} = a_\mu^{\text{QED}} + a_\mu^{\text{EW}} + a_\mu^{\text{HLO}} + a_\mu^{\text{HHO}} = 116\,591\,748\,(61) \times 10^{-11}\,. \tag{1.105}$$

Therefore, one can conclude that there is an observed excess in $a_\mu^{\rm exp}$ when compared to the SM prediction, which is given by $\Delta = a_\mu^{\rm exp} - a_\mu^{\rm SM} = 3.32 \times 10^{-9}$ at $3.8\,\sigma$ [141].

It is already known that SUSY electroweak contributions to a_μ can be significant, as large or larger than the SM electroweak contribution, when sleptons, charginos and neutralinos have masses within the range of a few hundred GeV [163–170]. Then, this observed excess could come from SUSY contributions, *i.e.* $\Delta = a_\mu^{\rm SUSY}$, and their corresponding predictions must be in agreement with this value.

1.8 Present experimental bounds on SUSY and Higgs boson masses

Finally, we present here the current experimental bounds on the Higgs and SUSY particle masses. Their corresponding bounds are based on the direct searches at the high energy colliders, LEP and Tevatron, and are reviewed in [10].

Regarding the Higgs masses, h^0, H^0 and A^0, the principal mechanism for producing the Higgs particles in e^+e^- collisions at LEP energies is Higgs-strahlung in the s-channel, $e^+e^- \to h^0Z^0, H^0Z^0$ and the pair production $e^+e^- \to h^0A^0, H^0A^0$ processes, with final states given by $b\bar{b}b\bar{b}$, $b\bar{b}\tau^+\tau^-$ and $\tau^+\tau^-\tau^+\tau^-$. At the Tevatron, the associated production $p\bar{p} \to (h^0 {\rm or} H^0)V$ (with $V \equiv W^\pm, Z^0$), and the Yukawa process $p\bar{p} \to h^0 b\bar{b}$ are the most promising search mechanisms. The gluon fusion processes $gg \to h^0, H^0, A^0$ have the highest cross section, but in these cases, only the Higgs to $\tau^+\tau^-$ decay mode is promising, since the $b\bar{b}$ decay mode is overhelmed by QCD background. The current mass bounds at 95% CL are $m_{h^0} > 92.8$ GeV and $m_{A^0} > 93.4$ GeV [10, 171]. These limits are obtained in the $m_{h^0} - max$ scenario [171] where some of the parameters have fixed values, in particular, $M_{SUSY} = 1$ TeV, $M_2 = 200$ GeV, $\mu = -200$ GeV and maximal stop mixing, $\chi_t = 2M_{SUSY}$, is assumed. Furthermore, values of $\tan\beta$ from 0.7 to 2.0 are excluded[3]. Morevover, the combined LEP data [172] exclude charged Higgs bosons $H^\pm$ with mass less than 78.6 GeV (95% CL), valid for arbitrary BR$(H^+ \to \tau^+\nu)$.

Concerning the experimental searches of SUSY particles, the absence of any signal from these particles at present experiments allows to set limits on their masses. With regard to the squark sector, the absence of any signal at Tevatron sets the lower limits on their masses in 89 GeV for sbottoms and 95.7 GeV for stops. Considering events with three or more jets and large missing E_T, a lower bound on $m_{\tilde{q}}$ of $m_{\tilde{q}} > 250$ GeV at 95 % CL is set [173] for the first two generations.

The limits on $m_{\tilde{g}}$ summarised here refer to the high-mass region ($m_{\tilde{g}} \gtrsim 5$ GeV), and include

[3]One should note that the exclusion in $\tan\beta$ can be smaller if the top mass turns out to be higher than the assumed value of 174.3 GeV, or if $M_{\rm SUSY}$ is taken to be larger than the assumed value of 1 TeV

the effects of cascade decays, evaluated assuming a fixed value of the parameters μ and $\tan\beta$. The limits are weakly sensitive to these parameters over much of parameter space and assume GUT relations between gaugino masses and the gauge coupling. The bound on the gluino mass for $m_{\tilde{q}} \geq m_{\tilde{g}}$ is $m_{\tilde{g}} \gtrsim 195$ GeV. If all the squarks have the same mass, then the gluino mass lower bound is 300 GeV. If, on the contrary, the squarks are much lighter than the gluino (in which case they decay via $\tilde{q} \to q\tilde{\chi}_1^0$), the lower bound on the gluino mass is generally higher, indeed larger than 300 GeV.

In the SUSY electroweak sector it is more difficult to set model independent bounds on the supersymmetric masses. The mass limits for the lightest neutralino is derived by constraining the MSSM paremeter space by the results from direct searches for neutralinos, charginos and sleptons, stop and sbottoms. The results hold for the full parameter space defined by values of $M_2 > 1$ TeV, $|\mu| \leq 2$ TeV with the $\tilde{\chi}_1^0$ as the lightest supersymmetric particle (LSP). Its mass bound is given by $m_{\tilde{\chi}_1^0} > 46$ GeV [174]. For the three heaviest neutralinos, the mass limits are obtained by constraining the MSSM parameter space with gaugino and sfermion universality at the GUT scale, using the negative direct searches for neutralinos, charginos and charged slpetons. Their corresponding bounds are given by [175] $m_{\tilde{\chi}_2^0} > 62.4$ GeV, $m_{\tilde{\chi}_3^0} > 99.9$ GeV and $m_{\tilde{\chi}_4^0} > 116.0$ GeV, respectively. On the other hand, experiments at LEP based on the analysis of the Z width and decays give a lower mass limit for the lightest chargino $\tilde{\chi}_1^\pm$ of approximately 45 GeV. For values of $M_2 < 1$ TeV and $|\mu| \leq 2$ TeV with $\tilde{\chi}_1^0$ as the LSP, a better limit on the chargino mass $\tilde{\chi}_1^\pm > 94$ GeV at 95 % CL is obtained [174].

In the slepton and sneutrino sector, an indirect limit on the mass of $m_{\tilde{\nu}} > 94$ GeV [174] is derived by constraining the MSSM parameter space from the results for direct searches of neutralinos and sleptons. This limit depends on the number of sneutrinos assumed to be degenerate in mass and has been calculated only considering $\tilde{\nu}_L$, with values $M_2 < 1$ TeV, $|\mu| \leq 1$ TeV, with $\tilde{\chi}_1^0$ as LSP and with no mixing in the third family. The limit on the mass for the charged sleptons assuming all three flavours to be degenerate is given by $m_{\tilde{l}} > 87.5$ GeV. If no degeneration among sleptons is assumed, the limits are $m_{\tilde{e}} > 73$ GeV [176], $m_{\tilde{\mu}} > 94$ GeV [174] and $m_{\tilde{\tau}} > 81.9$ GeV [174].

Chapter 2

LFV in leptonic τ, μ and Higgs decays

In this chapter we perform a detailed study of LFV leptonic decays, namely, radiative decays $l_j \to l_i\,\gamma$, Higgs decays $H \to l_j\,\bar{l}_i$ and leptonic decays into three leptons of equal flavour $l_j \to 3\,l_i$, within constrained SUSY-seesaw scenarios. Degenerate and hierarchical spectrum are considered for both heavy and light neutrinos. We systematically analyse the interesting relation between the leptonic mixing angle θ_{13} and LFV in muon and tau decays and discuss the interplay with the other relevant parameters. We require compatibility with low energy neutrino data, bounds on both LFV decays and charged lepton electric dipole moments, and study the implications from the requirement of successful baryogenesis via thermal leptogenesis. Particular emphasis is given to the implications that a future θ_{13} measurement can have on our knowledge of the heavy neutrino sector.

2.1 LFV radiative decays: $l_j \to l_i\,\gamma$

Among all LFV processes τ and μ radiative decays, more concretely $\mu \to e\,\gamma$ and $\tau \to \mu\,\gamma$ are at present the best channels to search for lepton flavour violation, due to their stringent current experimental bounds (see Table 2.1). In this section, analytical and numerical results, including the prospect for future improvements for the LFV radiative channels and the comparison with the present experimental bounds, are presented.

LFV decays	MEG	BABAR	Belle	Belle & BABAR
$\mathrm{BR}(\mu \to e\,\gamma)$	1.2×10^{-11} [58]	—	—	—
$\mathrm{BR}(\tau \to e\,\gamma)$	—	1.1×10^{-7} [177]	1.2×10^{-7} [66, 67]	9.4×10^{-8} [68]
$\mathrm{BR}(\tau \to \mu\,\gamma)$	—	6.8×10^{-8} [65]	4.5×10^{-8} [178]	1.6×10^{-8} [68]

Table 2.1: Present upper bounds for LFV radiative decays

2.1.1 Analytical results for LFV radiative decays

In order to perform the computation of LFV $l_j \to l_i\gamma$ decay rates, we start writing the relevant amplitudes for these processes. First we present the off-shell amplitude for $l_j \to l_i\gamma^*$, that is given by

$$T_\gamma = e\,\epsilon^{\mu *} u_i(p-q)\left[q^2\gamma_\mu\left(A_1^L P_L + A_1^R P_R\right) + m_{l_j} i\sigma_{\mu\nu}q^\nu\left(A_2^L P_L + A_2^R P_R\right)\right] u_j(p)\,, \tag{2.1}$$

where q is the photon momentum and e is the positron electric charge. Here, $A_1^{L,R}$ and $A_2^{L,R}$ are the vector and the dipole form factors, respectively.

Within the SUSY-sesaw models considered in this thesis, the Feynman diagrams contributing to T_γ amplitude are shown in Fig. B.1 of Appendix B. We can see clearly that the form factors $A_i^{L,R}$, $(i = 1, 2)$ receive contributions from two types of diagrams, sneutrino-chargino loops and slepton-neutralino loops. Then, each form factor can be written as a sum of two terms,

$$A_a^{L,R} = A_a^{(n)L,R} + A_a^{(c)L,R}, \quad (a = 1, 2)\,, \tag{2.2}$$

where $A_a^{(n)L,R}$ and $A_a^{(c)L,R}$ come from the contributions of neutralino and chargino loops, respectively, whose corresponding expressions are given in Appendix B. Notice that we have not neglected any of the fermion masses. If we neglect these masses in the previous formulas we get the same result as in [49]. The expressions for the N and C couplings are given in the Appendix A.

For the radiative decays $l_j \to l_i\gamma$, $(i \neq j)$, in which we are interested now, a real (on-shell) photon is emitted and only dipole form factors contribute. In this case, the branching ratios are given by

$$\mathrm{BR}(l_j \to l_i\,\gamma) \;=\; \frac{e^2}{16\,\pi}\,\frac{m_{l_j}^5}{\Gamma_{l_j}}\,\left(|A_2^L|^2 \,+\, |A_2^R|^2\right)\,, \tag{2.3}$$

where Γ_{l_j} is the total l_j lepton width. These branching ratios were computed firstly in [48, 49] in specific SUSY scenarios.

Finally, and regarding our estimation of the low-energy parameters, we consider the full one-loop RGE running. Nevertheless, for the forthcoming discussion, it will be clarifying and

interesting to compare the full results with the simplified estimation which is obtained within the LLog approximation. In the latter framework, the RGE generated flavour mixing in the slepton sector is summarised by the logarithmic contributions given in Eq. (1.84), which are originated by the running from M_X to the right handed mass scales m_{N_i}, $i = 1, 2, 3$. Concentrating on $\mu \to e\,\gamma$ decay, the dominant contribution stems from the RGE induced flavour mixing in $(\Delta m^2_{\tilde{L}})_{21}$. Within the framework of the mass insertion (MI) and LLog approximations, one then obtains a simple formula that at large $\tan\beta$ and for equal SUSY mass scales is given by

$$\begin{aligned} \mathrm{BR}(\mu \to e\,\gamma)_{\mathrm{approx}} &= \frac{\alpha^3\,\tan^2\beta}{G_F^2\,M_{\mathrm{SUSY}}^4}\,|\delta_{21}|^2 \\ &= 0.1 \times |\delta_{21}|^2 \left(\frac{100}{M_{\mathrm{SUSY}}(\mathrm{GeV})}\right)^4 \left(\frac{\tan\beta}{60}\right)^2 , \end{aligned} \tag{2.4}$$

where M_{SUSY} represents a generic SUSY mass, and δ_{21} is derived from

$$\delta_{21} = \frac{(\Delta m^2_{\tilde{L}})_{21}}{M^2_{\mathrm{SUSY}}}\,, \tag{2.5}$$

with $(\Delta m^2_L)_{21}$ given in Eq. (1.84) in terms of the neutrino Yukawa couplings. A similar expression can be obtained for $\tau \to \mu\gamma$ within the LLog approximation and the MI approach [51, 179],

$$\begin{aligned} \mathrm{BR}(\tau \to \mu\gamma)_{\mathrm{approx}} &= \frac{\alpha^3}{14400\pi^2}\frac{m_\tau^5}{\Gamma_\tau \sin^4\theta_W}\frac{|\delta_{32}|^2}{M^4_{\mathrm{SUSY}}}\tan^2\beta \\ &= 1.5 \times 10^{-2}\,|\delta_{32}|^2 \left(\frac{100}{M_{\mathrm{SUSY}}(\mathrm{GeV})}\right)^4 \left(\frac{\tan\beta}{60}\right)^2 . \end{aligned} \tag{2.6}$$

And similarly for $\tau \to e\,\gamma$, that we do not write explicitely here for shortness.

In the following sections we present the numerical results for the branching ratios of the LFV radiative decays arising in the CMSSM-seesaw scenario previously described. In particular, we aim at investigating the dependence of the BRs on the most relevant SUSY-seesaw parameters, and how the results would reflect the impact of a potential θ_{13} measurement. In some cases, we further discuss how the requirement of a viable BAU would affect the allowed parameter range, and in turn the BR predictions.

The input values used regarding the light neutrino masses and the U_{PMNS} matrix elements are given in Eq. (1.22) which are compatible with present experimental data (see, for instance, the analysis of [115–117]). As previously mentioned, we do not address the impact of non-vanishing U_{PMNS} phases (Dirac or Majorana) in the LFV branching ratios. The effects of Majorana phases on the BRs have been discussed in [180].

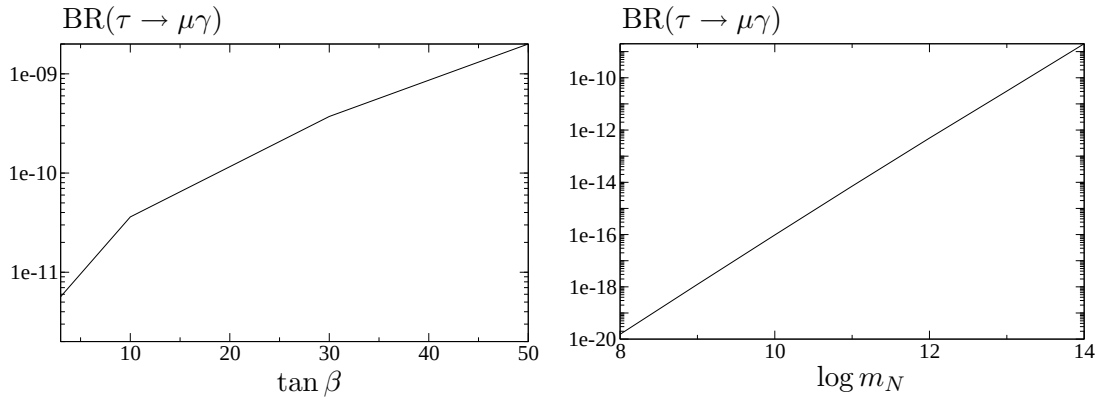

Figure 2.1: Dependence of $\tau \to \mu\,\gamma$ decay on $\tan\beta$ (left panel) for $m_N = 10^{14}$ GeV and on m_N (right panel) for $\tan\beta = 50$. The other input parameters are, $M_0 = 400$ GeV, $M_{1/2} = 300$ GeV, $A_0 = 0$ and sign(μ) > 0.

2.1.2 Dependence on the most relevant SUSY-seesaw parameters

We present in this section, from Fig. 2.1 to Fig. 2.4, the dependence of all the branching ratios of LFV radiative decays $l_j \to l_i\,\gamma$ on the most relevant parameters, namely, m_N in the case of degenerate heavy neutrinos, m_{N_3} in the hierarchical case, $\tan\beta$ and the θ_i angles. We work here in the context of the CMSSM-seesaw scenario that has been introduced in Chapter 1.

Degenerate neutrinos

The results of the BR($\tau \to \mu\,\gamma$) as a function of $\tan\beta$ are illustrated in Fig. 2.1 (left panel). In this plot we set $m_N = 10^{14}$ GeV and assume the matrix R to be real. Notice that in the degenerate case with real R these LFV ratios do not depend on the particular choice for R. This can be easily understood because the dependence on R drops in the relevant factor, $(Y_\nu^* Y_\nu^T)_{ij}$, appearing in the dominant δ_{LL}^{ij} slepton mixing, and due to the property $R^T R = \mathbb{1}$. From this figure we also see that the predicted rates are well below the experimental upper bounds for all $\tan\beta$ values, eventhough the total rates grow fast with $\tan\beta$.

We next comment on the relevance of the choice for the m_N values. In Fig. 2.1 we have also illustrated the BR($\tau \to \mu\,\gamma$) as a function of m_N for degenerate heavy neutrinos and $\tan\beta = 50$. The explored range in m_N is from 10^8 GeV up to 10^{14} GeV. The rates have a behaviour with m_N which corresponds approximately to BR($\tau \to \mu\,\gamma$) $\propto |m_N \log(m_N)|^2$. As before, these predicted branching ratios are well bellow the experimental upper bound, even at the largest m_N value of 10^{14} GeV.

For completeness, we also include the results of the other two LFV radiative decays, $\tau \to e\,\gamma$

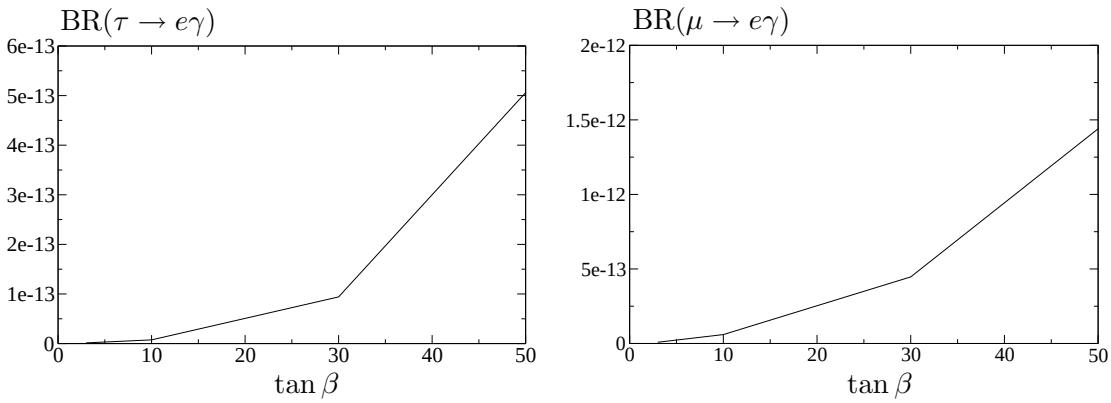

Figure 2.2: Dependence of BR($\tau \to e\,\gamma$) (left panel) and BR($\mu \to e\,\gamma$) (right panel) on $\tan\beta$ with degenerate heavy neutrinos and real R, for $m_N = 10^{14}$ GeV. The other input parameters are, $M_0 = 400$ GeV, $M_{1/2} = 300$ GeV, $A_0 = 0$ and sign(μ) > 0.

and $\mu \to e\,\gamma$ in Fig. 2.2, where the predictions are shown as a function of $\tan\beta$. These behaviours are very similar to those in BR($\tau \to \mu\,\gamma$). We also find that the rates for these two decays are well below their corresponding experimental bounds in the degenerate case, for all the explored values of $\tan\beta$ and m_N.

In summary, in the case of degenerate heavy neutrinos and for real R, we get LFV radiative decay rates which are still below their present experimental upper bounds.

Hierarchical neutrinos

We next present the results for hierarchical neutrinos which are much more promising. In this case the choice for R is very relevant. The results for the general complex R case and for the particular mass hierarchy $(m_{N_1}, m_{N_2}, m_{N_3}) = (10^8, 2\times10^8, 10^{14})$ GeV, are shown in Figs. 2.3 and 2.4. We will later explore other choices as well.

From these figures we first confirm that the LFV radiative decay rates are much larger in the hierarchical case than in the degenerate one. This is true even for the case of real R, which corresponds in our plots to the predictions at $\arg\theta_1 = \arg\theta_2 = \arg\theta_3 = 0$. Furthermore, we get severe restrictions on the maximum allowed decay rates coming from the experimental upper bounds.

In Fig. 2.3 we show the predictions of BR($l_j \to l_i\gamma$) as functions of $|\theta_2|$, for all the channels and for the different values of $\arg\theta_2 = 0, \pi/10, \pi/8, \pi/6, \pi/4$. In all these plots we set again $\tan\beta = 50$, $M_0 = 400$ GeV, $M_{1/2} = 300$ GeV, $A_0 = 0$, sign(μ) > 0 and $(m_{N_1}, m_{N_2}, m_{N_3}) = (10^8, 2\times10^8, 10^{14})$ GeV. The upper lines correspond to $\arg\theta_2 = \pi/4$ and the lower ones to

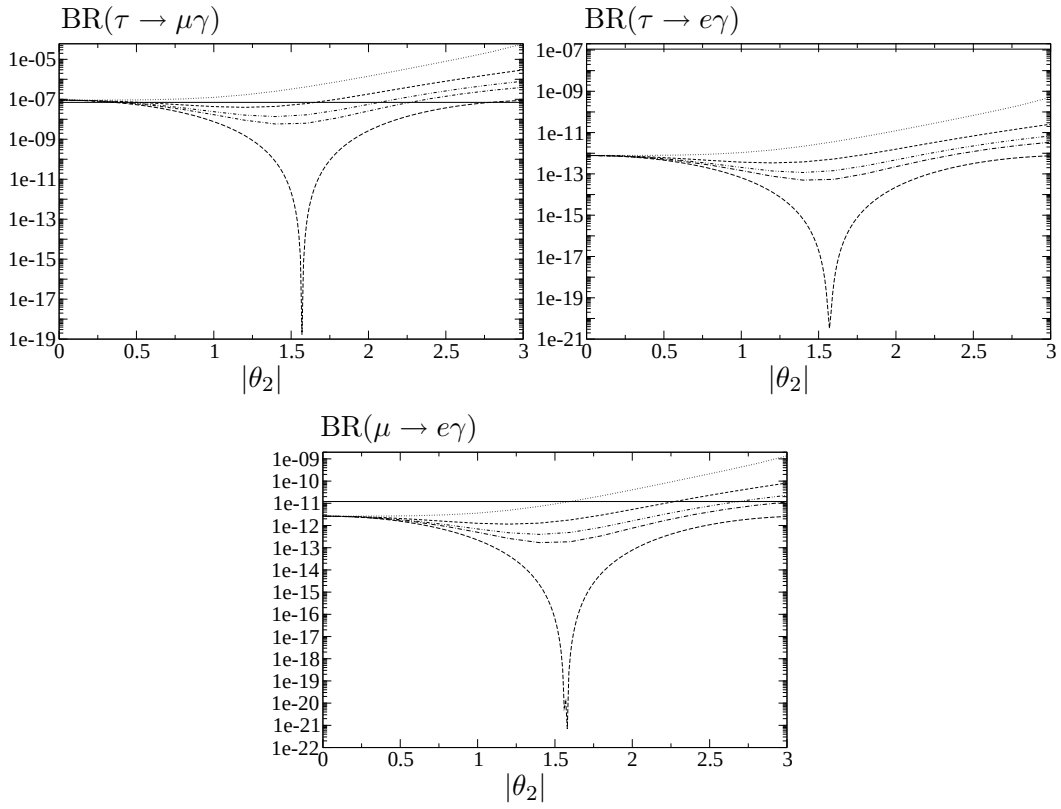

Figure 2.3: Dependence of LVF τ and μ radiative decays on $|\theta_2|$ with hierarchical heavy neutrinos and complex R, for $\arg\theta_2 = 0, \pi/10, \pi/8, \pi/6, \pi/4$ in radians (lower to upper lines), $(m_{N_1}, m_{N_2}, m_{N_3}) = (10^8, 2\times10^8, 10^{14})$ GeV, $\theta_1 = \theta_3 = 0$, $\tan\beta = 50$, $M_0 = 400$ GeV, $M_{1/2} = 300$ GeV, $A_0 = 0$ and sign$(\mu) > 0$. The horizontal lines are the upper experimental bounds. At present these bounds have been improved as summarised in Table 2.1.

$\arg\theta_2 = 0$. These lower lines are therefore the corresponding predictions for real R. It is clear that all the branching ratios have a soft behaviour with $|\theta_2|$ except for the case of real θ_2 where appears a narrow dip in each plot. In this Fig. 2.3 we see that all the rates obtained are below their experimental upper bounds, except for the processes $\tau \to \mu\gamma$ and $\mu \to e\gamma$, where the predicted rates for complex θ_2 with large $|\theta_2|$ are clearly above the allowed region. The most restrictive channel in this case is $\tau \to \mu\gamma$ where compatibility with data occurs just for real θ_2 and for complex θ_2 but with $|\theta_2|$ values near the region of the narrow dip.

Even more interesting are the predictions for BR$(l_j \to l_i\,\gamma)$ as functions of $|\theta_1|$, due to the large values of the relevant entries of the Y_ν coupling matrix, which are illustrated in Fig. 1.8. Concretely, $|Y_\nu^{13}|$ can be as large as ~ 0.2 for $|\theta_1| \sim 2.5$ and $\arg(\theta_1) = \pi/4$, and $|Y_\nu^{23}|$ and $|Y_\nu^{33}|$ are in the range $0.1 - 1$ for all studied complex θ_1 values. The results for BR$(l_j \to l_i\,\gamma)$ as

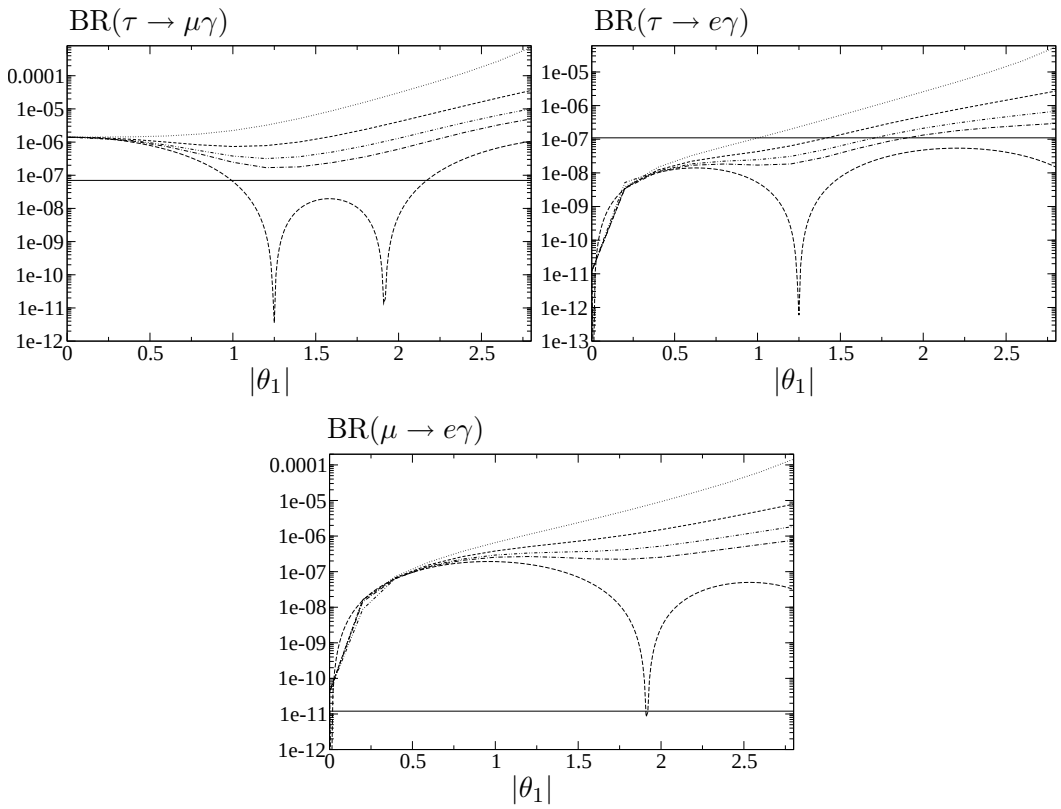

Figure 2.4: Dependence of LFV τ and μ radiative decays on $|\theta_1|$ with hierarchical heavy neutrinos and complex R, for $\arg\theta_1 = 0, \pi/10, \pi/8, \pi/6, \pi/4$ in radians (lower to upper lines), $(m_{N_1}, m_{N_2}, m_{N_3}) = (10^8, 2\times10^8, 10^{14})$ GeV, $\theta_2 = \theta_3 = 0$, $\tan\beta = 50$, $M_0 = 250$ GeV, $M_{1/2} = 150$ GeV and $A_0 = 0$. The horizontal lines are the upper experimental bounds. At present these bounds have been improved as summarised in Table 2.1.

functions of $|\theta_1|$, for different values of $\arg(\theta_1)$, are illustrated in Fig. 2.4. Here θ_2 and θ_3 are set to zero. The same set of CMSSM parameters and heavy neutrino masses as in Fig. 2.3 are taken for comparison. We see clearly that the restrictions are more severe in this case than in the previous one. In fact, all the rates cross the horizontal lines of the experimental bounds. The most restrictive channel is now the $\mu \to e\,\gamma$ decay. More specifically, we see that all the points in the plot of BR($\mu \to e\,\gamma$), except for the particular values $\theta_1 = 0$ and real θ_1 at the dip, are excluded by the experimental upper bound. Notice that the qualitative behaviour of these branching ratios with $|\theta_1|$ in Fig. 2.4 and the locations of the dips can be explained from the Yukawa coupling matrix behaviour in Fig. 1.8.

We have also explored the dependence with the complex θ_3 angle, and it turns out that the predictions for all rates are nearly constant with this angle. For instance, for $\tan\beta = 50$,

$M_0 = 400$ GeV, $M_{1/2} = 300$ GeV, $A_0 = 0$ and sign$(\mu) > 0$, we get BR$(\tau \to \mu\gamma) = 9.1 \times 10^{-8}$, BR$(\tau \to e\gamma) = 7.8 \times 10^{-13}$ and BR$(\mu \to e\gamma) = 2.6 \times 10^{-12}$. In this case only the prediction for BR$(\tau \to \mu\gamma)$ is in conflict with the experiment.

In summary, we obtain in the hierachical case much larger rates than in the degenerate one. We have found that the most relevant parameter is m_N in the case of degenerate heavy neutrinos or, equivantly, m_{N_3} in the hierarchical case. The SUSY parameter $\tan\beta$ also plays an important role due to the fact that these rates grow as $\tan^2\beta$.

2.1.3 Sensitivity to θ_{13}

We continue our study with the $R = \mathbb{1}$ case which represents the situation where there are no further neutrino mixings in the Yukawa couplings other than those induced by the $U_{\rm PMNS}$. In this case it turns out that the BR$(\mu \to e\,\gamma)$ shows a strong dependence on θ_{13}. It was first noticed in the context of SUSY GUTs [181] and later analysed in full detail by us [102, 109] in the context of constrained SUSY-seesaw scenarios. We performed by the first time a comprehensive study of all the leptonic decay channels $l_j \to l_i\,\gamma$ and $l_j \to 3\,l_i$ (in a full RGE approach), and concluded that both $\mu \to e\,\gamma$ and $\mu \to 3\,e$ do exhibit a clear sensitivity to θ_{13} and present promising prospects from the point of view of experimental detection. We first investigate here the sensitivity to θ_{13} of the BR$(l_j \to l_i\,\gamma)$ and later, in Section 2.3.3, we will discuss the case of $l_j \to 3\,l_i$. We also add some comments on the comparison between the full and the LLog approximation results.

In Fig. 2.5 we plot the branching ratios of the decays $\mu \to e\,\gamma$ and $\tau \to e\,\gamma$ as a function of θ_{13}, which we vary[1] in the range $[0°, 10°]$. We also display, for comparison, the lines associated with the present experimental bounds and future sensitivities. In each case, we consider as input the six SPS points, and take $\theta_i = 0$, so that in this case no BAU is generated and there is no flavour mixing arising from the right-handed neutrino sector. Regarding the neutrino masses, we have assumed $m_{\nu_1} = 10^{-5}$ eV, while the masses of the heavy right-handed are set to $m_N = (10^{10}, 10^{11}, 10^{14})$ GeV. In particular we have chosen m_{N_1} to avoid the gravitino problem in relation with non-thermal LSP production, as explained in Section 1.7.1. Notice that our choice of m_{N_3} leads to large values for the third family Yukawa couplings[2], specifically $(Y_\nu)_{33} \approx (Y_\nu)_{32} \approx 0.3$.

The first conclusion to be inferred from Fig. 2.5 is that the sensitivity to θ_{13} is clearly manifest in the $\mu \to e\,\gamma$ and $\tau \to e\,\gamma$ channels. Notice that for $\tau \to e\,\gamma$ the BR predictions for

[1] The scan step is purposely finer for small values of θ_{13}.

[2] Other approaches, for instance in GUT-inspired frameworks, allow to derive the values of m_{N_3} from unification of the Yukawa couplings of the third family, and this may lead to even larger values of $(Y_\nu)_{33}$. For example, an SO(10) GUT could lead to $m_{N_3} \approx 10^{15}$ GeV, as implied by $(Y_\nu)_{33} \approx 1$ (see, for example, [181]).

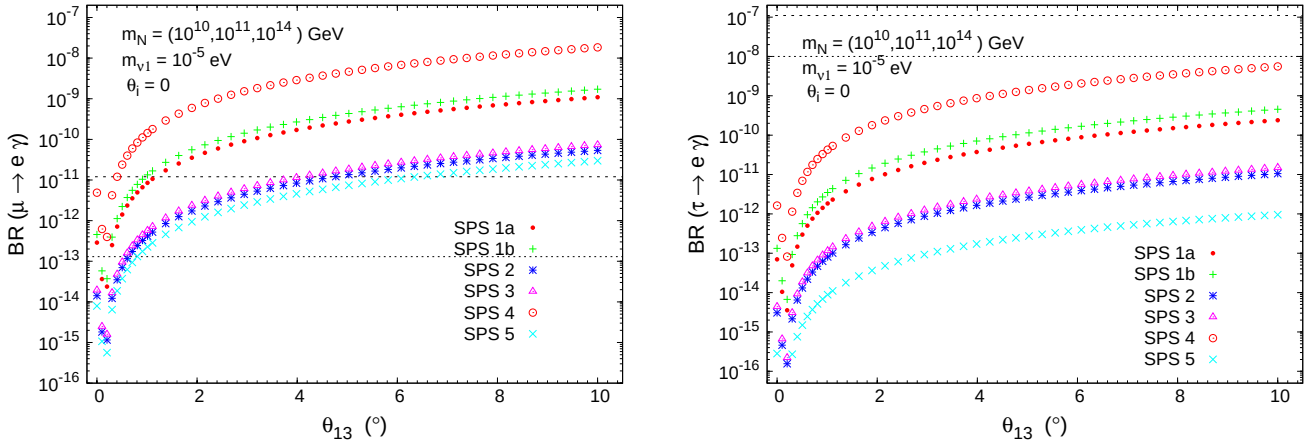

Figure 2.5: BR($\mu \to e\,\gamma$) and BR($\tau \to e\,\gamma$) as a function of θ_{13} (in degrees), for SPS 1a (dots), 1b (crosses), 2 (asterisks), 3 (triangles), 4 (circles) and 5 (times). A dashed (dotted) horizontal line denotes the present experimental bound (future sensitivity).

the explored θ_{13} values lie below the present and future experimental sensitivities[3], whereas for $\mu \to e\,\gamma$ the BRs are clearly above the experimental bound for various of the explored cases.

The observed qualitative behaviour with respect to θ_{13} can be easily understood from Eq. (1.85), which predicts that the dominant contribution proportional to $(L_{33}\,m_{N_3}\,m_{\nu_3})^2$ should grow as $(c_{13}\,s_{13})^2$. For small values of θ_{13} , the "dip" exhibited by the BRs is a consequence of a shift in θ_{13} arising from RGE running, changing it from $\theta_{13} \equiv \theta_{13}(m_Z)$ to $\theta_{13}(m_M)$. Renormalisation induces, in our example, that $\theta_{13}(m_M) \approx \theta_{13}(m_Z) - 0.2°$, so that the minimum of the BR is shifted from $\theta_{13} = 0°$ to $\theta_{13} \approx 0.2°$ (which is consistent with analytical estimates [183]). More explicitly, even when starting with a value $\theta_{13} = 0°$ at the EW scale, RGE running leads to the appearance of a negative value for $\theta_{13}(m_M)$ (or, equivalently, a non-zero positive θ_{13} and $\delta = \pi$).

Concerning the $\tau \to \mu\,\gamma$ channel, the corresponding branching ratios do not exhibit any noticeable dependence on θ_{13}, as expected from the analytical expressions of the LLog approximation. For the case $R = \mathbb{1}$, and taking for example $\theta_{13} = 5°$, these BRs are presented in Table 2.2.

The conclusion to be inferred from Figs. 2.5 and Table 2.2 is that, for the assumed value of m_{ν_1}, and for the chosen seesaw scenario (which is specified by θ_i and m_{N_i}), the experimental bounds for BR($\tau \to \mu\,\gamma$) already disfavour the CMSSM scenario of SPS 4 (for any value of θ_{13}).

[3]On the other hand, we remark that compared to θ_{13}, the uncertainties in the other neutrino oscillation parameters, θ_{23}, θ_{12}, Δm^2_{23} and Δm^2_{12}, are expected to have only a smaller effect on the LFV ratios (see e.g. [182])

BR	SPS 1a	SPS 1b	SPS 2	SPS 3	SPS 4	SPS 5
$\tau \to \mu\,\gamma$	4.2×10^{-9}	7.9×10^{-9}	1.8×10^{-10}	2.6×10^{-10}	9.7×10^{-8}	1.9×10^{-11}

Table 2.2: Predictions for the BR($\tau \to \mu\,\gamma$) corresponding to the SPS points. The values of m_{N_i} and m_{ν_1} are as specified in Fig. 2.5. In each case, the predicted values should be compared with the present bound (future prospect) BR($\tau \to \mu\,\gamma$) $< 1.6 \times 10^{-8}$ (10^{-8}).

From the comparative analysis of the θ_{13}-sensitive channels it is also manifest that $\mu \to e\,\gamma$ is the unique LFV radiative decay whose BRs are within the reach of present experiments, thus potentially allowing to constrain the values of θ_{13}. In fact, BR($\mu \to e\,\gamma$) suggests that SPS 4, 1(a and b), 3, 2 and 5 are disfavoured for values of θ_{13} larger than approximately 0.5°, 1°, 4°, 5° and 6°, respectively. Nevertheless, it is crucial to notice that, as can be seen from Eqs. (1.85) and (2.4), the value of m_{N_3} plays a very relevant role. For instance, by lowering m_{N_3} from 10^{14} GeV to 10^{13} GeV one could have compatibility with the experimental bound on BR($\mu \to e\,\gamma$) for $\theta_{13} \lesssim 2°$ for *all* SPS scenarios. Moreover, in this case, even SPS 4 would be in agreement with the experimental bound on BR($\tau \to \mu\,\gamma$).

The comparative size of the predicted BRs for each of the SPS points can be easily understood from the BRs dependence on the SUSY spectrum[4] and $\tan\beta$, which is approximately given by Eq. (2.4). However, it is worth emphasising that although the several approximations leading to Eq. (2.4) do provide a qualitative understanding of the LFV rates, they are not sufficiently accurate, and do fail in some regions of the CMSSM parameter space. In particular, for the SPS 5 scenario, we have verified that the LLog predictions for the BRs arising from Eq. (1.84) differ from our results by several orders of magnitude. We will return to this discussion at a later stage.

As already mentioned, in the context of SUSY GUTs, the dependence of the BR($\mu \to e\,\gamma$) on θ_{13} for the same set of SPS points was presented in [181]. Instead of the full computations, the analysis was done using the LLog approximation, and the amount of slepton flavour violation was parameterised by means of mass insertions. In general, and even though a different seesaw scenario was considered, the results are in fair agreement with Fig. 2.5, the only exception occurring for SPS 5. In fact, while [181] predicts the largest BR($\mu \to e\,\gamma$) for the SPS 5 case, our results of Fig. 2.5 show that the rates for this point are indeed the smallest ones. As already mentioned, this is due to the failure of the LLog for SPS 5.

Henceforth, and in view of the fact that not only is the decay $\mu \to e\,\gamma$ one of the most sensitive to θ_{13}, but it is also the most promising regarding experimental detection, we will mainly focus our discussion on the analysis of BR($\mu \to e\,\gamma$).

[4]For each SPS point, the associated spectrum can be found, for example, in [140].

2.1.4 Implications of a favourable BAU scenario on the sensitivity to θ_{13}

Motivated by the generation of a sufficient amount of CP asymmetry in the decay of the right-handed heavy neutrinos, one has to depart from the $R = \mathbb{1}$ case, and this will naturally affect the predictions for the several BRs. Nevertheless, it is worth stressing that the hierarchy of the SPS points regarding the relative predictions to the distinct LFV observables is not altered, and we also observe the same ordering as that emerging from Figs. 2.5 and Table 2.2, namely $\mathrm{BR}_4 > \mathrm{BR}_{1\mathrm{b}} \gtrsim \mathrm{BR}_{1\mathrm{a}} > \mathrm{BR}_3 \gtrsim \mathrm{BR}_2 > \mathrm{BR}_5$.

As discussed in Section 1.7.1, the R-matrix complex parameters θ_2 and θ_3 are instrumental in obtaining a value for the baryon asymmetry in agreement with experimental observation, while θ_1 plays a comparatively less relevant role. In what follows, we discuss how requiring a favourable BAU scenario would constrain the θ_i ranges, and how this would reflect on the BRs' sensitivity to θ_{13}.

Influence of θ_2

In view of the above, we begin by comparing the predictions of $\mathrm{BR}(\mu \to e\,\gamma)$ in the BAU constrained θ_2 range for two particular values of θ_{13}, $\theta_{13} = 0^\circ\,, 5^\circ$. We choose SPS 1a, and motivated from the discussion regarding Fig. 1.16, take $0 \lesssim |\theta_2| \lesssim \pi/4$, with $\arg\theta_2 = \{\pi/8\,,\, \pi/4\,,\, 3\pi/8\}$.

In Fig. 2.6, we display the numerical results, considering $m_{\nu_1} = 10^{-5}$ eV and $m_{\nu_1} = 10^{-3}$ eV, while for the heavy neutrino masses we take $m_N = (10^{10},\, 10^{11},\, 10^{14})$ GeV.

There are several important conclusions to be drawn from Fig. 2.6. Let us first discuss the case $m_{\nu_1} = 10^{-5}$ eV. As previously mentioned, one can obtain a baryon asymmetry in the range 10^{-10} to 10^{-9} for a considerable region of the analysed $|\theta_2|$ range. In particular, a deviation from the $R = \mathbb{1}$ case as small as, for instance, $\theta_2 = 0.05\, e^{\pi/8\, i}$ can account for an amount of BAU close to the WMAP value. A wide region with larger values of $|\theta_2|$ ($0.3 \lesssim |\theta_2| \lesssim 0.8$) can also accommodate a viable baryon asymmetry, as can be seen from Fig. 2.6. Notice also that there is a clear separation between the predictions of $\theta_{13} = 0^\circ$ and $\theta_{13} = 5^\circ$, with the latter well above the present experimental bound. At present, this would imply an experimental impact of θ_{13}, in the sense that the BR predictions become potentially detectable for this non-vanishing θ_{13} value. With the planned MEG sensitivity [184], both cases would be within experimental reach. However, this statement is strongly dependent on the assumed parameters, in particular m_{ν_1}. For instance, a larger value of $m_{\nu_1} = 10^{-3}$ eV, illustrated on the right panel of Fig. 2.6, leads to a very distinct situation regarding the sensitivity to θ_{13}. While for smaller values of $|\theta_2|$ the branching ratio displays a clear sensitivity to having θ_{13} equal or different from zero (a separation larger than two orders of magnitude for $|\theta_2| \lesssim 0.05$), the effect of θ_{13} is diluted for increasing values of $|\theta_2|$. For $|\theta_2| \gtrsim 0.3$ the $\mathrm{BR}(\mu \to e\,\gamma)$ associated with $\theta_{13} = 5^\circ$ can

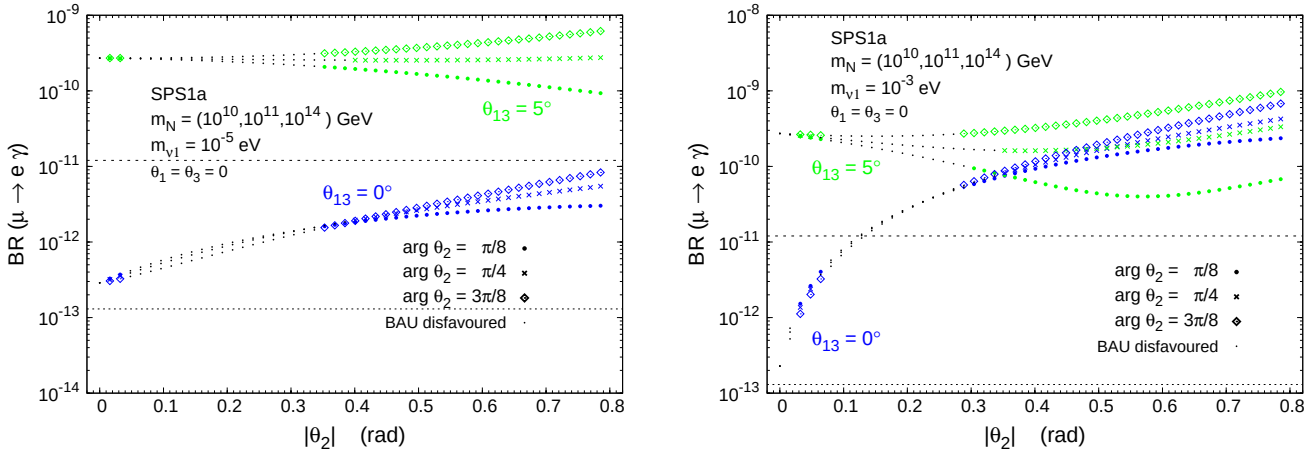

Figure 2.6: BR($\mu \to e\,\gamma$) as a function of $|\theta_2|$, for $\arg\theta_2 = \{\pi/8\,,\,\pi/4\,,\,3\pi/8\}$ (dots, times, diamonds, respectively) and $\theta_{13} = 0°$, $5°$ (blue/darker, green/lighter lines). We take $m_{\nu_1} = 10^{-5}$ (10^{-3}) eV, on the left (right) panel. In all cases black dots represent points associated with a disfavoured BAU scenario and a dashed (dotted) horizontal line denotes the present experimental bound (future sensitivity).

be even smaller than for $\theta_{13} = 0°$. This implies that in this case, a potential measurement of BR($\mu \to e\,\gamma$) would not be sensitive to θ_{13}.

Moreover, m_{ν_1} also affects the BAU-favoured regions. In general, larger values of m_{ν_1} (still smaller than 10^{-3} eV) widen the range of $|\theta_2|$ for which a viable BAU can be obtained. This can be understood from the fact that for very small (or zero) θ_2 and θ_3 (and with fixed m_{N_1}), m_{ν_1} controls the size of the Yukawa couplings to the lightest right-handed neutrino, N_1. On the other side, these are the Yukawa couplings governing the washout parameter $\widetilde{m}_1$ for thermal leptogenesis, as introduced in Eq. (1.97). For very small θ_2 and θ_3, an optimal value $\widetilde{m}_1 \approx 10^{-3}$ eV can be reached for $m_{\nu_1} \approx 10^{-3}$ eV (c.f. Eq. (1.99)), whereas smaller m_{ν_1} lead to suppressed leptogenesis in this case. For larger values of θ_2 and/or θ_3, which can be still consistent with leptogenesis, m_{ν_1} becomes less important, since the other light neutrino masses m_{ν_2} and/or m_{ν_3} contribute to $\widetilde{m}_1$ as well. In most of the following analysis, we will use $m_{\nu_1} \approx 10^{-3}$ eV and enable a successful thermal leptogenesis by introducing a small R-matrix rotation angle θ_2. In what concerns the sensitivity to θ_{13} via LFV, this is clearly a conservative choice since, as previously mentioned, lower values of m_{ν_1} (e.g. $m_{\nu_1} = 10^{-5}$ eV) would lead to a more favourable situation.

Whether or not a BAU-compatible SPS 1a scenario would be disfavoured by current experimental data on BR($\mu \to e\,\gamma$) requires a careful weighting of several aspects. Even though Fig. 2.6 suggests that for this particular choice of parameters only very small values of θ_2 and θ_{13} would be in agreement with current experimental data, a distinct choice of m_{N_3} (e.g. $m_{N_3} = 10^{13}$ GeV)

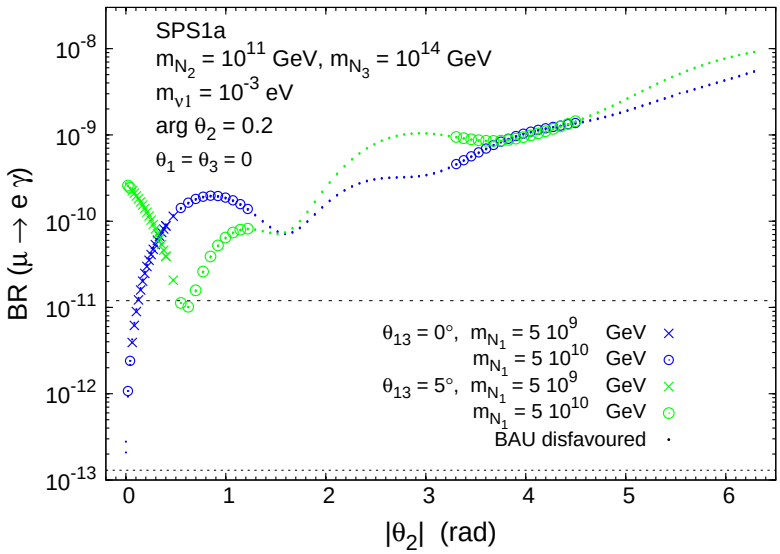

Figure 2.7: BR($\mu \to e\,\gamma$) as a function of $|\theta_2|$, for SPS 1a, with $\arg\theta_2 = 0.2$. $\theta_{13} = 0^\circ\,, 5^\circ$ (blue/darker, green/lighter lines, respectively), and $m_{N_1} = 5 \times 10^9$ GeV, 5×10^{10} GeV (crosses, circles, respectively). Dots represent points associated with a disfavoured BAU scenario for either $m_{N_1} = 5 \times 10^9$ or 5×10^{10} GeV and a dashed (dotted) horizontal line denotes the present experimental bound (future sensitivity).

would lead to a rescaling of the estimated BRs by a factor of approximately 10^{-2}. Although we do not display the associated plots here, in the latter case nearly the entire $|\theta_2|$ range would be in agreement with experimental data (in fact the points which are below the present MEGA bound on Fig. 2.6 would then lie below the projected MEG sensitivity).

Regarding the other SPS points, which are not shown here, we find BRs for SPS 1b comparable to those of SPS 1a. Smaller ratios are associated with SPS 2, 3 and 5, while larger (more than one order of magnitude) BRs occur for SPS 4.

Let us now consider how the value of m_{N_1} affects the amount of BAU, and thus indirectly the branching ratio associated to a given choice of θ_2 that accounts for a viable BAU scenario. In Fig. 2.7 we present the BR($\mu \to e\,\gamma$) as a function of $|\theta_2|$ for two distinct heavy neutrino spectra: $m_N = (5 \times 10^9,\, 10^{11},\, 10^{14})$ GeV and $m_N = (5 \times 10^{10},\, 10^{11},\, 10^{14})$ GeV (values for m_{N_1} respectively smaller and larger than what was previously considered). Regarding $\arg\theta_2$, we have chosen an example which represents a minimal deviation from the real case, $\arg\theta_2 = 0.2$, and set $\theta_1 = \theta_3 = 0$. We consider SPS 1a, and again show both cases associated with $\theta_{13} = 0^\circ\,, 5^\circ$. From this figure, it can be seen that in the case $m_{N_1} = 5 \times 10^9$ GeV, only one BAU-favoured window is opened, for small values of θ_2 ($0 < \theta_2 \lesssim \pi/4$). In contrast, for $m_{N_1} = 5 \times 10^{10}$ GeV, a second window opens, corresponding to the π periodicity evidenced in Fig. 1.16 (also

some additional points at very small $|\theta_2|$ are allowed). The width of the $|\theta_2|$ interval for this second window shrinks with decreasing m_{N_1}. In particular, for $m_{N_1} = 10^{10}$ GeV (not displayed) this interval becomes extremely small. The latter effect can be understood from the interplay of θ_2 and m_{N_1} on the relevant BAU parameters of Eq. (1.99). While $\widetilde{m}_1$ is unchanged and as long as $m_{N_1} \lesssim T_{\rm RH}$, the produced baryon asymmetry increases with m_{N_1}. For a given value of m_{N_1}, the disappearance of the second window associated with larger values of $|\theta_2|$ ($\pi \lesssim |\theta_2| \lesssim 3\,\pi/2$), is due to a stronger washout, which leads to values of $n_{\rm B}/n_\gamma$ below the viable BAU range of Eq. (1.101).

Finally, let us notice that the BAU-favoured ranges of θ_2 imply very distinct predictions for both the BRs, and the associated θ_{13} sensitivity. Even though the BRs arising from the second θ_2 window are significantly larger, in this case the sensitivity to θ_{13} is considerably reduced, as is clearly manifest in Fig. 2.7. All the previous facts taken into account, we will often rely on the choice $m_{N_1} = 10^{10}$ GeV and $\theta_2 = 0.05\, e^{0.2\, i}$ as a means of ensuring a viable BAU scenario via a minimal deviation from the $R = \mathbb{1}$ case.

Influence of θ_1

It has become clear from the previous analysis that a departure from the $R = \mathbb{1}$ case via non-vanishing values of θ_2 can significantly affect the BR sensitivity to θ_{13}. Here we will show that θ_1 plays an equally important role on the present discussion. In Figs. 2.8 and 2.9 we display the BR($\mu \to e\,\gamma$) as a function of $|\theta_1|$, for different values of its argument.

The effect of departing from the case $R = \mathbb{1}$ by varying θ_1 leads to important additional contributions to the considered LFV decays. Here, we have only presented the case $m_{N_3} = 10^{13}$ GeV, since for $m_{N_3} = 10^{14}$ GeV the experimental exclusion line is already crossed for very small values of θ_1 ($|\theta_1| \approx 0.1$). Opposed to the θ_2 case, and as expected from the analytical estimates, there is little dependence of the BR on the choice of the lightest neutrino mass[5]. Considering the other SPS scenarios leads to analogous results, the only difference lying in a global rescaling of the BR($\mu \to e\,\gamma$), and the discussion is similar to that regarding θ_2.

In the case of negative arguments, the influence of θ_1 is shown in Fig. 2.8. Notice that in all cases, for extremely small values of $|\theta_1|$ ($|\theta_1| \lesssim 0.1$), we again recover for $\theta_{13} = 5^\circ$ BRs which are larger, and clearly distinguishable from the $\theta_{13} = 0^\circ$ case. In contrast, for a large (negative) $\arg\theta_1$, the situation is reversed, and the predictions for BR($\mu \to e\,\gamma$) associated to $\theta_{13} = 5^\circ$ are actually smaller than for $\theta_{13} = 0^\circ$. This becomes manifest when $\arg\theta_1 \lesssim -\pi/2$, a regime for which the BR starts decreasing with increasing $|\theta_1|$. For real (and negative) θ_1,

[5]This dependence is only manifest for $\theta_{13} \approx 0^\circ$ and appears in terms proportional to m_{N_2}, so that it is considerably suppressed. On the other hand, and as it occurred for θ_2, larger values of m_{ν_1} widen the range of θ_1 for which a viable BAU scenario can be obtained.

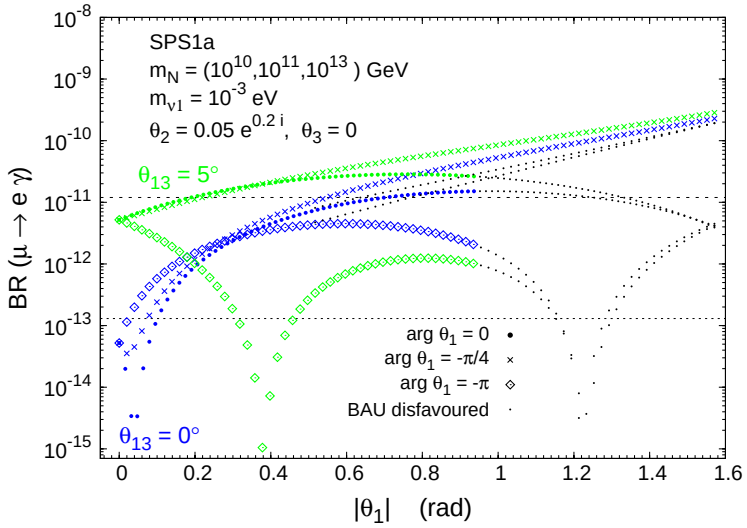

Figure 2.8: BR($\mu \to e\,\gamma$) as a function of $|\theta_1|$, for $\arg\theta_1 = \{0\,, -\pi/4\,, -\pi\}$ (dots, times, diamonds, respectively) and $\theta_{13} = 0^\circ\,, 5^\circ$ (blue/darker, green/lighter lines). BAU is enabled by the choice $\theta_2 = 0.05\,e^{0.2\,i}$ ($\theta_3 = 0$). In all cases black dots represent points associated with a disfavoured BAU scenario and a dashed(dotted) horizontal line denotes the present experimental bound (future sensitivity).

(i.e. $\arg\theta_1 = -\pi$) the effect is such that for $\theta_{13} = 5^\circ$ two local minima of the BR are present (although one disfavoured by BAU), both with an associated value of the BR below the planned MEG sensitivity (for this specific choice of SPS point and seesaw parameters). These "dips" reflect a cancellation between the terms proportional to m_{ν_2} and m_{ν_3} (see Eq. (1.85)), which in fact is also present for $\theta_{13} \approx 0^\circ$, albeit only for the second, BAU-disfavoured, $|\theta_1|$ value. It is worth pointing out that this apparent accidental cancellation for a specific choice of the R-matrix parameters could correspond to the occurrence of texture zeros in the neutrino Yukawa couplings. Although not stable under RGE effects, these zeros effectively translate into very small entries in the Yukawa couplings, which can account for the observed suppression of the BR [102] corresponding to the "dips" in Fig. 2.8. We would like to remark that, generically, the position and depth of these "dips" depend on the chosen values of all the seesaw parameters.

In Fig. 2.9 we present a few examples of $\arg\theta_1 > 0$. In this case, the discussion of the BRs and sensitivity to θ_{13} is very similar to that conducted for small negative arguments. That is, for small $|\theta_1|$ values, the predictions for the two θ_{13} cases are clearly distinguishable. On the other hand, and irrespective of the argument (positive or negative), for sufficiently large $|\theta_1|$, the lines corresponding to the cases $\theta_{13} = 0^\circ$ and 5° eventually meet, and thus for this choice of parameters the sensitivity of the BR to θ_{13} is lost.

Another relevant aspect to be inferred from Figs. 2.8 and 2.9 is how θ_1 affects the BAU

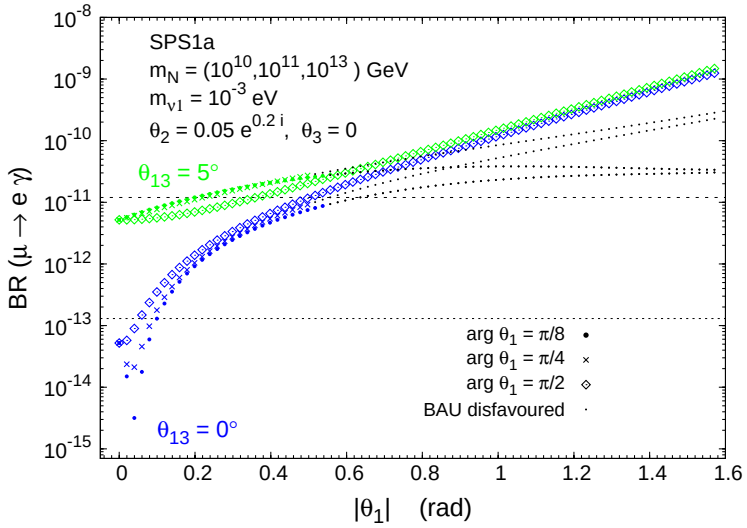

Figure 2.9: BR($\mu \to e\,\gamma$) as a function of $|\theta_1|$, for $\arg\theta_1 = \{\pi/8\,, \pi/4\,, \pi/2\}$ (dots, times, diamonds, respectively) and $\theta_{13} = 0^\circ\,, 5^\circ$ (blue/darker, green/lighter lines). BAU is enabled by the choice $\theta_2 = 0.05\,e^{0.2\,i}$ ($\theta_3 = 0$). In all cases black dots represent points associated with a disfavoured BAU scenario and a dashed(dotted) horizontal line denotes the present experimental bound (future sensitivity).

predictions enabled by θ_2. Unlike what occurs for θ_2 and θ_3, the role of θ_1 in accounting for the observed BAU is somewhat more indirect. In particular, and as mentioned in Section 1.7.1, θ_1 essentially deforms the favoured BAU areas in the $\theta_2 - \theta_3$ plane. For instance, and for the chosen BAU-enabling θ_2 value in Fig. 2.8, a real value of θ_1 larger than 0.9 leads to an estimated $n_{\rm B}/n_\gamma$ which is no longer within the viable BAU range of Eq. (1.101). A distinct situation occurs for the cases $\arg\theta_1 = -\pi/4$ and $\pi/2$, where the entire $|\theta_1|$ range successfully accounts for $n_{\rm B}/n_\gamma$ within $[10^{-10}, 10^{-9}]$.

To conclude this subsection, let us add two further comments. Regarding the influence of θ_3 it suffices to mention that although relevant with respect to BAU (see Fig. 1.17), we have not found a significant BR($\mu \to e\,\gamma$) dependence on the latter parameter. This is a consequence of having the Yukawa couplings to the heaviest right-handed neutrino dominating, since a θ_3 R-matrix rotation leaves unchanged the couplings $(Y_\nu)_{i3}$. In this case, the sensitivity to θ_{13} is very similar to what was found for the $R = \mathbb{1}$ case. In the remaining analysis we will fix $\theta_3 = 0$.

Dependence on the most relevant parameters: m_{N_3} and $\tan\beta$

Throughout the discussion regarding the dependence of the branching ratios on the R-matrix complex angles, it has often been stressed that the leading contributions to the BRs were those

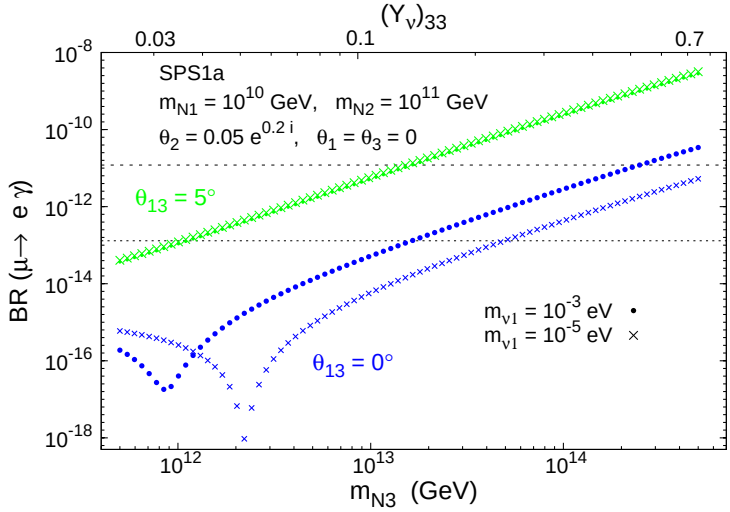

Figure 2.10: BR($\mu \to e\,\gamma$) as a function of m_{N_3} for SPS 1a, with $m_{\nu_1} = 10^{-5}$ eV and $m_{\nu_1} = 10^{-3}$ eV (times, dots, respectively), and $\theta_{13} = 0°$, $5°$ (blue/darker, green/lighter lines). BAU is enabled by the choice $\theta_2 = 0.05\,e^{0.2\,i}$ ($\theta_1 = \theta_3 = 0$). On the upper horizontal axis we display the associated value of $(Y_\nu)_{33}$. A dashed (dotted) horizontal line denotes the present experimental bound (future sensitivity).

proportional to the mass of the heaviest right-handed neutrino, m_{N_3}. This is indeed the most relevant parameter. Here, and to briefly summarise the effect of m_{N_3}, let us present the predictions for BR($\mu \to e\,\gamma$) as a function of the latter mass, while keeping m_{N_1} and m_{N_2} fixed. We have checked that the BRs do not significantly depend on m_{N_1} and m_{N_2}, apart from one exception for m_{N_2}, which we will later comment. The results for SPS 1a are displayed in Fig. 2.10. For completeness, we have included in the upper horizontal axis the associated value of $(Y_\nu)_{33}$ (with similar values being obtained for $(Y_\nu)_{32}$).

We find from Fig. 2.10 that the full RGE result grows with m_{N_3} in a very similar fashion to that predicted by the LLog approximation, i.e. $m_{N_3}^2 \log^2 m_{N_3}$. It is clear that without a predictive theoretical framework for m_{N_3} (e.g. GUT models) or indirect experimental evidence for the scale of the seesaw mechanism, there is a large uncertainty regarding the value of m_{N_3}. Within our chosen scenario of hierarchical heavy neutrinos with $m_{N_1} \ll m_{N_2} \ll m_{N_3}$, assuming that the observed BAU is generated via a mechanism of thermal leptogenesis (with $m_{N_1} \gtrsim 10^9$ GeV), and given the gauge coupling unification scale[6] ($M_X \approx 2 \times 10^{16}$ GeV), the natural choice for m_{N_3} would lie in the range [10^{10} GeV, 10^{15} GeV]. It is obvious from Fig. 2.10 that such an uncertainty in m_{N_3} translates into predictions for the BR ranging over many orders of magnitude.

[6]The possibility of larger LFV effects arising from the existence of a higher energy scale, e.g. $M_{\rm Planck}$, has been addressed by other authors. See, for instance [185].

Hence, one can at most extract an upper bound on m_{N_3} for the chosen set of input parameters. For instance, in Fig. 2.10, $m_{N_3} \gtrsim 10^{13}\,(10^{14})$ GeV is not allowed by the present experimental bounds on the BR($\mu \to e\,\gamma$) for $\theta_{13} = 5^\circ\,(0^\circ)$. Notice that, although the sensitivity to θ_{13} is clearly displayed in Fig. 2.10 (with more than two orders of magnitude separation of the $\theta_{13} = 0^\circ$ and 5° lines), without additional knowledge of m_{N_3} it will be very difficult to disentangle the several θ_{13} cases. However, this argument can be reversed. This strong dependence on m_{N_3} could indeed be used to derive hints on m_{N_3} from a potential BR measurement. We will return to this type of considerations in the following section.

It is also worth commenting on the local minima appearing in Fig. 2.10 for the lines associated with $\theta_{13} = 0^\circ$. As mentioned before, these "dips" are induced by the effect of the running of θ_{13}, shifting it from zero to a negative value. In the LLog approximation, the "dips" can be understood from Eq. (1.85) as a cancellation between the terms proportional to $m_{N_3}\,L_{33}$ and $m_{N_2}\,L_{22}$ in the limit $\theta_{13}(m_M) \to 0^-$ (with $\theta_1 = \theta_3 = 0$). The depth of the minimum is larger for smaller m_{ν_1}, as visible in Fig. 2.10. We have also checked that an analogous effect takes place when one investigates the dependence of BR($\mu \to e\,\gamma$) on m_{N_2}. It is only in this limit $\theta_{13}(m_M) \to 0^-$, and in the vicinity of the "dip", that m_{N_2} can visibly affect the BRs.

Regarding the other SPS points, with the exception of SPS 3 and 5, the results from the full RGE computation (not displayed here) are also in good agreement with the LLog approximation. The predicted BRs for SPS 3 are found to be larger than those of the LLog by a factor of approximately 3. This divergence is due to the fact that in the LLog approximation the effects of $M_{1/2}$ in the running of the soft-breaking parameters of Eq. (1.84) are not taken into account. Therefore, for low M_0 and large $M_{1/2}$ (as is the case of SPS 3), there is a significant difference between the results of the full and approximate computations, as previously noted by [186, 187]. Moreover, this difference becomes more evident for low values of $\tan\beta$.

The divergence of the two computations is more dramatic for SPS 5. This is shown in Fig. 2.11, where we compare the dependence of the BR($\mu \to e\,\gamma$) and BR($\tau \to \mu\,\gamma$) on m_{N_3}, as given from the full computation, and in the LLog approximation. The latter approximation over-estimates by more than four orders of magnitude the values of the BR($\mu \to e\,\gamma$). The full RGE and LLog results diverge even more regarding the BR($\tau \to \mu\,\gamma$), with a separation that can be as large as five orders of magnitude. It is also manifest from Fig. 2.11 that the qualitative behaviour of the full results with respect to m_{N_3} is no longer given by $m_{N_3}^2\,\log^2 m_{N_3}$. The reason for this divergence is associated to the large negative value of the trilinear coupling[7], A_0. We considered other large negative values of A_0, in all cases leading to the same conclusion. Taking large positive A_0 also leads to an important, albeit not as large, separation (for instance, three orders of magnitude for $A_0 = 1000$ GeV).

[7]The effect of the sign of A_0 in the failure of the LLog approximation has already been discussed in [186].

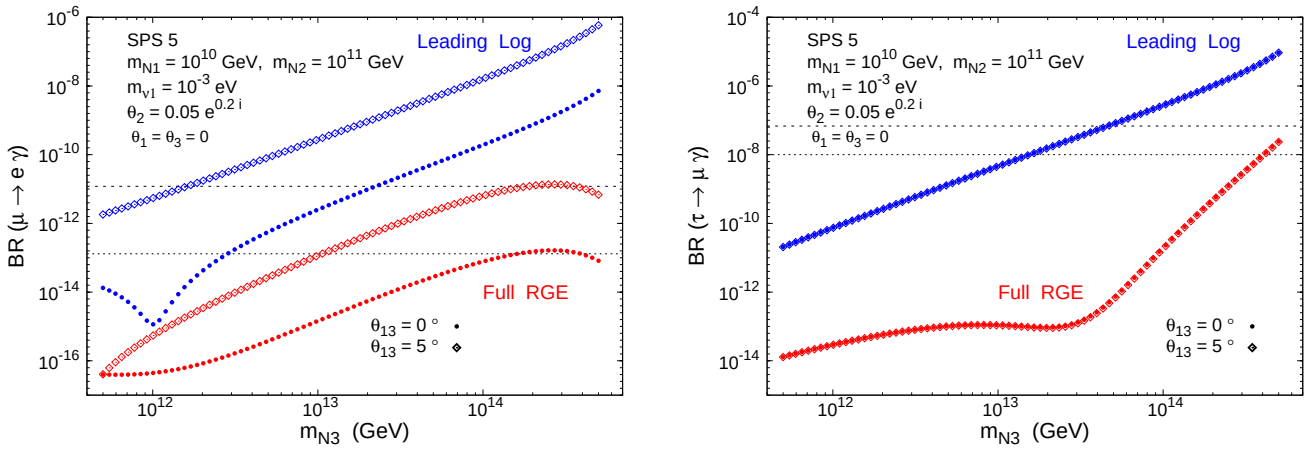

Figure 2.11: Prediction for BR($\mu \to e\,\gamma$) and BR($\tau \to \mu\,\gamma$) as a function of m_{N_3} for SPS 5, using the LLog approximation (upper blue lines) and full RGE (lower red lines). $\theta_{13} = 0°$, $5°$ (dots, diamonds, respectively). BAU is enabled by the choice $\theta_2 = 0.05\,e^{0.2\,i}$ ($\theta_1 = \theta_3 = 0$). A dashed (dotted) horizontal line denotes the present experimental bound (future sensitivity).

Finally, we briefly comment on the BR dependence on $\tan\beta$ for the hierarchical neutrino case. As we have already said, the BRs approximately grow as $\tan^2\beta$, and therefore this is also a relevant parameter. In Fig. 2.12, we plot a generalisation of the SPS points 1a and 4 (defined by M_0, $M_{1/2}$, A_0 and sign μ) with free $\tan\beta$, and present the sensitivity of the branching ratios to distinct values of θ_{13}. Again, as can be seen in Fig. 2.12, the sensitivity to θ_{13} is clearly manifest, in the sense that for a given $\tan\beta$ the predictions for the BRs are very distinct for different θ_{13} values. However, the $\tan\beta$ dependence is so important that two $\tan\beta$ values, for instance 10 and 20, lead to predictions of the BR that diverge as much as those one obtains from the comparison of $\theta_{13} = 3°$ and $5°$ (for a fixed value of $\tan\beta$). This implies that unless the experimental range for $\tan\beta$ is far more constrained than at present, we cannot conclude about the allowed/disallowed θ_{13} values from the present $\mu \to e\,\gamma$ bounds. Just like as argued for m_{N_3}, the strong BR dependence on $\tan\beta$ can be constructively used to further constrain $\tan\beta$ from a potential BR($\mu \to e\,\gamma$) measurement. We will address this topic in the following section.

2.1.5 Experimental prospects: hints on SUSY and Seesaw parameters from measuring θ_{13} and BRs

In the previous section, we analysed how the several free parameters of the SUSY-seesaw scenario affect the predictions for the BR($l_j \to l_i\,\gamma$). We also emphasised how the sensitivity of the latter ratios to θ_{13} can be altered by the uncertainty introduced from the indetermination of θ_i, $\tan\beta$

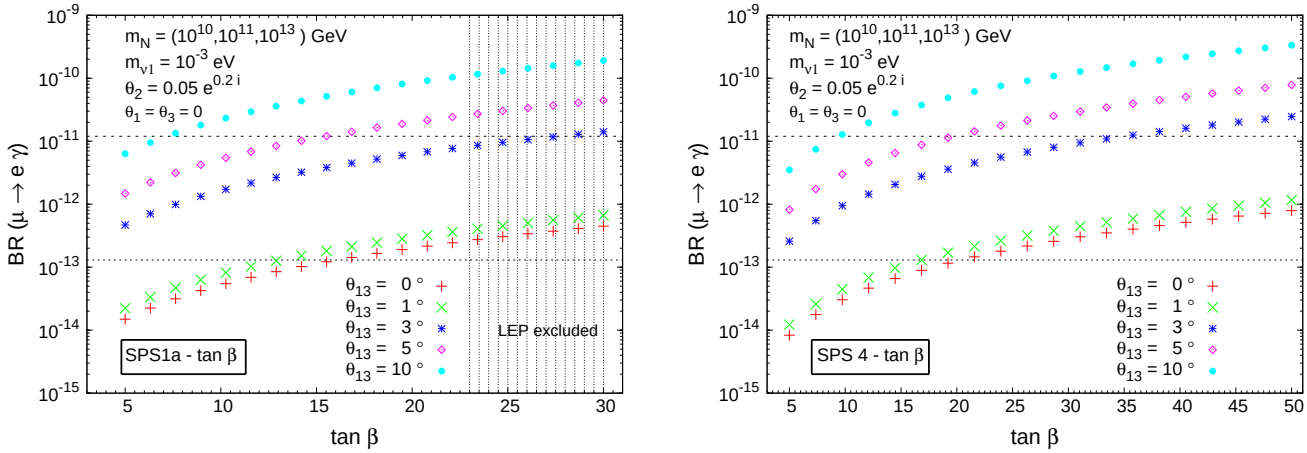

Figure 2.12: BR($\mu \to e\,\gamma$) as a function of $\tan\beta$, for $m_N = (10^{10}, 10^{11}, 10^{13})$ GeV, for SPS 1a (left) and SPS 4 (right). $\theta_{13} = 0°, 1°, 3°, 5°$, and $10°$ (crosses, times, asterisks, diamonds and dots, respectively). BAU is enabled by the choice $\theta_2 = 0.05\,e^{0.2\,i}$ ($\theta_1 = \theta_3 = 0$). A dashed (dotted) horizontal line denotes the experimental bound (future sensitivity). Vertical shaded regions correspond to regions with spectra excluded by LEP data.

and, most of all, m_{N_3}. The question we aim to address in this section is whether a joint measurement of the BRs and θ_{13} can shed some light on apparently unreachable parameters, like m_{N_3}.

The expected improvement in the experimental sensitivity to the LFV ratios (see Table 2.1) support the possibility that a BR be measured in the future, thus providing the first experimental evidence for new physics, even before its discovery at the LHC. The prospects are especially encouraging regarding $\mu \to e\,\gamma$, where the sensitivity will improve by at least two orders of magnitude. Moreover, and given the impressive effort on experimental neutrino physics, a measurement of θ_{13} will likely also occur in the future [90–99]. In what follows, let us envisage a future "toy"-like scenario, where we will assume the following hypothesis: (i) measurement of BR($\mu \to e\,\gamma$); (ii) measurement of θ_{13}; (iii) discovery of SUSY at the LHC, with a given spectrum. Furthermore, we assume that BAU is explained via thermal leptogenesis, with a hierarchical heavy-neutrino spectrum.

Under the above conditions, let us conduct the following exercise. First, choosing SPS 1a, $m_{N_1} = 10^{10}$ GeV, $m_{N_2} = 10^{11}$ GeV, $m_{\nu_1} = 10^{-3}$ eV, $\theta_2 = 0.05\,e^{0.2\,i}$ (a minimal BAU-enabling deviation from the $R = \mathbb{1}$ case), and with θ_{13} set to $1°$ ($\pm 0.1°$) and to $5°$ ($\pm 0.5°$), we predict the BRs as a function of $\tan\beta$ and m_{N_3}. We then plot the contour lines for constant BR values in the $m_{N_3} - \tan\beta$ plane. In Fig. 2.13 we display the corresponding contours for the central values of 1.2×10^{-n} with $n = 10, \ldots, 15$, allowing for a 10% spread-out around these values.

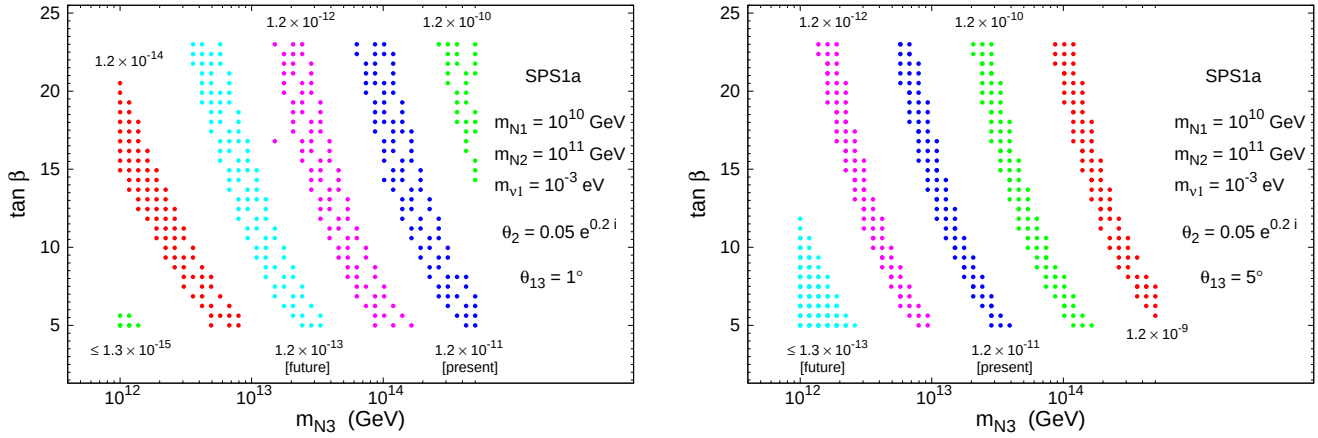

Figure 2.13: Contours of $\mathrm{BR}(\mu \to e\,\gamma) = (1.2 \pm 0.1) \times 10^{-n}$, with $n = 10, \ldots, 15$ in the $m_{N_3} - \tan\beta$ plane, for a generalised SPS 1a scenario. We assume $\theta_{13} = 1^\circ \pm 0.1^\circ$ ($5^\circ \pm 0.5^\circ$) on the left (right) panel. BAU is enabled by the choice $\theta_2 = 0.05\, e^{0.2\,i}$ ($\theta_1 = \theta_3 = 0$). The current experimental bound is associated with the darkest (blue) surface, while the future sensitivity is represented by the lightest (cyan) one.

The predicted contours should be compared with the present bound and future sensitivity of 1.2×10^{-11} [58] and 1.3×10^{-13} [184], respectively.

Given a potential SUSY discovery, the implications of a measurement of $\mathrm{BR}(\mu \to e\,\gamma)$ and θ_{13} are clearly manifest in Fig. 2.13. From this figure we first learn that, even in the absence of an experimental determination of $\tan\beta$, a potential measurement of $\mathrm{BR}(\mu \to e\,\gamma)$ and θ_{13} will allow to constrain m_{N_3}. For example, an hypothetical measurement of $\mathrm{BR}(\mu \to e\,\gamma) \approx 1.2(\pm 0.1) \times 10^{-12}$ would point towards the following allowed ranges of m_{N_3}:

$$\begin{aligned} \theta_{13} \approx 1^\circ \;&\Rightarrow\; 2 \times 10^{13}\ \mathrm{GeV} \lesssim m_{N_3} \lesssim 2 \times 10^{14}\ \mathrm{GeV}\,, \\ \theta_{13} \approx 5^\circ \;&\Rightarrow\; 1.5 \times 10^{12}\ \mathrm{GeV} \lesssim m_{N_3} \lesssim 10^{13}\ \mathrm{GeV}\,. \end{aligned} \tag{2.7}$$

Other assumptions for the BRs would equally lead to an order of magnitude interval for the constrained values of m_{N_3}. If in addition to the s-spectrum, we assume that $\tan\beta$ is experimentally determined, then the intervals for m_{N_3} presented in Eq. (2.7) can be significantly reduced. For instance, assuming that SPS 1a is indeed reconstructed (that is, $\tan\beta = 10$), then we would find

$$\begin{aligned} \theta_{13} \approx 1^\circ \;&\Rightarrow\; 4 \times 10^{13}\ \mathrm{GeV} \lesssim m_{N_3} \lesssim 7 \times 10^{13}\ \mathrm{GeV}\,, \\ \theta_{13} \approx 5^\circ \;&\Rightarrow\; 3 \times 10^{12}\ \mathrm{GeV} \lesssim m_{N_3} \lesssim 5 \times 10^{12}\ \mathrm{GeV}\,. \end{aligned} \tag{2.8}$$

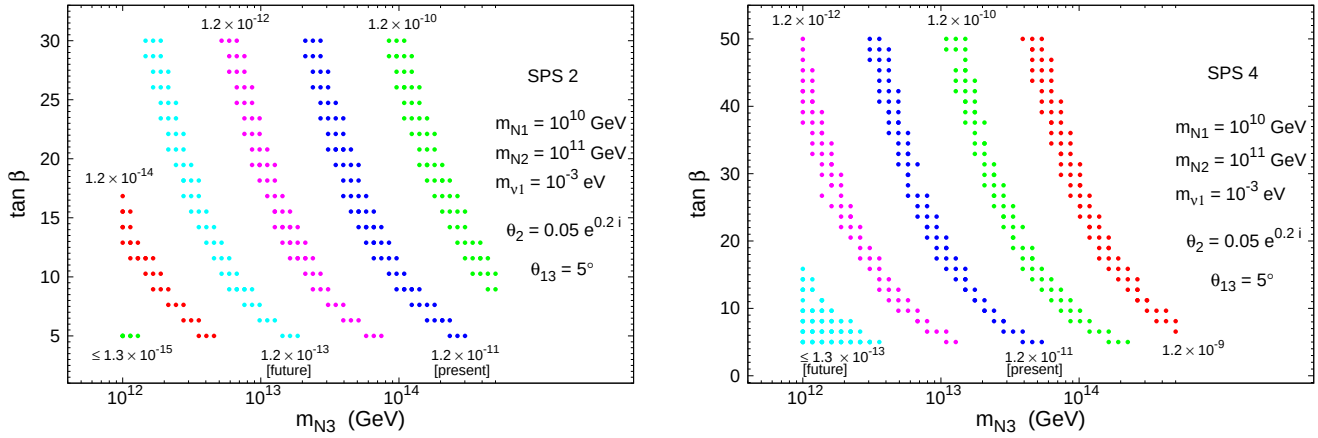

Figure 2.14: Contours of BR($\mu \to e\,\gamma$)= $(1.2\pm0.1)\times10^{-n}$, with $n = 10, \ldots, 15$ in the $m_{N_3}-\tan\beta$ plane for a generalised SPS 2 (left) and SPS 4 (right) scenarios. We assume $\theta_{13} = 5° \pm 0.5°$. BAU is enabled by the choice $\theta_2 = 0.05\, e^{0.2\, i}$ ($\theta_1 = \theta_3 = 0$).

The hypothetical reconstruction of any other SPS-like scenario would lead to similar one order of magnitude intervals for m_{N_3} but with distinct m_{N_3} central values. As expected, for the same BR and θ_{13} measurements, SPS 2, 3 and 5 lead to larger values of m_{N_3}, the contrary occurring for SPS 1b and 4. This can be seen in Fig. 2.14, where we present an analogous study to that of Fig. 2.13, but focusing on SPS 2 and SPS 4, and only considering $\theta_{13} = 5° \pm 0.5$.

Concerning the comparison with current experimental bounds, one can also draw some conclusions regarding the excluded regions of the m_{N_3}-tan β plane. From both Figs. 2.13 and 2.14, for $\theta_{13} = 5°$, and for the chosen set of input parameters, we infer that in all cases the upper-right regions of the m_{N_3}-tan β plane are clearly disfavoured. For instance, for SPS 1a, $m_{N_3} \gtrsim 10^{14}$ GeV would be excluded for any value of tan β. In the case of SPS 2, the exclusion region would be delimited by tan $\beta \gtrsim 10$ and $m_{N_3} \gtrsim 10^{14}$ GeV. The most pronounced exclusion region is for SPS 4, and is given by tan $\beta \gtrsim 20$, $m_{N_3} \gtrsim 10^{13}$ GeV. With the expected future sensitivity, these exclusion regions will be significantly enlarged.

A potential caveat to the previous discussion is the fact that, as seen in Section 2.1.4, there is a very important dependence of the BRs on the R-matrix parameters θ_i. Not only will this have implications on how accurate the indirect estimates of m_{N_3} are, but will also affect any judgement regarding the experimental viability of a SUSY-seesaw scenario. We recall that, as shown in Section 2.1.4, other choices of θ_2 (and θ_1) can lead to substantially smaller or larger BRs, therefore modifying the exclusion regions of Figs. 2.13 and 2.14.

To take into account the strong R-matrix dependence, let us conduct in what follows a

more comprehensive survey of the parameter space. For SPS 1a, and for distinct choices of the heaviest neutrino mass, we scan over the BAU-enabling R-matrix angles (setting θ_3 to zero) as

$$\begin{aligned} &0 \lesssim |\theta_1| \lesssim \pi/4\,, \qquad -\pi/4 \lesssim \arg\theta_1 \lesssim \pi/4\,, \\ &0 \lesssim |\theta_2| \lesssim \pi/4\,, \qquad\quad 0 \lesssim \arg\theta_2 \lesssim \pi/4\,, \\ &m_{N_3} = 10^{12}\,,\, 10^{13}\,,\, 10^{14}\,\mathrm{GeV}\,. \end{aligned} \tag{2.9}$$

Given that, as previously emphasised, $\mu \to e\,\gamma$ is very sensitive to θ_{13}, whereas this is not the case for $\mathrm{BR}(\tau \to \mu\,\gamma)$, and that both BRs display the same approximate behaviour with m_{N_3} and $\tan\beta$, we now propose to study the correlation between these two observables. This optimises the impact of a θ_{13} measurement, since it allows to minimise the uncertainty introduced from not knowing $\tan\beta$ and m_{N_3}, and at the same time offers a better illustration of the uncertainty associated with the R-matrix angles. In this case, the correlation of the BRs with respect to m_{N_3} means that, for a fixed set of parameters, varying m_{N_3} implies that the predicted point ($\mathrm{BR}(\tau \to \mu\,\gamma)$, $\mathrm{BR}(\mu \to e\,\gamma)$) moves along a line with approximately constant slope in the $\mathrm{BR}(\tau \to \mu\,\gamma)$-$\mathrm{BR}(\mu \to e\,\gamma)$ plane. On the other hand, varying θ_{13} leads to a displacement of the point along the vertical axis. In Fig. 2.15[8], we illustrate this correlation for SPS 1a, and for the previously selected m_{N_3} and $\theta_{1,2}$ ranges (c.f. Eq. (2.9)). We consider the following values, $\theta_{13} = 1^\circ$, 3°, 5° and 10°, and only include the BR predictions allowing for a favourable BAU. In addition, and as done throughout our analysis, we have verified that all the points in this figure lead to charged lepton EDM predictions which are compatible with present experimental bounds. More specifically, we have obtained values for the EDMs lying in the following ranges (in units of e.cm):

$$10^{-39} \lesssim |d_e| \lesssim 2\times10^{-35}\,,\, 6\times10^{-37} \lesssim |d_\mu| \lesssim 1.5\times10^{-32}\,,\, 10^{-34} \lesssim |d_\tau| \lesssim 4\times 10^{-31}\,. \tag{2.10}$$

For a fixed value of m_{N_3}, and for a given value of θ_{13}, the dispersion arising from a θ_1 and θ_2 variation produces a small area rather than a point in the $\mathrm{BR}(\tau \to \mu\,\gamma)$-$\mathrm{BR}(\mu \to e\,\gamma)$ plane. The dispersion along the $\mathrm{BR}(\tau \to \mu\,\gamma)$ axis is of approximately one order of magnitude for all θ_{13}. In contrast, the dispersion along the $\mathrm{BR}(\mu \to e\,\gamma)$ axis increases with decreasing θ_{13} (in agreement with the findings of Section 2.1.3), ranging from an order of magnitude for $\theta_{13} = 10^\circ$, to over three orders of magnitude for the case of small θ_{13} (1°). From Fig. 2.15 we can also infer that other choices of m_{N_3} (for $\theta_{13} \in [1^\circ, 10^\circ]$) would lead to BR predictions which would roughly lie within the diagonal lines depicted in the plot. Comparing these predictions for the shaded areas along the expected diagonal "corridor", with the allowed experimental region, allows to conclude about the impact of a θ_{13} measurement on the allowed/excluded m_{N_3} values.

[8] At the moment this plot was done the experimental upper bound for $\tau \to \mu\,\gamma$ was 6.8×10^{-8} [65], slightly different to the current bound 1.6×10^{-8} [68]

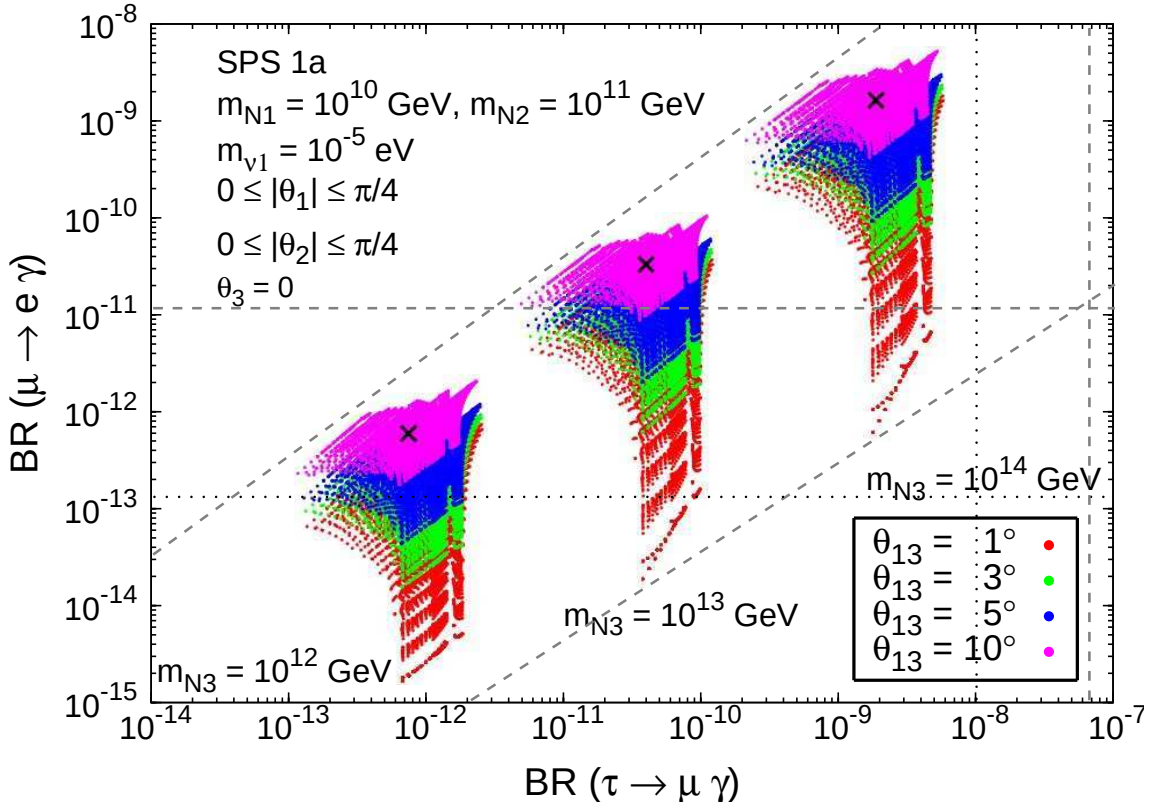

Figure 2.15: Correlation between BR($\mu \to e\,\gamma$) and BR($\tau \to \mu\,\gamma$) as a function of m_{N_3}, for SPS 1a. The areas displayed represent the scan over θ_i as given in Eq. (2.9). From bottom to top, the coloured regions correspond to $\theta_{13} = 1°$, $3°$, $5°$ and $10°$ (red, green, blue and pink, respectively). Horizontal and vertical dashed (dotted) lines denote the experimental bounds (future sensitivities).

The most important conclusion from Fig. 2.15 is that for SPS 1a, and for the parameter space defined in Eq. (2.9), an hypothetical θ_{13} measurement larger than $1°$, together with the present experimental bound on the BR($\mu \to e\,\gamma$), will have the impact of excluding values of $m_{N_3} \gtrsim 10^{14}$ GeV. This lends support to the hints already drawn from Fig. 2.13. Moreover, with the planned MEG sensitivity, the same θ_{13} measurement can further constrain $m_{N_3} \lesssim 3 \times 10^{12}$ GeV. The impact of any other θ_{13} measurement can be analogously extracted from Fig. 2.15.

Similar conclusions can be reached for the other SPS points, as seen in Fig. 2.16, where we only display the predictions corresponding to the point marked with a cross in the centre of the $\theta_{13} = 10°$ shaded area of Fig. 2.15 (taking into account all θ_{13} values would lead to replications of the shaded areas observed in Fig. 2.15). Regarding SPS 1b, the discussion is very similar to that of SPS 1a, and the inferred constrains on m_{N_3} are almost identical. SPS 2 and SPS 3 offer

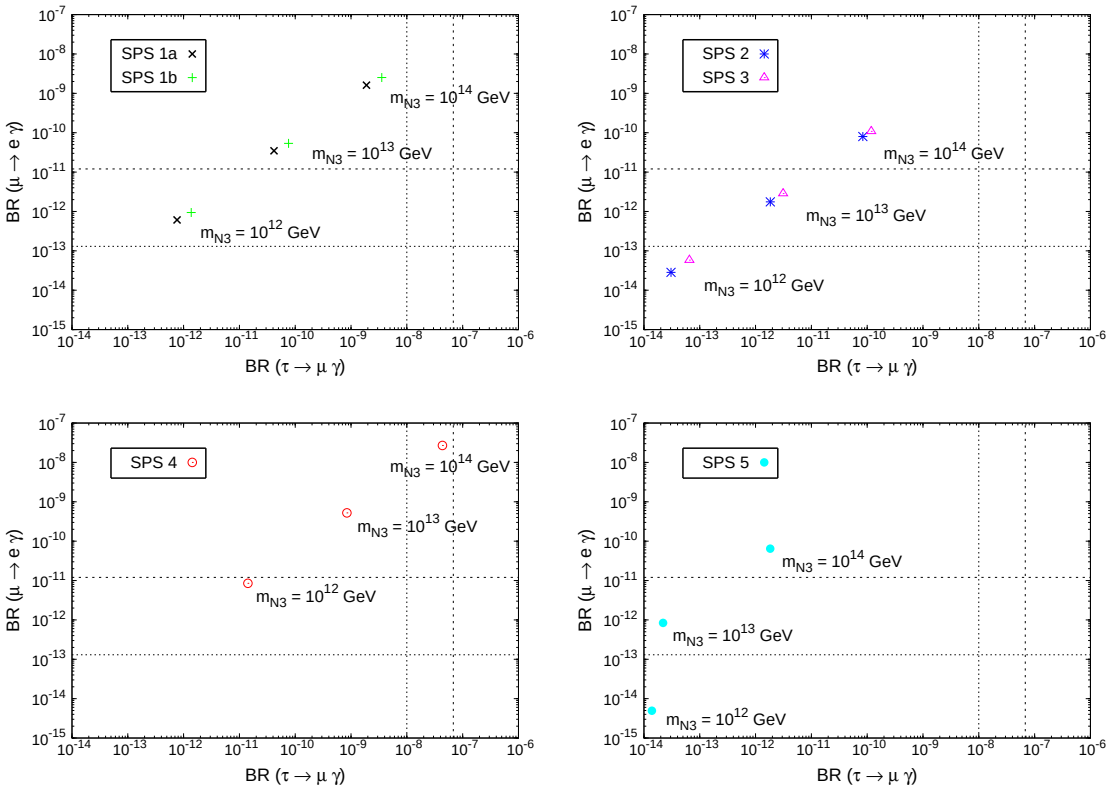

Figure 2.16: Correlation between BR($\mu \to e\,\gamma$) and BR($\tau \to \mu\,\gamma$) as a function of m_{N_3}. The points displayed mimic the behaviour of the central $\theta_{13} = 10°$ marked point in Fig. 2.15, for SPS points 1a, 1b, 2, 3, 4 and 5. Horizontal and vertical dashed (dotted) lines denote the experimental bounds (future sensitivities).

very close predictions, and when compared to SPS 1a, for the same θ_{13} measurement, allow to extract slightly weaker bounds on m_{N_3}. On the other hand, SPS 4 clearly provides the most stringent scenario and a measurement of $\theta_{13} = 10°$ is only compatible with $m_{N_3} \lesssim 10^{12}$ GeV. Notice also that this is the only case where the present experimental bound from BR($\tau \to \mu\,\gamma$) plays a relevant role. SPS 5 provides the weakest bounds on m_{N_3} but nevertheless still allows to exclude $m_{N_3} \gtrsim 10^{14}$ GeV from a measurement of $\theta_{13} = 10°$. Finally, it is interesting to notice that the observed correlations for SPS 5 are manifestly different from the other cases, in agreement with the findings of Section 2.1.3. In this case, varying m_{N_3} leads to predictions of the BR($\mu \to e\,\gamma$) and BR($\tau \to \mu\,\gamma$) which are not linearly correlated, opposed to what would be expected from the LLog approximation.

2.1.6 Summary

In this section, we have investigated lepton flavour violating radiative decays in the CMSSM extended by three right-handed (s)neutrinos, and used the seesaw mechanism to explain the smallness of the neutrino masses. We have parameterised the solutions to the seesaw equation in terms of a complex orthogonal matrix R and of the right-handed neutrino masses, requiring compatibility with low-energy data. We have considered scenarios of hierarchical light and heavy neutrinos. In addition, we imposed consistency with present bounds on charged lepton EDMs and baryogenesis via thermal leptogenesis taking into account constraints on the reheating temperature from non-thermal LSP production by gravitino decay. We have studied in great detail the sensitivity of the BRs of LFV radiative decays to θ_{13}, giving special emphasis to the $\mu \to e\,\gamma$ decay channel.

In a first stage, we have considered the simple case $R = \mathbb{1}$ where there are no additional neutrino mixings other than those in the $U_{\rm PMNS}$. We have found a very pronounced sensitivity to θ_{13} in the decay channels $\mu \to e\,\gamma$ and $\tau \to e\,\gamma$. Varying θ_{13} from 0° to 10°, the branching ratios for the above processes increase by several orders of magnitude. In view of the present experimental bounds and the expected future sensitivity, $\mu \to e\,\gamma$ is by far the most promising channel to study the sensitivity to θ_{13} in LFV processes. We have presented the predictions for the branching ratios for various SPS SUSY benchmark points. We further emphasised the importance of a full numerical computation, which we have found to differ significantly from the LLog approximation in some cases.

We have then explored how the sensitivity of BR($\mu \to e\,\gamma$) to θ_{13} is altered when we take into account the remaining SUSY-seesaw parameters. In this sense, we have found that the most relevant parameters are θ_1, θ_2, m_{N_3} and $\tan\beta$ and we have systematically studied their influence on the impact of θ_{13} on BR($\mu \to e\,\gamma$). We have also noticed that the sensitivity to θ_{13} improves for lower values of m_{ν_1} ($m_{\nu_1} \lesssim 10^{-3}$ eV). Compared to the special case $R = \mathbb{1}$, non-vanishing θ_i can have important consequences. In particular, the sensitivity to θ_{13} is considerably reduced for large values of $|\theta_1|$ and $|\theta_2|$. Generically, the separation between the BR predictions for distinct θ_{13} is reduced when we move from $R = \mathbb{1}$ to $R \neq \mathbb{1}$, and one could be led to the conclusion that the BR sensitivity to θ_{13} would be reduced. However, we have also found cases of $R \neq \mathbb{1}$ where, although this separation is reduced, the BR predictions are now larger (and can be above the experimental bounds) and different θ_{13} values can be distinguished even more efficiently than in the $R = \mathbb{1}$ case.

Regarding the right-handed neutrino masses, the most relevant one for the LFV BRs is clearly m_{N_3} (with a marginal role being played by m_{N_2}). Even though m_{N_1} does not directly affect the BRs, it nevertheless plays a relevant role with respect to baryogenesis. This, together with the assumption of hierarchical right-handed neutrinos, leads furthermore to an indirect

lower bound for m_{N_3}. For a given choice of θ_{13}, the dependence on m_{N_3} is so pronounced that for the investigated range $[10^{11}\,\text{GeV}, 10^{15}\,\text{GeV}]$, the BRs change by over six orders of magnitude. Thus, and even though the sensitivity to θ_{13} is clearly manifest (for instance, more than two orders of magnitude separation between the BR predictions of $\theta_{13} = 1^\circ$ and 5°, for a given value of θ_2) without additional knowledge of m_{N_3} it will be very difficult to disentangle the several θ_{13} cases.

In a similar fashion, the sensitivity of the BRs to θ_{13} can be altered by the uncertainty introduced from the indetermination of $\tan\beta$. The study of the generalised SPS points shows that changing $\tan\beta$ from 5 to 50 translates in $\text{BR}(\mu \to e\,\gamma)$ predictions which differ by two orders of magnitude, so that unless there is an experimental determination of $\tan\beta$, it will also be hard to distinguish the distinct θ_{13} predictions. Moreover, we have emphasised that this strong dependence on m_{N_3} and $\tan\beta$ can be constructively used as a means of extracting information on these parameters from a potential joint measurement of θ_{13} and $\text{BR}(\mu \to e\,\gamma)$.

Remarkably, within a particular SUSY scenario and scanning over specific θ_1 and θ_2 ranges for various values of θ_{13}, the comparison of the theoretical predictions for $\text{BR}(\mu \to e\,\gamma)$ and $\text{BR}(\tau \to \mu\,\gamma)$ with the present experimental bounds allows to set θ_{13}-dependent upper bounds on m_{N_3}. Together with the indirect lower bound arising from leptogenesis considerations, this clearly provides interesting hints on the value of the seesaw parameter m_{N_3}. For instance, in the SUSY scenario SPS1a and for values of θ_{13} in the present experimental allowed range, the present MEGA constraint on $\text{BR}(\mu \to e\gamma)$ already sets an upper bound on m_{N_3}, $m_{N_3} \lesssim 10^{13}$ GeV for $\theta_{13} \gtrsim 10^\circ$ and $m_{N_3} \lesssim 6 \times 10^{13}$ GeV for $\theta_{13} \gtrsim 3^\circ$, as inferred from Fig. 2.15. These bounds are even more stringent for the case of SPS4 (see Fig. 2.16) where the present contraint on $\text{BR}(\mu \to e\gamma)$ sets an upper bound of $m_{N_3} \lesssim 3 \times 10^{12}$ GeV for $\theta_{13} \gtrsim 10^\circ$ and $m_{N_3} \lesssim 10^{13}$ GeV for $\theta_{13} \gtrsim 3^\circ$. With the planned future sensitivities, these bounds would further improve by approximately one order of magnitude.

2.2 LFV Higgs decays

We are interested now in the LFV Higgs boson Decays (LFVHD), $H \to \tau\bar{\mu}$, $\tau\bar{e}$, $\mu\bar{e}$ (and obviously their CP conjugates), and the branching ratios that can be generated in the context of the CMSSM-seesaw models with parameters being compatible with the neutrino data and the most relevant data of τ and μ radiative decays.

Concretely, we will study $h^0, H^0, A^0 \to l_j \bar{l}_i$ decays, with $j \neq l$. The subject of LFVHD being generated from loops of SUSY particles has been considered previously in [188] and [56]. In [188] it was analyzed a specific SUSY-SU(5) scenario where the slepton-lepton misalignment was generated exclusively from the running of the trilinear A-terms. On the other hand, the

computation of [56] was not in the context of the MSSM-seesaw but in a more generic scenario for slepton-lepton misalignement. Besides, in [56], the effective lagrangian approach that is valid for large $\tan\beta$ values and large SUSY mass values is used. We present here instead, a complete one-loop computation in the SUSY-seesaw context and do not rely on any of the above approximations, that is we do not use either the MI approximation or the large $\tan\beta$ effective lagrangian approach and, therefore, our results are valid for all $\tan\beta$ values and all soft-SUSY-breaking mass values.

We will explore here the size of the branching ratios for the Higgs decays as a function of the relevant SUSY parameters, which within the context of CMSSM are M_0, $M_{1/2}$, A_0 and $\tan\beta$, and of the relevant seesaw parameters, which are m_{N_i} and the R matrix. For comparison, we will analyse in parallel the branching ratios for the $l_j \to l_i\gamma$ decays as a function of the same parameters. The requirement of compatibility with the present data on $l_j \to l_i\gamma$ decays, mainly $\mu \to e\,\gamma$ and $\tau \to \mu\,\gamma$, will provide us with the maximum allowed ratios for the Higgs decays. We will also study the behaviour of the LFVHD widths in the limit of very heavy SUSY masses and will find that the sleptons, sneutrinos, charginos and neutralinos do not decouple in this observables. For large SUSY masses, large $\tan\beta$ and particular choices of the seesaw parameters we will find agreement with the numerical results of [56].

2.2.1 Analytical results for LFVHD

The contributions to the LFVHD rates in the constrained SUSY-seesaw scenarios come from various sectors. The contributions from the charged Higgs sector and from the SM sector (i.e, $H^\pm$, $W^\pm$ and $G^\pm$) are kwonw to be very small [101] and will not be included here. The main contributions come from the genuine SUSY sector, concretely, from the one-loop diagrams with charginos, neutralinos, sleptons and sneutrinos shown in Fig. B.3, that we number for calculation purposes in the first row from 1 to 4 and in the second row from 5 to 8.

After the computation of the eight contributing one-loop diagrams, drawn in Fig. B.3, we find the analytical results presented in Appendix B which have been written in terms of the standard one-loop integrals, $C_0, B_0, C_{12}, ...$ etc, whose definitions can be found for instance in [189]. These provide the total contributions to the relevant form factors H_L and H_R that are related to the decay amplitude for $H \to l_j\bar{l}_i$ by

$$T_{\rm LFVHD} = \bar{u}_{l_j}(H_L P_L + H_R P_R) v_{l_i}\,. \tag{2.11}$$

The contributions of these one-loop diagrams to the form factors are given by

$$H^{(p)}_{L(R)} = H^{(p)}_{L(R),n} + H^{(p)}_{L(R),c} \tag{2.12}$$

with $p = 1, 2, 3$ for $H_p = (h^0, H^0, A^0)$. Here $H^{(p)}_{L(R),n}$ and $H^{(p)}_{L(R),c}$ are the the contributions of neutralino and chargino loops, respectively, given in Appendix B. The values of the involved couplings are given in Appendix A and the loop functions in Appendix C.

The LFVHD widths can be obtained finally from these form factors by

$$\begin{aligned}\Gamma(H_p \to l_j \bar{l}_i) &= \frac{1}{16\pi m_{H_p}} \sqrt{\left(1 - \left(\frac{m_{l_j} + m_{l_i}}{m_{H_p}}\right)^2\right)\left(1 - \left(\frac{m_{l_j} - m_{l_i}}{m_{H_p}}\right)^2\right)} \\ &\times \left((m_H^2 - m_{l_j}^2 - m_{l_i}^2)(|H_L|^2 + |H_R|^2) - 4 m_{l_j} m_{l_i} \mathrm{Re}\,(H_L H_R^*)\right) . \quad (2.13)\end{aligned}$$

Notice that since we will consider complex R matrices, the corresponding decay widths for the CP conjugate states, in general, can be different. We do not study here these CP conjugate decays and concentrate on the $H_p \to \tau\bar{\mu}, \tau\bar{e}, \mu\bar{e}$ decays, with $p = 1, 2, 3$.

2.2.2 Numerical results and discussion

We show from Figs. 2.17 to 2.20 the numerical results of the branching ratios for the LFVHD in the CMSSM-seesaw scenario. We have shown in the plots just the dominant channels, which are $H_x \to \tau\bar{\mu}$, and some comments will be added on the other channels. Similarly, for the comparison with the leptonic radiative decays, $l_j \to l_i\gamma$, we will show in the plots the most relevant one, which is $\mu \to e\,\gamma$ or $\tau \to \mu\,\gamma$, depending on the case.

The results of the branching ratios for the LFVHD, in the $\tau\bar{\mu}$ channel, as a function of the Majorana mass, m_N, with degenerate heavy neutrinos and real R, are illustrated in Fig. 2.17, for several $\tan\beta$ values, $\tan\beta = 3, 10, 30, 50$. The explored range in m_N is from 10^8 GeV up to 10^{14} GeV. We also show in this figure, the corresponding predicted rates for the most relevant lepton decay, which in this case is $\mu \to e\,\gamma$, and include its upper experimental bound. We have checked that the other channels are well within their experimental allowed range. From this figure we first see that the branching ratios for the light Higgs boson are smaller than the heavy Higgs ones in about two orders of magnitude. The ratios of H^0 and A^0 are very similar in all the plots and, for this scenario, they can reach values up to just 2.2×10^{-10} in the region of high $\tan\beta$ and high m_N. Besides, the rates for $\mu \to e\,\gamma$ decays are below the upper experimental bound for all explored $\tan\beta$ and m_N values. From these plots we also see clearly the high sensitivity to $\tan\beta$ of the LFVHD rates for all Higgs bosons which, at large $\tan\beta$, scale roughly as $(\tan\beta)^4$, in comparison with the LFV radiative decay rates which scale as $(\tan\beta)^2$. The dependence of both rates on m_N is that induced from the δ_{ij} dependence, and corresponds approximately to what is expected from the MI and LLog approximations, where $\mathrm{BR}(H_x \to l_j\bar{l}_i)$, $\mathrm{BR}(l_j \to l_i\gamma) \propto |\delta_{ij}|^2 \propto |m_N \log(m_N)|^2$.

In what regards to the relative importance of the various SUSY sectors to the LFVHD rates,

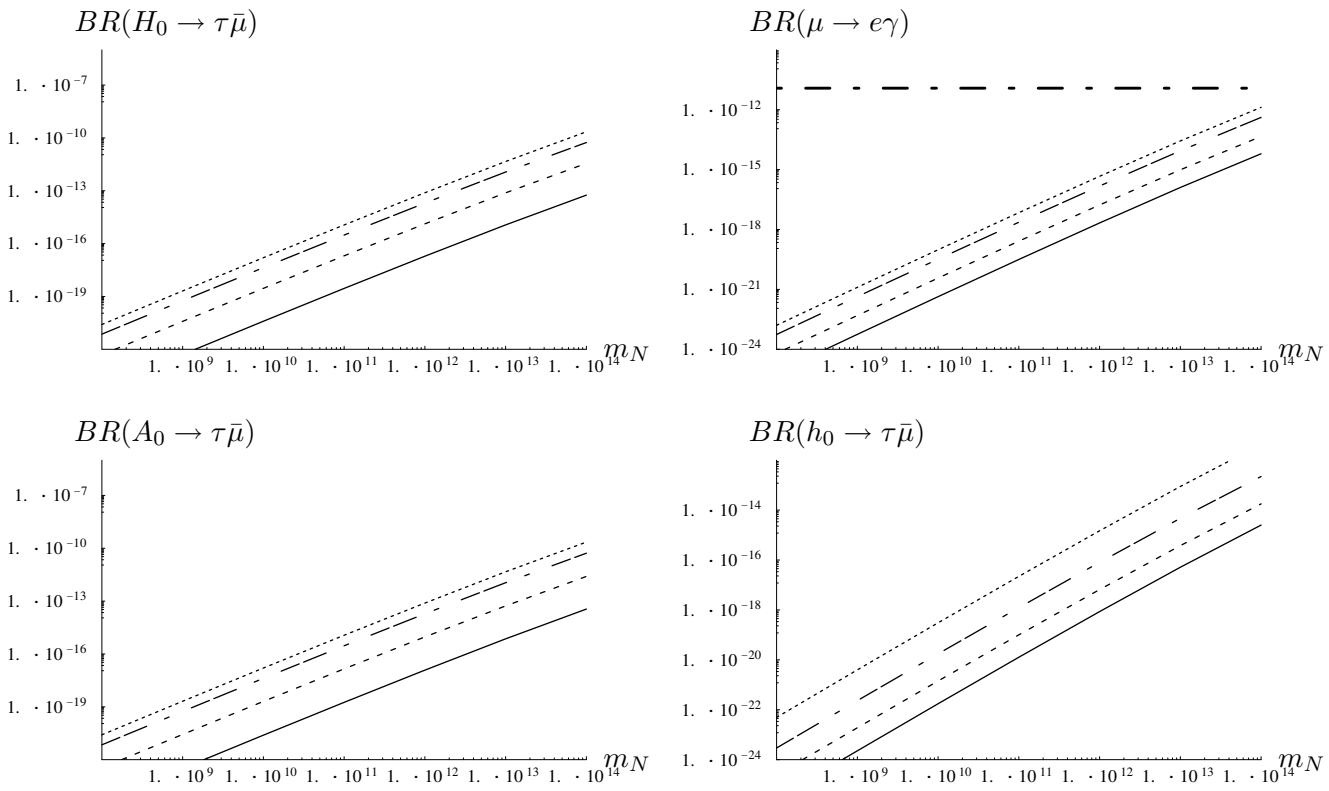

Figure 2.17: Dependence of BR($H_x \to \tau\bar{\mu}$) on m_N (GeV), with degenerate heavy neutrinos and real R, for several values of $\tan\beta$. **(a)** Upper-left panel, $H_x = H^0$, **(c)** lower-left panel, $H_x = A^0$ and **(d)** lower-right panel, $H_x = h^0$. **(b)** Upper-right panel: Dependence of BR($\mu \to e\,\gamma$) with m_N for several values of $\tan\beta$. In all plots, the solid, dashed, dashed-dotted and dotted lines are the preditions for $\tan\beta = 3, 10, 30$ and 50, respectively. The horizontal line in (b) is the upper experimental bound on BR($\mu \to e\,\gamma$). The other input parameters are, $M_0 = 400$ GeV $M_{1/2} = 300$ GeV, $A_0 = 0$ and sign(μ) > 0.

we have found that these are dominated by the chargino contributions, that is from the loop diagrams (1),(2),(3) and (4) in Fig. B.3. For instance, for $m_N = 10^{14}$ GeV , $M_0 = 400$ GeV, and $M_{1/2} = 300$ GeV, we have found the following ratios between the chargino and neutralino contributions to the H^0 form factors: $|H_L^{\tilde{\chi}^-}/H_L^{\tilde{\chi}^0}| = 6.1,\ 6,\ 7.3,\ 23.1$ for $\tan\beta = 3,\ 10,\ 30,\ 50$ respectively, where we have used a simplified notation, $H_L^{\tilde{\chi}^-} = H_{L,H^0}^{(2)} + H_{L,H^0}^{(4)} + H_{L,H^0}^{(6)} + H_{L,H^0}^{(8)}$, $H_L^{\tilde{\chi}^0} = H_{L,H^0}^{(1)} + H_{L,H^0}^{(3)} + H_{L,H^0}^{(5)} + H_{L,H^0}^{(7)}$ where the superscript refers to the corresponding diagram. Similar $\tilde{\chi}^-/\tilde{\chi}^0$ ratios are found for the corresponding H_R form factors. The relative ratio found of $H_L/H_R \simeq 17$ is nicely explained by the m_τ/m_μ ratio. For the lightest Higgs boson, we find $|H_L^{\tilde{\chi}^-}/H_L^{\tilde{\chi}^0}| = 1.5,\ 1.4,\ 1.7,\ 4$, correspondingly.

Concerning to the comparative size of the contributions from the various chargino loop diagrams we have found that, at large $\tan\beta$, the external leg corrections are clearly the dominant ones. Concretely, for $|(H^{(6)}_{L,H^0} + H^{(8)}_{L,H^0})/H^{\tilde{\chi}^-}_L|$, $|H^{(2)}_{L,H^0}/H^{\tilde{\chi}^-}_L|$ and $|H^{(4)}_{L,H^0}/H^{\tilde{\chi}^-}_L|$, we get the respective percentages, 60.6%, 39.3% and 0.1%, for $\tan\beta = 10$ and 93.8%, 6.2%, 0% for $\tan\beta = 50$.

The branching ratios for the Higgs boson decays into $\tau\bar{e}$ and $\mu\bar{e}$ are much smaller than the $\tau\bar{\mu}$ ones, as expected, and we do not show plots for them. For instance, for $m_N = 10^{14}$ GeV, and $\tan\beta = 50$ we find $\mathrm{BR}(H^{(x)} \to \tau\bar{\mu})/BR(H^{(x)} \to \tau\bar{e}) = 3.9 \times 10^3$ and $\mathrm{BR}(H^{(x)} \to \tau\bar{\mu})/BR(H^{(x)} \to \mu\bar{e}) = 1.3 \times 10^6$ for the three Higgs bosons.

All the previous results are for fixed $M_0 = 400$ GeV and $M_{1/2} = 300$ GeV. The dependence with M_0 and $M_{1/2}$ will be discussed later on within the context of hierarchical neutrinos.

In summary, the LFVHD rates for degenerate heavy neutrinos are very small, at most 2.2×10^{-10}, for the explored range of the seesaw parameters and $\tan\beta$. Obviously, larger values of these LFVHD ratios could be obtained for larger $\tan\beta$ values, but we have not considered them here.

We next present the results for hierarchical neutrinos. The results for real and complex R and for the mass hierarchy $(m_{N_1}, m_{N_2}, m_{N_3}) = (10^8, 2 \times 10^8, 10^{14})$ GeV, are shown in Figs. 2.18 and 2.19, respectively. From these figures we first confirm that the LFVHD and LFV radiative decay rates are larger in this case than for degenerate heavy neutrinos. In the following we study the restrictions on the maximum allowed Higgs decay rates coming from the experimental LFV radiative decay bounds, in the case of hierarchical neutrinos.

For instance, the case of real θ_1, that is illustrated in Figs. (2.18a) and (2.18b) for $\tan\beta = 50$, $M_0 = 400$ GeV and $M_{1/2} = 300$ GeV, shows that compatibility with $\mu \to e\,\gamma$ data occurs only in the very narrow dips at around $\theta_1 = 0$, 1.9 and π. The presence of these narrow regions where the $\mu \to e\,\gamma$ rates are drastically suppresed were already pointed out in [114] and commented in Section 2.1 and correspond clearly to the minima of $|\delta_{12}|$ in Fig. (1.1c). Notice that it is precisely at the points $\theta_1 = 0, \pi$ where the $\mathrm{BR}(H^0, A^0 \to \tau\bar{\mu})$ rates reach their maximum values, although these are not large, just about 1.3×10^{-8}. Notice also, that these maxima correspond clearly to the maxima of $|\delta_{23}|$ in Fig. (1.1c). We have checked that for lower $\tan\beta$ values, the allowed regions in θ_1 widen and are placed at the same points, but the corresponding maximum values of the LFVHD rates get considerably reduced. The alternative case of real $\theta_2 \neq 0$, with $\theta_1 = \theta_3 = 0$ is illustrated in Figs. (2.18c) and (2.18d). We see that the behaviour of $\mathrm{BR}(H_x \to \tau\bar{\mu})$ with θ_2 is very similar to that with θ_1 of Fig. (2.18a) and the maximum values of about 1.3×10^{-8} are now placed at $\theta_2 = 0, \pi$. $\mathrm{BR}(\mu \to e\,\gamma)$ also reaches its maximum at $\theta_2 = 0, \pi$, but it is still well below the experimental bound. In particular, for $\tan\beta = 50$, $M_0 = 400$ GeV and $M_{1/2} = 300$ GeV this maximum value is 3×10^{-12}. Notice, that the behaviour with θ_2 is explained once again

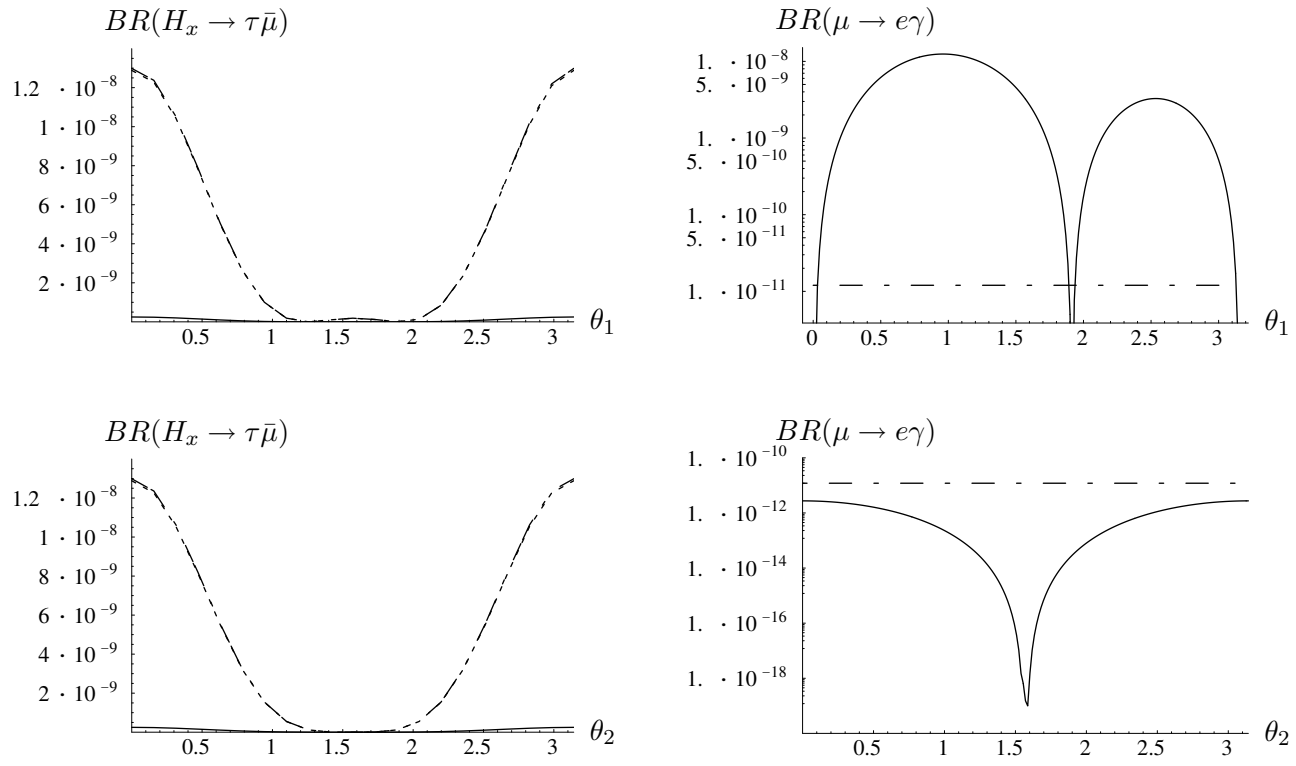

Figure 2.18: **(a)** Left panel: Dependence of BR($H_x \to \tau\bar{\mu}$) with θ_1. Solid, dashed and dashed-dotted lines (the two later undistinguishible here) correspond to $H_x = (h^0, H^0, A^0)$ respectively. **(b)** Right panel: Dependence of BR($\mu \to e\,\gamma$) with θ_1. The horizontal dashed-dotted line is the upper experimental bound. Both panels are for hierarchical neutrinos and for real $\theta_1 \neq 0$, $(m_{N_1}, m_{N_2}, m_{N_3}) = (10^8, 2 \times 10^8, 10^{14})$ GeV, $\theta_2 = \theta_3 = 0$, $\tan\beta = 50$, $M_0 = 400$ GeV, $M_{1/2} = 300$ GeV, $A_0 = 0$ and sign(μ) > 0, that corresponds to SPS 4. **(c)**, lower left panel, and **(d)**, lower right panel, are as in (a) and (b) respectively, but for $\theta_2 \neq 0$ and $\theta_1 = \theta_3 = 0$

in terms of the corresponding δ_{ij} behaviour. Regarding the dependence with θ_3, not shown in the plots, a different situation is found, where BR($H_x \to \tau\bar{\mu}$) is approximately constant, and for the heavy Higgs bosons it is around 1.3×10^{-8}. BR($\mu \to e\,\gamma$), BR($\tau \to \mu\,\gamma$) and BR($\tau \to e\,\gamma$) are also approximately constant with θ_3. In addition, we have checked that these three leptonic constant decay rates are within the experimental allowed range. In summary, for real R we find that the maximum allowed LFVHD rates are at or below 1.3×10^{-8}.

The case of complex R is certainly more promising. The examples shown in Figs. (2.19a) and (2.19c) are for the most favourable case, among the ones studied here, of complex $\theta_2 \neq 0$ with $\theta_1 = \theta_3 = 0$. It shows that considerably larger BR($H_x \to \tau\bar{\mu}$) rates than in the real R

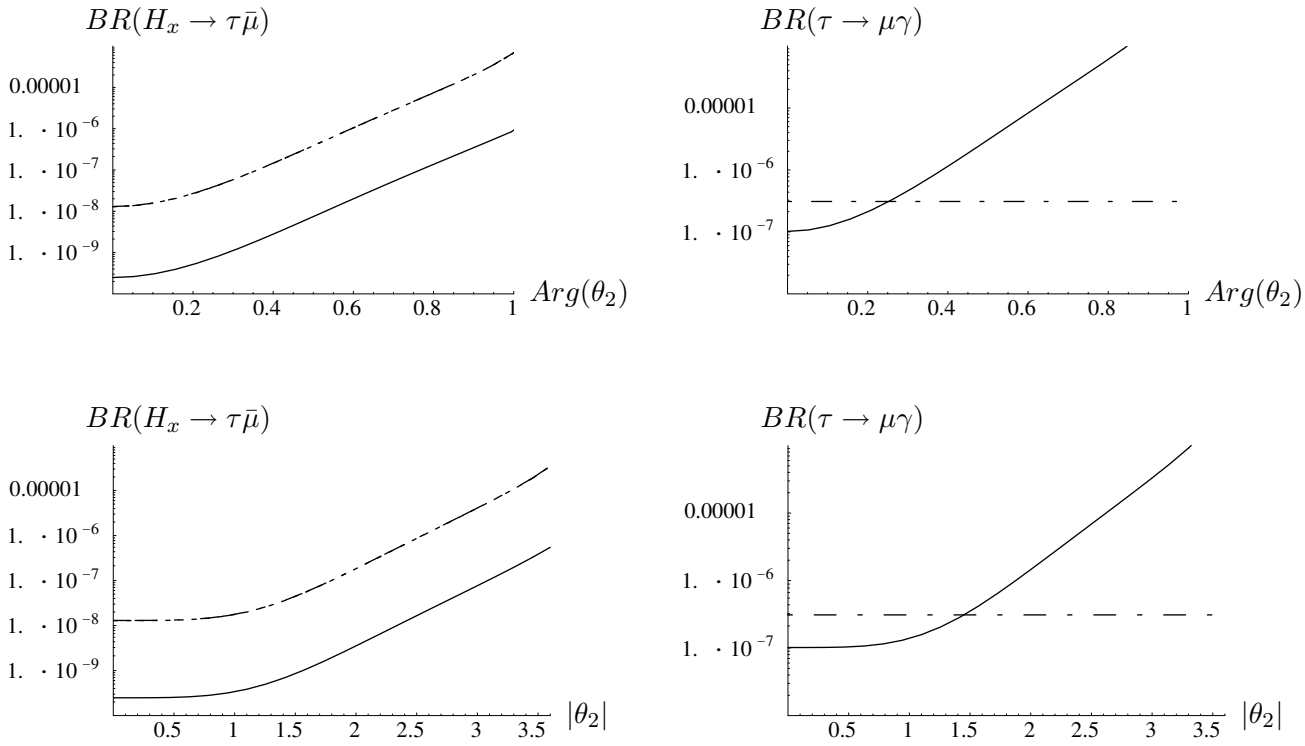

Figure 2.19: **(a)** Upper-left panel: Dependence of BR($H_x \to \tau\bar{\mu}$) on argθ_2 for $|\theta_2| = \pi$. **(b)** Upper-right panel: Dependence of BR($\tau \to \mu\,\gamma$) onarg θ_2 for $|\theta_2| = \pi$. **(c)** Lower-left panel: Dependence of BR($H_x \to \tau\bar{\mu}$) on $|\theta_2|$ forarg $\theta_2 = \pi/4$. **(d)** Lower-right panel: Dependence of BR($\tau \to \mu\,\gamma$) on $|\theta_2|$ for arg$\theta_2 = \pi/4$. All figures are for hierarchical neutrinos and complex θ_2 and $\theta_1 = \theta_3 = 0$. The rest of parameters are fixed to: $(m_{N_1}, m_{N_2}, m_{N_3}) = (10^8, 2\times 10^8, 10^{14})$ GeV, $\tan\beta = 50$, $M_0 = 400$ GeV and $M_{1/2} = 300$ GeV. Solid, dashed and dashed-dotted (the two later undistinguishible here) lines in the left panels correspond to $H_x = (h^0, H^0, A^0)$ respectively. The horizontal line in the right panels is the experimental upper bound on $\tau \to \mu\,\gamma$. At present this bound has been improved as summarised in Table 2.1.

case are found. For the explored θ_2 values in these plots, the Higgs rates grow with both $|\theta_2|$ andarg θ_2 and, for the selected values of the parameters in this figure, they reach values up to around 5×10^{-5}. We have checked that the predicted rates for BR($\tau \to e\gamma$) are well below the experimental upper bound and that the $\mu \to e\,\gamma$ decay is, in this case, less restrictive than the $\tau \to \mu\,\gamma$ decay. Notice that the smallness of the $\mu \to e\,\gamma$ and $\tau \to e\,\gamma$ decay rates, in the case under study of $\theta_2 \neq 0$, is not maintained if our hypothesis on $\theta_{13} = 0$ is changed. For instance, for $\theta_{13} = 5^o$, which is also allowed by neutrino data, we get BR($\mu \to e\,\gamma$) $\sim 2.4\times 10^{-8}$, for $\theta_2 = \pi e^{i\frac{\pi}{10}}$, well above the experimental upper bound. This is why we keep $\theta_{13} = 0$ in all this

section. Therefore, in this case of complex $\theta_2 \neq 0$ with $\theta_{13} = 0$, the relevant LFV radiative decay is $\tau \to \mu\,\gamma$ which is illustrated in Figs. (2.19b) and (2.19d) together with its experimental bound. We see that the allowed region by $\tau \to \mu\,\gamma$ data of the $(|\theta_2|, \arg\theta_2)$ parameter space implies a reduction in the Higgs rates, leading to a maximum allowed value of just 5×10^{-8}.

These results are for fixed values of $(m_{N_1}, m_{N_2}, m_{N_3}) = (10^8, 2 \times 10^8, 10^{14})$ GeV and for the SPS 4 input parameters, namely, $\tan\beta = 50$, $M_0 = 400$ GeV, $M_{1/2} = 300$ GeV, $A_0 = 0$ and $\text{sign}(\mu) > 0$. We have found that other choices of the soft-SUSY breaking mass parameters, M_0 and $M_{1/2}$, are more efficient in order to get larger maximum allowed Higgs ratios. For instance, for $M_0 = M_{1/2} = 1200$ GeV, we find maximum allowed values of around 5.6×10^{-6}. The reason for this improvement is the different behaviour with these parameters of the LFVHD and the lepton decay rates, which will be studied in more detail next.

In Fig. 2.20 we show the dependence of $\text{BR}(H^0 \to \tau\bar{\mu})$ and $\text{BR}(\tau \to \mu\gamma)$ with M_0 and $M_{1/2}$ for hierarchical neutrinos with $(m_{N_1}, m_{N_2}, m_{N_3}) = (10^8, 2 \times 10^8, 10^{14})$ GeV and fixed values of $\tan\beta = 50$, $\theta_2 \neq 0$, and $\theta_1 = \theta_3 = 0$. We see clearly in these plots the different behaviour of these two observables with the soft SUSY breaking mass parameters. Figs. (2.20a) and (2.20c) show a milder depencence of $\text{BR}(H^0 \to \tau\bar{\mu})$ on M_0 and $M_{1/2}$ than that of $\text{BR}(\tau \to \mu\,\gamma)$ in Figs. (2.20b) and (2.20d), respectively. This implies that for large enough values of M_0 or $M_{1/2}$ or both the $\text{BR}(\tau \to \mu\,\gamma)$ rates get considerably suppresed, due to the decoupling of the heavy SUSY particles in the loops, and enter into the allowed region by data, whereas the $\text{BR}(H^0 \to \tau\bar{\mu})$ rates are not much reduced. In fact, we see in Figs. (2.20e) and (2.20f) that for the choice $M_0 = M_{1/2}$ the τ decay ratio crosses down the upper experimental bound at around $M_0 = 1200$ GeV whereas the Higgs decay ratio is still quite large $\sim 6 \times 10^{-6}$ in the high M_0 region, around $M_0 \simeq 2000$ GeV. This behaviour with the soft-SUSY breaking parameters is a clear indication that the heavy SUSY particles in the loops do not decouple in the LFVHD, in much the same way as it has been shown to happen in the case of Higgs decays into quarks with change of flavour [190]. Notice that the non-decoupling of the SUSY particles in the LFVHD is a consequence of the non-decoupling in the effective $H^{(x)}\tau\mu$ couplings and these in turn can induce large contributions to other LFV processes that are mediated by Higgs exchange as, for instance, $\tau \to 3\,\mu$ [53], some LFV semileptonic τ decays and $\mu - e$ conversion in nuclei. These Higgs-mediated LFV processes will be analysed later on.

2.2.3 Non-decoupling behaviour of SUSY particles in LFVHD

In order to explore numerically the non-decoupling behaviour of the SUSY particles in the contributing loops to the LFVHD we consider, instead of CMSSM, a simpler and more generic MSSM scenario, with the δ_{ij} being free parameters, which we now fix to some particular values, concretely $\delta_{32} = -0.4$, and $\delta_{21} = \delta_{31} = 0$. For simplicity, we also assume a common SUSY

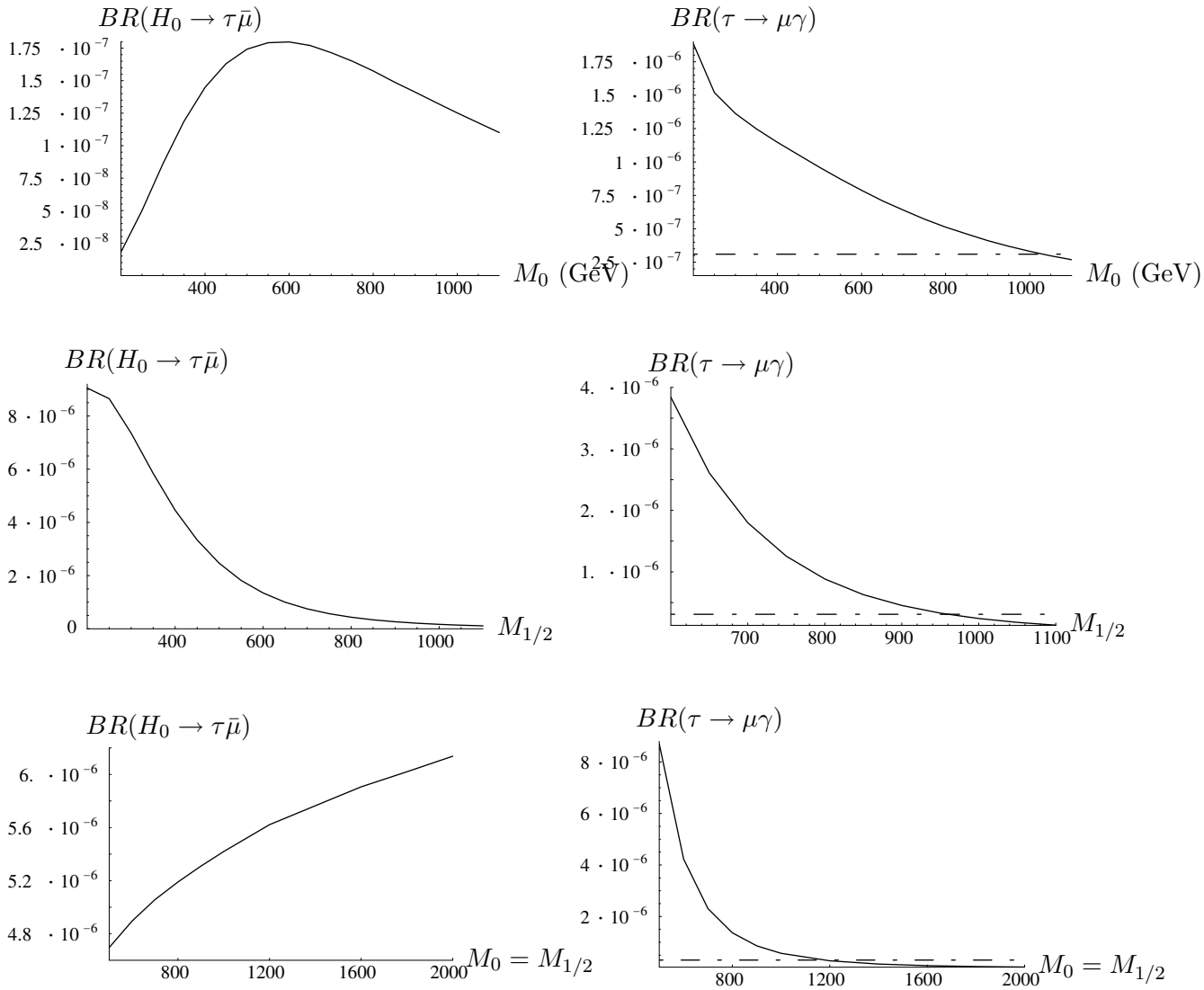

Figure 2.20: Dependence on M_0 (GeV) and $M_{1/2}$ (GeV) with $(m_{N_1}, m_{N_2}, m_{N_3}) = (10^8, 2 \times 10^8, 10^{14})$ GeV, $\theta_1 = \theta_3 = 0$ and $\tan\beta = 50$. **(a)** Upper left panel: Behaviour of BR$(H^0 \to \tau\bar{\mu})$ with $M_0(GeV)$ for $M_{1/2} = 300$ GeV and $\theta_2 = \pi e^{0.4i}$. **(b)** Upper right panel: Same as (9a) but for BR$(\tau \to \mu\,\gamma)$. **(c)** Medium left panel: Behaviour of BR$(H^0 \to \tau\bar{\mu})$ with $M_{1/2}(GeV)$ for $M_0 = 400$ GeV and $\theta_2 = \pi e^{0.8i}$. **(d)** Medium right panel: Same as (9c) but for BR$(\tau \to \mu\,\gamma)$. **(e)** Lower left panel: Behaviour of BR$(H^0 \to \tau\bar{\mu})$ with $M_0 = M_{1/2}(GeV)$ for $\theta_2 = \pi e^{0.8i}$. **(f)** Lower right panel: Same as (9e) but for BR$(\tau \to \mu\,\gamma)$. The horizontal line in the right panels is the upper experimental bound on BR$(\tau \to \mu\,\gamma)$. At present this bound has been improved as summarised in Table 2.1.

mass at the electroweak scale, $M_{\rm SUSY} \equiv m_{\tilde{L},l} = m_{\tilde{E},l} = M_0 = \mu$ and choose $M_2 = \frac{2}{3}\mu$, $M_1 = \frac{5}{3}\tan^2\theta_W M_2$. This particular value of δ_{32} corresponds roughly to the predicted δ_{32} in the MSSM-seesaw with the parameters set in Fig. (2.20e). Finally, the BR($H^0 \to \tau\bar{\mu}$) is shown in Fig. 2.21 as a function of this common $M_{\rm SUSY}$ scale, for $\tan\beta = 50$ and $m_{H^0} = 340$ GeV. We see clearly that for large $M_{\rm SUSY}$ the branching ratio approaches to a constant non-vanishing value, which for these input parameter values is of about 10^{-5}, and therefore the charginos, neutralinos, charged sleptons and sneutrinos do not decouple in this observable.

Finally, the mathematical demonstration of a non-decoupling behaviour of the SUSY particles relies in the analytical computation of the one-loop $H\tau\mu$ vertex for asymptotically large SUSY masses. We have performed this computation in the simplest case where all the SUSY masses are equal and got the following asymptotic limits for the dominant form factor H_L, in the regime of small δ_{32} and large $\tan\beta$:

$$H_{L,c}^{(A^0)} = iH_{L,c}^{(H^0)} = i\,\frac{g^3}{16\pi^2}\,\frac{m_\tau}{12 m_W}\,\delta_{32}\,\tan^2\beta\,, \tag{2.14}$$

$$H_{L,n}^{(A^0)} = iH_{L,n}^{(H^0)} = i\,\frac{g^3}{16\pi^2}\,\frac{m_\tau}{24 m_W}\,(1-3\tan^2\theta_W)\,\delta_{32}\,\tan^2\beta\,. \tag{2.15}$$

The fact that these form factors tend to a constant at infinitely large $M_{\rm SUSY}$ shows clearly the non-decoupling of the SUSY particles. Similar simple results are found for the relevant form factors in the other LFV leptonic decays.

From these simple expressions we can estimate quite easily the LFVHD ratios. For instance, for the parameters chosen in Fig. 2.21, we get BR($H^0 \to \tau\bar{\mu}$) $\simeq 3\times 10^{-6}$ in reasonable agreement with our numerical result in this figure and in Fig. (2.20e). Notice also that this asymptotic result agrees with the result from the effective lagrangian approach in [56]. Finally, it is worth mentioning that this non-decoupling behaviour is in contrast with the behaviour of BR($\mu \to e\,\gamma$), which scales as $(M_W/M_{\rm SUSY})^4$, and explains the comparatively large LFVHD rates found here.

2.2.4 Summary

In this section we have studied in full detail the lepton flavour violating Higgs boson decays within the CMSSM-seesaw scenario. We find that the largest ratios are for $H_0 \to \tau\bar{\mu}$ and $A_0 \to \tau\bar{\mu}$ decays with similar rates. After exploring the dependence of the $H_0 \to \tau\bar{\mu}$ decay rates with all the involved parameters of the CMSSM-seesaw scenario, and by requiring compatibility with data of the correlated predictions for $\mu \to e\gamma$, $\tau \to e\gamma$ and $\tau \to \mu\gamma$ decays, we find that $BR(H_0 \to \tau\bar{\mu})$ as large as 10^{-5}, for hierarchical neutrinos and large $M_{\rm SUSY}$ can be reached. These ratios are mostly sensitive to $\tan\beta$, the heaviest neutrino mass m_{N_3} and the complex angle θ_2, which have been taken in the range $3 < \tan\beta < 50$, $10^8\,{\rm GeV} < m_{N_3} < 10^{14}\,{\rm GeV}$ and $(|\theta_2|, \arg\theta_2) \leq (3.5, 1)$ respectively. The largest allowed ratios found in this work of about

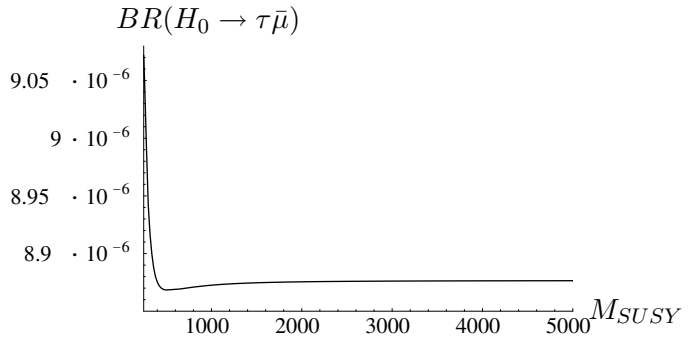

Figure 2.21: Behaviour of $H^0 \to \tau\bar{\mu}$ in a generic MSSM scenario as a function of the common SUSY mass, $M_{\rm SUSY}({\rm GeV}) \equiv m_{\tilde{L},l} = m_{\tilde{E},l} = M_0 = \mu$. The gaugino soft masses are set to $M_2 = 2/3\,\mu$ and $M_1 = \frac{5}{3}\tan^2\theta_W M_2$. Here we fix $\delta_{32} = -0.4$, $\delta_{21} = \delta_{31} = 0$, $\tan\beta = 50$ and $m_{H^0} = 340$ GeV.

10^{-5} are for $\tan\beta = 50$, $m_{N_3} = 10^{14}$ GeV, large $M_{\rm SUSY}$ in the TeV range and for our choice of $\theta_2 = \pi e^{0.8i}$, $\theta_1 = \theta_3 = 0$, but a more refined analysis of the full parameter space could lead to even larger rates. In particular, it is obvious that larger $\tan\beta$ values will enhance considerably the rates and lead to Higgs ratios closer to the future experimental reach of 10^{-4} at LHC [191] and e^+e^- and $\mu^+\mu^-$ colliders [192], but we have not tried this because it would require to perform a resummation of the large $\tan\beta$ contributions that is beyond the scope of this thesis.

2.3 LFV decays into three leptons: $l_j \to 3\, l_i$

Our aim in this section is to analyse the branching ratios that can be generated for the LFV decays into three leptons, namely $\mu \to 3\,e$, $\tau \to 3\,e$ and $\tau \to 3\,\mu$, in the context of the CMSSM-seesaw scenarios. These LFV processes have previously been studied in the SUSY-seesaw context by several authors [49–53, 71, 114, 139, 181, 182, 185, 193–202], under some specific assumptions for both seesaw parameters, m_D and m_M, and for the CMSSM parameters, M_0, $M_{1/2}$, A_0, sign(μ) and $\tan\beta$.

The present study of these decay channels updates, completes and corrects the previous anlayses in several respects. First we include, by the first time to our knowledge, the full set of SUSY one-loop contributions to the $l_j \to 3\, l_i$ decays, namely, the photon, the Z boson, and the Higgs bosons penguin diagrams, and the box diagrams. The most complete computation so far of these $l_j \to 3\, l_i$ decays was done in [49] where the contributions from the photon and Z boson penguin diagrams and from the box diagrams were included, but they focused on the particular

choice of degenerate heavy Majorana neutrinos and they presented numerical results just for $\mu \to 3e$ decays. We extend this previous study by including in addition the Higgs penguin diagrams mediated by the three neutral MSSM bosons, H^0, h^0 and A^0, and correct their results for the Z penguin contributions. We also extend their study in that we present results for the three decays, $\mu \to 3e$, $\tau \to 3\mu$ and $\tau \to 3e$ and consider both possible scenarios, degenerate and hierarchical heavy neutrinos. There are other interesting LFV τ leptonic decays, like $\tau \to \mu e^+ e^-$ and $\tau \to e\mu^+\mu^-$, that we do not consider in this thesis.

The current experimental upper bounds of $l_j \to 3\, l_i$ channels are shown in Table 2.3.

LFV decays	SINDRUM	BABAR	Belle
BR($\mu \to 3\, e$)	1×10^{-12} [59]	—	—
BR($\tau \to 3\, e$)	—	4.3×10^{-8} [70]	3.6×10^{-8} [69]
BR($\tau \to 3\, \mu$)	—	5.3×10^{-8} [70]	3.2×10^{-8} [69]

Table 2.3: Present upper bounds for $l_j \to 3\, l_i$ decays

2.3.1 Analytical results for $l_j \to 3\, l_i$ decays

In this section we present the analytical results for the LFV τ and μ decays into three leptons with the same flavour, within the constrained SUSY-seesaw scenarios that we have presented in Chapter 1. We perform a complete one-loop computation of the τ and μ decay widths for all the three possible channels, $\tau \to 3\,\mu$, $\tau \to 3\, e$ and $\mu \to 3\, e$, and include all the contributing SUSY-loops. We present each contribution separately, γ-penguin, Z-penguin, Higgs-penguin and boxes. The contributions from the Higgs-penguin diagrams are, to our knowledge, computed exactly by the first time here. We have also reviewed the analytical results in [49] and correct their results for the Z-penguin contributions. Notice that we make the computation in the physical mass eigenstate basis. That is, we consider the one-loop contributions from charged sleptons, $\tilde{l}_X$ $(X = 1, .., 6)$, sneutrinos $\tilde{\nu}_X$ $(X = 1, 2, 3)$, charginos $\tilde{\chi}^-_A$ $(A = 1, 2)$, and neutralinos $\tilde{\chi}^0_A$ $(A = 1, .., 4)$. The interactions in the physical mass eigenstate basis that are needed for this computation are collected in the form of Feynman rules in Appendix A.

First, we define the amplitudes for the $l^-_j(p) \to l^-_i(p_1) l^-_i(p_2) l^+_i(p_3)$ decays as the sum of the various contributions shown in Fig. 2.22,

$$T(l_j \to 3\, l_i) = T_{\gamma-\text{penguin}} + T_{Z-\text{penguin}} + T_{H-\text{penguin}} + T_{\text{boxes}}\,. \tag{2.16}$$

In the following we present the results for these contributions in terms of some convenient form factors.

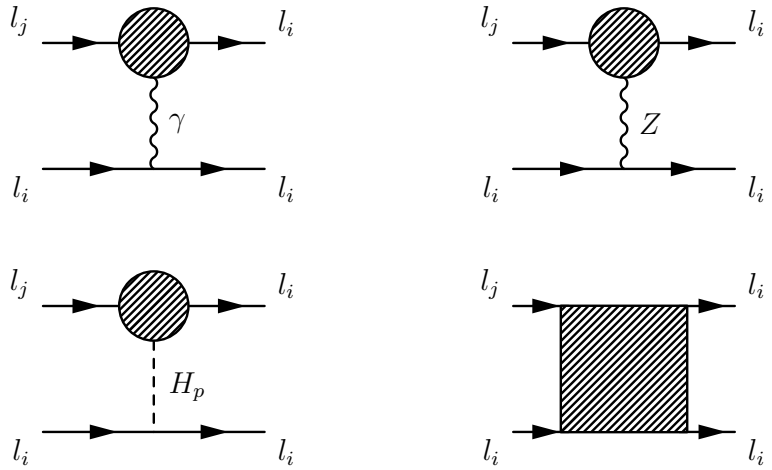

Figure 2.22: Photon-, Z-, H-penguin and box diagrams contributing to $l_j \to 3\, l_i$ decays.

γ-penguin contributions

The diagrams in Fig. 2.22 where a photon is exchanged are called γ-penguin diagrams and their contributing loops are shown in Fig. B.1. The result for the γ-penguin amplitude contributing to the $l_j \to 3\, l_i$ decays is usually written as

$$\begin{aligned} T_{\gamma-\text{penguin}} &= \bar{u}_i(p_1)\left[q^2\gamma_\mu(A_1^L P_L + A_1^R P_R) + im_{l_j}\sigma_{\mu\nu}q^\nu\left(A_2^L P_L + A_2^R P_R\right)\right] u_j(p) \\ &\times \frac{e^2}{q^2}\bar{u}_i(p_2)\gamma^\mu v_i(p_3) - (p_1 \leftrightarrow p_2)\,, \end{aligned} \tag{2.17}$$

where q is the photon momentum and e is the positron electric charge. The photon-penguin amplitude has two contributions in the SUSY-seesaw scenarios from the chargino and neutralino sectors respectively, as can be seen in the structure of the form factors in Eq. (2.2). Notice that in this case, in contrast to LFV radiative decays $l_j \to l_i\gamma$, both vector ($A_1^{L,R}$) and dipole ($A_2^{L,R}$) form factors contribute, due to the fact that an off-shell photon can be also exchanged. The neutralino and chargino contributions are given by Eqs. (B.4)-(B.8), repectively.

Z-penguin contributions

The diagrams in Fig. 2.22 where a Z boson is exchanged are called Z-penguin diagrams and their contributing loops are shown in Fig. B.2. The amplitude in this case is

$$\begin{aligned} T_{Z-\text{penguin}} &= \frac{1}{m_Z^2}\bar{u}_i(p_1)\left[\gamma_\mu\left(F_L P_L + F_R P_R\right)\right] u_j(p) \\ &\times \bar{u}_i(p_2)\left[\gamma^\mu\left(Z_L^{(l)} P_L + Z_R^{(l)} P_R\right)\right] v_i(p_3) - (p_1 \leftrightarrow p_2)\,, \end{aligned} \tag{2.18}$$

where, as before, $F_{L(R)} = F^{(n)}_{L(R)} + F^{(c)}_{L(R)}$. The expressions for these form factors are given in Appendix B. Notice that all the loop functions are evaluated at zero external momenta which is a very good approximation in these leptonic decays. That is,

$$B(m_1^2, m_2^2) = B(0, m_1^2, m_2^2)\,, \tag{2.19}$$

$$C(m_1^2, m_2^2, m_3^2) = C(0, 0, m_1^2, m_2^2, m_3^2)\,. \tag{2.20}$$

The expressions for the couplings are collected in Appendix A and the loop functions [189] are given in the Appendix C. Notice that our result for the Z-penguin contributions differs significantly from the result in [49]. In fact, these authors did not consider all the diagrams in these Z-penguin contributions, which we think is not justified.

Box contributions

The box-type diagrams are shown in Fig. B.4. We have computed these diagrams and found a result in agreement with [49]. The amplitude for these box contributions can be written as

$$\begin{aligned}
T_{\text{boxes}} &= e^2 B_1^L \left[\bar{u}_i(p_1)\left(\gamma^\mu P_L\right) u_j(p)\right]\left[\bar{u}_i(p_2)\left(\gamma_\mu P_L\right) v_i(p_3)\right] \\
&+ e^2 B_1^R \left[\bar{u}_i(p_1)\left(\gamma^\mu P_R\right) u_j(p)\right]\left[\bar{u}_i(p_2)\left(\gamma_\mu P_R\right) v_i(p_3)\right] \\
&+ e^2 B_2^L \left\{\left[\bar{u}_i(p_1)\left(\gamma^\mu P_L\right) u_j(p)\right]\left[\bar{u}_i(p_2)\left(\gamma_\mu P_R\right) v_i(p_3)\right] - (p_1 \leftrightarrow p_2)\right\} \\
&+ e^2 B_2^R \left\{\left[\bar{u}_i(p_1)\left(\gamma^\mu P_R\right) u_j(p)\right]\left[\bar{u}_i(p_2)\left(\gamma_\mu P_L\right) v_i(p_3)\right] - (p_1 \leftrightarrow p_2)\right\} \\
&+ e^2 B_3^L \left\{\left[\bar{u}_i(p_1) P_L u_j(p)\right]\left[\bar{u}_i(p_2) P_L v_i(p_3)\right] - (p_1 \leftrightarrow p_2)\right\} \\
&+ e^2 B_3^R \left\{\left[\bar{u}_i(p_1) P_R u_j(p)\right]\left[\bar{u}_i(p_2) P_R v_i(p_3)\right] - (p_1 \leftrightarrow p_2)\right\} \\
&+ e^2 B_4^L \left\{\left[\bar{u}_i(p_1)\left(\sigma_{\mu\nu} P_L\right) u_j(p)\right]\left[\bar{u}_i(p_2)\left(\sigma^{\mu\nu} P_L\right) v_i(p_3)\right] - (p_1 \leftrightarrow p_2)\right\} \\
&+ e^2 B_4^R \left\{\left[\bar{u}_i(p_1)\left(\sigma_{\mu\nu} P_R u_j(p)\right)\right]\left[\bar{u}_i(p_2)\left(\sigma^{\mu\nu} P_R\right) v_i(p_3)\right] - (p_1 \leftrightarrow p_2)\right\}\,,
\end{aligned} \tag{2.21}$$

where

$$B_a^{L,R} = B_a^{(n)L,R} + B_a^{(c)L,R} \quad a = 1, ..., 4\,. \tag{2.22}$$

The different neutralino and chargino contributions are given in Appendix B.

Higgs-penguin contributions

The diagrams in Fig. 2.22 where a Higgs boson is exchanged are called Higgs-penguin diagrams. The contributing loops are shown in Fig. B.3 and have been computed here by the first time. These were usually not considered in the literature. In particular, in the most complete study so far of [49] these Higgs-penguin diagrams were not included. However, they are expected to be relevant at large $\tan\beta$ [53]. We will therefore include them here. Specifically, we include

the contributions from the three neutral MSSM Higgs bosons, h^0, H^0 and A_0 and consider all SUSY-loops.

In this case, it is convenient to write the amplitude as

$$\begin{aligned} T_{\rm Higgs} &= e^2 B^L_{2,\rm Higgs} \left\{ [\bar{u}_i(p_1)\,(\gamma^\mu P_L)\,u_j(p)]\,[\bar{u}_i(p_2)\,(\gamma_\mu P_R)\,v_i(p_3)] - (p_1 \leftrightarrow p_2) \right\} \\ &+ e^2 B^R_{2,\rm Higgs} \left\{ [\bar{u}_i(p_1)\,(\gamma^\mu P_R)\,u_j(p)]\,[\bar{u}_i(p_2)\,(\gamma_\mu P_L)\,v_i(p_3)] - (p_1 \leftrightarrow p_2) \right\} \\ &+ e^2 B^L_{3,\rm Higgs} \left\{ [\bar{u}_i(p_1) P_L u_j(p)]\,[\bar{u}_i(p_2) P_L v_i(p_3)] - (p_1 \leftrightarrow p_2) \right\} \\ &+ e^2 B^R_{3,\rm Higgs} \left\{ [\bar{u}_i(p_1) P_R u_j(p)]\,[\bar{u}_i(p_2) P_R v_i(p_3)] - (p_1 \leftrightarrow p_2) \right\} , \end{aligned} \tag{2.23}$$

where

$$B^{L,R}_{a,\rm Higgs} = B^{(n)L,R}_{a,\rm Higgs} + B^{(c)L,R}_{a,\rm Higgs} \quad a = 2,3\,. \tag{2.24}$$

The first term represents the neutralino contribution, which we find to be

$$e^2 B^{(n)L}_{2,\rm Higgs} = \sum_{p=1}^{3} \left(-\frac{1}{2}\right) \frac{1}{m^2_{H_p}} H^{(p)}_{L,n} S^{(p)}_{R,i}\,, \tag{2.25}$$

$$e^2 B^{(n)L}_{3,\rm Higgs} = \sum_{p=1}^{3} \frac{1}{m^2_{H_p}} H^{(p)}_{L,n} S^{(p)}_{L,i}\,, \tag{2.26}$$

$$B^{(n)R}_{a,\rm Higgs} = B^{(n)L}_{a,\rm Higgs}\Big|_{L\leftrightarrow R} \quad a = 2,3\,, \tag{2.27}$$

with $H_p (p = 1,2,3) = h^0, H^0, A^0$ and where $H^{(p)}_{L,n}$, $H^{(p)}_{R,n}$ are given in eqs. (B.17) and (B.18). Correspondingly, the result for the chargino contribution is given by

$$e^2 B^{(c)L}_{2,\rm Higgs} = \sum_{p=1}^{3} \left(-\frac{1}{2}\right) \frac{1}{m^2_{H_p}} H^{(p)}_{L,c} S^{(p)}_{R,i}\,, \tag{2.28}$$

$$e^2 B^{(c)L}_{3,\rm Higgs} = \sum_{p=1}^{3} \frac{1}{m^2_{H_p}} H^{(p)}_{L,c} S^{(p)}_{L,i}\,, \tag{2.29}$$

$$B^{(c)R}_{a,\rm Higgs} = B^{(c)L}_{a,\rm Higgs}\Big|_{L\leftrightarrow R} \quad a = 2,3\,, \tag{2.30}$$

where $H^{(p)}_{L(R),c}$ can be obtained from the previous $H^{(p)}_{L(R),n}$ by replacing everywhere

$$\begin{aligned} \tilde{l} &\to \tilde{\nu} \\ \tilde{\chi}^0 &\to \tilde{\chi}^- \\ N^{L(R)} &\to C^{L(R)} \\ D_{L(R)} &\to W_{L(R)}\,. \end{aligned}$$

The values of the couplings and the loop functions are given in Appendices A and C, respectively.

$l_j \to 3\, l_i$ decay width

The decay width for $l_j \to 3\, l_i$ can then be written in terms of the previous form factors as [49]

$$\begin{aligned}
\Gamma(l_j \to 3\, l_i) &= \frac{e^4}{512\pi^3} m_{l_j}^5 \Big[\left|A_1^L\right|^2 + \left|A_1^R\right|^2 - 2\left(A_1^L A_2^{R*} + A_2^L A_1^{R*} + h.c.\right) \\
&+ \left(\left|A_2^L\right|^2 + \left|A_2^R\right|^2\right)\left(\frac{16}{3}\log\frac{m_{l_j}}{m_{l_i}} - \frac{22}{3}\right) + \frac{1}{6}\left(\left|B_1^L\right|^2 + \left|B_1^R\right|^2\right) + \frac{1}{3}\left(\left|\hat{B}_2^L\right|^2 + \left|\hat{B}_2^R\right|^2\right) \\
&+ \frac{1}{24}\left(\left|\hat{B}_3^L\right|^2 + \left|\hat{B}_3^R\right|^2\right) + 6\left(\left|B_4^L\right|^2 + \left|B_4^R\right|^2\right) - \frac{1}{2}\left(\hat{B}_3^L B_4^{L*} + \hat{B}_3^R B_4^{R*} + h.c.\right) \\
&+ \frac{1}{3}\left(A_1^L B_1^{L*} + A_1^R B_1^{R*} + A_1^L \hat{B}_2^{L*} + A_1^R \hat{B}_2^{R*} + h.c.\right) \\
&- \frac{2}{3}\left(A_2^R B_1^{L*} + A_2^L B_1^{R*} + A_2^L \hat{B}_2^{R*} + A_2^R \hat{B}_2^{L*} + h.c.\right) \\
&+ \frac{1}{3}\Big\{2\left(|F_{LL}|^2 + |F_{RR}|^2\right) + |F_{LR}|^2 + |F_{RL}|^2 \\
&+ \left(B_1^L F_{LL}^* + B_1^R F_{RR}^* + \hat{B}_2^L F_{LR}^* + \hat{B}_2^R F_{RL}^* + h.c.\right) \\
&+ 2\left(A_1^L F_{LL}^* + A_1^R F_{RR}^* + h.c.\right) + \left(A_1^L F_{LR}^* + A_1^R F_{RL}^* + h.c.\right) \\
&- 4\left(A_2^R F_{LL}^* + A_2^L F_{RR}^* + h.c.\right) - 2\left(A_2^L F_{RL}^* + A_2^R F_{LR}^* + h.c.\right)\Big\}\Big] \,, \qquad (2.31)
\end{aligned}$$

where

$$F_{LL} = \frac{F_L Z_L^{(l)}}{g^2 \sin^2\theta_W m_Z^2} \,, \qquad (2.32)$$

$$F_{RR} = F_{LL}|_{L\leftrightarrow R} \,, \qquad (2.33)$$

$$F_{LR} = \frac{F_L Z_R^{(l)}}{g^2 \sin^2\theta_W m_Z^2} \,, \qquad (2.34)$$

$$F_{RL} = F_{LR}|_{L\leftrightarrow R} \,. \qquad (2.35)$$

Notice that we have put the Higgs contributions together with the box ones in order to follow closely the way of presentation of [49]

$$\hat{B}_2^{L,R} = B_2^{L,R} + B_{2,\text{Higgs}}^{L,R} \,, \qquad (2.36)$$

$$\hat{B}_3^{L,R} = B_3^{L,R} + B_{3,\text{Higgs}}^{L,R} \,. \qquad (2.37)$$

Note also that we have corrected the result in [49] for the term that goes with $\left(\left|A_2^L\right| + \left|A_2^R\right|\right)$.

2.3.2 Numerical results for $l_j \to 3\, l_i$ decays

We present in this section the numerical results for all the branching ratios of LFV $l_j \to 3\, l_i$ decays in the context of the constrained SUSY-seesaw scenarios that have been introduced in the previous chapter. We focus here on the different diagrams contributing to these processes,

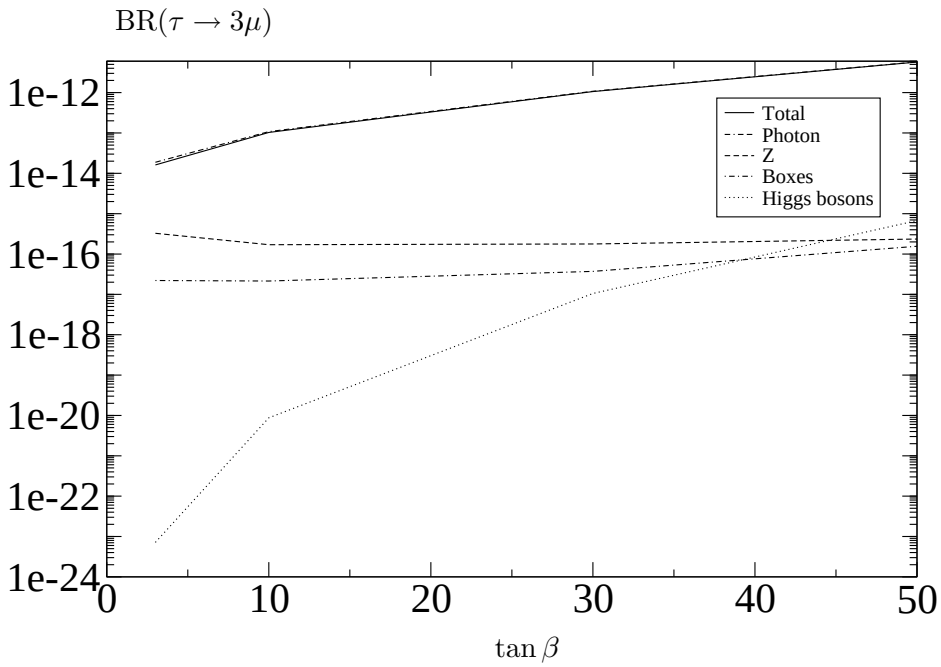

Figure 2.23: Dependence of LVF $\tau \to 3\,\mu$ decay on $\tan\beta$ with degenerate heavy neutrinos and real R, for $m_N = 10^{14}$ GeV. The other input parameters are, $M_0 = 400$ GeV, $M_{1/2} = 300$ GeV, $A_0 = 0$ and sign$(\mu) > 0$.

presented in Section 2.3.1, and also compare the results with those of the radiative decays $\tau \to \mu\,\gamma$, $\tau \to e\,\gamma$ and $\mu \to e\,\gamma$. The reason to consider these radiative decays together with the decays into three leptons is that there are interesting correlations among them that provide additional information in testing SUSY. Specifically, we show in this section the correlations between the ratios of $\tau \to 3\,\mu$ and $\tau \to \mu\,\gamma$; between $\tau \to 3\,e$ and $\tau \to e\,\gamma$; and between $\mu \to 3\,e$ and $\mu \to e\,\gamma$. In all this numerical analysis we require compatibility with the neutrino data and with the present upper experimental bounds for all these branching ratios, as given explicitely in Chapter 1.

Degenerate case

We show in Fig. 2.23 through Fig. 2.26 the numerical results of the branching ratios for the LFV $l_j \to 3\, l_i$ decays with degenerate heavy neutrinos of mass m_N. We show our predictions for the three channels, $\tau \to 3\,\mu$, $\tau \to 3\,e$ and $\mu \to 3\,e$, and similarly, for the comparison with the LFV radiative decays, we also show in the plots the correlated decay, $\tau \to \mu\,\gamma$, $\tau \to e\,\gamma$ and $\mu \to e\,\gamma$, respectively.

The results of the branching ratios for the $\tau \to 3\,\mu$ decay as a function of $\tan\beta$ are illustrated in Fig. 2.23. In these plots we set $m_N = 10^{14}$ GeV and assume the matrix R to be real. From this figure we see that the predicted rates are well below its experimental upper bound for all $\tan\beta$ values, even though the total rates grow fast with $\tan\beta$. Comparing this figure with Fig. 2.1 we also see clearly the mentioned correlation between the $\tau \to 3\,\mu$ and $\tau \to \mu\,\gamma$ rates. In fact, this correlation is an inmediate consequence of the dominance of the γ-penguin contributions which clearly governs the size of the $\tau \to 3\,\mu$ rates. This is clearly illustrated in Fig. 2.23, where the various contributions are shown separately. In fact, the contributions from the γ-penguin diagrams are almost undistinguishable from the total rates for all $\tan\beta$ values. For low $\tan\beta$ values the next dominant contribution is from the Z-penguin diagrams, but this is still more than one order of magnitude smaller than the γ-penguin contribution. The contributions from the box diagrams are even smaller. We also learn that the Z and boxes contributions do not depend significantly on $\tan\beta$, while the photon contribution goes approximately as $(\tan\beta)^2$ at large $\tan\beta$. In this large $\tan\beta$ region it is interesting to note that the total Higgs contribution becomes larger than the Z contribution and the boxes, due to the fact that it grows approximately as $(\tan\beta)^6$. In this total Higgs contribution the dominant penguins are those with H^0 and A^0 exchanged, which are several orders of magnitude larger than the h^0-penguin contribution. However, in spite of this huge enhacement of the total Higgs contribution occurring at large $\tan\beta$, its relative size as compared to the photon-penguin contribution is still negligible. For instance, for the values set in this figure of $M_0 = 400$ GeV, $M_{1/2} = 300$ GeV, $A_0 = 0$, sign$\mu > 0$ and $m_N = 10^{14}$ GeV, the Higgs contribution is still four orders of magnitude smaller than the photon-penguin contribution at $\tan\beta = 50$.

We have checked that other choices of parameters, specially lower M_0 and $M_{1/2}$ lead to larger contributions from the Higgs-penguins, since one gets ligther SUSY spectra and more importantly lighter H^0 and A^0 bosons. However, the present experimental lower bounds on the MSSM particle masses, do not allow to decrease much these M_0 and $M_{1/2}$ values, so that in this CMSSM context the relevant m_{H_0}, and m_{A_0} masses can never get low enough values such that their corresponding Higgs-penguin contributions be competitive with the γ-penguin ones. From this figure we conclude then that the leading γ-penguin approximation works extremely well, for all $\tan\beta$ values. In this approximation one gets[9]

$$\frac{BR(l_j \to 3l_i)}{BR(l_j \to l_i\gamma)} = \frac{\alpha}{3\pi}\left(\log\frac{m_{l_j}^2}{m_{l_i}^2} - \frac{11}{4}\right), \tag{2.38}$$

which leads to the approximate values of $\frac{1}{440}$, $\frac{1}{94}$ and $\frac{1}{162}$ for $(l_j l_i) = (\tau\mu), (\tau e)$ and (μe),

[9]The corresponding result for $\tau \to \mu e^+ e^-$ is

$$\frac{BR(\tau \to \mu e^+ e^-)}{BR(\tau \to \mu\,\gamma)} = \frac{\alpha}{3\pi}\left(\log\frac{m_\tau^2}{m_e^2} - 3\right).$$

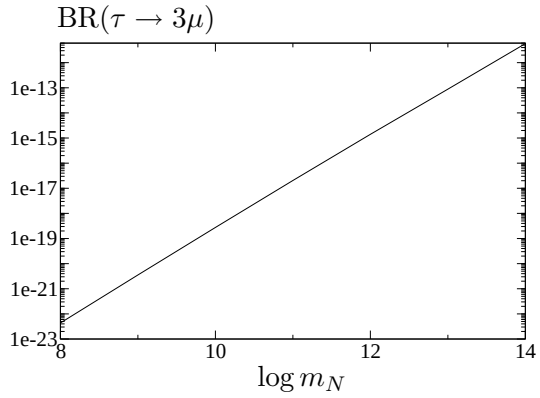

Figure 2.24: Dependence of $\tau \to 3\,\mu$ decay on m_N with degenerate heavy neutrinos and real R, for $\tan\beta = 50$. The other input parameters are, $M_0 = 400$ GeV, $M_{1/2} = 300$ GeV, $A_0 = 0$ and $\text{sign}(\mu) > 0$.

respectively. As will be seen later it also works extremely well in the other channels. These nearly constant values of the ratios of branching ratios will be showing along this work. Obviously, if these ratios could be measured they could provide interesting information.

Now we comment on the relevance of the choice for the m_N values. In Fig. 2.24 we have illustrated the BR($\tau \to 3\,\mu$) as a function of m_N for degenerate heavy neutrinos and $\tan\beta = 50$, with an explored range for m_N that is from 10^8 GeV up to 10^{14} GeV. If we compare this figure with Fig. 2.1 we clearly see that both channels, $\tau \to 3\,\mu$ and $\tau \to \mu\,\gamma$, have the same behaviour with m_N which corresponds approximately to BR($\tau \to 3\,\mu$), BR($\tau \to \mu\,\gamma$) $\propto |m_N \log(m_N)|^2$. Again, the predicted branching ratios are well bellow their experimental upper bounds, even at the largest m_N value of 10^{14} GeV.

For completeness, we also include the results of the other two channels $\tau \to 3\,e$ and $\mu \to 3\,e$ in Fig. 2.25, where the predictions are shown as a function of $\tan\beta$. Their corresponding behaviours are very similar to those in BR($\tau \to 3\,\mu$). We see again that the leading γ-penguin approximation works extremely well for these channels, and the previously mentioned values of the branching ratios give a pretty good answer. We find again that the rates for all these decays are well below their corresponding experimental bounds, in the degenerate case, for all the explored values of $\tan\beta$ and m_N.

To end up the study of the degenerate case, we have also explored the dependence of the largest ratios BR($\tau \to 3\,\mu$) and BR($\tau \to \mu\,\gamma$) with the SUSY parameters M_0 and $M_{1/2}$. These results are shown in Fig. 2.26. We see clearly a similar behaviour in the two channels and their rates decrease as expected when increasing the soft SUSY breaking mass parameters. This implies that for large enough values of M_0 or $M_{1/2}$ the branching ratios are considerably

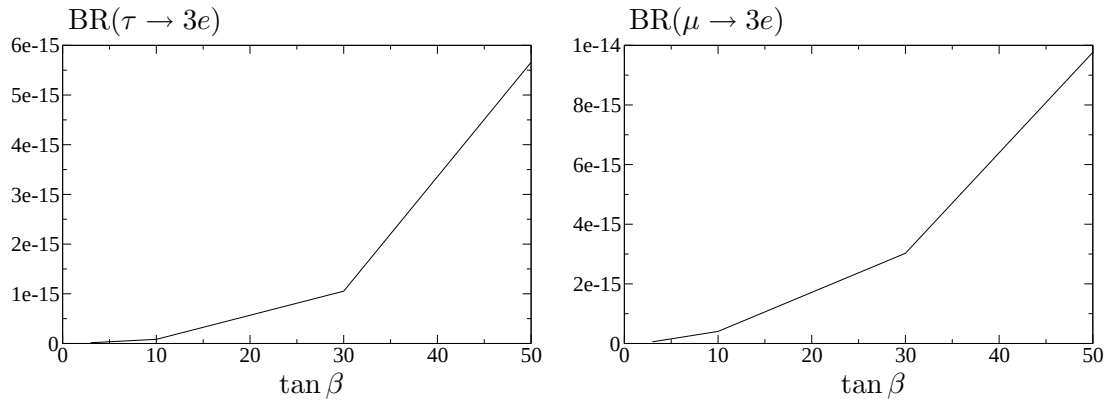

Figure 2.25: Dependence of BR($\tau \to 3\,e$) (left panel) and BR($\mu \to 3\,e$) (right panel) on $\tan\beta$ with degenerate heavy neutrinos and real R, for $m_N = 10^{14}$ GeV. The other input parameters are, $M_0 = 400$ GeV, $M_{1/2} = 300$ GeV, $A_0 = 0$ and sign(μ) > 0.

suppresed, due to the decoupling of the heavy SUSY particles in the dominant loops which are common to both observables. Thus, looking at these plots we can obviously conclude that the lighter the SUSY spectrum is, the larger branching ratios we get. However, as already said, the more interesting region of low M_0 and/or $M_{1/2}$ values, being close to 100 GeV, is not allowed by the present experimental lower bounds on the MSSM particle masses.

In summary, as in the previous study of the LFV radiative decays, the case of degenerate heavy neutrinos drive us to LFV τ and μ decay rates which are still below their present experimental upper bounds, for all the explored values of the CMSSM-seesaw parameters.

Hierarchical case

We next present the results for the more promising case of hierarchical neutrinos, where the choice for R is very relevant. The results for the general complex R case and for the particular mass hierarchy $(m_{N_1}, m_{N_2}, m_{N_3}) = (10^8, 2 \times 10^8, 10^{14})$ GeV, are shown in Fig. 2.27 through Fig. 2.32. We will later explore other choices as well.

From these figures we first confirm that the LFV τ and μ decay rates $l_j \to 3\,l_i$ are much larger in the hierarchical case than in the degenerate one. This is true even for the case of real R, which corresponds in our plots to the predictions at $\arg\theta_1 = \arg\theta_2 = \arg\theta_3 = 0$. Furthermore, we get severe restrictions on the maximum allowed decay rates coming from the experimental upper bounds.

The predictions for BR($\tau \to 3\,\mu$) as a function of $|\theta_2|$ are depicted in Fig. 2.27. Here θ_1 and θ_3 are set to zero, and $\arg\theta_2 = \pi/4$. From now on the arguments of θ_1, θ_2 and θ_3 are written in

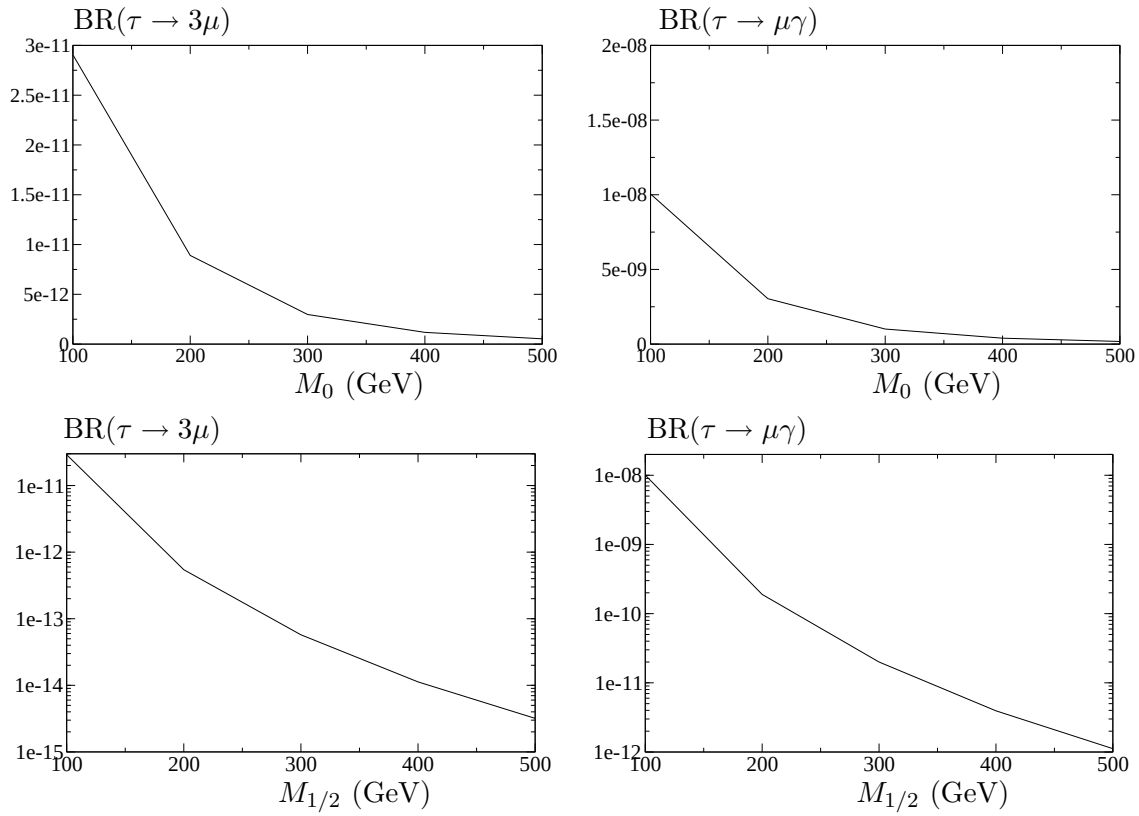

Figure 2.26: Dependence of BR($\tau \to 3\,\mu$) and BR($\tau \to \mu\,\gamma$) on M_0 and $M_{1/2}$, with degenerate heavy neutrinos and real R, for $m_N = 10^{14}$ GeV and $\tan\beta = 50$. (a) Upper-left panel, BR($\tau \to 3\,\mu$) as a function of M_0 for $M_{1/2} = 100$ GeV, (b) upper-right panel, BR($\tau \to \mu\,\gamma$) as a function of M_0 for $M_{1/2} = 100$ GeV, (c) lower-left panel, BR($\tau \to 3\,\mu$) as a function of $M_{1/2}$ for $M_0 = 100$ GeV, (d) lower-right panel, BR($\tau \to \mu\,\gamma$) as a function of $M_{1/2}$ for $M_0 = 100$ GeV. In all the plots we take $A_0 = 0$ and sign(μ) > 0.

radians. The other parameters are set to $\tan\beta = 50$, $M_0 = 400$ GeV, $M_{1/2} = 300$ GeV, $A_0 = 0$ and sign(μ) > 0. In Fig. 2.27 we show separately the various contributions to BR($\tau \to 3\,\mu$). The dominant one is again the photon-penguin contribution (which is undistinguisible from the total in this figure) and the others are several orders of magnitude smaller. We also see that the relative size of the subdominant contributions have changed respect to the previously studied degenerate case. Now the Higgs contribution is larger than the boxes one and this is larger than the Z one. This is so because the largest $\tan\beta = 50$ value has been set. All the rates for $\tau \to 3\,\mu$ in this plot are within the allowed range by the experimental bound, which is placed just at the upper line of the rectangle.

In Fig. 2.28 we show the predictions of BR($l_j \to 3\, l_i$) as functions of $|\theta_2|$, for all the channels

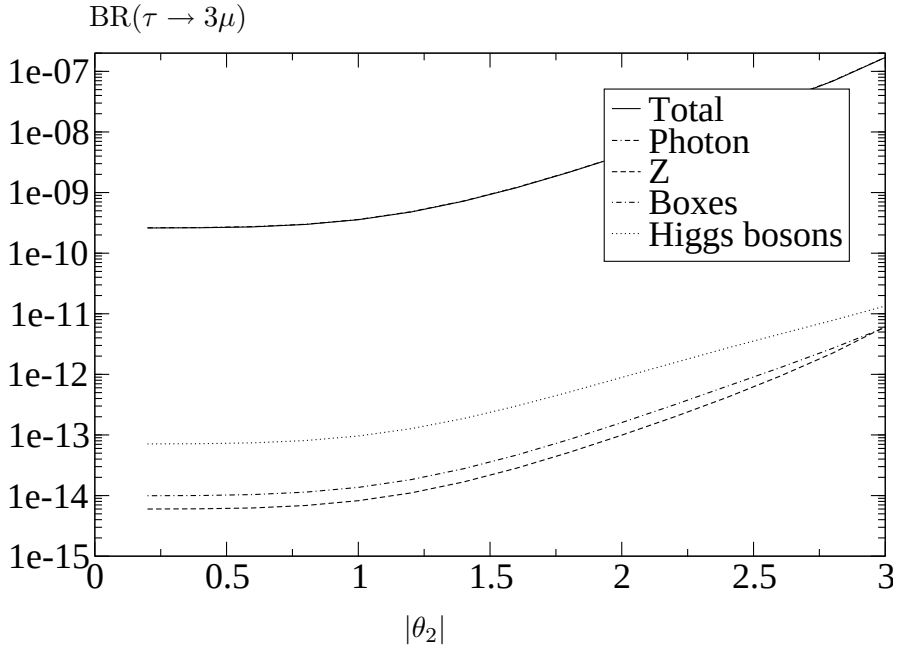

Figure 2.27: Dependence of BR($\tau \to 3\,\mu$) on $|\theta_2|$ for hierarchical neutrinos and for $\arg\theta_2 = \pi/4$, $(m_{N_1}, m_{N_2}, m_{N_3}) = (10^8, 2\times 10^8, 10^{14})$ GeV, $\theta_1 = \theta_3 = 0$, $\tan\beta = 50$, $M_0 = 400$ GeV, $M_{1/2} = 300$ GeV, $A_0 = 0$ and sign(μ) > 0.

and for the different values of $\arg\theta_2 = 0, \pi/10, \pi/8, \pi/6, \pi/4$. In all these plots we set again $\tan\beta = 50$, $M_0 = 400$ GeV, $M_{1/2} = 300$ GeV, $A_0 = 0$, sign(μ) > 0 and $(m_{N_1}, m_{N_2}, m_{N_3}) = (10^8, 2\times 10^8, 10^{14})$ GeV. The upper lines correspond to $\arg\theta_2 = \pi/4$ and the lower ones to $\arg\theta_2 = 0$. These lower lines are therefore the corresponding predictions for real R. It is clear that all the branching ratios have a soft behaviour with $|\theta_2|$ except for the case of real θ_2 where appears a narrow dip in each plot. In this Fig. 2.28 we see that all the rates obtained are below their experimental upper bounds. We also see that the rates for BR($\mu \to 3e$) enter in conflict with experiment at the upper corner of large $|\theta_2|$ and large $\arg\theta_2 = \pi/4$.

The results for BR($l_j \to 3\,l_i$) as functions of $|\theta_1|$, for different values of arg (θ_1), are illustrated in Fig. 2.29. Here θ_2 and θ_3 are set to zero. The same set of CMSSM parameters and heavy neutrino masses as in Fig. 2.28 are taken for comparison. We see clearly that the restrictions are more severe in this case than in the previous one. In this sense, the predictions for BR($\mu \to 3\,e$) are mostly excluded, except for the region close to zero and the dip. Notice that the qualitative behaviour of these all branching ratios with $|\theta_1|$ in Fig. 2.29 and the locations of the dips can be explained from the Yukawa coupling matrix behaviour in Fig. 1.8.

The scenario most seriously in conflict with experiment is shown in Fig. 2.30 where the

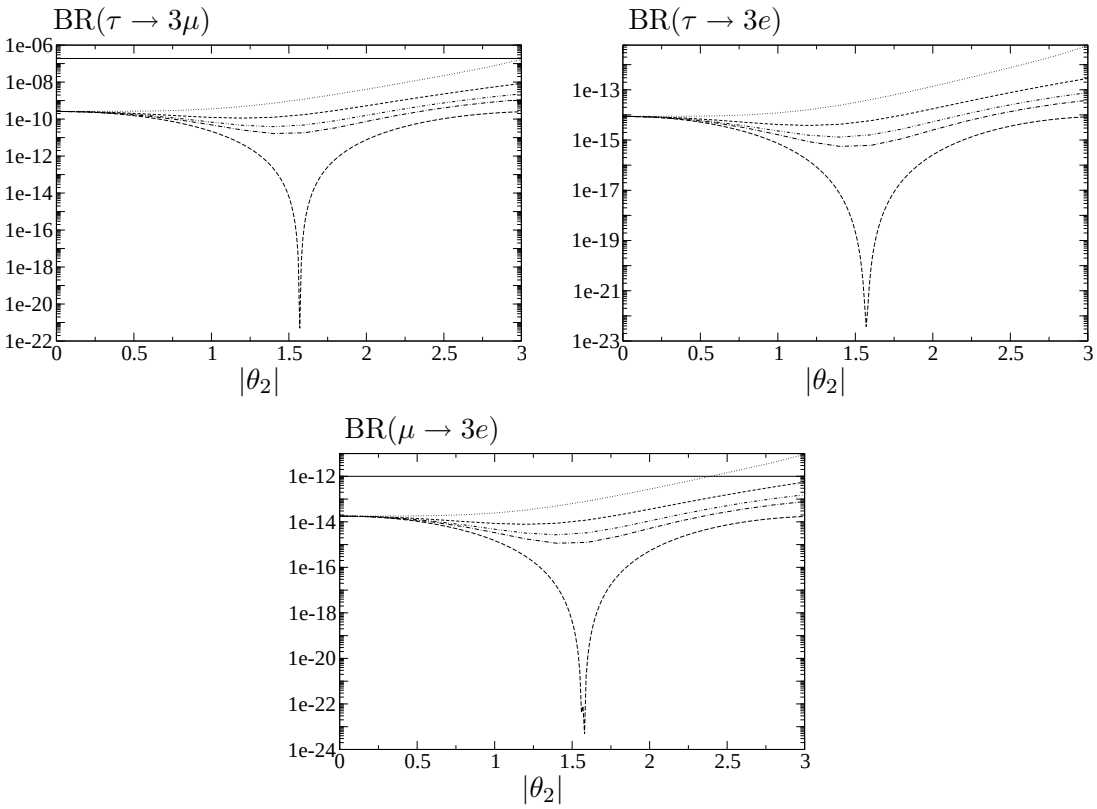

Figure 2.28: Dependence of LVF τ and μ decays $l_j \to 3\, l_i$ on $|\theta_2|$ with hierarchical heavy neutrinos and complex R, for $\arg\theta_2 = 0, \pi/10, \pi/8, \pi/6, \pi/4$ in radians (lower to upper lines), $(m_{N_1}, m_{N_2}, m_{N_3}) = (10^8, 2\times 10^8, 10^{14})$ GeV, $\theta_1 = \theta_3 = 0$, $\tan\beta = 50$, $M_0 = 400$ GeV, $M_{1/2} = 300$ GeV, $A_0 = 0$ and sign$(\mu) > 0$. The horizontal lines are the corresponding upper experimental bound of each channel. At present these bounds have been improved as summarised in Table 2.3.

predictions for BR($l_j \to 3\, l_i$) are again plotted as a function of $|\theta_1|$ and for the same choices of $\arg\theta_1$ as in the previous case, but now the SUSY parameters are set to the lower values $M_0 = 250$ GeV and $M_{1/2} = 150$ GeV. These lead to a lighter MSSM spectrum and and in consequence to higher rates.

We conclude from Fig. 2.30 that the predictions for BR($\mu \to e\gamma$) are totally excluded by present data. The predictions for BR($\tau \to 3\mu$) start being sensitive to the present experimental bounds for large complex θ_1 values in the upper corner of the plot.

As in the case of LFV radiative decays, we have also explored the dependence with the complex θ_3 angle, and we have found that the predictions for all rates are nearly constant with this angle. For instance, for $\tan\beta = 50$, $M_0 = 400$ GeV, $M_{1/2} = 300$ GeV, $A_0 = 0$ and sign$(\mu) >$

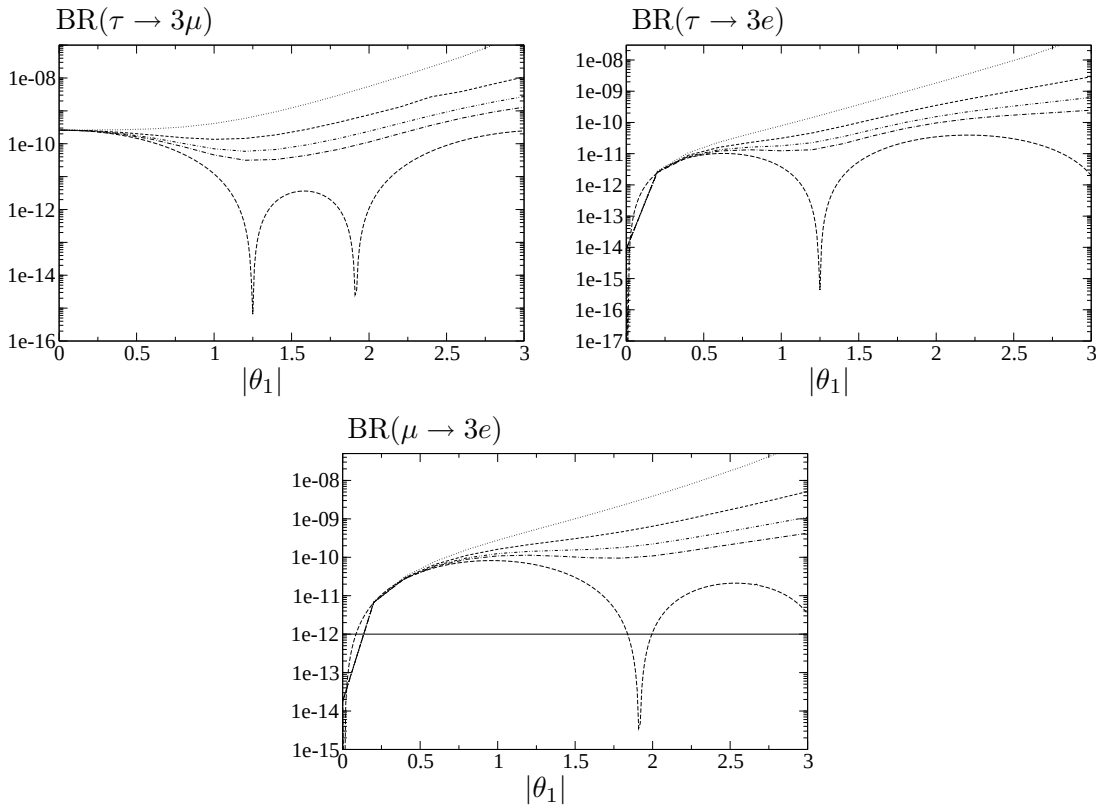

Figure 2.29: Dependence of LFV τ and μ decays $l_j \to 3\, l_i$ on $|\theta_1|$ with hierarchical heavy neutrinos and complex R, for $\arg\theta_1 = 0, \pi/10, \pi/8, \pi/6, \pi/4$ in radians (lower to upper lines), $(m_{N_1}, m_{N_2}, m_{N_3}) = (10^8, 2\times 10^8, 10^{14})$ GeV, $\theta_2 = \theta_3 = 0$, $\tan\beta = 50$, $M_0 = 400$ GeV, $M_{1/2} = 300$ GeV and $A_0 = 0$. The horizontal lines are the corresponding upper experimental bounds of each channel. At present these bounds have been improved as summarised in Table 2.3.

0, we get $\mathrm{BR}(\tau \to 3\mu) = 2.6\times 10^{-10}$, $\mathrm{BR}(\tau \to 3e) = 8.8\times 10^{-15}$ and $\mathrm{BR}(\mu \to 3e) = 1.8\times 10^{-14}$.

The dependence of $\mathrm{BR}(\tau \to 3\,\mu)$ and $\mathrm{BR}(\tau \to \mu\,\gamma)$ on the SUSY parameters M_0 and $M_{1/2}$ is illustrated in Fig. 2.31. We see a similar behaviour as in the degenerate case, where a suppresion of the branching ratios occurs for large values of M_0 and/or $M_{1/2}$. Whereas the ratios for $\mathrm{BR}(\tau \to 3\,\mu)$ enter in to the allowed region by the experimental bound for large enough M_0 and/or $M_{1/2}$, the ratios for $B(\tau \to \mu\,\gamma)$ are well above their bound for all M_0 and $M_{1/2}$ values explored. The main point again is the particular value of θ_2 with large $|\theta_2|$ and large $\arg\theta_2$, which generates large rates.

With the purpose of exploring other choices of the SUSY parameters, we have also generated results for the specific value $A_0 = -100$ and found very close predictions to the $A_0 = 0$ case, the lines in the plots being nearly undistinguisable respect to this case. We have also run the

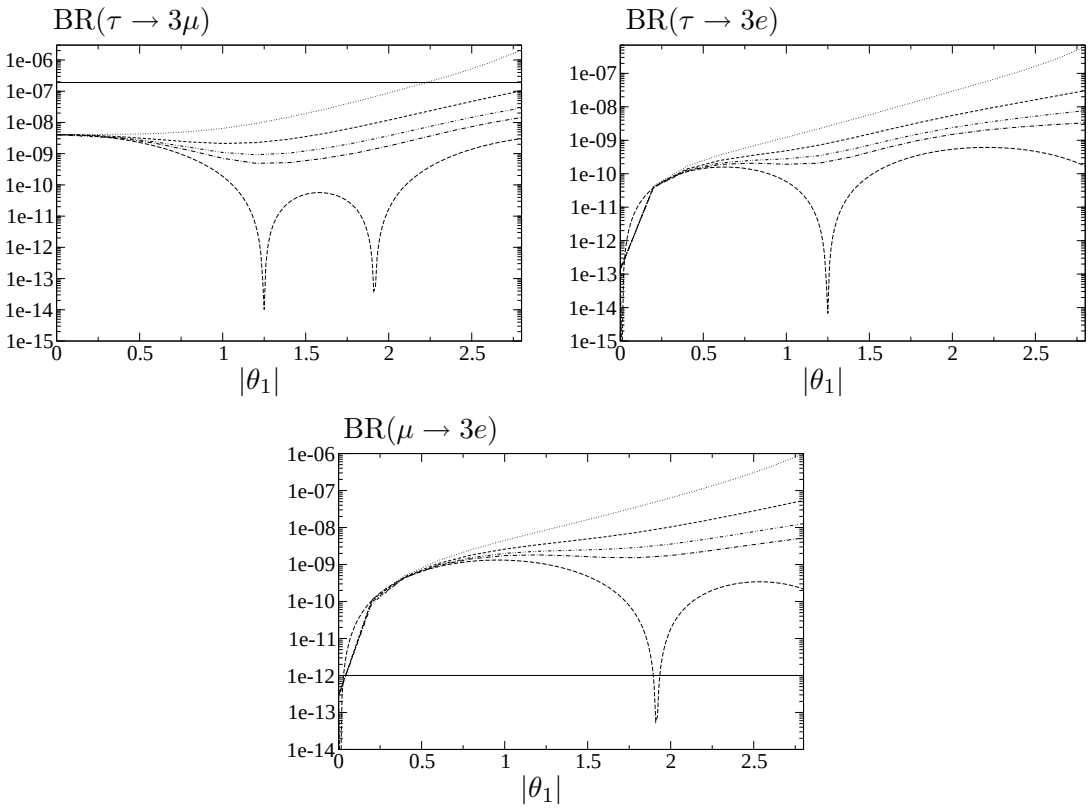

Figure 2.30: Dependence of LFV τ and μ decays on $|\theta_1|$ with hierarchical heavy neutrinos and complex R, for $\arg\theta_1 = 0, \pi/10, \pi/8, \pi/6, \pi/4$ in radians (lower to upper lines), $(m_{N_1}, m_{N_2}, m_{N_3}) = (10^8, 2 \times 10^8, 10^{14})$ GeV, $\theta_2 = \theta_3 = 0$, $\tan\beta = 50$, $M_0 = 250$ GeV, $M_{1/2} = 150$ GeV and $A_0 = 0$. The horizontal lines are the corresponding upper experimental bound of each channel. At present these bounds have been improved as summarised in Table 2.3.

alternative case of sign$(\mu) < 0$, and found again very close predictions to the sign$(\mu) > 0$ case, with the lines in the plots being undistinguisable from this case.

Finally, we have also tried another input values for the heavy neutrino masses. The results for BR$(\tau \to 3\mu)$ are shown in Fig. 2.32. Here we compare the predictions for the three following set of values, $(m_{N_1}, m_{N_2}, m_{N_3}) = (10^8, 2\times10^8, 10^{14})$ GeV, $(10^{10}, 2\times10^{10}, 10^{14})$ GeV and $(10^8, 2\times 10^8, 10^{12})$ GeV. We conclude that the relevant mass is the heaviest one, m_{N_3}, and the scaling with this mass is approximately as the scaling with the common mass m_N in the degenerate case. Because of this, the rates for the two first sets are nearly undistinguisable, and the rates for the third set are about four orders of magnitude below.

In summary, we obtain in the hierachical case much larger rates than in the degenerate one, and one must pay attention to these values, because the rates in several channels do enter in

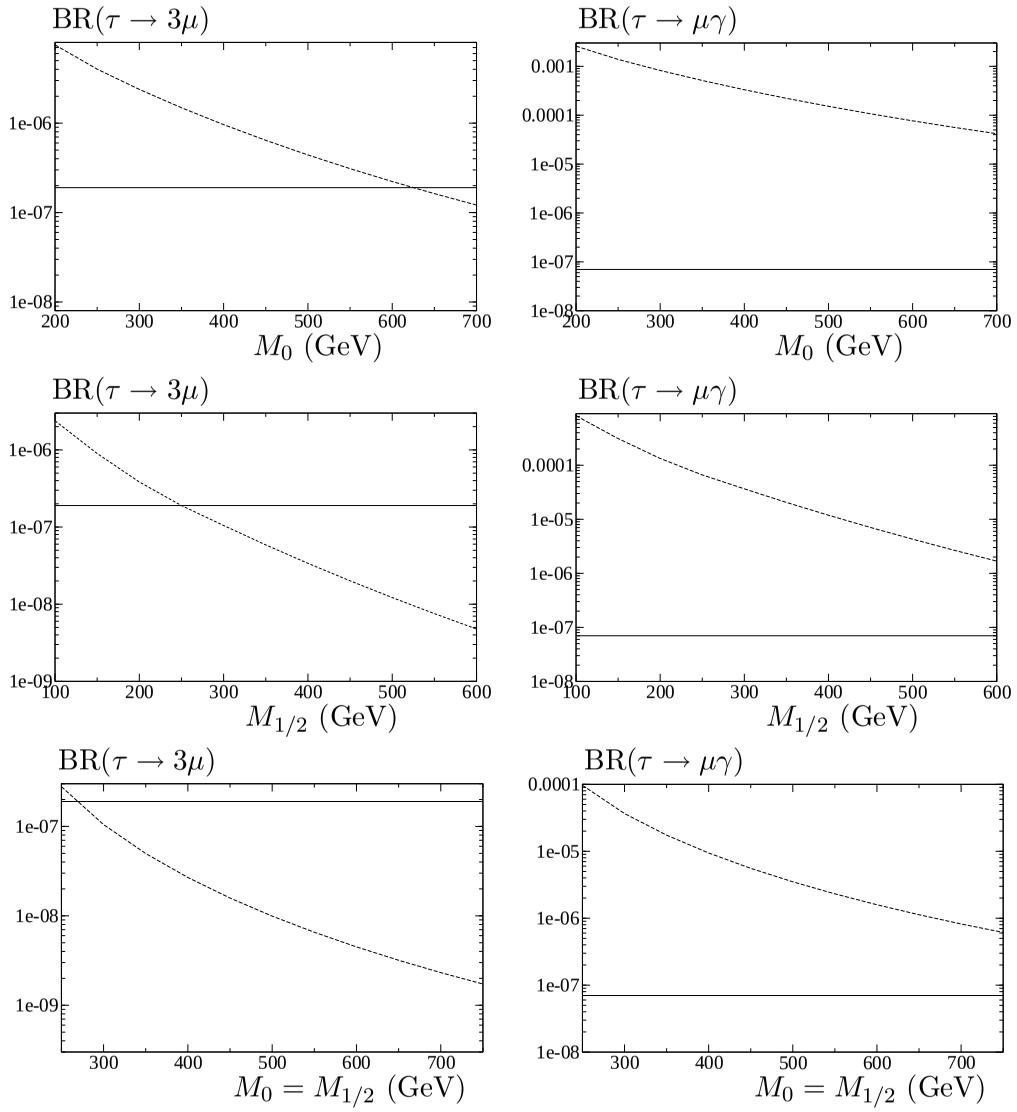

Figure 2.31: Dependence of BR($\tau \to 3\,\mu$) and BR($\tau \to \mu\,\gamma$) on M_0 and $M_{1/2}$ with hierarchical heavy neutrinos, for $m_N = (10^8, 2\times10^8, 10^{14})$ GeV, $\tan\beta = 50$, $\theta_2 = 2.8\,e^{\pi/4}$ ($\theta_1 = \theta_3 = 0$), $A_0 = 0$ and sign(μ) > 0. (a) Upper-left panel, BR($\tau \to 3\,\mu$) as a function of M_0 for $M_{1/2} = 100$ GeV, (b) upper-right panel, BR($\tau \to \mu\,\gamma$) as a function of M_0 for $M_{1/2} = 100$ GeV, (c) middle-left panel, BR($\tau \to 3\,\mu$) as a function of $M_{1/2}$ for $M_0 = 200$ GeV, (d) middle-right panel, BR($\tau \to \mu\,\gamma$) as a function of $M_{1/2}$ for $M_0 = 200$ GeV, (e) lower-left panel, BR($\tau \to 3\,\mu$) as a function of $M_0 = M_{1/2}$, (f) lower-right panel, BR($\tau \to \mu\,\gamma$) as a function of $M_0 = M_{1/2}$. The horizontal lines are the upper bound of each channel. At present these bounds have been improved as summarised in Tables 2.1 and 2.3.

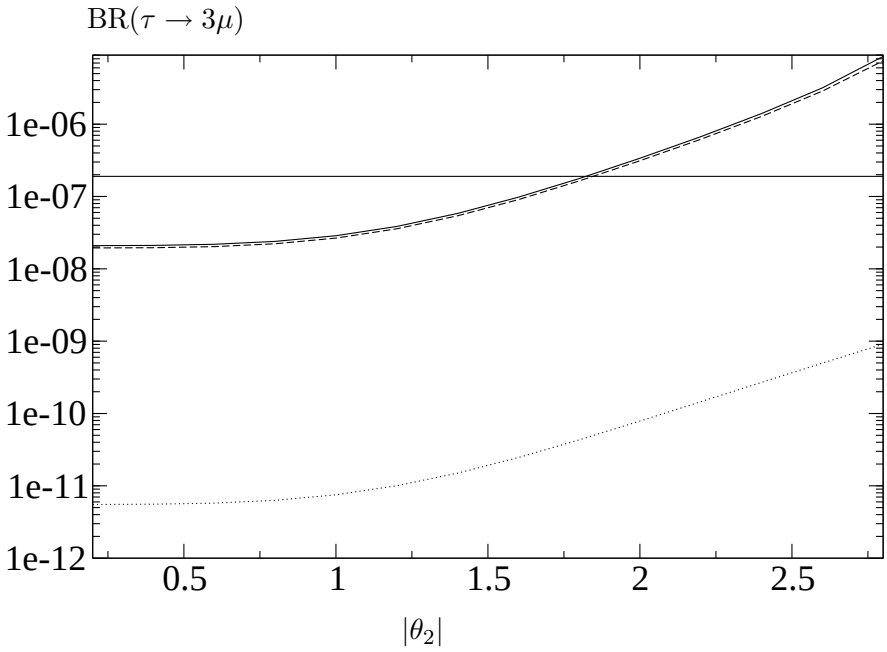

Figure 2.32: Dependence of LFV $\tau \to 3\,\mu$ on $|\theta_2|$ with hierarchical heavy neutrinos, for different m_{N_i} choices. Solid line is for $(m_{N_1}, m_{N_2}, m_{N_3}) = (10^8, 2 \times 10^8, 10^{14})$ GeV, dashed line is for $(m_{N_1}, m_{N_2}, m_{N_3}) = (10^{10}, 2 \times 10^{10}, 10^{14})$ GeV, and dotted line is for $(m_{N_1}, m_{N_2}, m_{N_3}) = (10^8, 2 \times 10^8, 10^{12})$ GeV. The rest of parameters are set to $\tan\beta = 50$, $M_0 = 200$ GeV, $M_{1/2} = 100$ GeV, $A_0 = 0$, sign$(\mu) > 0$ and arg$(\theta_2) = \pi/4$. The horizontal line is the experimental bound of $\tau \to 3\,\mu$. At present this bound has been improved as summarised in Table 2.3.

conflict with the experimental bounds. More specifically, the choice of a complex R matrix with large modules and/or large arguments of θ_1 and/or θ_2 and a light SUSY spectrum is very constrained by data. We also confirm that the experimental upper bounds of the processes $l_j \to l_i\,\gamma$ are more restrictive than the $l_j \to 3\, l_i$ ones but all together will allow to extract large excluded regions of the CMSSM-seesaw parameter space.

2.3.3 Sensitivity to θ_{13}

We have also investigated, as in Section 2.1.3 for $l_j \to l_i\,\gamma$ decays, how sensitive to θ_{13} the BR$(l_j \to 3\, l_i)$ are and we have found that these ratios present a similar behaviour with θ_{13} as their corresponding correlated LFV radiative decays.

In Fig. 2.33 we plot the branching ratios of $\mu \to 3\, e$ and $\tau \to 3\, e$ decays as a function of θ_{13}, which we vary in the range $[0°, 10°]$. We also display, for comparison, the lines associated with the present experimental bounds and future sensitivities. In each case, we consider as input the

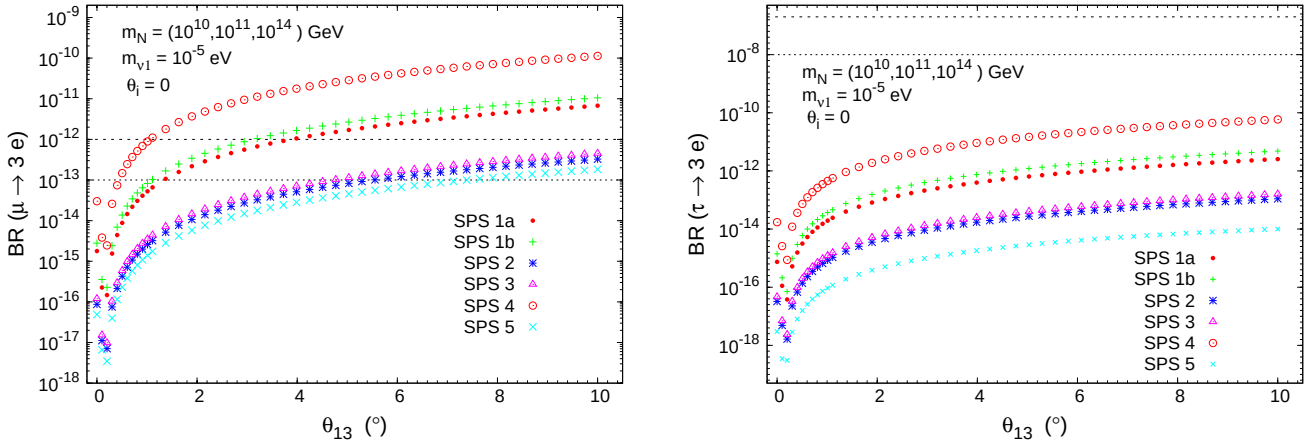

Figure 2.33: BR($\mu \to 3\,e$) and BR($\tau \to 3\,e$) as a function of θ_{13} (in degrees), for SPS 1a (dots), 1b (crosses), 2 (asterisks), 3 (triangles), 4 (circles) and 5 (times). A dashed (dotted) horizontal line denotes the present experimental bound (future sensitivity).

six SPS points, and take $\theta_i = 0$, so there is no flavour mixing arising from the right-handed neutrino sector. Regarding the neutrino masses, we have assumed $m_{\nu_1} = 10^{-5}$ eV, while the masses of the heavy right-handed are set here to $m_N = (10^{10}, 10^{11}, 10^{14})$ GeV.

One can infer from Fig. 2.33 that both $\mu \to 3\,e$ and $\tau \to 3\,e$ channels display a strong dependence on θ_{13}, as their correlated $\mu \to e\,\gamma$ and $\tau \to e\,\gamma$ decays. The observed qualitative behaviour with respect to θ_{13} can also be easily understood from Eq. (1.85). Regarding the $\tau \to 3\,\mu$ channel, the corresponding branching ratios do not exhibit any noticeable dependence on θ_{13}, as expected from $\tau \to \mu\,\gamma$ results in Section 2.1.3. For the case $R = \mathbb{1}$, and taking for example $\theta_{13} = 5°$, these BRs are presented in Table 2.4.

BR	SPS 1a	SPS 1b	SPS 2	SPS 3	SPS 4	SPS 5
$\tau \to 3\,\mu$	9.4×10^{-12}	1.8×10^{-11}	4.1×10^{-13}	5.9×10^{-13}	2.2×10^{-10}	4.3×10^{-14}

Table 2.4: Predictions for the BR($\tau \to 3\,\mu$) corresponding to the SPS points. The values of m_{N_i} and m_{ν_1} are as specified in Fig. 2.33. In each case, the predicted values should be compared with the present bound (future prospect) BR($\tau \to 3\,\mu$) $< 3.2 \times 10^{-8}$ (10^{-8}).

The main conclusion to be inferred from Figs. 2.33 and Table 2.4 is that, for the assumed value of m_{ν_1}, and for the chosen seesaw scenario (which is specified by θ_i and m_{N_i}), $\mu \to 3\,e$ is the decay whose BRs are within the reach of present experiments, thus potentially allowing to constrain the values of θ_{13}. In fact, if we do a similar analysis as for BR($\mu \to e\,\gamma$) in Section 2.1.3, BR($\mu \to 3\,e$) would exclude θ_{13} values above 1°, 3° and 4° for SPS 4, 1a and 1b, respectively.

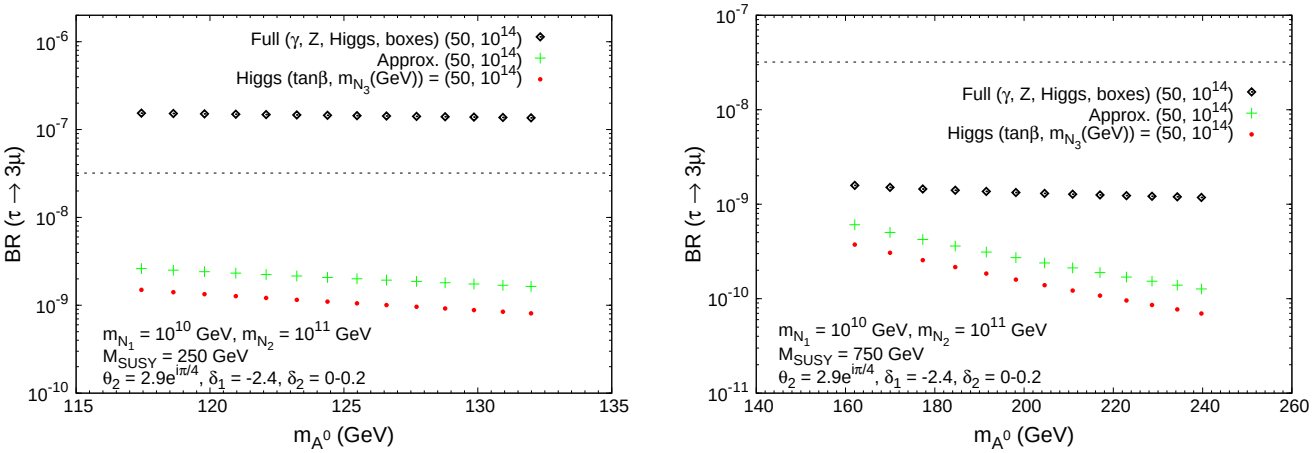

Figure 2.34: Comparison between the full and approximate results for $\tau \to 3\mu$ as a function of m_{A^0} in the NUHM scenario, for $M_{\rm SUSY} = M_0 = M_{1/2} = 250$ GeV (left panel) and for $M_{\rm SUSY} = M_0 = M_{1/2} = 750$ GeV (right panel). The dashed horizontal line is the present experimental upper bound [69].

2.3.4 $l_j \to 3\, l_i$ in NUHM-seesaw scenarios

As we have already explained, the NUHM-seesaw scenarios possess the interesting peculiarity of a light Higgs sector. In the NUHM scenarios that are considered here with small Higgs masses, one may guess that the Higgs-mediated contribution could dominate the rates at large $\tan\beta$, but it is not so as will be shown next. By using the tau-muon-Higgs form factors in Eq. 2.14 and plugging it into the exact formula for the Higgs contribution [102], we get in the large $\tan\beta$ limit

$$\begin{aligned} {\rm BR}(\tau \to 3\mu)_{H_{\rm approx}} &= \frac{G_F^2}{2048\pi^3}\frac{m_\tau^7 m_\mu^2}{\Gamma_\tau}\left(\frac{1}{m_{H^0}^4}+\frac{1}{m_{A^0}^4}+\frac{2}{3m_{H^0}^2 m_{A^0}^2}\right)\left|\frac{g^2\delta_{32}}{96\pi^2}\right|^2 (\tan\beta)^6 \quad (2.39)\\ &= 1.2\times 10^{-7}\,|\delta_{32}|^2\left(\frac{100}{m_{A^0}({\rm GeV})}\right)^4\left(\frac{\tan\beta}{60}\right)^6, \quad (2.40)\end{aligned}$$

which is in good agreement with the original result in [53] and also with posterior estimates [71, 203]. The comparison between the full (i.e. including one-loop SUSY diagrams mediated by γ, Z, h_0, H_0, A_0 and box diagrams which are taken from [102]) and the approximate numerical results for this channel is shown in Fig. 2.34. We see that the formula in Eq. (2.40) predicts rates that are about a factor of 2 larger than the exact Higgs-mediated contribution. Therefore, for large $\tan\beta$ values, it provides a good estimate of the Higgs contribution. However, the total rates are much larger than the Higgs contribution, since the photon-mediated diagrams give by far the dominant contribution in this channel. For instance, we see in Fig. 2.34 that the total

and Higgs rates differ in about two orders of magnitude for $M_{\rm SUSY} \sim 250$ GeV and in more than a factor 5 for $M_{\rm SUSY} \sim 750$ GeV. It is remarkable that, in this channel, the photon dominance holds largely even in scenarios with very heavy SUSY spectra, as for $M_{\rm SUSY} \sim 750$ GeV, and Higgs bosons as light as $m_H = 160$ GeV. Therefore, the total rates for this channel can be better approximated by the simplified formula of the photon-mediated contribution of Eq. 2.38,

$$\begin{aligned} {\rm BR}(\tau \to 3\mu)_{\gamma_{\rm approx}} &= \frac{\alpha}{3\pi}\left(\log\frac{m_\tau^2}{m_\mu^2} - \frac{11}{4}\right) {\rm BR}(\tau \to \mu\gamma) \\ &= 2.3 \times 10^{-3}\ {\rm BR}(\tau \to \mu\gamma) \\ &= 3.4 \times 10^{-5}\, |\delta_{32}|^2 \left(\frac{100}{M_{\rm SUSY}({\rm GeV})}\right)^4 \left(\frac{\tan\beta}{60}\right)^2, \end{aligned} \tag{2.41}$$

where the last line has been obtained by using the result of ${\rm BR}(\tau \to \mu\gamma)$ in the MI approximation for equal SUSY mass scales and in the large $\tan\beta$ limit. It is also interesting to compare this estimate with the present experimental upper bound for this channel summarised in Table 2.3. We see in Fig. 2.34 that, for the chosen parameters in this plot, the predicted rates are above the present experimental bound for $M_{\rm SUSY} < 300$ GeV.

2.3.5 Summary

We have shown in this section that the LFV τ and μ decays do provide a very efficient tool to look for indirect SUSY signals.

With the motivation in mind of testing SUSY we have studied exhaustively the particular decays $\tau \to 3\mu$, $\tau \to 3e$ and $\mu \to 3e$, and the correlated radiative decays $\tau \to \mu\gamma$, $\tau \to e\gamma$ and $\mu \to e\gamma$. All of these channels have quite challenging experimental bounds and they are expected to improve in the future . We have explored the dependence of the branching ratios for these LFV processes with the various parameters involved, namely, the SUSY and seesaw parameters. We have computed and analyzed in full detail all the contributions from the SUSY-loops to the $l_j \to 3\, l_i$ decays. Our analytical results for these decays correct and complete previous results in the literature. In particular we have presented the results for the separate contributions from the γ-penguin, the Z-penguin, the Higgs-penguin and the box diagrams and shown explicitely the γ-penguin dominance. In the numerical estimates we have presented results for both the $l_j \to 3\, l_i$ and the correlated radiative decays $l_j \to l_i\, \gamma$.

For the degenerate heavy neutrinos case, we have got rates for all the studied LFV τ and μ decays that are below the present experimental upper bounds. The largest rates we get, within the explored range of the seesaw and SUSY parameter space, are for the τ decays. Specifically, $BR(\tau \to \mu\gamma) \sim 10^{-8}$ and $BR(\tau \to 3\,\mu) \sim 3 \times 10^{-11}$, corresponding to the extreme values of $\tan\beta = 50$ and $m_N = 10^{14}$ GeV and for the lowest explored values of M_0 and $M_{1/2}$. The case

of hierarchical heavy neutrinos turns out to be much more interesting.

We have analysed in detail the behaviour of the branching ratios with the SUSY and seesaw parameters also in the hierarchical case. The largest ratios found are again for $\tau \to \mu\,\gamma$ and $\tau \to 3\,\mu$ decays. All the LFV τ and μ decay rates are mainly sensitive to $\tan\beta$, the heaviest neutrino mass m_{N_3}, which we have set to $m_{N_3} = 10^{14}$ GeV, and the complex angles in the R matrix θ_1 and θ_2, which have been taken in the range $3 < \tan\beta < 50$, $0 < |\theta_i| < 3$ and $0 < \arg\theta_i < \pi/4$. For the values of these parameters at the upper limit of this studied interval we have found that some of the predicted branching ratios are clearly above the corresponding experimental upper bounds. The most restrictive channels turn out $\mu \to e\,\gamma$, $\mu \to 3\,e$ and $\tau \to \mu\,\gamma$. Therefore, we get in this region important restrictions on the posible values of the SUSY and seesaw parameters. In particular, for $\theta_2 = 2.8e^{i\pi/4}$, we get that the whole studied range of $100\,\text{GeV} < M_0, M_{1/2} < 800\,\text{GeV}$ with $\tan\beta = 50$ is totally excluded by $\tau \to \mu\,\gamma$. Values of M_0 and $M_{1/2}$ in the low region below 250 GeV are also excluded by $\tau \to 3\,\mu$ data. The case of θ_1 is even more restrictive, because the predictions for $\mu \to e\,\gamma$, $\mu \to 3\,e$ and $\tau \to \mu\,\gamma$ totally exclude a light SUSY scenario, for practicaly all θ_1 values.

Perhaps, the most striking result is that even for the most conservative choice of $R = \mathbb{1}$, that is $\theta_1 = \theta_2 = \theta_3 = 0$, there are also important restrictions at low M_0, $M_{1/2}$ and large $\tan\beta$ values. In particular, for $\tan\beta = 50$, values lower or equal than $M_0 = 250$ GeV and $M_{1/2} = 150$ GeV are totally excluded by $\tau \to \mu\,\gamma$, $\mu \to e\,\gamma$ and $\mu^- \to 3\,e$ data.

Finally, we have also studied the $\tau \to 3\,\mu$ decay in the NUHM-seesaw context and concluded that, although the Higgs-mediated contributions can be increased in these scenarios by some orders of magnitude, the photon dominance still holds largely even in scenarios with very heavy SUSY spectra. Therefore, the total rates for this channel can be approximated by the formula of the photon-mediated contribution.

Some approximate formulae valid at large $\tan\beta$ and large M_{SUSY} have been also presented, which are useful for future comparison with data.

Chapter 3

LFV in semileptonic τ decays

In this chapter LFV semileptonic τ decay channels are studied, which are also of interest because of the recently reported sensitivity by BELLE and BABAR collaborations [72–75] that are, for some channels, already competitive with the LFV τ leptonic ones. We have focused our study on the following semileptonic τ decays:

- $\tau \to \mu PP$ with $PP = \pi^+\pi^-, \pi^0\pi^0, K^+K^-, K^0\bar{K}^0$,
- $\tau \to \mu P$ with $P = \pi^0, \eta^0, \eta'^0$,
- $\tau \to \mu V$ with $V = \rho^0, \phi$,

whose present upper experimental bounds (90% CL) are summarised in Table 3. As in the previous chapters, we work here within the context of two types of constrained SUSY-seesaw scenarios: the CMSSM-seesaw and the NUHM-seesaw. A full one-loop computation of the branching ratios for these decays are presented and the importance of the various contributions, the γ-, Z-, and Higgs bosons mediated ones are analysed. The hadronisation of quark bilinears is performed within the chiral framework. We further present here a set of approximate formulae for all the semileptonic channels which we believe can be useful for further comparison with present and future data. A comparison with other works in the literature is also performed in this chapter.

3.1 Theoretical framework for LFV semileptonic τ decays

In this section we describe the theoretical framework for the computation of the LFV semileptonic τ decay rates. First we summarise the relevant parameters for the study of LFV in the τ-μ

LFV semilep. τ decays	BABAR	Belle	BABAR & Belle
$\mathrm{BR}(\tau \to \mu\eta)$	1.5×10^{-7} [74]	6.5×10^{-8} [73]	5.1×10^{-8} [68]
$\mathrm{BR}(\tau \to \mu\eta')$	1.4×10^{-7} [74]	1.3×10^{-7} [73]	5.3×10^{-8} [68]
$\mathrm{BR}(\tau \to \mu\pi)$	1.1×10^{-7} [74]	1.2×10^{-7} [73]	5.8×10^{-8} [68]
$\mathrm{BR}(\tau \to \mu\rho)$	—	2.0×10^{-7} [72]	—
$\mathrm{BR}(\tau \to \mu\phi)$	—	1.3×10^{-7} [204]	—
$\mathrm{BR}(\tau \to \mu\pi^+\pi^-)$	—	4.8×10^{-7} [72]	—
$\mathrm{BR}(\tau \to \mu\pi^0\pi^0)$	—	—	—
$\mathrm{BR}(\tau \to \mu K^+K^-)$	—	8.0×10^{-7} [72]	—
$\mathrm{BR}(\tau \to \mu K^0\bar{K}^0)$	—	—	—

Table 3.1: Present upper bounds for LFV semileptonic τ decays.

sector, and later we present the main ingredients to perform the hadronisation of quark bilinears within the context of Chiral Perturbation Theory (χPT) and Resonance Chiral Theory (RχT).

3.1.1 Relevant parameters for LFV semileptonic τ decays in SUSY-seesaw scenarios

As we have said, we also choose to work here in two different constrained SUSY-seesaw scenarios: the CMSSM-seesaw with similar input parameters as in mSUGRA models, and the NUHM-seesaw scenario with two additional parameters defining the non-universal soft Higgs masses. Both scenarios and their relevant parameters have been reviewed in Chapter 1. Besides, in order to reduce the number of SUSY-seesaw input parameters we will set for the numerical estimates in this chapter $M_0 = M_{1/2}$, $\mathrm{sign}(\mu) > 0$ and $A_0 = 0$. Notice that the most important difference with respect to the CMSSM case is that in these NUHM scenarios there can be light Higgs masses even for large M_{SUSY} values.

Concerning our choice for the size of the physical neutrino parameters, we shall focus in this chapter on scenarios where both light and heavy neutrinos are hierarchical, and set the numerical values for the light neutrino parameters to the values given in Section 1.1, which are compatible with present data [10, 115–117]. We further set here $\theta_{13} = 0$ and neglect m_{ν_1}.

In order to illustrate more quantitatively how important can be the size of the flavour mixing between the stau and smuon sectors in the CMSSM-seesaw scenario, we recall our predictions in Section 1.5 of the relevant mixing parameter for $\tau - \mu$ transitions δ_{32} as a function of $|\theta_2|$ and m_{N_3} in Figs. 1.3 and 1.4. This phenomenological parameter δ_{32} measures the amount of flavour mixing between the second and third slepton generations in the left-handed sector (LL),

which is by far the dominant one. The corresponding mixing in the right-handed slepton sector is extremely suppressed by the smallness of the lepton masses which appear as global factors in the definitions of those (RR and RL) mixings (see, for instance, [102]). We have checked that $|\delta_{32}|$ is practically independent on θ_3 and the corresponding predictions with respect to θ_1 are very similar to those of θ_2. Moreover, as we have also commented in Section 1.5, δ_{32} is not very dependent on the values of $\tan\beta$ and $m_{N_{1,2}}$. Therefore, for the rest of this chapter we will fix the values of these two heavy neutrino masses to $m_{N_{1,2}} = 10^{10}, 10^{11}$ GeV. We will further set $\theta_{1,3} = 0$ and use θ_2 and m_{N_3} as input neutrino parameters.

3.1.2 Hadronisation of quark bilinear currents

Semileptonic decays of the tau lepton are a relatively clean scenario from the strong interaction point of view. Hadrons in the final state stem from the hadronisation of quark bilinears, namely $\overline{\psi}\,\Gamma\psi$, where ψ is a vector in the $SU(3)_F$ flavour space and Γ is, in general, a matrix both in the spinor and the flavour space.

An appropriate framework to handle the procedure of hadronisation is provided by the large-N_C expansion of $SU(N_C)$ QCD [205], being N_C the number of colours. In short it stays that in the $N_C \to \infty$ limit any Green function is given by meromorphic expressions provided by the tree level diagrams of a Lagrangian theory with an infinite spectrum of zero-width states. Though we do not know how to implement fully this limit, a fruitful [206] if debatable [207] approach lies in cutting the spectrum, keeping only the lightest multiplets of resonances. We will attach to this tenet as a guiding principle.

A suitable tool to realise the $1/N_C$ expansion is provided by chiral Lagrangians. In those processes where hadron resonances do not play a dynamical role, χPT [208, 209] is the appropriate scheme to describe the strong interaction of Goldstone bosons (π, K and η). This is the case, for instance, of $\tau \to \mu P$ (being P short for a pseudoscalar meson). When resonances participate in the dynamics of the process, as in $\tau \to \mu PP$, it is necessary to include them as active degrees of freedom into the Lagrangian as it is properly done in the RχT frame [210]. Hence we will make use of RχT, that naturally includes χPT, to hadronise the relevant currents that appear in the processes under study here.

We consider bilinear light quark operators coupled to external sources and added to the massles QCD Lagrangian:

$$\mathcal{L}_{\rm QCD} \,=\, \mathcal{L}^0_{\rm QCD} + \overline{q}\,[\gamma_\mu\,(v^\mu \,+\, \gamma_5\,a^\mu) \,-\, (\,s \,-\, i\,p\,\gamma_5)]\,q\,, \tag{3.1}$$

where vector ($v^\mu = v^\mu_i\lambda^i/2$), axial-vector ($a^\mu = a^\mu_i\lambda^i/2$), scalar ($s = s_i\lambda^i$) and pseudoscalar ($p = p_i\lambda^i$) fields are matrices in the flavour space, and $\mathcal{L}^0_{\rm QCD}$ is the massless QCD Lagrangian[1].

[1]The Gell-Mann matrices λ^i are normalised as $\langle\lambda_i\lambda_j\rangle = 2\delta_{ij}$ and the gluons are denoted here by G_μ.

This Lagrangian density gives the QCD generating functional $\mathcal{Z}_{\rm QCD}\,[v,a,s,p]$ as

$$e^{i\,\mathcal{Z}_{\rm QCD}[v,a,s,p]} \,=\, \int [\,DG_\mu\,][\,Dq\,][\,D\overline{q}\,]\, e^{i\,\int d^4x\,\mathcal{L}_{\rm QCD}[q,\overline{q},G,v,a,s,p]}\,. \tag{3.2}$$

In order to construct the corresponding Lagrangian theory in terms of the lightest hadron modes we need to specify them. The lightest $U(3)$ nonet of pseudoscalar mesons

$$\begin{aligned}\phi(x) \;&=\; \sum_{a=0}^{8}\,\frac{\lambda_a}{\sqrt{2}}\,\varphi_a \qquad\qquad (3.3)\\ &=\; \left(\begin{array}{ccc} \frac{1}{\sqrt{2}}\,\pi^0+\frac{1}{\sqrt{6}}\,\eta_8+\frac{1}{\sqrt{3}}\eta_0 & \pi^+ & K^+ \\ \pi^- & -\frac{1}{\sqrt{2}}\,\pi^0+\frac{1}{\sqrt{6}}\,\eta_8+\frac{1}{\sqrt{3}}\eta_0 & K^0 \\ K^- & \bar{K}^0 & -\frac{2}{\sqrt{6}}\,\eta_8+\frac{1}{\sqrt{3}}\eta_0 \end{array}\right)\,,\end{aligned}$$

is realised nonlinearly into the unitary matrix in the flavour space,

$$u(\varphi)=\exp\left[i\,\frac{\Phi}{\sqrt{2}F}\right]. \tag{3.4}$$

Hence the leading $\mathcal{O}(p^2)$ χPT $SU(3)_L\otimes SU(3)_R$ chiral Lagrangian is[2]

$$\mathcal{L}_\chi^{(2)} \;=\; \frac{F^2}{4}\,\langle u_\mu\,u^\mu \,+\, \chi_+\rangle\,, \tag{3.5}$$

where

$$\begin{aligned} u_\mu \;&=\; i[u^\dagger(\partial_\mu - ir_\mu)u - u(\partial_\mu - i\ell_\mu)u^\dagger]\,,\\ \chi_+ \;&=\; u^\dagger\chi u^\dagger + u\chi^\dagger u \quad,\quad \chi = 2B_0(s+ip)\;\;, \end{aligned} \tag{3.6}$$

and $\langle\ldots\rangle$ is short for a trace in the flavour space. Interactions with electroweak bosons can be accommodated through the vector $v_\mu=(r_\mu+\ell_\mu)/2$ and axial-vector $a_\mu=(r_\mu-\ell_\mu)/2$ external fields. The scalar field s incorporates explicit chiral symmetry breaking through the quark masses $s=\mathcal{M}+...$ and, finally, $F\simeq F_\pi\simeq 92.4$ MeV is the pion decay constant and $B_0F^2=-\langle 0|\overline{\psi}\psi|0\rangle_0$ in the chiral limit. The chiral tensor χ provides masses to the Goldstone bosons through the external scalar field, as can be seen in Eq. (3.6). Indeed in the isospin limit we have

$$\chi \,=\, 2\,B_0\,\mathcal{M}\,+...\,=\,\left(\begin{array}{ccc} m_\pi^2 & & \\ & m_\pi^2 & \\ & & 2m_K^2-m_\pi^2 \end{array}\right)\,+\,.... \tag{3.7}$$

[2]Notice that though we include a $U(3)$ nonet we are not relying on the $U(3)_L\otimes U(3)_R$ chiral Lagrangian [211] on grounds of predictability, as the latter introduces unknown functions.

Hence we identify

$$\begin{aligned} B_0\, m_u &= B_0\, m_d = \frac{1}{2}\, m_\pi^2 \,, \\ B_0\, m_s &= m_K^2 - \frac{1}{2}\, m_\pi^2 \,, \end{aligned} \tag{3.8}$$

that will be useful when considering the Higgs contributions. The mass eigenstates η and η' are defined from the octet η_8 and singlet η_0 states through the rotation

$$\begin{pmatrix} \eta \\ \eta' \end{pmatrix} = \begin{pmatrix} \cos\theta & -\sin\theta \\ \sin\theta & \cos\theta \end{pmatrix} \begin{pmatrix} \eta_8 \\ \eta_0 \end{pmatrix} , \tag{3.9}$$

and we input[3] a value of $\theta \simeq -18^\circ$.

The hadronisation of a final state of two pseudoscalars is driven by vector and scalar resonances though the latter, because of their higher masses, play a lesser role and we will not include them in the following. We will introduce the vector resonances in the antisymmetric formalism; hence the nonet of resonance fields $V_{\mu\nu}$ [210] is defined by analogy with Eq. (3.3) with the same flavour structure. By demanding the chiral symmetry invariance the resonance Lagrangian reads as

$$\mathcal{L}_V \,=\, \mathcal{L}_{\rm kin}^V \,+\, \mathcal{L}_{(2)}^V \,, \tag{3.10}$$

where

$$\begin{aligned} \mathcal{L}_{\rm kin}^V &= -\frac{1}{2}\langle\, \nabla^\lambda V_{\lambda\mu} \nabla_\nu V^{\nu\mu} \,\rangle + \frac{M_V^2}{4}\, \langle\, V_{\mu\nu} V^{\mu\nu} \,\rangle \,, \\ \mathcal{L}_{(2)}^V &= \frac{F_V}{2\sqrt{2}} \langle V_{\mu\nu} f_+^{\mu\nu} \rangle + i\, \frac{G_V}{\sqrt{2}} \langle V_{\mu\nu} u^\mu u^\nu \rangle \;, \end{aligned} \tag{3.11}$$

and in the latter the subscript (2) indicates the chiral order of the tensor accompanying the vector field. In Eq. (3.11) we have used the definitions

$$\begin{aligned} \nabla_\mu X &\equiv \partial_\mu X + [\,\Gamma_\mu, X] \;, \\ \Gamma_\mu &= \frac{1}{2}\,[\, u^\dagger (\partial_\mu - i r_\mu) u + u (\partial_\mu - i \ell_\mu) u^\dagger \,] \;, \\ f_+^{\mu\nu} &= u F_L^{\mu\nu} u^\dagger + u^\dagger F_R^{\mu\nu} u \,, \end{aligned} \tag{3.12}$$

being $F_{L,R}^{\mu\nu}$ the field strength tensors associated with the external right and left fields. The couplings F_V and G_V are real.

Accordingly our RχT framework is provided by

$$\mathcal{L}_{\rm R\chi T} \,=\, \mathcal{L}_\chi^{(2)} \,+\, \mathcal{L}_V \,, \tag{3.13}$$

[3]The values of θ in the literature range between $\theta \sim -12^\circ$ up to $\theta \sim -20^\circ$ [212].

and the contribution of the low modes to the QCD functional is formally given by

$$e^{i\,\mathcal{Z}_{\rm QCD}[v,a,s,p]}\Big|_{\text{low modes}} = \int [Du][DV]\, e^{i\int d^4x\,\mathcal{L}_{\rm R\chi T}[u,V,v,a,s,p]}\,. \tag{3.14}$$

With this identification we can already carry out the hadronisation of the bilinear quark currents included in Eq. (3.1) by taking the appropriate partial derivatives, with respect to the external auxiliary fields, of the functional action,

$$\begin{aligned} V^i_\mu = \overline{q}\,\gamma_\mu\,\frac{\lambda^i}{2}\,q \;&=\; \frac{\partial\,\mathcal{L}_{\rm R\chi T}}{\partial\, v^\mu_i}\bigg|_{j=0}\,, \qquad A^i_\mu = \overline{q}\,\gamma_\mu\,\gamma_5\,\frac{\lambda^i}{2}\,q \;=\; \frac{\partial\,\mathcal{L}_{\rm R\chi T}}{\partial\, a^\mu_i}\bigg|_{j=0}\,, \\ S^i = -\,\overline{q}\,\lambda^i\,q \;&=\; \frac{\partial\,\mathcal{L}_{\rm R\chi T}}{\partial\, s_i}\bigg|_{j=0}\,, \qquad P^i = \overline{q}\,i\gamma_5\lambda^i\,q \;=\; \frac{\partial\,\mathcal{L}_{\rm R\chi T}}{\partial\, p_i}\bigg|_{j=0}\,, \end{aligned} \tag{3.15}$$

where $j=0$ indicates that all external currents are set to zero. This gives

$$\begin{aligned} V^i_\mu &= \frac{F^2}{4}\,\langle\,\lambda^i\,\Big(u\,u_\mu\,u^\dagger\,-\,u^\dagger\,u_\mu\,u\Big)\,\rangle\,-\,\frac{F_V}{2\sqrt{2}}\,\langle\,\lambda^i\,\partial^\nu\,\Big(u^\dagger\,V_{\nu\mu}\,u\,+\,u\,V_{\nu\mu}\,u^\dagger\Big)\,\rangle\,, \\ A^i_\mu &= \frac{F^2}{4}\,\langle\,\lambda^i\,\Big(u\,u_\mu\,u^\dagger\,+\,u^\dagger\,u_\mu\,u\Big)\,\rangle\,, \\ S^i &= \frac{1}{2}\,B_0F^2\,\langle\,\lambda^i\,\Big(u^\dagger u^\dagger\,+\,uu\Big)\rangle\,, \\ P^i &= \frac{i}{2}\,B_0F^2\,\langle\,\lambda^i\,\Big(u^\dagger u^\dagger\,-\,uu\Big)\rangle\,. \end{aligned} \tag{3.16}$$

With these expressions we are able to hadronise the final states in $\tau\to\mu PP$ and $\tau\to\mu P$ processes as we explain now.

γ contribution

The photon contribution to the decay into two pseudoscalar mesons is driven by the electromagnetic current

$$V^{\rm em}_\mu \;=\; \sum_q^{u,d,s} Q_q\,\overline{q}\,\gamma_\mu\,q \;=\; V^3_\mu\,+\,\frac{1}{\sqrt{3}}\,V^8_\mu\,, \tag{3.17}$$

where Q_q is the electric charge of the q quark in units of the positron charge e. The electromagnetic form factor is then defined as

$$\langle\,P_1(p_1)P_2(p_2)\,|\,V^{em}_\mu\,|\,0\,\rangle \;=\; (p_1-p_2)_\mu\,F_V^{P_1P_2}(s)\,, \tag{3.18}$$

where $F_V^{P_1P_2}(s)$ is steered by both $I=1$ and $I=0$ vector resonances, in particular the $\rho(770)$ that is the lightest of resonances. Due to the $q^2=0$ pole of the photon propagator this is, by far, the dominant contribution to this hadronic final state. Hence the result is more sensitive to

the construction of this form factor. Accordingly we will elaborate a more complete expression than the one provided by the vector current in Eq. (3.16) though it will reduce to this one in the $N_C \to \infty$ limit, including only one multiplet of resonances and at $q^2 \ll M_\rho^2$. A proper construction of $F_V^{P_1 P_2}(s)$ is given in Appendix D.

Z^0 contribution

Here both vector and axial-vector currents do contribute. In terms of the quark fields these are

$$\begin{aligned} J_\mu^Z &= V_\mu^Z + A_\mu^Z \,, \\ V_\mu^Z &= \frac{g}{2\,\cos\theta_W}\,\overline{q}\,\gamma_\mu\,\left[2\sin^2\theta_W Q - T_3^{(q)}\right]\,q \,, \\ A_\mu^Z &= \frac{g}{2\,\cos\theta_W}\,\overline{q}\,\gamma_\mu\,\gamma_5\,T_3^{(q)}\,q \,, \end{aligned} \tag{3.19}$$

with $Q = \mathrm{diag}(2,-1,-1)/3$ and $T_3^{(q)} = \mathrm{diag}(1,-1,-1)/2$ the electric charge and weak hypercharges, respectively, g is the $SU(2)$ gauge coupling and θ_W is the weak angle.

In order to proceed to the hadronisation of these currents one has to write the currents in Eq. (3.19) in terms of V_μ^i and A_μ^i defined in Eq. (3.16). This gives

$$\begin{aligned} V_\mu^Z &= \frac{g}{2\,\cos\theta_W}\,\frac{F^2}{2}\,\left[2\,\sin^2\theta_W\,\langle\, Q\,\left(uu_\mu u^\dagger - u^\dagger u_\mu u\right)\rangle\,-\,\langle\, T_3^{(q)}\,\left(uu_\mu u^\dagger - u^\dagger u_\mu u\right)\rangle\right]\,, \\ A_\mu^Z &= \frac{g}{2\,\cos\theta_W}\,\frac{F^2}{2}\langle\, T_3^{(q)}\,\left(uu_\mu u^\dagger + u^\dagger u_\mu u\right)\rangle\,. \end{aligned} \tag{3.20}$$

Notice that the vector current contributes to an even number of pseudoscalar mesons while the axial-vector current provides 1, 3,... mesons.

Higgs bosons contribution

Hadronisation of scalar Higgs bosons like h^0 and H^0 into two pseudoscalar mesons proceeds through the scalar current while the pseudoscalar A^0 Higgs boson hadronises through the pseudoscalar current into one pseudoscalar meson. As Higgs bosons are rather massive the hadronisation is not so sensitive to resonances as in the case of the photon contribution. Hence we will not elaborate on scalar of pseudoscalar form factors (analogous to the vector case defined by Eq. (3.18)) that, moreover, are not so well known. We will rely in the following scalar and pseudoscalar currents:

$$\begin{aligned} \overline{u}\,\Gamma\,u &= \frac{1}{2}J^3 + \frac{1}{2\sqrt{3}}J^8 + \frac{1}{\sqrt{6}}J^0 \,, \\ \overline{d}\,\Gamma\,d &= -\frac{1}{2}J^3 + \frac{1}{2\sqrt{3}}J^8 + \frac{1}{\sqrt{6}}J^0 \,, \\ \overline{s}\,\Gamma\,s &= -\frac{1}{\sqrt{3}}J^8 + \frac{1}{\sqrt{6}}J^0 \,, \end{aligned} \tag{3.21}$$

where $\Gamma = -1$ for $J^i \equiv S^i$, $\Gamma = i\gamma_5$ for $J^i \equiv P^i$ and the S^i and P^i currents are given in Eq. (3.16).

3.2 Analytical results for LFV semileptonic τ decays

In this section we present the analytical results of the branching ratios for the LFV semileptonic τ decays: $\tau \to \mu PP$, with $PP = \pi^+\pi^-$,$\pi^0\pi^0$, K^+K^-, $K^0\bar{K}^0$ and $\tau \to \mu P$, with $P = \pi$, η and η'. The predictions for the $\tau \to \mu\rho^0$ and $\tau \to \mu\phi^0$ channels, which are related to $\tau \to \mu\pi^+\pi^-$ and $\tau \to \mu K^+K^-, \mu K^0\bar{K}^0$, respectively, will also be included.

In the previous related literature there are, to our knowledge, just a few theoretical computations of some of these LFV semileptonic τ decays induced by SUSY-loops. In particular, $\tau \to \mu\eta$ was first computed in [54] within the context of the unconstrained MSSM and in the approximation of large $\tan\beta$. A more refined analysis of this channel, $\tau \to \mu\eta'$, $\tau \to \mu\pi^0$, and $\tau \to \mu\rho^0$ was done in [203] for the unconstrained MSSM scenario and large $\tan\beta$ approximation as well, but they used an effective lagrangian framework for the LFV operators. An estimate of $\tau \to \mu\eta$ with the use of the MI approximation for the relevant lepton flavour mixing parameter between the τ and μ sectors, δ_{32}, has been performed in [179]. The decay mode $\tau \to \mu K^+K^-$ has been estimated in [213] within the MI and LLog approximations for δ_{32}, and taking into account only the Higgs-mediated contribution in the large $\tan\beta$ limit. In all these previous works no connection with the neutrino sector was considered and the hadronisation of quark bilinears in the final state is simply parameterised in terms of the proper meson decay constants and meson masses.

Our analysis presented here is more complete in several aspects. First, we include both Z-boson and A^0-boson mediated contributions to $\tau \to \mu P$ ($P = \eta, \eta', \pi^0$), and both γ and H^0, h^0-bosons mediated contributions to $\tau \to \mu K^+K^-$ and $\tau \to \mu\rho^0$. The other channels, $\tau \to \mu K^0\bar{K}^0$ and $\tau \to \mu\pi^0\pi^0$ have not been estimated previously. We include γ and H^0, h^0-bosons mediated contributions in $\tau \to \mu K^0\bar{K}^0$. The case $\tau \to \mu\pi^0\pi^0$ can only be mediated by H^0, h^0-bosons. Second, we do not use either the MI nor the LLog approximation and our analytical computation is valid for all $\tan\beta$ values. Third, we make a connection with neutrino physics by requiring compatibility through all this work with the neutrino data for masses and mixing angles. Fourth, we perform the hadronisation of quark bilinears with close attention to the chiral constraints, guided by the RχT [210] that has proven to be a robust framework for the analyses of hadrodynamics when resonances are involved. The γ amplitude, due to its pole at $q^2 = 0$, is most sensitive to the hadronisation procedure. Hence the hadronisation of the electromagnetic current, that drives the γ contributions, has been carried out by a careful construction of the vector form factor that matches both the chiral low-energy limit and the asymptotic smoothing

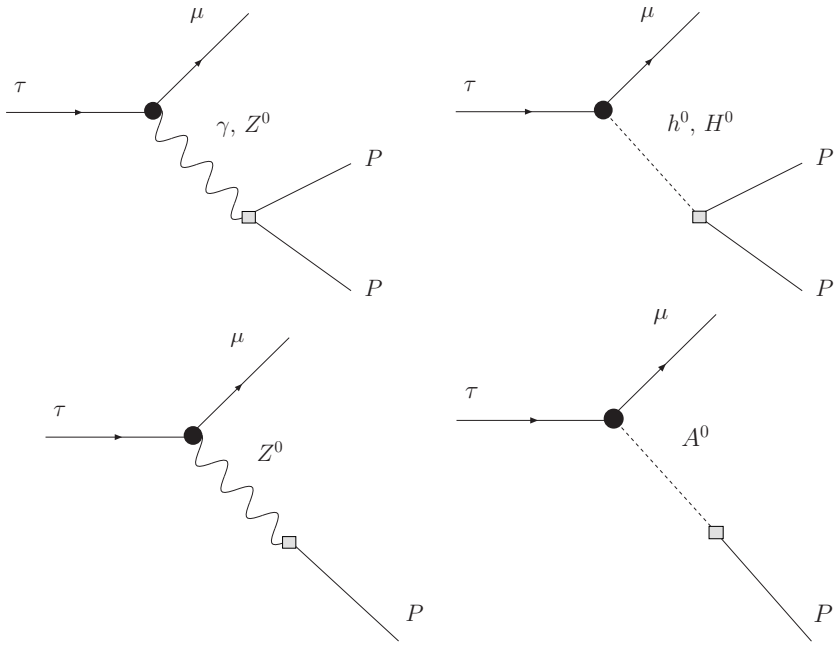

Figure 3.1: Contributions to LFV semileptonic τ decays into one and two pseudoscalar mesons.

at high q^2 [214]. Those final states driven by heavy intermediate bosons like the Z^0 or Higgses, on the other side, do not require such an involved scheme. In these cases we have used the leading chiral approximation that we know, for sure, it has to be fulfilled by the hadronisation. The advantage of our approach is that it provides the most successful description up to date of the hadronic tau decays and it can be systematically improved by further developments of the appropriate form factors, whether axial-vector, scalar or pseudoscalar cases.

3.2.1 Predictions for $\tau \to \mu PP$

The semileptonic $\tau \to \mu PP$ channels can be mediated by a photon, a Z gauge boson and a CP-even Higgs boson, h^0 and H^0. The various contributing diagrams are depicted in Fig. 3.1. In these diagrams, the LFV vertex is represented by a black circle and the hadronic vertex by a white box. The Z-mediated contribution is expected to be much smaller than the γ-mediated contribution due to the $\mathcal{O}(1/m_Z^2)$ suppression factor in the amplitude from the Z propagator. This has been shown to happen in the leptonic channels like $\tau \to 3\mu$, where the Z-mediated contribution to its branching ratio has been estimated to be a factor $10^{-3} - 10^{-5}$ smaller than the γ-mediated contribution, for $\tan\beta = 5 - 50$ [102]. Consequently, we have neglected here the Z contribution to the $\tau \to \mu PP$ decays. By using again this comparison with $\tau \to 3\mu$, the γ contribution to $\tau \to \mu PP$ is expected to be the dominant one, and the h^0 and H^0-mediated

contributions are expected to be relevant only at large $\tan\beta$. Therefore, we have included these three γ, h^0 and H^0 contributions in the computation.

The total amplitude for the $\tau \to \mu PP$ process can be written as

$$T = T_\gamma + T_H \,, \tag{3.22}$$

where T_γ and $T_H = T_{h^0} + T_{H^0}$ are the amplitudes of the γ-mediated and H-mediated contributions respectively. First we present the result of T_γ and T_H in terms of the final state quarks, that is for $\tau \to \mu\overline{q}q$, and in terms of the corresponding τ-μ LFV form factors:

$$\begin{aligned} T_\gamma &= \overline{\mu}\left[k^2\gamma_\mu\left(A_1^L P_L + A_1^R P_R\right) + i m_\tau \sigma_{\mu\nu}k^\nu\left(A_2^L P_L + A_2^R P_R\right)\right]\tau \\ &\quad \times \frac{e^2 Q_q}{k^2}\,\overline{q}\gamma^\mu q\,, \end{aligned} \tag{3.23}$$

$$\begin{aligned} T_H &= \sum_{h^0,H^0}\frac{1}{m_{H_p}^2}\Big\{H_L^{(p)}S_{L,q}^{(p)}\left[\overline{\mu}P_L\tau\right]\left[\overline{q}P_L q\right] + H_R^{(p)}S_{R,q}^{(p)}\left[\overline{\mu}P_R\tau\right]\left[\overline{q}P_R q\right] \\ &\quad + H_L^{(p)}S_{R,q}^{(p)}\left[\overline{\mu}P_L\tau\right]\left[\overline{q}P_R q\right] + H_R^{(p)}S_{L,q}^{(p)}\left[\overline{\mu}P_R\tau\right]\left[\overline{q}P_L q\right]\Big\}\,, \end{aligned} \tag{3.24}$$

where, k is the photon momentum, Q_q the electric charge of the quark q in units of the positron charge e, $P_{L,R} = (1 \mp \gamma_5)/2$, m_τ is the τ lepton mass, and m_{h^0}, m_{H^0} are the Higgs boson masses. Notice that the momentum of the Higgs propagators has been neglected against the Higgs boson mass. The Higgs boson couplings to quarks are correspondingly given by

$$S_{L,u}^{(p)} = \frac{g}{2m_W}\left(\frac{-\sigma_2^{(p)*}}{\sin\beta}\right)m_u, \qquad S_{L,(d,s)}^{(p)} = \frac{g}{2m_W}\left(\frac{\sigma_1^{(p)*}}{\cos\beta}\right)m_{d,s}, \qquad S_{R,q}^{(p)} = S_{L,q}^{(p)*}, \tag{3.25}$$

where m_q is the q quark mass, m_W the W gauge boson mass, g the $SU(2)$ gauge coupling, and

$$\sigma_1^{(p)} = \begin{pmatrix} \sin\alpha \\ -\cos\alpha \\ i\sin\beta \end{pmatrix}, \qquad \sigma_2^{(p)} = \begin{pmatrix} \cos\alpha \\ \sin\alpha \\ -i\cos\beta \end{pmatrix}. \tag{3.26}$$

The three entries for the index (p) in the previous expressions and in the following ones correspond to $H_p = h^0, H^0, A^0$, respectively. The angle α rotates, as usual, from the electroweak neutral Higgs basis to the mass eigenstate basis.

The LFV form factors $A_{1,2}^{L,R}$ in Eq. (3.23) describe the effective $\gamma\tau\mu$ vertex and get contributions from the SUSY one-loop diagrams depicted in Fig. B.1. The full results for these form factors can be found in Appendix B. Notice that we are presenting all the results in the physical mass eigenstate basis for all the particles involved. Therefore the LFV is encoded in the physical slepton and sneutrino masses and in the corresponding slepton and sneutrino rotation matrices. The latter appear in the chargino-sneutrino-lepton and neutralino-slepton-lepton couplings.

Similarly, the LFV form factors $H_{L,R}^{(p)}$ in Eq. (3.24) describe the effective $H_p\tau\mu$ vertex and get contributions from the SUSY one-loop diagrams shown in Fig. B.3. These set of diagrams where computed in [101] and the results are collected in Appendix B. Again the LFV is encoded in the slepton and sneutrino masses and in the rotation matrices.

The next step is to hadronise the quark bilinears appearing in Eqs. (3.23) and (3.24). For this, we proceed as explained in Sec. 3.1.2. The quark bilinears in T_γ, $[\overline{q}\gamma_\mu q]$, are hadronised via the electromagnetic current in Eq. (3.17) which, for the final state with two mesons $P_1(p_1)P_2(p_2)$, is then written in terms of the corresponding electromagnetic form factor, $F_V^{P_1P_2}$, by means of Eq. (3.18). Thus, one gets the photon amplitude in terms of the final state hadrons

$$T_\gamma \;=\; \frac{e^2}{k^2}\,F_V^{P_1P_2}(k^2)\,\overline{\mu}\left[k^2(\not{p}_1-\not{p}_2)\left(A_1^L P_L + A_1^R P_R\right) + 2\,i\,m_\tau\,p_1^\mu\sigma_{\mu\nu}\,p_2^\nu\left(A_2^L P_L + A_2^R P_R\right)\right]\tau. \tag{3.27}$$

The expressions of the $F_V^{P_1P_2}$ form factors for each of the final states, $P_1P_2 = \pi^+\pi^-$, K^+K^- and $K^0\bar{K}^0$ are collected in Appendix D. Obviously, the $\pi^0\pi^0$ final state does not get photon-mediated contributions since γ does not couple to $\pi^0\pi^0$. Hence we set $F_V^{\pi^0\pi^0} = 0$.

The quark bilinears in T_H, $[\overline{q}P_{L,R}q]$, when hadronised in a final state of two mesons, get contributions just from scalar currents, S^i, but not from pseudoscalar currents, P^i. Then, one substitutes $[\overline{q}P_{L,R}q]$ by $[(-1/2)(-\overline{q}q)]$, where $(-\overline{q}q)$ is given in Eq. (3.21), and the relevant scalar currents, S^0, S^3 and S^8, are written in terms of two mesons by using Eq. (3.16). This gives

$$\begin{aligned}
S^3 &= -B_0\left[\frac{2}{\sqrt{3}}\left(\cos\theta-\sqrt{2}\sin\theta\right)\pi^0\eta \;+\; \frac{2}{\sqrt{3}}\left(\sqrt{2}\cos\theta+\sin\theta\right)\pi^0\eta' \;+\; K^+K^- \;-\; K^0\bar{K}^0\right],\\
S^8 &= \frac{B_0}{\sqrt{3}}\Big[K^+K^- \;+\; K^0\bar{K}^0 \;-\; 2\pi^+\pi^- \;-\; \pi^0\pi^0 \;+\; \left(\cos^2\theta \;+\; 2\sqrt{2}\sin\theta\cos\theta\right)\,\eta\eta\\
&\qquad + 2\left(\sqrt{2}\sin^2\theta+\sin\theta\cos\theta-\sqrt{2}\cos^2\theta\right)\,\eta\eta'\Big]\;,\\
S^0 &= -B_0\sqrt{\frac{2}{3}}\left[\,2\pi^+\pi^- \;+\; 2K^+K^- \;+\; 2K^0\bar{K}^0 \;+\; \pi^0\pi^0 \;+\; \eta\eta\right]\;.
\end{aligned} \tag{3.28}$$

Thus, one gets the Higgs boson amplitude in terms of the final state hadrons

$$T_H \;=\; \sum_{p=h^0,H^0}\overline{\mu}\left[\,c_{PP}^{(p)} \;+\; d_{PP}^{(p)}\,\gamma_5\right]\,\tau\,, \tag{3.29}$$

where

$$\begin{aligned}
c_{PP}^{(p)} &= \frac{g}{2m_W}\frac{1}{2m_{H_p}^2}\,\left(J_L^{(p)}(PP)+J_R^{(p)}(PP)\right)\left(H_R^{(p)}+H_L^{(p)}\right)\,,\\
d_{PP}^{(p)} &= \frac{g}{2m_W}\frac{1}{2m_{H_p}^2}\,\left(J_L^{(p)}(PP)+J_R^{(p)}(PP)\right)\left(H_R^{(p)}-H_L^{(p)}\right)\,,
\end{aligned} \tag{3.30}$$

and

$$\begin{aligned}
J_L^{(p)}(\pi^+\pi^-) &= J_L^{(p)}(\pi^0\pi^0) \,=\, \frac{1}{4}\left(\left(\frac{-\sigma_2^{(p)*}}{\sin\beta}\right) m_\pi^2 + \left(\frac{\sigma_1^{(p)*}}{\cos\beta}\right) m_\pi^2\right) , \\
J_L^{(p)}(K^+K^-) &= \frac{1}{4}\left(\left(\frac{-\sigma_2^{(p)*}}{\sin\beta}\right) m_\pi^2 + \left(\frac{\sigma_1^{(p)*}}{\cos\beta}\right) (2m_K^2 - m_\pi^2)\right) , \\
J_L^{(p)}(K^0\bar{K}^0) &= \frac{1}{2}\left(\frac{\sigma_1^{(p)*}}{\cos\beta}\right) m_K^2 \,, \\
J_R^{(p)}(PP) &= J_L^{(p)*}(PP) \,. \qquad (3.31)
\end{aligned}$$

Notice that in Eq. (3.31) we have already used the relations between the quark and the meson masses of χPT given in Eq. (3.8).

Finally, we get the following result for the branching ratio:

$$\mathrm{BR}(\tau \to \mu PP) \,=\, \frac{\kappa_{PP}}{64\,\pi^3\, m_\tau^2\, \Gamma_\tau} \int_{s_{\min}}^{s_{\max}} ds \int_{t_{\min}}^{t_{\max}} dt\; \frac{1}{2} \sum_{i,f} |T|^2 \,, \qquad (3.32)$$

where Γ_τ is the total τ decay width, and the coefficient κ_{PP} is 1 for $PP = \pi^+\pi^-, K^+K^-, K^0\bar{K}^0$ and 1/2 for $PP = \pi^0\pi^0$. In addition

$$\begin{aligned}
t_{\min}^{\max} &= \frac{1}{4s}\left[\left(m_\tau^2 - m_\mu^2\right)^2 - \left(\lambda^{1/2}\left(s, m_P^2, m_P^2\right) \mp \lambda^{1/2}\left(m_\tau^2, s, m_\mu^2\right)\right)^2\right] , \\
s_{\min} &= 4m_P^2 \;,\; s_{\max} = (m_\tau - m_\mu)^2 \;,\; \lambda(x,y,z) = (x+y-z)^2 - 4xy \,. \qquad (3.33)
\end{aligned}$$

The averaged squared amplitude is,

$$\frac{1}{2}\sum_{i,f} |T|^2 \,=\, \frac{1}{8\, m_\tau}\left[g_1(s) \,+\, g_2(s)\, t \,+\, g_3(s)\, t^2\right] . \qquad (3.34)$$

where

$$\begin{aligned}
g_1(s) &= h_0 \,+\, h_1\, s \,+\, h_2\, s^2 \,+\, h_3\, s^3 \,, \\
g_2(s) &= j_1\, s \,+\, j_2\, s^2 \,+\, j_3\, s^3 \,, \\
g_3(s) &= k_1\, s \,+\, k_2\, s^2 \,, \qquad (3.35)
\end{aligned}$$

with

$$
\begin{aligned}
h_0 &= -8M_P^2 m_\tau^2 \left(m_\mu^2 - m_\tau^2\right)^2 \left(A_2^- A_2^{-*} + A_2^+ A_2^{+*}\right) \\
&\quad + 2\left(m_\mu + m_\tau\right)^2 c_H c_H^* \, + \, 2\left(m_\mu - m_\tau\right)^2 d_H d_H^* \,, \\
h_1 &= -8m_\tau^2 \left(m_\tau m_\mu + M_P^2\right)^2 \, A_2^- A_2^{-*} - 8m_\tau^2 \left(m_\tau m_\mu - M_P^2\right)^2 \, A_2^+ A_2^{+*} \\
&\quad + 8\left(m_\mu - m_\tau\right) m_\tau \left(m_\mu + m_\tau\right)^2 M_P^2 \, \left(A_1^{-*} A_2^- + A_1^- A_2^{-*}\right) \\
&\quad + 8\left(m_\mu - m_\tau\right)^2 m_\tau \left(m_\mu + m_\tau\right) M_P^2 \, \left(A_1^{+*} A_2^+ + A_1^+ A_2^{+*}\right) \\
&\quad - 2\left(m_\mu + m_\tau\right) \left(m_\mu^2 + m_\tau^2 + 2M_P^2\right) \left(c_H A_1^{+*} + c_H^* A_1^+\right) \\
&\quad + 2m_\tau \left(m_\mu^2 + m_\tau^2 + 2M_P^2\right) \, \left(c_H A_2^{+*} + c_H^* A_2^+\right) \\
&\quad - 2\left(m_\mu - m_\tau\right) \, \left(m_\mu^2 + m_\tau^2 + 2M_P^2\right) \left(d_H A_1^{-*} + d_H^* A_1^-\right) \\
&\quad + 2m_\tau \left(m_\mu^2 + m_\tau^2 + 2M_P^2\right) \, \left(d_H A_2^{-*} + d_H^* A_2^-\right) \\
&\quad - 2c_H c_H^* - 2d_H d_H^* \,, \\
h_2 &= 2\left[\left(m_\mu^2 + m_\tau^2\right)^2 + 4M_P^4 + 8m_\mu m_\tau M_P^2\right] \, A_1^+ A_1^{+*} \\
&\quad + 2\left[\left(m_\mu^2 + m_\tau^2\right)^2 + 4M_P^4 - 8m_\mu m_\tau M_P^2\right] \, A_1^- A_1^{-*} \\
&\quad + 2m_\tau^2 \left[\left(m_\mu - m_\tau\right)^2 + 4M_P^2\right] \, A_2^+ A_2^{+*} \, + \, 2m_\tau^2 \left[\left(m_\mu + m_\tau\right)^2 + 4M_P^2\right] \, A_2^- A_2^{-*} \\
&\quad - 2m_\tau \left(m_\mu - m_\tau\right) \left[\left(m_\mu + m_\tau\right)^2 + 4M_P^2\right] \left(A_1^{-*} A_2^- + A_1^- A_2^{-*}\right) \\
&\quad - 2m_\tau \left(m_\mu + m_\tau\right) \left[\left(m_\mu - m_\tau\right)^2 + 4M_P^2\right] \left(A_1^{+*} A_2^+ + A_1^+ A_2^{+*}\right) \\
&\quad + 2\left(m_\mu + m_\tau\right) \left(c_H A_1^{+*} + c_H^* A_1^+\right) \, + \, 2\left(m_\mu - m_\tau\right) \left(d_H A_1^{-*} + d_H^* A_1^-\right) \\
&\quad - 2m_\tau \left[c_H A_2^{+*} + c_H^* A_2^+ + d_H A_2^{-*} + d_H^* A_2^-\right] \,, \\
h_3 &= -2\left(m_\mu - m_\tau\right)^2 \, A_1^- A_1^{-*} \, - \, 2\left(m_\mu + m_\tau\right)^2 \, A_1^+ A_1^{+*} \, - \, 2m_\tau^2 \, \left[A_2^- A_2^{-*} + A_2^+ A_2^{+*}\right] \\
&\quad + 2m_\tau \left(m_\mu - m_\tau\right) \, \left[A_1^- A_2^{-*} + A_1^{-*} A_2^-\right] \, + \, 2m_\tau \left(m_\mu + m_\tau\right) \, \left[A_1^+ A_2^{+*} + A_1^{+*} A_2^+\right] \,,
\end{aligned}
$$

$$
\begin{aligned}
j_1 &= 8m_\tau^2 \left(m_\mu^2 + m_\tau^2 + 2M_P^2\right) \left(A_2^- A_2^{-*} + A_2^+ A_2^{+*}\right) \\
&\quad - 4m_\tau \left[c_H A_2^{+*} + c_H^* A_2^+ + d_H A_2^{-*} + d_H^* A_2^-\right] \\
&\quad + 4\left(m_\mu + m_\tau\right) \left(c_H A_1^{+*} + c_H^* A_1^+\right) \, + \, 4\left(m_\mu - m_\tau\right) \left(d_H A_1^{-*} + d_H^* A_1^-\right) \,, \\
j_2 &= -8\left(m_\mu^2 + m_\tau^2 + 2M_P^2\right) \, \left[A_1^+ A_1^{+*} + A_1^- A_1^{-*}\right] \, - \, 8m_\tau^2 \, \left[A_2^+ A_2^{+*} + A_2^- A_2^{-*}\right] \,, \\
j_3 &= 8 \, \left(A_1^- A_1^{-*} + A_1^+ A_1^{+*}\right) \,, \\
k_1 &= -8m_\tau^2 \, \left(A_2^- A_2^{-*} + A_2^+ A_2^{+*}\right) \,, \\
k_2 &= 8 \, \left(A_1^- A_1^{-*} + A_1^+ A_1^{+*}\right) \,,
\end{aligned}
\tag{3.36}
$$

and

$$
A_i^\pm \;=\; \frac{e^2}{2\,s} \, F_V^{PP}(s) (A_i^R \pm A_i^L) \;,\; c_H = c_{PP}^{(h^0)} \, + \, c_{PP}^{(H^0)} \;,\; d_H = d_{PP}^{(h^0)} \, + \, d_{PP}^{(H^0)} \,. \tag{3.37}
$$

3.2.2 Predictions for $\tau \to \mu P$

The semileptonic $\tau \to \mu P$ channel can be mediated by a Z gauge boson and a CP-odd A^0 Higgs boson, as represented in Fig. 3.1. Both contributions are included here. The total amplitude for this $\tau \to \mu P$ decay can then be written as

$$T \;=\; T_Z \;+\; T_{A^0}\,, \tag{3.38}$$

where T_Z and T_{A^0} are the Z and A^0 mediated amplitudes, respectively. As in the previous case, these are first evaluated in terms of the final state quarks, that is for $\tau \to \mu\overline{q}q$, and in terms of the corresponding $\tau - \mu$ LFV form factors:

$$T_Z \;=\; \frac{1}{m_Z^2}\overline{\mu}\left[\gamma_\mu(F_L P_L + F_R P_R)\right]\tau \;.\; \overline{q}\left[\gamma^\mu\left(Z_L^{(q)}P_L + Z_R^{(q)}P_R\right)\right]q\,, \tag{3.39}$$

$$\begin{aligned} T_{A^0} \;=\; \frac{1}{m_{A^0}^2}\Big\{ & H_L^{(A^0)}S_{L,q}^{(A^0)}\left[\overline{\mu}P_L\tau\right]\left[\overline{q}P_L q\right] \;+\; H_R^{(A^0)}S_{R,q}^{(A^0)}\left[\overline{\mu}P_R\tau\right]\left[\overline{q}P_R q\right] \\ & + H_L^{(A^0)}S_{R,q}^{(A^0)}\left[\overline{\mu}P_L\tau\right]\left[\overline{q}P_R q\right] \;+\; H_R^{(A^0)}S_{L,q}^{(A^0)}\left[\overline{\mu}P_R\tau\right]\left[\overline{q}P_L q\right]\Big\}\,, \end{aligned} \tag{3.40}$$

where $Z_L^{(q)} = (-g/\cos\theta_W)(T_3^{(q)} - Q_q \sin^2\theta_W)$ and $Z_R^{(q)} = (g/\cos\theta_W)Q_q \sin^2\theta_W$ are the Z couplings to quarks, and $S_{L,q}^{(A^0)}$ and $S_{R,q}^{(A^0)}$ are the A^0 couplings to quarks, which are given by the third entry in Eqs. (3.25) and (3.26).

The LFV form factors $F_{L,R}$ in Eq. (3.39) describe the effective $Z\tau\mu$ vertex and receive contributions from the SUSY one-loop diagrams depicted in Fig. B.2. The results for these form factors where found in [49] and corrected in [102]. We collect them in Appendix B. The LFV form factors $H_{L,R}^{(A^0)}$ in Eq. (3.40) describe the effective $A^0\tau\mu$ vertex and, as in the previous $H\tau\mu$ vertices with $H = h^0, H^0$, receive contributions from the one-loop diagrams in Fig. B.3. The corresponding results are collected in Appendix B.

The hadronisation of the quark bilinears in T_Z proceeds by means of the vector and axial-vector currents in Eq. (3.19), which in turn are written in terms of one P meson by means of Eq. (3.20). This leads to

$$V_\mu^Z \;=\; 0, \tag{3.41}$$

$$A_\mu^Z \;=\; -\frac{g}{2\cos\theta_W}F\left\{C(\pi^0)\,\partial_\mu\pi^0 + C(\eta)\,\partial_\mu\eta + C(\eta')\,\partial_\mu\eta'\right\}, \tag{3.42}$$

where the $C(P)$ functions are given by,

$$\begin{aligned} C(\pi^0) \;&=\; 1, \\ C(\eta) \;&=\; \frac{1}{\sqrt{6}}\left(\sin\theta + \sqrt{2}\cos\theta\right), \\ C(\eta') \;&=\; \frac{1}{\sqrt{6}}\left(\sqrt{2}\sin\theta - \cos\theta\right). \end{aligned} \tag{3.43}$$

The hadronisation into one pseudoscalar meson P of the quark bilinears in T_{A^0} proceed via the pseudoscalar currents P^i. Concretely, P^0, P^3 and P^8, whose expressions in terms of one P meson can be obtained from Eq. (3.16). This leads to:

$$\begin{aligned} P^3 &= 2B_0 F\,\pi^0\,, \\ P^8 &= 2B_0 F\left(\cos\theta\,\eta + \sin\theta\,\eta'\right)\,, \\ P^0 &= 2B_0 F\left(-\sin\theta\,\eta + \cos\theta\,\eta'\right)\,. \end{aligned} \tag{3.44}$$

Finally, by putting all together, we get the following result for the branching ratio:

$$\mathrm{BR}(\tau\to\mu P) = \frac{1}{4\pi}\,\frac{\lambda^{1/2}(m_\tau^2,m_\mu^2,m_P^2)}{m_\tau^2\,\Gamma_\tau}\,\frac{1}{2}\sum_{i,f}|T|^2\,, \tag{3.45}$$

where the $\lambda(x,y,z)$ function is defined in Eq. (3.33) and again Γ_τ is the total decay width of the τ lepton. The averaged squared amplitude is given by,

$$\frac{1}{2}\sum_{i,f}|T|^2 = \frac{1}{4\,m_\tau}\sum_{k,m}\left[2m_\mu m_\tau\left(a_P^k a_P^{m\,*} - b_P^k b_P^{m\,*}\right) + (m_\tau^2+m_\mu^2-m_P^2)\left(a_P^k a_P^{m\,*} + b_P^k b_P^{m\,*}\right)\right], \tag{3.46}$$

with $k,m = Z, A^0$, and

$$\begin{aligned} a_P^Z &= -\frac{g}{2\cos\theta_W}\frac{F}{2}\frac{C(P)}{m_Z^2}\,(m_\tau - m_\mu)\,(F_L+F_R)\,, \\ b_P^Z &= \frac{g}{2\cos\theta_W}\frac{F}{2}\frac{C(P)}{m_Z^2}\,(m_\tau + m_\mu)\,(F_R-F_L)\,, \\ a_P^{A^0} &= \frac{g}{2m_W}\frac{F}{2m_{A^0}^2}\left(B_L^{(A^0)}(P) - B_R^{(A^0)}(P)\right)\left(H_L^{(A^0)} + H_R^{(A^0)}\right)\,, \\ b_P^{A^0} &= \frac{g}{2m_W}\frac{F}{2m_{A^0}^2}\left(B_L^{(A^0)}(P) - B_R^{(A^0)}(P)\right)\left(H_R^{(A^0)} - H_L^{(A^0)}\right)\,. \end{aligned} \tag{3.47}$$

The $B_{L,R}^{(A^0)}(P)$ functions are given, correspondingly, by the third entry of:

$$\begin{aligned} B_L^{(p)}(\pi) &= \frac{m_\pi^2}{4}\left(\frac{-\sigma_2^{(p)*}}{\sin\beta} - \frac{\sigma_1^{(p)*}}{\cos\beta}\right)\,, \\ B_L^{(p)}(\eta) &= \frac{1}{4\sqrt{3}}\left[\frac{-\sigma_2^{(p)*}}{\sin\beta}m_\pi^2\left(\cos\theta - \sqrt{2}\sin\theta\right) + \frac{\sigma_1^{(p)*}}{\cos\beta}\left[\left(3m_\pi^2-4m_K^2\right)\cos\theta - 2\sqrt{2}m_K^2\sin\theta\right]\right]\,, \\ B_L^{(p)}(\eta') &= \frac{1}{4\sqrt{3}}\left[\frac{-\sigma_2^{(p)*}}{\sin\beta}m_\pi^2\left(\sin\theta + \sqrt{2}\cos\theta\right) + \frac{\sigma_1^{(p)*}}{\cos\beta}\left[\left(3m_\pi^2-4m_K^2\right)\sin\theta + 2\sqrt{2}m_K^2\cos\theta\right]\right]\,, \\ B_R^{(p)}(P) &= B_L^{(p)*}(P)\,, \end{aligned} \tag{3.48}$$

where the $\sigma_{1,2}^{(p)}$ functions are defined in Eq. (3.26). Notice that in this Eq. (3.48) the relations between the quark and meson masses of Eq. (3.8) have been used again.

3.2.3 Predictions for $\tau \to \mu\rho$ and $\tau \to \mu\phi$

The $\tau \to \mu\rho^0$ decay is related to the $\tau \to \mu\pi^+\pi^-$ channel since the ρ decay proceeds mainly to $\pi^+\pi^-$. Indeed a ρ^0 is not an asymptotic state: the experiment reconstructs its structure from the two observed pions. In addition, from the chiral point of view, two pions in a $J = I = 1$ state are indistinguishable from a ρ. Therefore one has to define the branching ratio of $\tau \to \mu\rho^0$ in close relation to that of $\tau \to \mu\pi^+\pi^-$ as follows,

$$\mathrm{BR}(\tau \to \mu\rho^0) = \frac{1}{64\,\pi^3\,m_\tau^2\,\Gamma_\tau}\int_{s_{\min}}^{s_{\max}} ds \left[\int_{t_{\min}}^{t_{\max}} dt\,\frac{1}{2}\sum_{i,f}|T_\gamma|^2\right]_{\pi^+\pi^-}, \tag{3.49}$$

where T_γ is defined in Eq. (3.27) and all functions and form factors involved are as those of $\tau \to \mu\pi^+\pi^-$ decay, with the exception of the integration limits in s which are now

$$s_{\min} = M_\rho^2 - \frac{1}{2}M_\rho\Gamma_\rho\,, \qquad s_{\max} = M_\rho^2 + \frac{1}{2}M_\rho\Gamma_\rho\,. \tag{3.50}$$

Similarly, the $\tau \to \mu\phi$ decay is related to the $\tau \to \mu K^+K^-$ and $\tau \to \mu K^0\bar{K}^0$ decays since the ϕ decays proceeds mainly to K^+K^- and to $K^0\bar{K}^0$. Therefore, we define

$$\mathrm{BR}(\tau \to \mu\phi) = \frac{1}{64\,\pi^3\,m_\tau^2\,\Gamma_\tau}\left\{\int_{s_{\min}}^{s_{\max}} ds \left[\int_{t_{\min}}^{t_{\max}} dt\,\frac{1}{2}\sum_{i,f}|T_\gamma|^2\right]_{K^+K^-} + \int_{s_{\min}}^{s_{\max}} ds \left[\int_{t_{\min}}^{t_{\max}} dt\,\frac{1}{2}\sum_{i,f}|T_\gamma|^2\right]_{K^0\bar{K}^0}\right\}, \tag{3.51}$$

where again T_γ is defined in Eq. (3.27) and all functions and form factors involved are as those of $\tau \to \mu K^+K^-$ and $\tau \to \mu K^0\bar{K}^0$ correspondingly, except for the integration limits in s which are now

$$s_{\min} = M_\phi^2 - \frac{1}{2}M_\phi\Gamma_\phi\,, \qquad s_{\max} = M_\phi^2 + \frac{1}{2}M_\phi\Gamma_\phi\,. \tag{3.52}$$

In Eqs. (3.50,3.52), $\Gamma_\rho = \Gamma_\rho(M_\rho^2)$ and $\Gamma_\phi = \Gamma_\phi(M_\phi^2)$.

3.3 Numerical results and discussion

In this section we present the numerical results of the LFV semileptonic $\tau \to \mu PP$ and $\tau \to \mu P$ decay rates within the constrained SUSY-seesaw scenarios described in Chapter 1. Since our main goal is to explore if the predicted rates can or cannot reach the present experimental sensitivities we will focus mainly on choices of the input parameter values that lead to large δ_{32} and therefore to large LFV semileptonic τ decay rates. As we have seen in the Section 1.5,

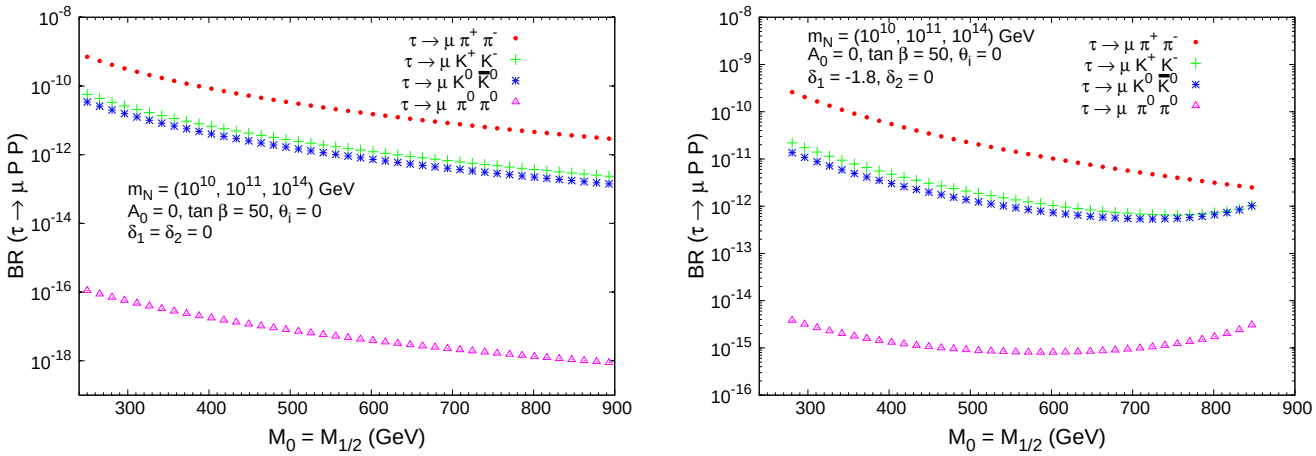

Figure 3.2: BR($\tau \to \mu PP$) for $PP = \pi^+\pi^-, K^+K^-, K^0\bar{K}^0, \pi^0\pi^0$ as a function of $M_{\rm SUSY} = M_0 = M_{1/2}$ in the contrained MSSM-seesaw scenarios: CMSSM (left panel) and NUHM (right panel).

within the scenario with hierarchical heavy neutrinos and for $\theta_{1,3} = 0$, this means large values of θ_2 and large values of m_{N_3}. On the other hand, since all these rates grow with $\tan\beta$, in the following numerical analysis we will focus mainly on large $\tan\beta$ values. In the first subsection we will present the numerical results, from our full computation of the LFV semileptonic tau decay rates and will explore the dependence with the most relevant parameters in the constrained SUSY-seesaw scenarios. In the second subsection we will include a comparison between our full and some approximate results in the large $\tan\beta$ region. Moreover, we will also analyse to what extent the Higgs dominance hypothesis holds for these LFV semileptonic τ decays and compare our predictions with other results in the literature. We will conclude this section by showing that for some particular choices of the input parameters, the rates for some channels indeed reach the present experimental sensitivity.

3.3.1 LFV semileptonic τ decay rates

Firstly, we present the results for the simplest case of $\theta_2 = 0$ and study the relative importance of the various contributions to the decay rates that have been presented in the previous section. Then we explore the increase in the rates for larger values of θ_2. Since we are setting in the whole numerical analysis $A_0 = 0$ and $\text{sign}(\mu) = +1$, the relevant SUSY parameter will be $M_{\rm SUSY} = M_0 = M_{1/2}$. In the study of the behaviour of the rates with $M_{\rm SUSY}$ we pay special attention to the decoupling or non-decoupling behaviour of the SUSY particles at large $M_{\rm SUSY}$.

In Fig. 3.2 we display the prediction of BR($\tau \to \mu PP$), with $PP = \pi^+\pi^-$, K^+K^-, $K^0\bar{K}^0$,

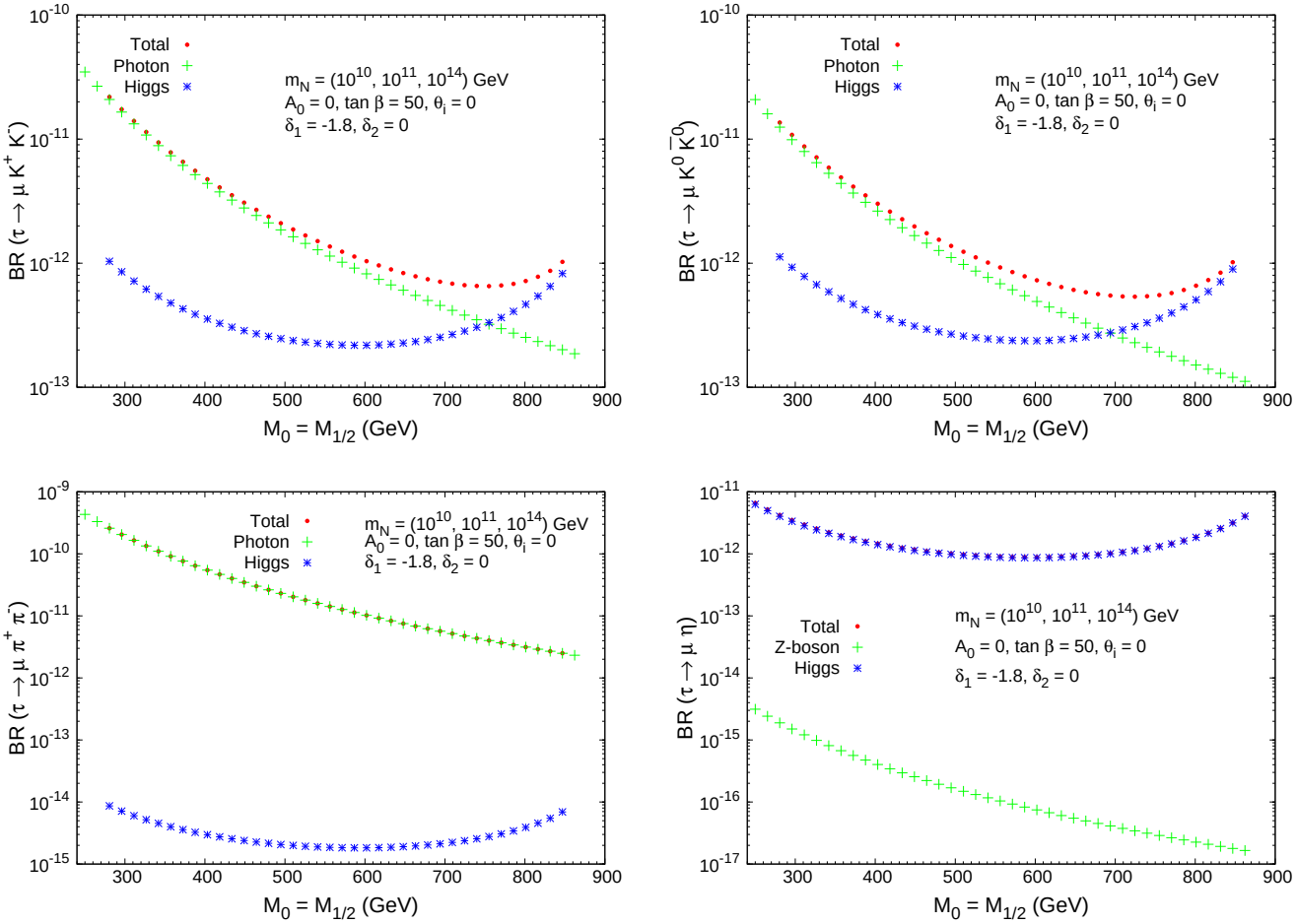

Figure 3.3: Rates of the various contributions to BR($\tau \to \mu K^+ K^-$) (upper left panel), BR($\tau \to \mu K^0 \bar{K}^0$) (upper right panel), BR($\tau \to \mu \pi^+ \pi^-$) (lower left panel) and BR($\tau \to \mu \eta$) (lower right panel) as a function of $M_{\rm SUSY} = M_0 = M_{1/2}$ in the NUHM scenario.

$\pi^0\pi^0$, as a function of $M_{\rm SUSY}$ and for the particular choice of $\theta_i = 0$ ($i = 1, 2, 3$). We consider both CMSSM (left panel) and NUHM (right panel) scenarios. We set here $\tan\beta = 50$ and our "reference" values of $m_{N_{1,2,3}} = (10^{10}, 10^{11}, 10^{14})$ GeV. For the NUHM case we set in addition $\delta_1 = -1.8$ and $\delta_2 = 0$, which have been shown in [104] to lead to low Higgs boson mass values. Concretely, for $\theta_i = 0$ and 250 GeV $< M_{\rm SUSY} <$ 900 GeV the predicted masses are within the range 110 GeV $< m_{A^0}, m_{H^0} <$ 180 GeV, which are indeed very close to their present experimental bounds.

The first obvious conclusion from Fig. 3.2 is that the rates of the different channels exhibit the following hierarchy, BR($\tau \to \mu\pi^+\pi^-$) > BR($\tau \to \mu K^+ K^-$) $\gtrsim$ BR($\tau \to \mu K^0 \bar{K}^0$) $\gg$ BR($\tau \to$

$\mu\pi^0\pi^0$). This hierarchy can be understood in terms of the dominant electromagnetic contribution and the relative phase space suppression. We also see that the decoupling behaviour for large $M_{\rm SUSY}$ is clearly manifest in the universal case, where all the rates decrease as $M_{\rm SUSY}$ grows. In contrast, it turns out that, in the NUHM case, the decoupling behaviour is only manifest in the $\tau \to \mu\pi^+\pi^-$ channel, whereas the $\tau \to \mu K^+K^-$, $\tau \to \mu K^0\bar{K}^0$ and $\tau \to \mu\pi^0\pi^0$ rates do not decrease with $M_{\rm SUSY}$ in the large $M_{\rm SUSY}$ region. This behaviour can be better comprehended by analysing separately the different contributions to these channels, as shown in Fig. 3.3.

The results displayed in Fig 3.3 for the $\tau \to \mu\pi^+\pi^-$ channel show the dominance of the photon-mediated contribution in this case, which is in fact indistinguishable from the total rate in this plot, for all the explored parameter values. The Higgs-mediated contribution is subdominant by far due to the highly suppressed couplings of the Higgs to the light u and d quarks, which after the hadronisation of the corresponding quark bilinears result in $H\pi^+\pi^-$ couplings proportional to m_π^2 (see Eq. (3.31)). This plot also exhibits the non-decoupling behaviour of the SUSY particles in the Higgs-mediated contribution. The particular pattern of this contribution as a function of $M_{\rm SUSY}$ is a consequence of two facts. First, the well known constant behaviour with $M_{\rm SUSY}$ of the LFV $H\tau\mu$ form factor at large $M_{\rm SUSY}$. Second, the encountered Higgs mass behaviour with $M_{\rm SUSY}$, analysed in [104], which, for this choice of $\delta_{1,2}$ and for the studied $M_{\rm SUSY}$ interval, first grows softly, reaches a maximum and then decreases softly.

The $\tau \to \mu\pi^0\pi^0$ channel is only mediated by the Higgs bosons and a similar suppression of $H\pi^0\pi^0$ couplings as in the $H\pi^+\pi^-$ case occurs, leading to very low predicted rates. These low rates and the non-decoupling behaviour of this channel can be clearly seen in Fig. 3.2.

The results for the $\tau \to \mu K^+K^-$ channel that are depicted in Fig 3.3 are interesting because the photon- and the Higgs-mediated contributions compete in this decay. In fact the Higgs-mediated contribution can equalise, or even exceed that of the photon, dominating the total rate in the large $M_{\rm SUSY}$ region. Both photon- and Higgs-mediated contributions are similar around $M_{\rm SUSY} = 750$ GeV. The reason for this larger Higgs contributions than in the previously studied $\pi\pi$ case is because of the larger Higgs couplings to the strange quarks which result in HKK couplings proportional to m_K^2 (see Eq. (3.31)).

The results for the $\tau \to \mu K^0\bar{K}^0$ channel in Fig 3.3 are very similar to those for $\tau \to \mu K^+K^-$. One difference is the point where the Higgs-mediated contribution crosses the photon one, which for $\tau \to \mu K^0\bar{K}^0$ is around $M_{\rm SUSY} = 700$ GeV. Another interesting difference is that this rate is always slightly smaller than $\tau \to \mu K^+K^-$ due to the fact that the photon-mediated contribution to $\tau \to \mu K^0\bar{K}^0$ occurs just by the meson resonances, whereas the $\tau \to \mu K^+K^-$ channel can also be mediated via pure electromagnetic interaction. This difference is clearly summarised in the several contributions to the $F_V^{K^+K^-}$ and $F_V^{K^0\bar{K}^0}$ form factors in Eq. (D.3) of Appendix D.

The predictions of BR($\tau \to \mu P$), with P being here a pseudoscalar meson π, η, η' or a vector

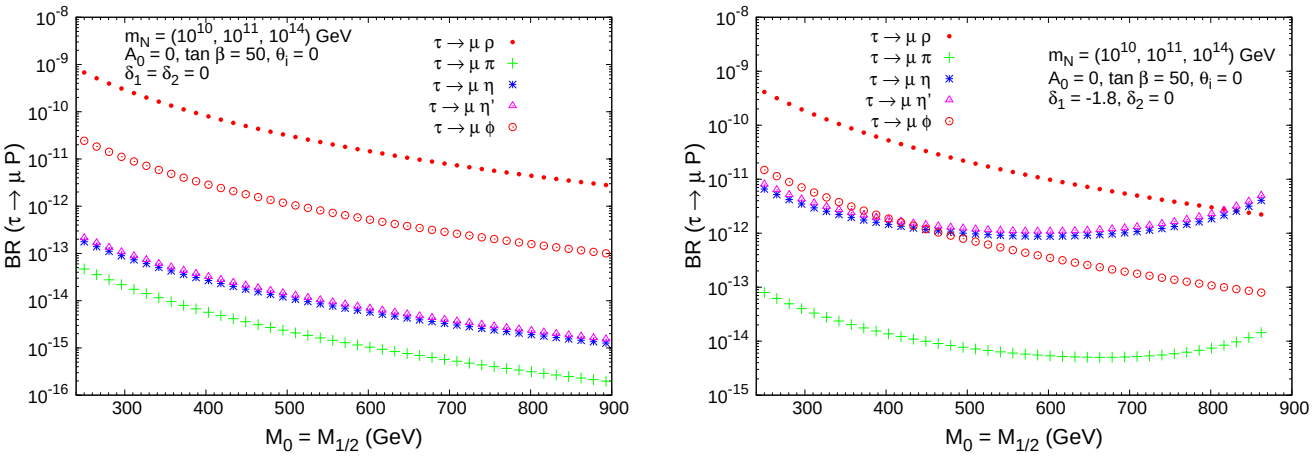

Figure 3.4: BR($\tau \to \mu P$) for $P = \rho, \pi, \eta, \eta'$ as a function of $M_{\rm SUSY} = M_0 = M_{1/2}$ in the contrained MSSM-seesaw scenarios: CMSSM (left panel) and NUHM (right panel).

resonance ρ, ϕ, as a function of $M_{\rm SUSY}$ are displayed in Fig. 3.4. We also consider CMSSM (left panel) and NUHM (right panel) scenarios. In the universal case we find the following hierarchy, $\mathrm{BR}(\tau \to \mu\rho) > \mathrm{BR}(\tau \to \mu\phi) > \mathrm{BR}(\tau \to \mu\eta') \gtrsim \mathrm{BR}(\tau \to \mu\eta) > \mathrm{BR}(\tau \to \mu\pi)$. We obtain again the expected decoupling behaviour for large $M_{\rm SUSY}$ in this universal scenario, while in the NUHM scenario the non-decoupling behaviour is clearly manifest for $\tau \to \mu\eta$, $\tau \to \mu\eta'$ and $\tau \to \mu\pi$. The $\tau \to \mu\rho$ rates in the NUHM scenario are the largest ones, except in the large $M_{\rm SUSY}$ region, where $\tau \to \mu\eta$ and $\tau \to \mu\eta'$ rates exceed them. These two channels are by far dominated by the Higgs-mediated contributions in the full $M_{\rm SUSY}$ explored interval, as can be seen for the η case in Fig 3.3. The reason for this Higgs dominance is because of the large Higgs couplings to the strange components of the η and η' mesons, which result in large $A^0 - \eta$ and $A^0 - \eta'$ "mixings" proportional to m_K^2 as explicitely given in Eq. (3.48).

One of the most important outcomes from the previous analysis, corresponding to the $\theta_i = 0$ choice, is that for both scenarios and for the chosen input parameters, the predicted rates for both $\tau \to \mu PP$ and $\tau \to \mu P$ channels do no reach their corresponding experimental bounds, and even in the best cases of $\tau \to \mu\pi^+\pi^-$ and $\tau \to \mu\rho$ they are still two orders of magnitude below their present experimental sensitivities. In the following, we will therefore focus on larger values of θ_2.

In order to reach the larger rates as possible in the $\theta_i \neq 0$ case, one needs to explore first the optimal values of δ_1 and δ_2 which lead to light Higgs bosons. We have summarised the predictions for the relevant Higgs boson mass, m_{A^0} (and m_{H^0}), as a function of $\delta_{1,2}$ and $M_{\rm SUSY}$ in Figs. 1.14 and 1.15 for the extreme value of $\theta_2 = 2.9e^{i\pi/4}$. The reason for this particular

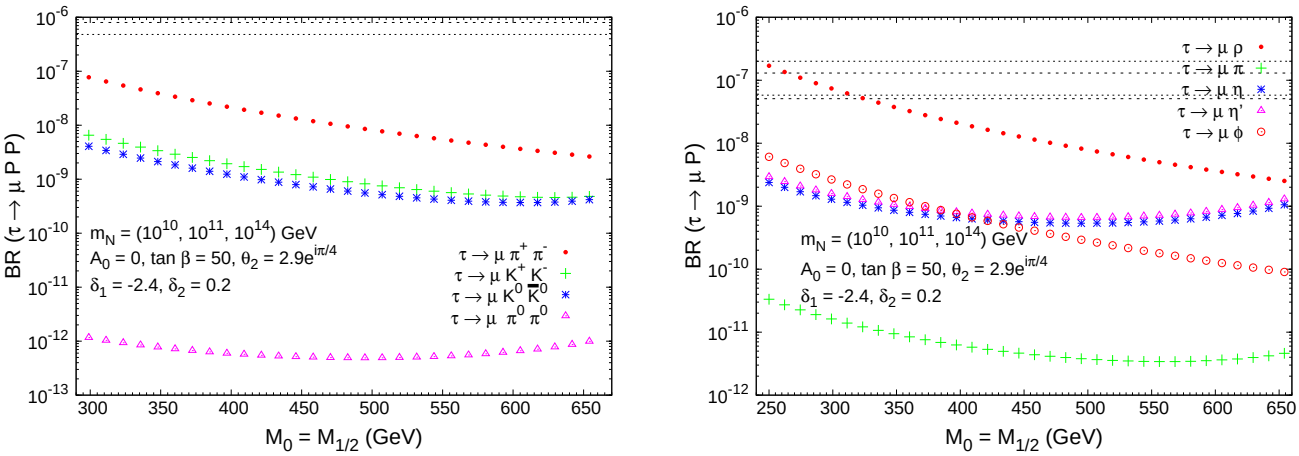

Figure 3.5: Predictions of BR($\tau \to \mu PP$) and BR($\tau \to \mu P$) as a function of $M_{\rm SUSY}$ in the NUHM scenario for a large $\tau - \mu$ mixing driven by $\theta_2 = 2.9e^{i\pi/4}$.

choice of θ_2 is due to the fact that it leads to the maximum value of $|\delta_{32}|$ which is compatible with our hypothesis of perturbativity, as shown in Fig. 1.3 and discussed in Section 1.5. The most interesting solutions with important phenomenological implications are found for negative δ_1 within the range $(-3, -2)$ and very small and positive δ_2, the choices selected in Figs. 1.14 and 1.15. From these figures it is clear that we are able to find values of m_{A^0} and m_{H^0} that are significantly smaller than in the universal case ($\delta_1 = \delta_2 = 0$).

The corresponding predictions for $\theta_2 = 2.9e^{i\pi/4}$ of the nine LFV semileptonic τ decays studied in this chapter as a function of $M_{\rm SUSY}$ are shown in Fig. 3.5. In this case, we work with $\delta_1 = -2.4$ and $\delta_2 = 0.2$, that drive us to Higgs boson masses around 150 GeV even for heavy SUSY spectra, as can be seen in Figs. 1.14 and 1.15. In this Fig. 3.5 we can see that, compared to predictions in Figs. 3.2 and 3.4, the new choice of θ_2 increase all the rates about two orders of magnitude. All the rates exhibit the same hierarchy as in the previous plots, being BR($\tau \to \mu\pi^+\pi^-$) and BR($\tau \to \mu\rho$) the largest ones. Indeed, the predictions of these two latter channels reach their present experimental sensitivities at the low $M_{\rm SUSY}$ region, below 200 GeV and 250 GeV, respectively, for this particular choice of input parameters.

3.3.2 Comparison between the full and approximate results

It is interesting and useful to provide simple formulae which can approximate reasonably well our full predictions. The most popular approximation when predicting LFV rates is to work with expressions that are valid only in the large $\tan\beta$ region. The justification for this is obvious since all these LFV rates are known to grow with $\tan\beta$. It is specially important in scenarios

where the LFV rates are dominated by the Higgs mediated diagrams, since these latter grow much faster with $\tan\beta$ than the photon or Z boson mediated ones. Accordingly, we will pay more attention to the semileptonic $\tau \to \mu P$ and $\tau \to \mu PP$ channels that can be dominated by the Higgs bosons and whose present experimental sensitivities are the best ones. This leads us mainly to the $\tau \to \mu\eta$ and $\tau \to \mu K^+K^-$ channels. The other approximation which is used frequently in the literature, due to its simplicity, is the MI approximation, where the tau-muon LFV is encoded in the dimesionless parameter δ_{32}, already introduced in Section 1.5, and whose expression in the LLog approximation is given in Eqs. (1.93) and (1.86).

We start by recalling the large $\tan\beta$ limit of the tau-muon-Higgs form factors that are the relevant ones for the LFV Higgs-mediated processes. The full one-loop Higgs form factors were computed in [101] (see also [102]) and are collected in Appendix B. As we have said previously, at large $\tan\beta$, H_L dominates H_R by about a factor m_τ/m_μ. Moreover, $H_L^{A^0}$ and $H_L^{H^0}$ are by far the largest form factors in this limit, and one can safely neglect $H_L^{h^0}$. More specifically, by using the MI approximation, their chargino and neutralino contributions in the large $\tan\beta$ limit give, correspondingly, the results [101] in Eq. (2.14) that we rewrite here for completeness,

$$H_{L,c}^{(A^0)} = iH_{L,c}^{(H^0)} = i\,\frac{g^3}{16\pi^2}\,\frac{m_\tau}{12m_W}\,\delta_{32}\,\tan^2\beta\,, \tag{3.53}$$

$$H_{L,n}^{(A^0)} = iH_{L,n}^{(H^0)} = i\,\frac{g^3}{16\pi^2}\,\frac{m_\tau}{24m_W}\,(1-3\tan^2\theta_W)\,\delta_{32}\,\tan^2\beta\,. \tag{3.54}$$

One can further verify that H_c dominates H_n by about a factor 20, so that in the following we will take $H_L \simeq H_{L,c}$.

On the other hand, we also consider the large $\tan\beta$ limit of the functions that define the Higgs couplings to one meson, $B(P)$ in Eq. (3.48), and to two mesons, $J(PP)$ in Eq. (3.31). It leads to the following results:

$$\begin{aligned}
B_L^{(A^0)}(\eta) &= -B_R^{(A^0)}(\eta) = -i\frac{1}{4\sqrt{3}}\tan\beta\left[(3m_\pi^2-4m_K^2)\cos\theta - 2\sqrt{2}m_K^2\sin\theta\right],\\
B_L^{(A^0)}(\eta') &= -B_R^{(A^0)}(\eta') = -i\frac{1}{4\sqrt{3}}\tan\beta\left[(3m_\pi^2-4m_K^2)\sin\theta + 2\sqrt{2}m_K^2\cos\theta\right],\\
B_L^{(A^0)}(\pi) &= -B_R^{(A^0)}(\pi) = i\frac{1}{4}\tan\beta\, m_\pi^2\,,\\
J_L^{(H^0)}(K^+K^-) &= J_R^{(H^0)}(K^+K^-) = -\frac{1}{4}\tan\beta\,(2m_K^2-m_\pi^2)\,,\\
J_L^{(H^0)}(K^0\bar{K}^0) &= J_R^{(H^0)}(K^0\bar{K}^0) = -\frac{1}{2}\tan\beta\, m_\pi^2\,,\\
J_L^{(H^0)}(\pi^+\pi^-) &= J_R^{(H^0)}(\pi^+\pi^-) = J_L^{(H^0)}(\pi^0\pi^0) = J_R^{(H^0)}(\pi^0\pi^0) = -\frac{1}{4}\tan\beta\, m_\pi^2\,.
\end{aligned} \tag{3.55}$$

By using the above sequence of approximations and by neglecting the muon mass, we finally get

the following simple results:

$$\begin{aligned}\mathrm{BR}(\tau\to\mu\eta)_{H_{\rm approx}} &= \frac{1}{8\pi m_\tau^3}\left(m_\tau^2-m_\eta^2\right)^2\left|\frac{g}{2m_W}\frac{F}{m_{A^0}^2}B_L^{(A^0)}(\eta)\,H_{L,c}^{(A^0)}\right|^2\frac{1}{\Gamma_\tau}\\ &= 1.2\times10^{-7}\,|\delta_{32}|^2\left(\frac{100}{m_{A^0}(\mathrm{GeV})}\right)^4\left(\frac{\tan\beta}{60}\right)^6, \qquad (3.56)\end{aligned}$$

and

$$\begin{aligned}\mathrm{BR}(\tau\to\mu K^+K^-)_{H_{\rm approx}} &= \frac{1}{128m_\tau\pi^3}\left|\frac{g}{2m_W}\frac{1}{m_{H^0}^2}J_L^{(H^0)}(K^+K^-)H_{L,c}^{(H^0)}\right|^2\frac{1}{\Gamma_\tau}\\ &\times\int_{s_{min}}^{s_{max}}ds\,(t_{max}-t_{min})(1-\frac{s}{m_\tau^2})\\ &= 2.8\times10^{-8}\,|\delta_{32}|^2\left(\frac{100}{m_{H^0}(\mathrm{GeV})}\right)^4\left(\frac{\tan\beta}{60}\right)^6, \qquad (3.57)\end{aligned}$$

where s_{max}, s_{min}, t_{max} and t_{min} are given in Eq. (3.33). The results for the other channels can be similarly obtained by using the corresponding $B(P)$ or $J(PP)$ functions and the corresponding meson masses (with an additional 1/2 factor in the case of $BR(\tau\to\mu\pi^0\pi^0)$ to account for identical final state particles). We get

$$\mathrm{BR}(\tau\to\mu\eta')_{H_{\rm approx}} = 1.5\times10^{-7}\,|\delta_{32}|^2\left(\frac{100}{m_{A^0}(\mathrm{GeV})}\right)^4\left(\frac{\tan\beta}{60}\right)^6, \qquad (3.58)$$

$$\mathrm{BR}(\tau\to\mu\pi)_{H_{\rm approx}} = 3.6\times10^{-10}\,|\delta_{32}|^2\left(\frac{100}{m_{A^0}(\mathrm{GeV})}\right)^4\left(\frac{\tan\beta}{60}\right)^6, \qquad (3.59)$$

$$\mathrm{BR}(\tau\to\mu K^0\bar{K}^0)_{H_{\rm approx}} = 3.0\times10^{-8}\,|\delta_{32}|^2\left(\frac{100}{m_{H^0}(\mathrm{GeV})}\right)^4\left(\frac{\tan\beta}{60}\right)^6, \qquad (3.60)$$

$$\mathrm{BR}(\tau\to\mu\pi^+\pi^-)_{H_{\rm approx}} = 2.6\times10^{-10}\,|\delta_{32}|^2\left(\frac{100}{m_{H^0}(\mathrm{GeV})}\right)^4\left(\frac{\tan\beta}{60}\right)^6 \qquad (3.61)$$

$$\mathrm{BR}(\tau\to\mu\pi^0\pi^0)_{H_{\rm approx}} = 1.3\times10^{-10}\,|\delta_{32}|^2\left(\frac{100}{m_{H^0}(\mathrm{GeV})}\right)^4\left(\frac{\tan\beta}{60}\right)^6. \qquad (3.62)$$

In all the above approximate results of the LFV semileptonic tau decay rates we see explicitely the strong dependence with both $\tan\beta$ and the corresponding Higgs boson mass, being $(\tan\beta)^6$ and $(1/m_H)^4$, respectively, which are characteristic of the Higgs mediated processes.

Regarding the comparison with other works, first, we notice that our numerical prediction for $\mathrm{BR}(\tau\to\mu\eta)$ in Eq. (3.56) does not agree with the original estimate in [54] that gives a decay rate a factor 7 larger than ours. We believe that the discrepancy comes from our different approaches to describe the hadronisation of quark bilinears. Our numerical result is closer to that in [203] whose prediction is larger than ours in a factor of 2. Notice that the comparison with this latter

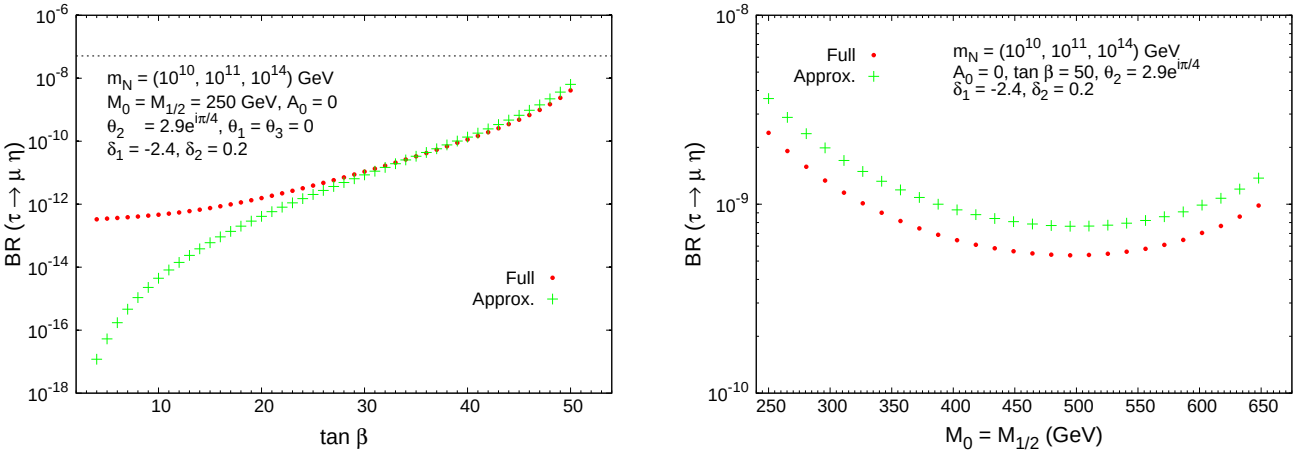

Figure 3.6: Comparison between the predicted rates of $\mathrm{BR}(\tau \to \mu\eta)$ in the NUHM from our full one-loop computation and from the approximate result of Eq. (3.56) as a function of $\tan\beta$ (left panel) and $M_{\rm SUSY} = M_0 = M_{1/2}$ (right panel).

work must be done by switching off the bottom-loop induced contributions and the higher order loop-effects enhanced by $\tan\beta$ factors which were taken into account in [203] but we are not including here. This means setting their ξ_q parameters to $\xi_b = 0$ and $\xi_s = 1$ in their formulae. We believe that this small discrepancy is mainly due to the different approaches for hadronisation. In particular, they neglect the $m_{u,d}$ masses whereas we are taking into account chiral symmetry breaking effects via the explicit m_π^2 and m_K^2 dependences, which are well determined in the χPT approach. On the other hand, our prediction for $\mathrm{BR}(\tau \to \mu\eta')$ is slightly above $\mathrm{BR}(\tau \to \mu\eta)$, due basically to the larger Higgs coupling to η', $|B_L(\eta')^{(A_0)}| > |B_L(\eta)^{(A_0)}|$. The prediction in [203] of $\mathrm{BR}(\tau \to \mu\eta')$ is, however, a factor 100 smaller than ours. The prediction for $\mathrm{BR}(\tau \to \mu\pi)$ here and in [203] agree within a factor of 2. Finally, the prediction for $\mathrm{BR}(\tau \to \mu K^+K^-)$ in [213] is larger than our result in about a factor 50.

The goodness of the above approximate result for $\tau \to \mu\eta$ in Eq. (3.56) can be seen in Fig. 3.6, where it is compared with the full result as a function of $\tan\beta$ and $M_{\rm SUSY}$. It is clear that, for $\tan\beta$ values larger than about 30, the approximation is quite good, providing rates that are at most a factor of 2 above the full predictions. Moreover, the behaviour with $\tan\beta$ of the full result at this region is well described by the $(\tan\beta)^6$ behaviour of the approximate one. Regarding the behaviour with $M_{\rm SUSY}$, we see again that the approximate and full results differ by less than a factor of 2 and they both follow the same pattern. The displayed dependence with $M_{\rm SUSY}$ can be easily understood from the dependence of m_{A^0} with this parameter, as it was shown in Fig. 1.15. For the studied range in this plot, $250 < M_{\rm SUSY}\,(\mathrm{GeV}) < 650$, this leads to a relatively small variation in the rates of about $\mathrm{BR}_{\rm max}/\mathrm{BR}_{\rm min} \sim 5$.

The Higgs dominance approach, however, is not so good for other LFV tau decay channels. In particular, it is clearly not a good approximation for $\tau \to 3\mu$ because, as we have shown in Section 2.3.4, there are other contributions from γ-mediated, Z-mediated and box diagrams that enter into the full computation [49, 102], and, moreover, the photon-mediated diagrams give by far the dominant contribution in this decay.

Similarly to the $\tau \to 3\mu$ channel, the semileptonic $\tau \to \mu PP$ decays (with the exception of $\tau \to \mu\pi^0\pi^0$) are clearly dominated by the photon contribution and therefore they can be better approximated by the corresponding simplified formulae of this contribution. By neglecting the muon mass we have found the following approximate result:

$$\begin{aligned} \mathrm{BR}(\tau \to \mu PP)_{\gamma_{\mathrm{approx}}} &= \int_{4m_P^2}^{m_\tau^2} ds \left(1 - \frac{s}{m_\tau^2}\right)^2 \left(1 + \frac{2m_\tau^2}{s}\right) \left(1 - \frac{4m_P^2}{s}\right)^{3/2} |F_V^{PP}(s)|^2 \\ &\quad \times \frac{\alpha}{24\, m_\tau^2} \mathrm{BR}(\tau \to \mu\gamma). \end{aligned} \tag{3.63}$$

And from this we get

$$\begin{aligned} \mathrm{BR}(\tau \to \mu\pi^+\pi^-)_{\gamma_{\mathrm{approx}}} &= 2.5 \times 10^{-3}\ \mathrm{BR}(\tau \to \mu\gamma) \\ &= 3.7 \times 10^{-5}\, |\delta_{32}|^2 \left(\frac{100}{M_{\mathrm{SUSY}}(\mathrm{GeV})}\right)^4 \left(\frac{\tan\beta}{60}\right)^2, \end{aligned} \tag{3.64}$$

$$\begin{aligned} \mathrm{BR}(\tau \to \mu K^+K^-)_{\gamma_{\mathrm{approx}}} &= 2.0 \times 10^{-4}\ \mathrm{BR}(\tau \to \mu\gamma) \\ &= 3.0 \times 10^{-6}\, |\delta_{32}|^2 \left(\frac{100}{M_{\mathrm{SUSY}}(\mathrm{GeV})}\right)^4 \left(\frac{\tan\beta}{60}\right)^2, \end{aligned} \tag{3.65}$$

$$\begin{aligned} \mathrm{BR}(\tau \to \mu K^0\bar{K}^0)_{\gamma_{\mathrm{approx}}} &= 1.2 \times 10^{-4}\ \mathrm{BR}(\tau \to \mu\gamma) \\ &= 1.8 \times 10^{-6}\, |\delta_{32}|^2 \left(\frac{100}{M_{\mathrm{SUSY}}(\mathrm{GeV})}\right)^4 \left(\frac{\tan\beta}{60}\right)^2, \end{aligned} \tag{3.66}$$

$$\begin{aligned} \mathrm{BR}(\tau \to \mu\rho)_{\gamma_{\mathrm{approx}}} &= 2.3 \times 10^{-3}\ \mathrm{BR}(\tau \to \mu\gamma) \\ &= 3.4 \times 10^{-5}\, |\delta_{32}|^2 \left(\frac{100}{M_{\mathrm{SUSY}}(\mathrm{GeV})}\right)^4 \left(\frac{\tan\beta}{60}\right)^2, \end{aligned} \tag{3.67}$$

$$\begin{aligned} \mathrm{BR}(\tau \to \mu\phi)_{\gamma_{\mathrm{approx}}} &= 8.4 \times 10^{-5}\ \mathrm{BR}(\tau \to \mu\gamma) \\ &= 1.3 \times 10^{-6}\, |\delta_{32}|^2 \left(\frac{100}{M_{\mathrm{SUSY}}(\mathrm{GeV})}\right)^4 \left(\frac{\tan\beta}{60}\right)^2. \end{aligned} \tag{3.68}$$

As can be clearly seen in Fig. 3.7 these results approach pretty well the full rates for most of the M_{SUSY} studied region. For $\mathrm{BR}(\tau \to \mu\pi^+\pi^-)$, they are indeed indistinguishable in this plot. It is only at very large $M_{\mathrm{SUSY}} \geq 750$ GeV that the approximate result of $\mathrm{BR}(\tau \to \mu K^+K^-)$

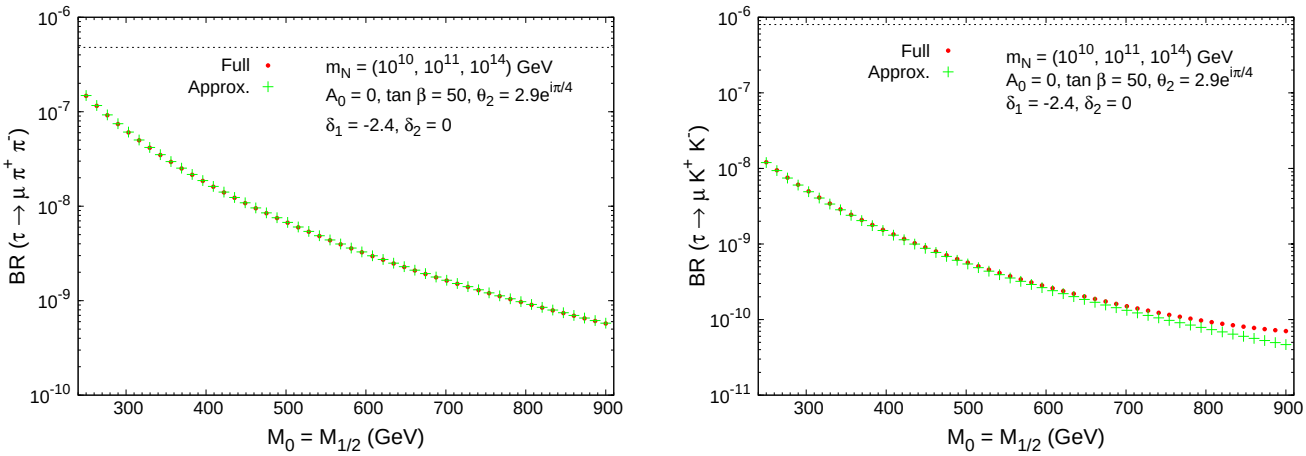

Figure 3.7: Comparison between the full rates and the approximate results in the NUHM scenario by considering just the photon-mediated contributions for $\tau \to \mu\pi^+\pi^-$ (left panel) and $\tau \to \mu K^+ K^-$ (right panel) as a function of $M_{\rm SUSY} = M_0 = M_{1/2}$. The dashed horizontal lines are the present experimental upper bounds [72].

separates slightly from the full result, due to the Higgs contribution which competes with the photon one in this region.

For completeness and comparison, we also include here the predictions for the leading LFV τ decay channel, $\tau \to \mu\gamma$. Fig. 3.8 displays the predictions of the full and approximate rates for this $\tau \to \mu\gamma$ channel. The full rates are taken from [102] and have been reported in Chapter 2, and the approximate ones are given by the result of the MI approach in Eq. (2.6) [51, 179]. In this case, and for the chosen parameters in this plot, the approximate and the full results agree to better than a factor 2. We have verified, however, that for other choices of $\delta_{1,2}$ the difference between them can be larger. Regarding this difference, we emphasise that in using the MI approach and LLog approximation one has to be carefull because they are known to fail in some regions of the CMSSM parameter space. For instance, in [138], the departure of the MI from the exact result is estimated to be up to 50% for $|\delta_{32}| \sim 1$. In [103] it has been found that the use of the MI and LLog for large trilinear couplings, $A_0 \sim \mathcal{O}$ (1 TeV), can fail in several orders of magnitude.

The most evident conclusion from Fig. 3.8 is that for the chosen parameters in this plot and for $M_{\rm SUSY} < 1600$ GeV, the $\tau \to \mu\gamma$ rates are above the present experimental sensitivity, therefore this tau decay channel is at present the most competitive one in setting bounds on the $\tau - \mu$ LFV. However, besides experimental issues, the limitation of this channel is that it is not sensitive at all to the Higgs sector. In this sense, the semileptonic channels are more interesting,

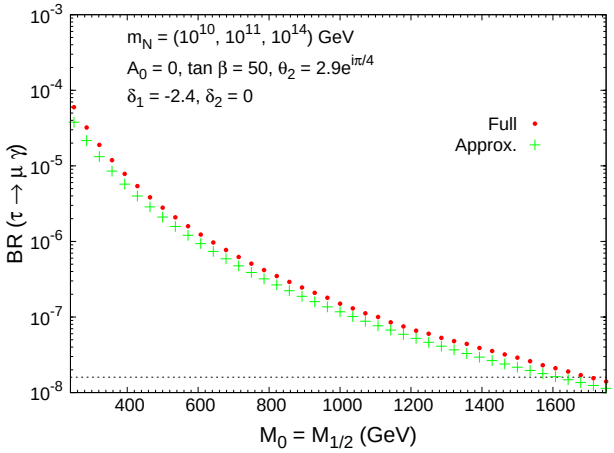

Figure 3.8: Comparison between the full one-loop prediction [49] and approximate results of Eq. (2.6) for $\tau \to \mu\gamma$ as a function of $M_{\rm SUSY} = M_0 = M_{1/2}$ in the NUHM scenario. The horizontal line is the present experimental upper bound [68].

and can be clearly competitive in the large $M_{\rm SUSY} \sim \mathcal{O}(1 - 2\,\text{TeV})$ region.

In Figs. 3.9 and 3.10 we plot finally the predictions for BR($\tau \to \mu K^+ K^-$) and BR($\tau \to \mu\eta$) as a function of one of the most relevant parameters for these Higgs-mediated processes which is the corresponding Higgs boson mass. Firstly, we see again that the approximate and exact results of the Higgs contribution agree within a factor of two for both channels, but the agreement of the full result with respect to the Higgs contribution is clearly worse in the case of $\tau \to \mu K^+ K^-$ than in $\tau \to \mu\eta$. In the latter, the agreement is quite good because the Z-mediated contribution is negligible, and this holds for all $M_{\rm SUSY}$ values in the studied interval, 250 GeV $< M_{\rm SUSY} <$ 750 GeV . In the first, it is only for large $M_{\rm SUSY}$ that the H-mediated contribution competes with the γ-mediated one and the Higgs rates approach the total rates. For instance, Fig. 3.9 shows that for $M_{\rm SUSY} = 750$ GeV and $m_{H^0} = 160$ GeV the total rate is about a factor 2 above the Higgs rate, but for $m_{H^0} = 240$ GeV it is already more than a factor 5 above.

In these figures we have also explored larger values of m_{N_3} and $\tan\beta$, by using in those cases the approximate formula, and in order to conclude about the values that predict rates comparable to the present experimental sensitivity. We can conclude then that, at present, it is certainly $\tau \to \mu\eta$ the most competitive LFV semileptonic tau decay channel. The parameter values that provide rates being comparable to the present sensitivities in this channel are $\tan\beta = 60$ and $m_{N_3} = 10^{15}$ GeV which correspond to $|\delta_{32}| \simeq 2$. These large rates, however, should be taken with care and be considered just as an order of magnitude estimate since, as we have explained in Sec. 2.1, they correspond to neutrino Yukawa couplings which are clearly in the non-perturbative

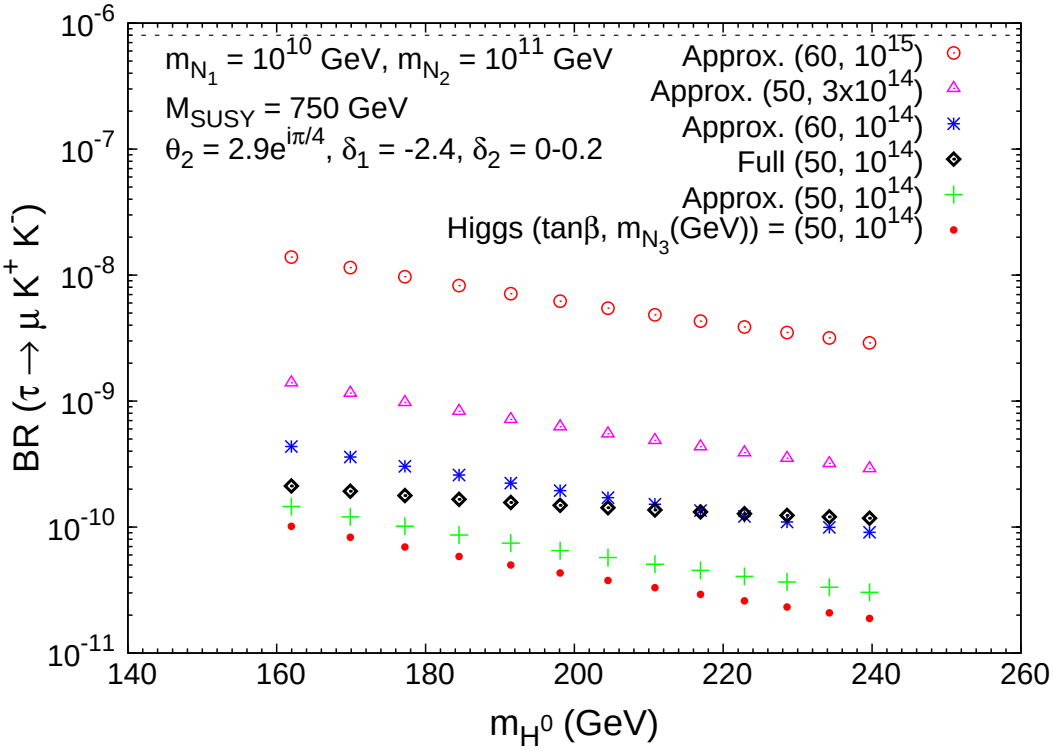

Figure 3.9: Predictions for BR($\tau \to muK^+K^-$) as a function of m_{H^0} in the NUHM scenario. A comparison between the full one-loop computation and the approximation given by Eq. (3.57) for various choices of large $\tan\beta$ and m_{N_3} is included. The horizontal line is the present experimental upper bound [72].

regime. This is why we do not provide the corresponding full rates for them.

3.4 Summary

In this chapter we have presented a complete one-loop computation of the branching ratios for the LFV semileptonic τ decays within the context of two constrained SUSY-seesaw scenarios, the CMSSM-seesaw and the NUHM-seesaw. We have included both analytical and numerical results for the particular channels: $\tau \to \mu PP$, with $PP = \pi^+\pi^-, \pi^0\pi^0, K^+K^-, K^0\bar{K}^0$; $\tau \to \mu P$ with $P = \pi, \eta, \eta'$; and $\tau \to \mu\rho$, $\tau \to \mu\phi$. The analysis of the channels $\tau \to \mu PP$, with $PP = \pi^+\pi^-, \pi^0\pi^0, K^0\bar{K}^0$, and $\tau \to \mu\rho$, $\tau \to \mu\phi$ are, to our knowledge, the first ones in the literature within the CMSSM-seesaw context. In addition, we have compared our predictions for $\tau \to \mu K^+K^-$ and for $\tau \to \mu P$ with $P = \pi, \eta, \eta'$ with previous predictions in the literature and found some discrepancies.

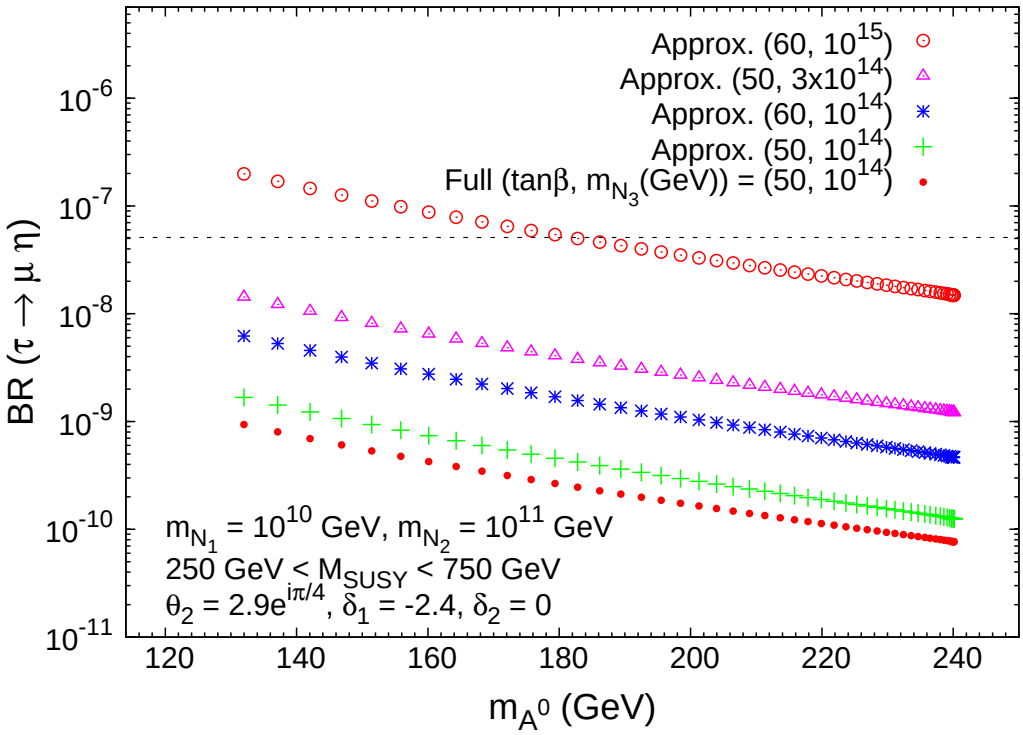

Figure 3.10: Predictions for BR($\tau \to \mu\eta$) as a function of m_{A^0} in the NUHM scenario. A comparison between the full one-loop computation and the approximation given by Eq. (3.57) for various choices of large $\tan\beta$ and m_{N_3} is included. The horizontal line is the present experimental upper bound [68].

The results for $\tau \to \mu\pi^+\pi^-$ demonstrate that this channel is clearly dominated by the photon-mediated contribution in all the studied region of 100 GeV $< M_{\rm SUSY} <$ 1000 GeV. In fact it is by far the $\tau \to \mu PP$ channel with the highest rates, reaching values close to its present experimental bound at 4.8×10^{-7} for some input parameter values. Concretely, it happens for low $M_{\rm SUSY} \sim 100 - 200$ GeV, large $\tan\beta \sim 50 - 60$, large $m_{N_3} \sim 10^{14} - 10^{15}$ GeV and large $\arg\theta_2 \sim \pi/4 - \pi/2$ (these two latter parameters producing a large $\delta_{32} \sim \mathcal{O}(1)$). In contrast, $\tau \to \mu\pi^0\pi^0$ can only be mediated by h^0 and H^0 Higgs bosons and their rates are very small. Besides, they can not be compared to data, since there is no bound in this channel. The cases of $\tau \to \mu K^+K^-$ and $\tau \to \mu K^0\bar{K}^0$ decays are much more interesting. In these two channels, the photon-mediated contribution dominates in most of the studied region of $M_{\rm SUSY}$, except at large $M_{\rm SUSY} > 750$ GeV values, where the Higgs-mediated and the γ-mediated contributions can compete. This competition happens in specific constrained scenarios of NUHM type with low $m_{H^0} \sim 100 - 200$ GeV values and very heavy SUSY spectrum with $M_{\rm SUSY} > 750$ GeV.

This peculiar MSSM spectrum and the fact that Higgs bosons couple stronger to K^+K^- (and $K^0\bar{K}^0$) than to $\pi^+\pi^-$ (and $\pi^0\pi^0$) is the reason why the H- and γ-mediated contributions can compete in $\tau \to \mu K^+K^-$ but not in $\tau \to \mu\pi^+\pi^-$. Furthermore, due to the fact that the photon diagram still dominates BR($\tau \to \mu K^+K^-$) in a large region of the parameter space with 100 GeV $< M_{\rm SUSY} <$ 750 GeV, the involved hadronic form factors do play a crutial role in the final rates. Consequently, our results for this channel are in disagreement with those of [213] where they only included the Higgs-mediated contribution. We have also shown that the largest predicted rates for BR($\tau \to \mu K^+K^-$) are, as in $\tau \to \mu\pi^+\pi^-$, at the region with low $M_{\rm SUSY} \sim 100 - 200$ GeV, large $\tan\beta \sim 50 - 60$, large $m_{N_3} \sim 10^{14} - 10^{15}$ GeV and large $\arg\theta_2 \sim \pi/4 - \pi/2$ values. However, the predicted rates do not reach yet the present experimental sensitivity, which in this channel is at 8×10^{-7}.

The results for $\tau \to \mu\eta$ and $\tau \to \mu\eta'$ demonstrate that these two channels are largely dominated by the A^0-mediated contribution and their predicted rates are very competitive in the case of NUHM scenarios with low $m_{A^0} \sim 100-200$ GeV values and large $\tan\beta \sim 50-60$. This is in qualitative agreement with previous estimates in the literature. However, we have found some important numerical discrepancies with respect to the estimate in [54]. Concretely, the predicted rates in the present work are smaller than those in [54] by a factor of about 7. We believe that these discrepancies are due to the different procedures of quark bilinear hadronisation. We claim that our results which are based on the well defined and more refined hadronisation prescription by χPT provide a better estimate. The rates for BR($\tau \to \mu\eta$) have also been compared with those in [179, 203] which are within the different context of non-constrained MSSM and with input δ_{32} not being connected to neutrino physics nor seesaw mechanism. We have checked, that the predicted rates are in reasonable agreement with these two works for, $\delta_{32} \sim \mathcal{O}(1)$, which in our case is reached by input seesaw parameters of $m_{N_3} \sim 10^{14} - 10^{15}$ GeV and large $\arg\theta_2 \sim \pi/4 - \pi/2$.

In addition, we have presented in this chapter a set of useful approximate formulae for all the semileptonic τ decays that we have compared with the full-one loop results and concluded that they give reasonable good estimates, say differing in less than a factor of two respect to the full result. We have also compared these results to those for the leptonic channel, $\tau \to 3\mu$, and the radiative decay, $\tau \to \mu\gamma$.

Chapter 4

$\mu - e$ conversion in nuclei

In this chapter we will focus on $\mu - e$ conversion in nuclei, and work again in the context of the CMSSM-seesaw and the NUHM-seesaw scenarios. At present, the most relevant $\mu - e$ flavour violating processes are $\mu \to e\gamma$, $\mu \to 3e$ and $\mu - e$ conversion in nuclei. The current experimental bounds on the muon decays have been collected in Tables 2.1 and 2.3 and set to $\text{BR}(\mu \to e\gamma) < 1.2 \times 10^{-11}$ [58] and $\text{BR}(\mu \to 3e) < 1.0 \times 10^{-12}$ [59]. Regarding $\mu - e$ conversion in heavy nuclei, the most stringent constraints at present arise for Titanium and Gold, respectively with $\text{CR}(\mu - e, \text{Ti}) < 4.3 \times 10^{-12}$ [60] and $\text{CR}(\mu - e, \text{Au}) < 7 \times 10^{-13}$ [61]. In the future, one expects significant improvements in the sensitivities to these LFV rates. For instance, MEG aims at reaching a sensitivity for $\mu \to e\gamma$ of 10^{-13} [62] in the very near future, which could further be improved to 10^{-14} in the next 4-5 years [63]. Although the situation for $\text{BR}(\mu \to 3e)$ is less certain, one does not expect the sensitivities to be better than $10^{-13} - 10^{-14}$ [63]. Undoubtedly, the most challenging prospects concern the experimental sensitivities to $\mu - e$ conversion in Titanium nuclei. The dedicated J-PARC experiment PRISM/PRIME has announced a remarkable improvement, albeit in a further future, of 10^{-18} [64].

4.1 Analytical results for $\mu - e$ conversion

In this section we report the analytical results for the $\mu - e$ conversion rates in terms of the parameters introduced in Chapter 1. We emphasise again that all the results are obtained in terms of physical mass eigenstates (with full propagators) for all MSSM particles entering in the computation, namely, charginos $\tilde{\chi}^-_A (A = 1, 2)$, neutralinos $\tilde{\chi}^0_A (A = 1, ..., 4)$, charged sleptons $\tilde{l}^-_X (X = 1, ..., 6)$, sneutrinos $\tilde{\nu}^-_X (X = 1, 2, 3)$ and the neutral Higgs bosons, h^0 and H^0.

For the presentation of the results we closely follow the general parameterisation (and approximations) of [52]. One starts with the most general effective Lagrangian for four-fermion

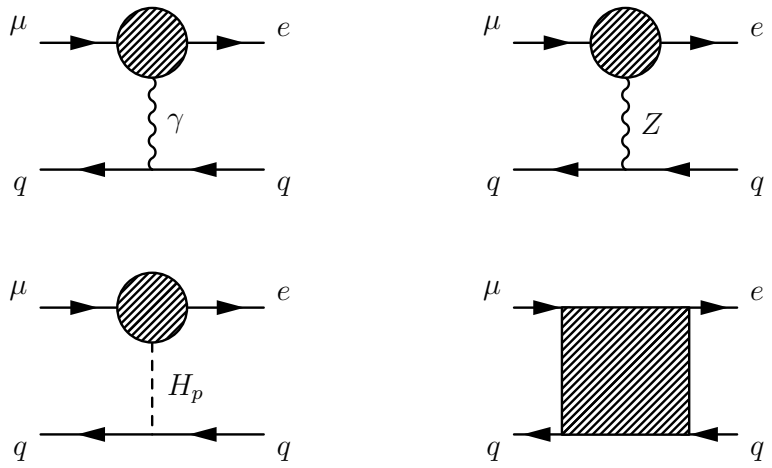

Figure 4.1: Photon-, Z-, H-penguin and box diagrams contributing to $\mu - e$ conversion in nuclei.

interactions which describes coherent $\mu - e$ conversion. At the quark level, this is given by

$$\mathcal{L}_{\text{eff}} = -\frac{G_F}{\sqrt{2}} \sum_q \left\{ \left[g_{LS(q)} \bar{e}_L \mu_R + g_{RS(q)} \bar{e}_R \mu_L \right] \bar{q} q + \left[g_{LV(q)} \bar{e}_L \gamma^\mu \mu_L + g_{RV(q)} \bar{e}_R \gamma^\mu \mu_R \right] \bar{q} \gamma_\mu q \right\} , \tag{4.1}$$

where G_F is the Fermi coupling. Notice that only scalar (S) and vector (V) effective operators do contribute, with couplings given by $g_{LS(q)}, g_{RS(q)}$ and $g_{LV(q)}, g_{RV(q)}$ (respectively left and right, in both cases). This effective Lagrangian at the quark level is then converted into an effective Lagrangian at the nucleon level, by means of the appropriate nucleon form factors [215–217]. In the limit of negligible momentum dependence of the nucleon form factors, (a reasonable approximation given the small momentum transfer in the $\mu - e$ process), the quark matrix elements can be simply replaced by the nucleon matrix elements as follows

$$\begin{aligned} \langle p | \, \bar{q} \, \Gamma_K \, q \, | p \rangle &= G_K^{(q,p)} \, \bar{p} \, \Gamma_K \, p \, , \\ \langle n | \, \bar{q} \, \Gamma_K \, q \, | n \rangle &= G_K^{(q,n)} \, \bar{n} \, \Gamma_K \, n \, , \end{aligned} \tag{4.2}$$

where $\Gamma_K = (1, \gamma_\mu)$ respectively for $K = (S, V)$. The numerical values of the relevant G_K's are [52, 218]

$$\begin{aligned} G_V^{(u,p)} &= G_V^{(d,n)} = 2 \, ; \quad G_V^{(d,p)} = G_V^{(u,n)} = 1 \, ; \\ G_S^{(u,p)} &= G_S^{(d,n)} = 5.1 \, ; \quad G_S^{(d,p)} = G_S^{(u,n)} = 4.3 \, ; \\ G_S^{(s,p)} &= G_S^{(s,n)} = 2.5 \, . \end{aligned} \tag{4.3}$$

The conversion rates are then predicted in terms of the relevant isoscalar, $g_{XK}^{(0)}$, and isovector

couplings, $g^{(1)}_{XK}$ (with $X = L, R$ and $K = S, V$), which are given by

$$g^{(0)}_{XK} = \frac{1}{2} \sum_{q=u,d,s} \left(g_{XK(q)} G^{(q,p)}_K + g_{XK(q)} G^{(q,n)}_K \right) ,$$
$$g^{(1)}_{XK} = \frac{1}{2} \sum_{q=u,d,s} \left(g_{XK(q)} G^{(q,p)}_K - g_{XK(q)} G^{(q,n)}_K \right) . \tag{4.4}$$

Further working under the approximation of equal proton and neutron densities in the nucleus, and of a non-relativistic muon wave function for the $1\,s$ state, the final formula for the $\mu - e$ conversion rate, relative to the the muon capture rate, can be finally written as

$$\begin{aligned} \mathrm{CR}(\mu - e, \mathrm{Nucleus}) = & \frac{p_e\, E_e\, m_\mu^3\, G_F^2\, \alpha^3\, Z_{\mathrm{eff}}^4\, F_p^2}{8\,\pi^2\, Z} \\ & \times \left\{ \left| (Z+N) \left(g^{(0)}_{LV} + g^{(0)}_{LS} \right) + (Z-N) \left(g^{(1)}_{LV} + g^{(1)}_{LS} \right) \right|^2 + \right. \\ & \left. \left| (Z+N) \left(g^{(0)}_{RV} + g^{(0)}_{RS} \right) + (Z-N) \left(g^{(1)}_{RV} + g^{(1)}_{RS} \right) \right|^2 \right\} \frac{1}{\Gamma_{\mathrm{capt}}} , \end{aligned} \tag{4.5}$$

where Z and N are the number of protons and neutrons in the nucleus, while Z_{eff} is an effective atomic charge, obtained by averaging the muon wave function over the nuclear density [219]. F_p is the nuclear matrix element and Γ_{capt} denotes the total muon capture rate. The other quantities in the above formula correspond to the muon mass, m_μ, the momentum and energy of the electron, p_e and E_e (which are set to m_μ in the numerical evaluation), and the electromagnetic coupling constant, α.

We have computed the full set of one-loop diagrams contributing to the quantity $\mathrm{CR}(\mu - e, \mathrm{Nucleus})$: γ-penguins, Z- and Higgs-boson penguins and box diagrams. These are schematically drawn at the quark level in Fig. 4.1, and receive contributions from several diagrams, mediated by SUSY particles, which are collected in Appendix B. The analytical results of the computation are summarised in terms of the contributions of these diagrams to the vector and scalar couplings,

$$g_{LV(q)} = g^{\gamma}_{LV(q)} + g^{Z}_{LV(q)} + g^{\mathrm{B}}_{LV(q)} ,$$
$$g_{LS(q)} = g^{H}_{LS(q)} + g^{\mathrm{B}}_{LV(q)} . \tag{4.6}$$

In the above, the photon couplings $g^{\gamma}_{LX(q)}$, the Z-boson couplings $g^{Z}_{LX(q)}$, the H-boson couplings $g^{H}_{LS(q)}$, and the couplings arising from the boxes $g^{\mathrm{B}}_{LX(q)}$ (with $X = V, S$) are respectively given

by

$$
\begin{aligned}
g^{\gamma}_{LV(q)} &= \frac{\sqrt{2}}{G_F} e^2 Q \left(A_1^L - A_2^R \right) \,, \\
g^{Z}_{LV(q)} &= -\frac{\sqrt{2}}{G_F} \, \frac{Z_L^q + Z_R^q}{2} \, \frac{F_L}{m_Z^2} \,, \\
g^{\mathrm{B}}_{LV(q)} &= -\frac{\sqrt{2}}{G_F} \left(B_q^{(n)LV} + B_q^{(c)LV} \right) \,, \\
g^{H}_{LS(q)} &= -\frac{\sqrt{2}}{G_F} \frac{1}{2} \sum_p \frac{1}{m_{H_p}^2} H_L^{(p)} \left(S_{L,q}^{(p)} + S_{R,q}^{(p)} \right) \,, \\
g^{\mathrm{B}}_{LS(q)} &= -\frac{\sqrt{2}}{G_F} \left(B_q^{(n)LS} + B_q^{(c)LS} \right) \,.
\end{aligned}
\tag{4.7}
$$

Likewise, for the right-handed couplings we find

$$
\begin{aligned}
g_{RV(q)} &= g_{LV(q)}\big|_{L \leftrightarrow R} \,, \\
g_{RS(q)} &= g_{LS(q)}\big|_{L \leftrightarrow R} \,.
\end{aligned}
\tag{4.8}
$$

The explicit formulae for the form factors of the photon ($A^{(L,R)}_{(1,2)}$), of the Z-boson ($F_{(L,R)}$), of the Higgs-boson ($H^{(p)}_{(L,R)}$, where $p = 1,2,3$ corresponds to $H_p = h^0, H^0, A^0$), and of the box diagrams ($B_q^{(n,c)(L,R)(V,S)}$) are listed in Appendix B. In each case, the relevant couplings $Z^q_{(L,R)}$, $S^{(p)}_{(L,R)q}$, etc., can be found in Appendix A.

It is important to stress that $S^{(3)}_{L,q} + S^{(3)}_{R,q}$ vanishes and therefore there are no contributions from the CP-odd Higgs boson A^0. This is a consequence of working in the approximation of coherent $\mu - e$ conversion, in which case the initial and final nucleus state is the same, thus leading to vanishing matrix elements for pseudoscalar currents like $\langle \mathrm{Nucleus} \,|\, \bar{q}\, \gamma_5\, q \,|\, \mathrm{Nucleus} \rangle$. Also notice that from the values of the $S^{(p)}_{(L,R)q}$ Higgs couplings, one can anticipate that in the large $\tan\beta$ and small Higgs mass regime, the dominant Higgs contribution will be that of H^0.

When compared to the results obtained in [49], our expressions coincide in the formulae for the photon-penguins. Up to a global sign, the vector contributions from boxes also agree. Discrepancies occur regarding the Z-penguins, and the differences can be read by comparing our expressions in Eqs. (B.11) of Appendix B, with those of Eqs.(22-29) in [49]. As previously mentioned, we have included in addition scalar contributions from boxes and Higgs-mediated diagrams not considered in [49].

A connection between our results for the Higgs contributions and those reported in [55] can be established in the large $\tan\beta$ limit, writing the output in the MI approximation format. Under these conditions, and considering the limit of a common mass for all SUSY particles involved, which is much larger than the SM particle masses, $M_{\mathrm{soft}} \sim \mu \sim M_{\mathrm{SUSY}} >> m_W$, one

arrives at the following simple expression for the dominant H^0 form factor [101]

$$H_L^{(2)} \;=\; \frac{g^3}{(4\pi)^2}\,\frac{m_\mu}{12\,m_W}\,\delta_{21}\,\tan^2\beta\,\left[1+\frac{1}{2}(1-3\tan^2\theta_W)\right]\,, \tag{4.9}$$

where the first term arises from chargino mediated loops, while the second stems from neutralino mediated contributions.

From the above, one can finally obtain a simple expression for the H^0 contribution to the conversion rate, which is clearly dominated by the strange quark coupling, due to the enhancement in the coupling by m_s. This arises via $g_{LS}^{(0)} \simeq g_{LS(s)}^{H^0} G_S^{(s,p)}$ with

$$g_{LS(s)}^{H^0} \;=\; \frac{\sqrt{2}}{G_F}\,\frac{1}{2}\,\frac{1}{m_{H^0}^2}\,H_L^{(2)}\,\frac{g m_s}{m_W}\,\tan\beta\,. \tag{4.10}$$

Plugging this simplified result for the $g_{LS}^{(0)}$ coupling into the approximate conversion rate for the Higgs-dominated case,

$$\mathrm{CR}(\mu-e,\mathrm{Nucleus}) \simeq \frac{p_e\,E_e\,m_\mu^3\,G_F^2\,\alpha^3\,Z_{\mathrm{eff}}^4\,F_p^2}{8\pi^2\,Z}\,\left\{\left|(Z+N)\,g_{LS}^{(0)}\right|^2\right\}\,\frac{1}{\Gamma_{\mathrm{capt}}}\,, \tag{4.11}$$

we obtain the expected $\tan^6\beta$ enhancement of the H^0 contribution. Moreover, the dependence on the Higgs mass $\left(\frac{1}{m_{H^0}^4}\right)$, as well as the typical prefactor $|\delta_{21}|^2$ accounting for the lepton flavour changing effect are equally recovered. Within this approximation, and taking a specific value of $\delta_{21} = 10^{-3}$, allows to obtain an order-of-magnitude estimate for the conversion rate in the case of Titanium nuclei,

$$\mathrm{CR}(\mu-e,\mathrm{Ti}) \;\simeq\; \mathcal{O}(10^{-12})\,\left(\frac{115\,\mathrm{GeV}}{m_{H^0}}\right)^4\,\left(\frac{\tan\beta}{50}\right)^6\,, \tag{4.12}$$

in agreement with the estimate of [55].

Finally, it is worth mentioning that the heavy SUSY particles do not decouple in the Higgs contributions to the $\mu-e$ conversion rates. This can be understood from the previous result of $H_L^{(2)}$ in Eq. (4.9), which is constant in the large M_{SUSY} limit. This SUSY non-decoupling effect has also been noticed in association to other Higgs-mediated LFV processes [53, 56, 101, 179, 203]. In particular we have emphasised in previous chapters that this non-decoupling behaviour happens in the $\tau \to 3\,\mu$ and some LFV semileptonic τ decays.

4.2 Numerical results and discussion

In this section we present the numerical results of the $\mu-e$ conversion rates in nuclei within the SUSY-seesaw context. We begin by addressing the CMSSM-seesaw, and then proceed to

the NUHM-seesaw. In both scenarios, we consider the dependence of the theoretical predictions for the conversion rates on the most relevant SUSY-seesaw parameters. In our discussion, we will give a particular emphasis to the most significant differences between the CMSSM- and NUHM-seesaw scenarios.

The numerical results presented in this section are mainly devoted to the particular case of Titanium nuclei, given that one expects a notable improvement of future experimental sensitivities in that case [64]. However, some additional predictions for other nuclei are also included here, for comparison. The case of Gold nuclei is of particular interest, since at present the most stringent bound is that of CR($\mu - e$, Au) [61].

In what follows, we begin by presenting the predictions for the $\mu - e$ conversion rates in Titanium nuclei within the CMSSM-seesaw.

4.2.1 Universality: CMSSM-seesaw

The numerical results of the CR($\mu - e$, Ti) within the CMSSM-seesaw scenario are displayed in Figs. 4.2 through 4.5. The following discussion is focused on the most relevant parameters, namely m_{N_i}, $\theta_{1,2,3}$, θ_{13}, $\tan\beta$, M_0 and $M_{1/2}$.

In Fig. 4.2, we display the prediction of CR($\mu - e$, Ti) as a function of the heavy neutrino masses for the various SPS points, and for the particular choice $\theta_i = 0$ ($i = 1, 2, 3$) and $\theta_{13} = 5^\circ$. We also consider the case of degenerate and hierarchical heavy neutrino spectra (respectively left and right panels). In both scenarios for degenerate and hierarchical heavy neutrinos, we find a strong dependence on the the heavy neutrino masses. We also see that the rates for the various SPS points exhibit the following hierarchy, $\mathrm{BR}_4 > \mathrm{BR}_{1\mathrm{b}} \gtrsim \mathrm{BR}_{1\mathrm{a}} > \mathrm{BR}_3 \gtrsim \mathrm{BR}_2 > \mathrm{BR}_5$. This behaviour can be understood in terms of the growth of the CRs with $\tan\beta$, and from the different mass spectra associated with each point.

In the case of degenerate heavy neutrinos, we find the expected fast growing behaviour of CR($\mu - e$, Ti) as a function of the common neutrino mass m_N. For the values of m_N within the studied interval $\left[10^9\,\mathrm{GeV}, 10^{15}\,\mathrm{GeV}\right]$, the predictions for the CR($\mu - e$, Ti) range vary over ten orders of magnitude. We also see that, for the chosen input parameter values, the predicted rates cross the experimental bound for the large m_N region. In the latter, the Yukawa couplings can be large (for instance, Y^ν_{33} and Y^ν_{32} can be $\mathcal{O}(1)$, while Y^ν_{22} and Y^ν_{21} can be of $\mathcal{O}(10^{-3})$), leading to excessively large rates, so that these large m_N values are disfavoured by data. The experimental bound is saturated for m_N values ranging from 2×10^{13} GeV for SPS 4 up to about 10^{15} GeV for SPS 5. In the case of hierarchical heavy neutrinos a similar behaviour of the predicted rates is found with respect to the heaviest neutrino mass, m_{N_3}. We have also checked that the conversion rates do not significantly depend on m_{N_1} and m_{N_2}, provided that

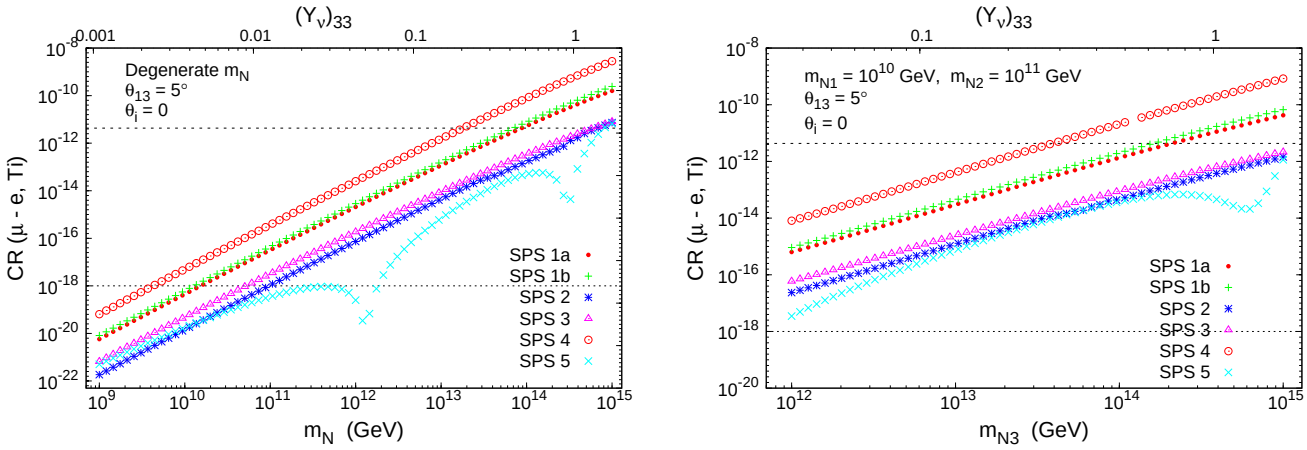

Figure 4.2: CR($\mu - e$, Ti) as a function of the relevant heavy neutrino mass: m_N (on the left) and m_{N_3} (on the right), respectively associated with the degenerate and hierarchical cases. The predictions for SPS 1a (dots), 1b (crosses), 2 (asterisks), 3 (triangles), 4 (circles) and 5 (times) are included. On the upper horizontal axis we display the associated value of $(Y_\nu)_{33}$. In each case, we set $\theta_{13} = 5°$, and consider the limit where $\theta_i = 0$. A dashed (dotted) horizontal line denotes the present experimental bound (future sensitivity).

their values are kept well below m_{N_3}. With the planned future sensitivity of 10^{-18} it will be possible to reach into wider regions of the heavy neutrino spectrum. Heavy neutrino masses above 10^{12} GeV can be probed for the several considered scenarios.

For most of the studied points, the previously illustrated dependence of the rates on the heavy neutrino masses is in agreement with the expected behaviour $|m_N \log m_N|^2$ obtained in the LLog approximation (as derived from Eq. (1.85)). However, a clear departure from this approximation is found for some points, the most remarkable being the case of SPS 5. This failure of the LLog approximation has been known to happen in some scenarios, for instance those with either large A_0, or low M_0 and large $M_{1/2}$ [103].

The predictions for CR($\mu - e$, Ti) as a function of the R-matrix angles, $\theta_{1,2,3}$, are displayed in Fig. 4.3. In this case we have fixed the other relevant parameters as $\theta_{13} = 5°$, $m_N = 10^{13}$ GeV and $m_{N_i} = (10^{10}, 10^{11}, 10^{13})$ GeV (degenerate and hierarchical heavy neutrinos, respectively) and chosen SPS 1a. To fully explore the variation of the rates with the complex angles[1] θ_i, we

[1]Complex θ_i may imply the presence of CP violation in the neutrino Yukawa couplings. In addition to affecting the LFV rates, these phases will induce contributions to flavour-conserving CP violating observables, as is the case of charged lepton electric dipole moments (EDMs). Throughout the present study we have verified that the associated predictions for the charged lepton EDMs are in agreement with the current experimental bounds [10] which have been summarised in Section 1.7.2.

have scanned the intervals $0 < |\theta_i| < \pi$ rad and $0 \leq \arg\theta_i \leq \frac{\pi}{2}$ rad. From this figure we see that the dependence on the three θ_i is very similar in the degenerate case, whereas the same does not occur for hierarchical heavy neutrinos. In the former, the rates smoothly grow with both modulus and argument, and are independent of θ_i in the real case. In the latter, the rates are almost independent of θ_3, and present a different minima pattern regarding θ_1 and θ_2. The deep minima occuring in the real case are a consequence of the corresponding minima appearing in the relevant elements of the Yukawa couplings (as given by Eq. (1.19)). Notice that the observed behaviour of CR($\mu - e$, Ti) as a function of θ_i can be indeed easily understood from the simple analytical expression obtained in the LLog approximation (cf. Eq. (1.85)).

The most important outcome from Fig. 4.3 is that for both cases of degenerate and hierarchical heavy neutrinos, complex values of θ_i can increase the $\mu - e$ conversion rates by almost five orders of magnitude with respect to the $\theta_i = 0$ case. Only for a few specific choices of θ_i (for instance real θ_1 or θ_2, in the hierarchical case) can we observe a strong decrease with respect to the $\theta_i = 0$ case, but clearly this is not a generic situation.

In the following, and in order to simplify the analysis with respect to the other parameters, we will set $\theta_i = 0$, and assume that the corresponding predictions for the CR($\mu - e$, Ti) will constitute a representative case for the lowest conversion rates.

In Fig. 4.4 we show the dependence of the $\mu - e$ conversion rates on the light neutrino mixing angle θ_{13}. The other parameters are set to $m_N = 10^{14}$ GeV, $m_{N_i} = (10^{10}, 10^{11}, 10^{14})$ GeV, (respectively for degenerate and hierarchical heavy neutrinos) and $\theta_i = 0$. All the SPS points in Table 1.2 have been considered. For degenerate heavy neutrinos, the dependence on θ_{13} is softer than what is observed for the hierarchical case, leading to a variation in the rates of at most one order of magnitude in the studied range of $0^\circ \leq \theta_{13} \leq 10^\circ$ (the only exception being SPS 5, where the variation can reach up to two orders of magnitude). In contrast, this figure clearly manifests the very strong sensitivity of the CR($\mu - e$, Ti) to the θ_{13} mixing angle for hierarchical heavy neutrinos. In the hierarchical case, a variation of θ_{13} in the studied interval leads to an increase in the conversion rates by as much as five orders of magnitude. This huge variation is due to the strong decrease of this observable for very small θ_{13} angles, as can be easily understood from the dependence on this angle of the dominant $(L_{33} m_{N_3} \sqrt{m_{\nu_3}} c_1 c_2 s_{13})$ term in Eq. (1.85). Furthermore, the minimum of CR$(\mu - e, \mathrm{Ti})$ is expected to occur at a vanishing mixing angle, but this being the value at the seesaw scale, i.e., $\theta_{13}(m_M) = 0$. The deep minima in Fig. 4.4 are at $\theta_{13}(m_Z) \simeq 0.2^\circ$, which is precisely the RGE shifted value at m_Z from $\theta_{13}(m_M) = 0$. As θ_{13} grows, the predictions for SPS 4, SPS 1a and SPS 1b cross the present experimental bound. In particular, notice that for SPS 4, and for the present choice of input parameters, θ_{13} values larger than 2° would be excluded by present data.

In the previous chapters we have reported on an equally remarkable sensitivity to θ_{13} in

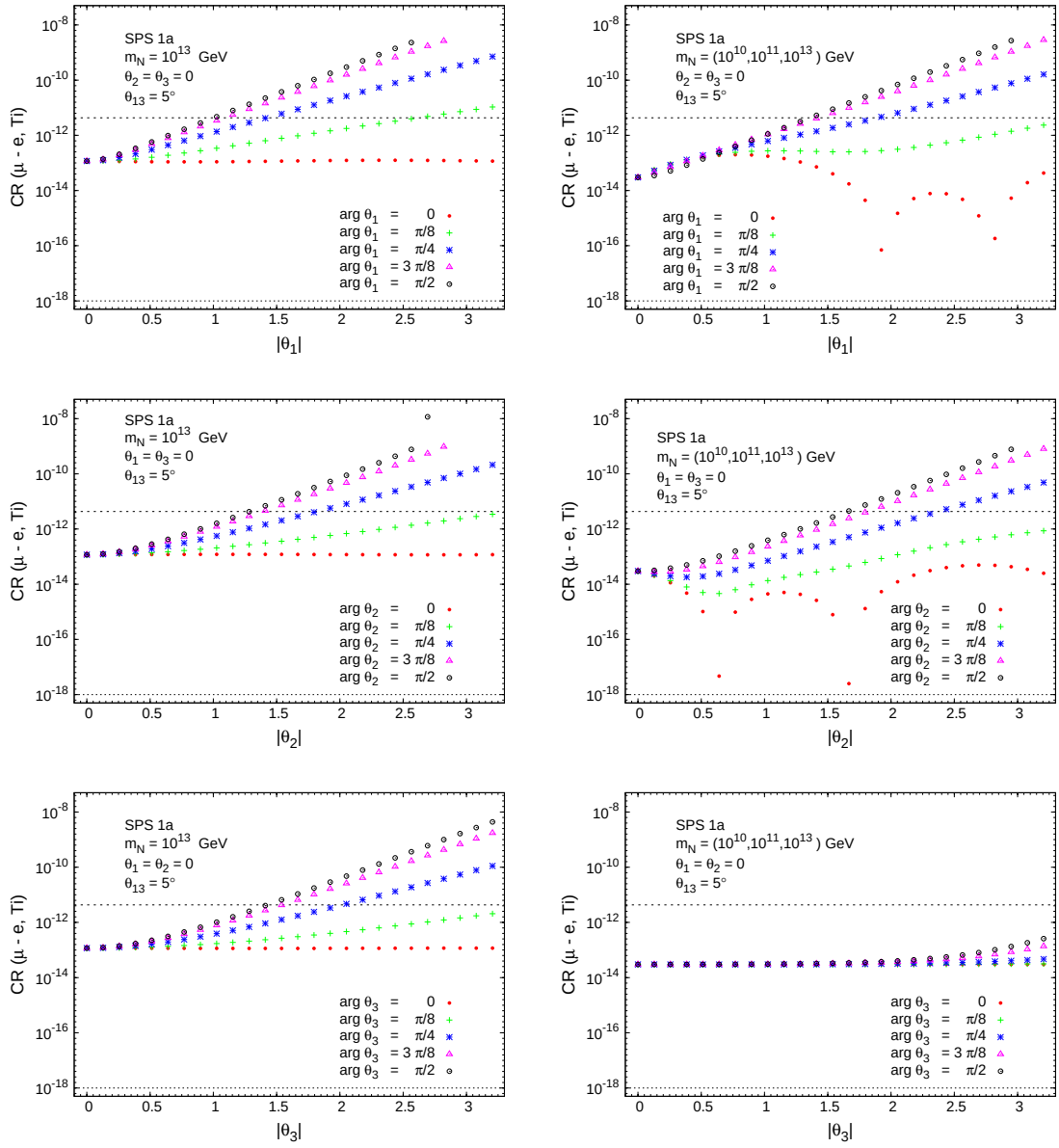

Figure 4.3: From top to bottom, CR($\mu - e$, Ti) as a function of $|\theta_i|$ ($i = 1, 2, 3$), for $\arg\theta_i = \{0, \pi/8\,, \pi/4\,, 3\pi/8, \pi/2\}$ (dots, crosses, asterisks, triangles and circles, respectively). Both $|\theta_i|$ and $\arg\theta_i$ are given in radians. On the left we consider degenerate heavy neutrinos (with $m_N = 10^{13}$ GeV), while on the right the hierarchical case is displayed (with $m_{N_i} = (10^{10}, 10^{11}, 10^{13})$ GeV). In all cases we take $\theta_{13} = 5°$, and set the CMSSM parameters to the SPS 1a case. A dashed (dotted) horizontal line denotes the present experimental bound (future sensitivity).

other $\mu - e$ violating processes, like $\mu \to e\gamma$ and $\mu \to 3e$, and also in tau decays as is the case of $\tau \to e\gamma$ and $\tau \to 3e$ [103]. This interesting behaviour with θ_{13} was proposed by us in [103]

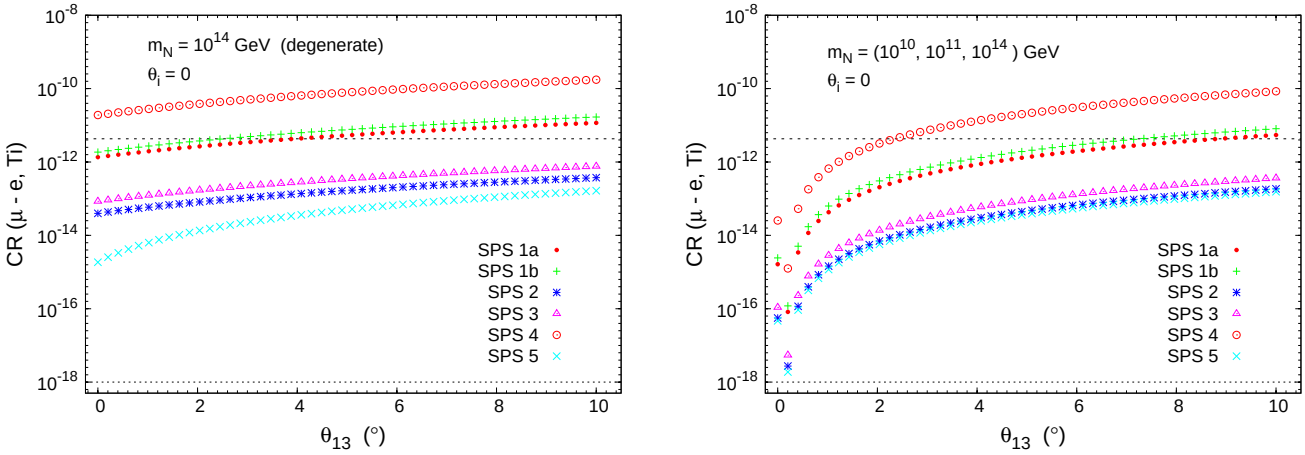

Figure 4.4: CR($\mu - e$, Ti) as a function of θ_{13} (in degrees), for SPS 1a (dots), 1b (crosses), 2 (asterisks), 3 (triangles), 4 (circles) and 5 (times). On the left we consider degenerate heavy neutrinos (with $m_N = 10^{14}$ GeV), while on the right the hierarchical case is displayed (with $m_{N_i} = (10^{10}, 10^{11}, 10^{14})$ GeV). In both cases we choose $\theta_i = 0$. A dashed (dotted) horizontal line denotes the present experimental bound (future sensitivity).

as a powerful tool to test the seesaw-I hypothesis for neutrino mass generation and, in case of a measurement of these branching ratios, as a unique way to derive some hints on the seesaw parameters, especially on the value of m_{N_3}. The $\mu - e$ conversion rates here presented will certainly add new interesting information on this type of analysis. Fig. 4.4 also shows that with the expected future sensitivity of 10^{-18}, the full $0° \leq \theta_{13} \leq 10°$ interval can be thoroughly covered.

In the following study we will restrict ourselves to the hierarchical case where we have found this strong sensitivity to θ_{13}. For definiteness, we will also fix the heavy neutrino masses and θ_{13} to "reference" values of $m_{N_i} = (10^{10}, 10^{11}, 10^{14})$ GeV and $\theta_{13} = 5°$.

Fig. 4.5 illustrates the predictions for the CR($\mu - e$, Ti) as a function of $\tan\beta$, M_0 and $M_{1/2}$. Here we have separately displayed the various contributions to the $\mu - e$ conversion rates in order to conclude about their relative importance in this CMSSM-seesaw scenario. We set the values of the remaining CMSSM parameters to $M_0 = M_{1/2} = 250$ GeV in the study with $\tan\beta$ (left panel) and to $\tan\beta = 30$ in the study with $M_{\rm SUSY} \equiv M_0 = M_{1/2}$ (right panel), taking $A_0 = 0$ in both cases. We choose our "reference" values of $m_{N_{1,2,3}} = (10^{10}, 10^{11}, 10^{14})$ GeV, $\theta_{13} = 5°$, and $\theta_i = 0$.

In both panels of Fig. 4.5 we clearly observe the dominance of the photon-mediated contributions, which are in fact indistinguishable from the total CR, for all the explored parameter

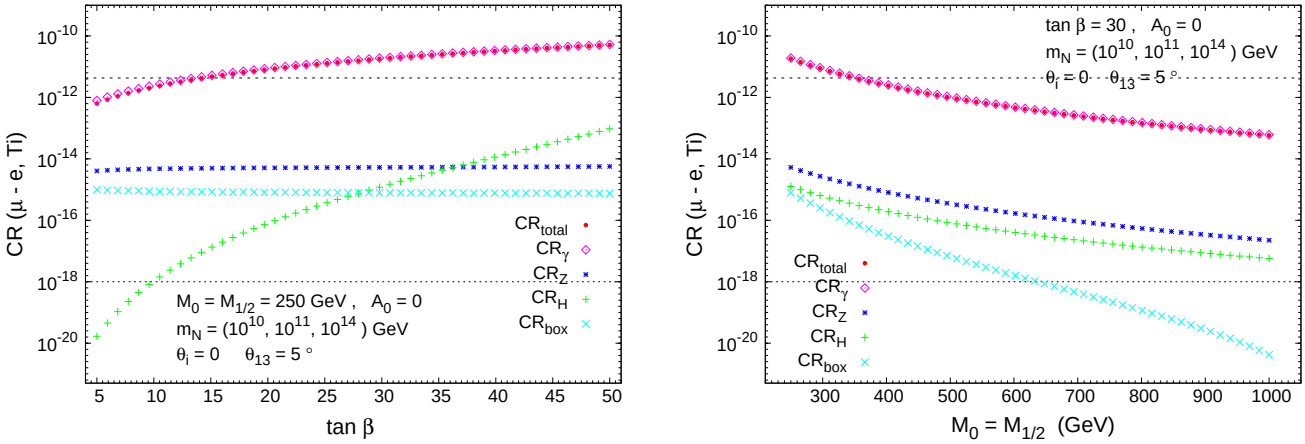

Figure 4.5: Contributions to CR($\mu - e$, Ti): total (dots), γ-penguins (diamonds), Z-penguins (asterisks), H-penguins (crosses) and box diagrams (times). On the left we present the dependence on $\tan\beta$, for $M_0 = M_{1/2} = 250$ GeV and $A_0 = 0$. On the right, we exhibit the evolution as a function of $M_0 (= M_{1/2})$, for $\tan\beta = 30$ and $A_0 = 0$. In either case, we consider hierarchical heavy neutrinos with $m_{N_i} = (10^{10}, 10^{11}, 10^{14})$ GeV, and set $\theta_{13} = 5°$, and $\theta_i = 0$. A dashed (dotted) horizontal line denotes the present experimental bound (future sensitivity).

ranges. The dependence of the various contributions on $\tan\beta$ illustrates the expected fast growing behaviour with $\tan^6\beta$ of the Higgs-mediated contributions, and the milder $\tan^2\beta$ dependence of the photon-mediated ones. In addition, we see that the Z boson-mediated and the box diagram contributions are almost independent of $\tan\beta$. Although not displayed in this plot, we have also verified that the Higgs-mediated contribution is largely dominated by the exchange of H^0, which is indeed the Higgs boson with enhanced couplings to charged leptons in the large $\tan\beta$ regime.

The decoupling behaviour for large $M_{\rm SUSY}$ of each of these contributions (CR_γ, CR_Z, CR_H and $\mathrm{CR}_{\rm box}$) is clearly manifested in the right panel of Fig. 4.5. The most important conclusion from this figure is that, within a CMSSM-seesaw scenario, the γ-penguin diagrams completely dominate the conversion rates, even for the largest $\tan\beta$ considered ($\tan\beta$ =50). Therefore, the total CR($\mu - e$, Ti) does not manifest the Higgs contributions, so that in this universal scenario there is no chance for the $\mu - e$ conversion process to provide any information on the Higgs sector. We will see next that the situation is remarkably different in the non-universal case, where the Higgs contributions turn out to be much larger than in the universal case.

4.2.2 Non-universality: NUHM-seesaw

The numerical results for the NUHM-seesaw scenario are collected in Figs. 1.12 through 4.9.

In order to study the influence of the hypothesis of non-universal Higgs soft SUSY breaking masses, $M_{H_{1,2}}$, on the $\mu - e$ conversion rates, we have first explored the impact of the non-universality parameters δ_1 and δ_2 on the predicted Higgs boson masses. The values for these parameters have been taken to lie within the interval $-2 \leq \delta_{1,2} \leq 2$. The predictions for the relevant Higgs boson mass, m_{H^0}, as a function of $\delta_{1,2}$ and $M_{\rm SUSY}$ have been summarised in Figs. 1.12 and 1.13. The other parameters are set to the values of $m_{N_i} = (10^{10}, 10^{11}, 10^{14})$ GeV, $\theta_i = 0$, $A_0 = 0$, $\theta_{13} = 5^\circ$ and sign$(\mu) = +1$. It is obvious that the most important difference with respect to the CMSSM case is that in these NUHM scenarios there can be light Higgs masses even for large $M_{\rm SUSY}$ values.

In the following we present the predictions of the $\mu - e$ conversion rates in Titanium nuclei within the NUHM-seeesaw scenario. First we display in Fig. 4.6 the CR$(\mu - e, {\rm Ti})$ as a function of $M_0 = M_{1/2} = M_{\rm SUSY}$ and of A_0 for the particular choice $\delta_1 = -1.8$ and $\delta_2 = 0$. In order to illustrate the impact of the non-universality hypothesis on the conversion rates, we have separately displayed in this plot the various contributions from the γ-, Z-, Higgs-mediated penguins and box diagrams. We observe a very distinct behaviour with $M_{\rm SUSY}$ of the Higgs-mediated contributions when compared to what was found for the CMSSM (universal) case, shown in Fig. 4.5. In fact, for the choice of input parameters in this plot, the Higgs-mediated contribution can equal, or even exceed that of the photon, dominating the total conversion rate in the large $M_{\rm SUSY}$ region. Both photon- and Higgs-mediated contributions are similar around $M_{\rm SUSY} = 700$ GeV. These larger Higgs contributions are the obvious consequence of the lighter Higgs boson mass values encountered in this region, as previously illustrated in Figs. 1.12 and 1.13. The non-decoupling behaviour of the SUSY particles for the large $M_{\rm SUSY}$ regime can be seen in the Higgs contribution, and thus in the total rates for the Higgs-dominated case.

For completeness, we have also explored other choices of A_0 and sign(μ). The case of sign$(\mu) = -1$, whose numerical results are not presented here, does not evidence any interesting new feature. In fact, there is a much more reduced δ_1, δ_2 parameter space allowing for the correct $SU(2) \times U(1)$ breaking. In addition, for sign$(\mu) = -1$ we have not found solutions displaying as small values of m_{H^0} as in the case of sign$(\mu) = +1$. The predicted Higgs contributions to the conversion rates are correspondingly smaller, and therefore less interesting. Regarding A_0, the right panel in Fig. 4.6 shows that all the contributions are essentially independent of the value of the universal trilinear coupling, so that our selected value, $A_0 = 0$, is in fact a good representative point.

Within the NUHM-seesaw scenario, we have also studied the $\mu - e$ conversion rates for other nuclei. The case of Gold is particularly interesting since its present experimental bound of

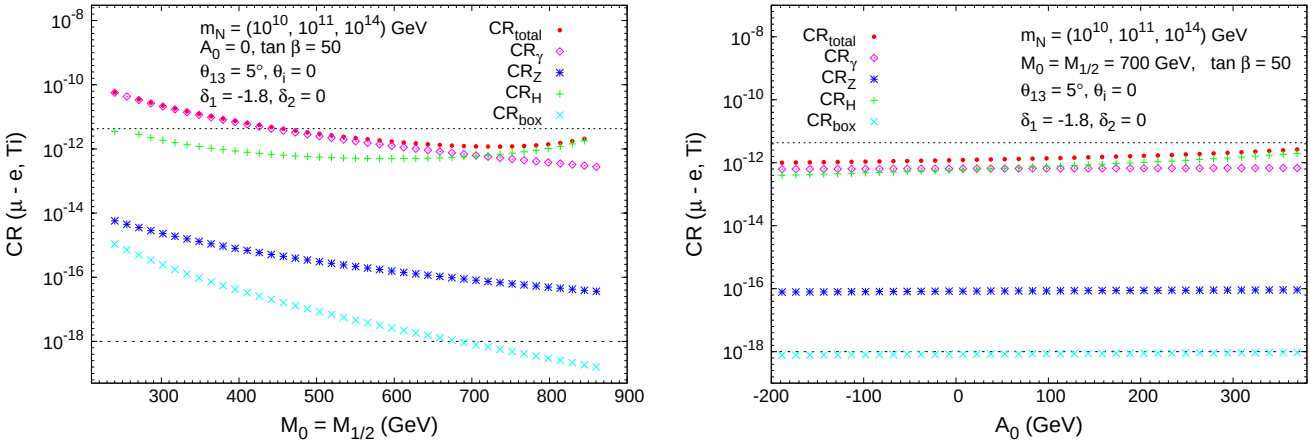

Figure 4.6: Contributions to CR($\mu - e$, Ti) as a function of $M_0 (= M_{1/2})$ (left) and A_0 (right): total (dots), γ-penguins (diamonds), Z-penguins (asterisks), H-penguins (crosses) and box diagrams (times), for $\delta_1 = -1.8$ and $\delta_2 = 0$. We set $\tan\beta = 50$ and take $\theta_{13} = 5°$, $\theta_i = 0$ and $m_{N_i} = (10^{10}, 10^{11}, 10^{14})$ GeV. On the left $A_0 = 0$, while on the right we choose $M_0 (= M_{1/2}) = 700$ GeV. In each case, a dashed (dotted) horizontal line denotes the present experimental bound (future sensitivity).

7×10^{-13} [61] is more stringent than the present bound for Titanium (4.3×10^{-12} [60]). In Fig. 4.7 we display the predicted $\mu - e$ conversion rates for Al, Ti, Sr, Sb, Au and Pb, as a function of $M_{\rm SUSY}$. We have chosen two light, two moderate and two heavy nuclei and we have fixed the other parameters to those of the previously elected non-universality reference point (with $\delta_1 = -1.8$ and $\delta_2 = 0$). For completeness, the values of the relevant parameters for these nuclei, $Z_{\rm eff}$, F_p and $\Gamma_{\rm capture}$, have been collected in Table 4.1 and follow [220]. In this figure we clearly see that throughout most of the explored $M_{\rm SUSY}$ interval, the relative conversion rates obey the hierarchy CR($\mu - e$, Sb) > CR($\mu - e$, Sr) > CR($\mu - e$, Ti) > CR($\mu - e$, Au) > CR($\mu - e$, Pb) > CR($\mu - e$, Al), in agreement with the generic results in [220]. We do not find a significant difference in the large $M_{\rm SUSY}$ region, where the Higgs contribution dominates the ratios. The predicted rates for Ti, Au and Pb tend to converge whereas the corresponding curve for Al nuclei deviates slightly from the others at large $M_{\rm SUSY}$, but we do not consider these differences among the predictions for the various nuclei to be relevant. The most important conclusion from Fig. 4.7 concerns the fact that we have found predictions for Gold nuclei which, for the input parameters in this plot, are clearly above its present experimental bound throughout the explored $M_{\rm SUSY}$ interval. However, it should be recalled that the formulae here used for these estimates come from approximations that may not properly work for the case of very heavy nuclei. These heavy nuclei deserve a more dedicated and refined study.

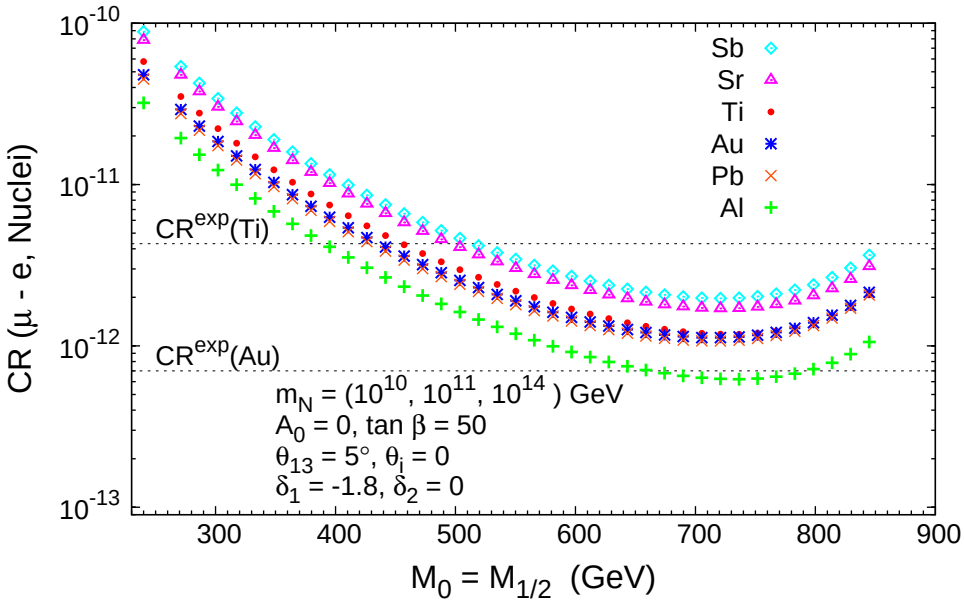

Figure 4.7: $\mu - e$ conversion rates for various nuclei as a function of $M_0 = M_{1/2}$ in the NUHM-seesaw. We display the theoretical predictions for Sb, Sr, Ti, Au, Pb and Al nuclei (diamonds, triangles, dots, asterisks, times and crosses, respectively). We have taken $m_{N_i} = (10^{10}, 10^{11}, 10^{14})$ GeV, $A_0 = 0$, $\tan\beta = 50$, $\theta_{13} = 5^\circ$ and $\theta_i = 0$. The non-universality parameters are set to $\delta_1 = -1.8$ and $\delta_2 = 0$. From top to bottom, the horizontal dashed lines denote the present experimental bounds for CR($\mu - e$, Ti) and CR($\mu - e$, Au).

Before proceeding with our analysis, let us briefly mention that for the region investigated in Fig. 4.7, the SUSY contributions to the anomalous magnetic moment of the muon, $a_\mu = (g_\mu - 2)$, range from $a_\mu^{\rm SUSY} = 10^{-8}$ for $M_{\rm SUSY} = 250$ GeV to $a_\mu^{\rm SUSY} = 10^{-9}$, in association with $M_{\rm SUSY} = 850$ GeV. The latter values are in fair agreement with the observed excess in $a_\mu^{\rm exp}$ when compared to the SM prediction, which, at the 3.8 σ is given by $a_\mu^{\rm SUSY} = a_\mu^{\rm exp} - a_\mu^{\rm SM} = 3.32 \times 10^{-9}$ at 3.8σ (for a review, see for instance [141] and references therein).

To complete our study of the $\mu - e$ conversion rates in the NUHM-seesaw scenario we have compared the theoretical predictions for the CR($\mu - e$, Ti) with those for the BR($\mu \to e\gamma$). We recall that both observables are sensitive to the same leptonic mixing given by the slepton mass matrix entries connecting the first and the second generation. In the usual photon-penguin dominated case, the latter two quantities are known to be highly correlated, and this is indeed what occurred for the CMSSM-seesaw discussed in Section 4.2.1. In other seesaw scenarios, as for instance, SUSY-GUT seesaw [221] or the inverse seesaw [222], this strong correlation still

${}^{A}_{Z}$Nucleus	$Z_{\rm eff}$	F_p	$\Gamma_{\rm capt}$(GeV)
${}^{27}_{13}$Al	11.5	0.64	4.64079×10^{-19}
${}^{48}_{22}$Ti	17.6	0.54	1.70422×10^{-18}
${}^{80}_{38}$Sr	25.0	0.39	4.61842×10^{-18}
${}^{121}_{51}$Sb	29.0	0.32	6.71711×10^{-18}
${}^{197}_{79}$Au	33.5	0.16	8.59868×10^{-18}
${}^{207}_{82}$Pb	34.0	0.15	8.84868×10^{-18}

Table 4.1: Values of $Z_{\rm eff}$, F_p and $\Gamma_{\rm capt}$ for different nuclei, as taken from [220].

persists. However, for some scenarios where the photon-mediated diagrams are no longer the dominant contributions to the conversion rates, the strong correlation between CR($\mu - e$, Ti) and BR($\mu \to e\gamma$) can be lost. For instance, this loss of correlation has been found in the case of Littlest Higgs Models, as recently pointed out in [223].

We have also found an interesting loss of correlation in the present case of the NUHM-scenario, where, as previously discussed, the Higgs contributions can be the dominant ones. The departure from the strongly correlated regime for (CR($\mu - e$, Ti), BR($\mu \to e\gamma$)) is illustrated in Fig. 4.8, considering several choices of the neutrino mixing angle $\theta_{13} = 10^\circ, 5^\circ, 1^\circ, 0.2^\circ$. For all plots the predictions for (CR($\mu - e$, Ti), BR($\mu \to e\gamma$)) have been derived for several choices of the non-universality parameter δ_1, scanning over the following interval 250 GeV $\leq M_{\rm SUSY} \leq$ 1000 GeV. In each of the panels, the predictions for (CR($\mu - e$, Ti), BR($\mu \to e\gamma$)) that correspond to $\delta_1 = \delta_2 = 0$ fall upon a straight line, which strongly supports the correlated behaviour of the two observables in this case. As $M_{\rm SUSY}$ increases within the considered interval, (CR($\mu - e$, Ti), BR($\mu \to e\gamma$)) moves left and downwards along the straight line due to the obvious decrease of the rate with $M_{\rm SUSY}$.

However a clear departure from the previous strongly correlated predictions is found for other values of δ_1, δ_2. In particular, for the specific δ_1 and δ_2 values where, as previously shown, the Higgs contributions dominate the $\mu - e$ conversion rates, the predicted (CR($\mu - e$, Ti), BR($\mu \to e\gamma$)) points exhibit a different behaviour, deviating from the straight line associated with the universal case. The separation between the correlated and uncorrelated regimes is maximal for the $\delta_1 = -1.8$, $\delta_2 = 0$ non-universal case, as can be clearly understood from our previous results. We find this loss of correlation a very promising phenomenon that could be fully explored if future sensitivities of 10^{-18} are reached.

Secondly, it is clear from Fig. 4.8 that even in the most pessimistic situation of very small θ_{13}, the theoretical predictions for CR($\mu - e$, Ti), and in particular the corresponding curved line, are well above the horizontal line at 10^{-18}. This is quite a challenging possibility, since

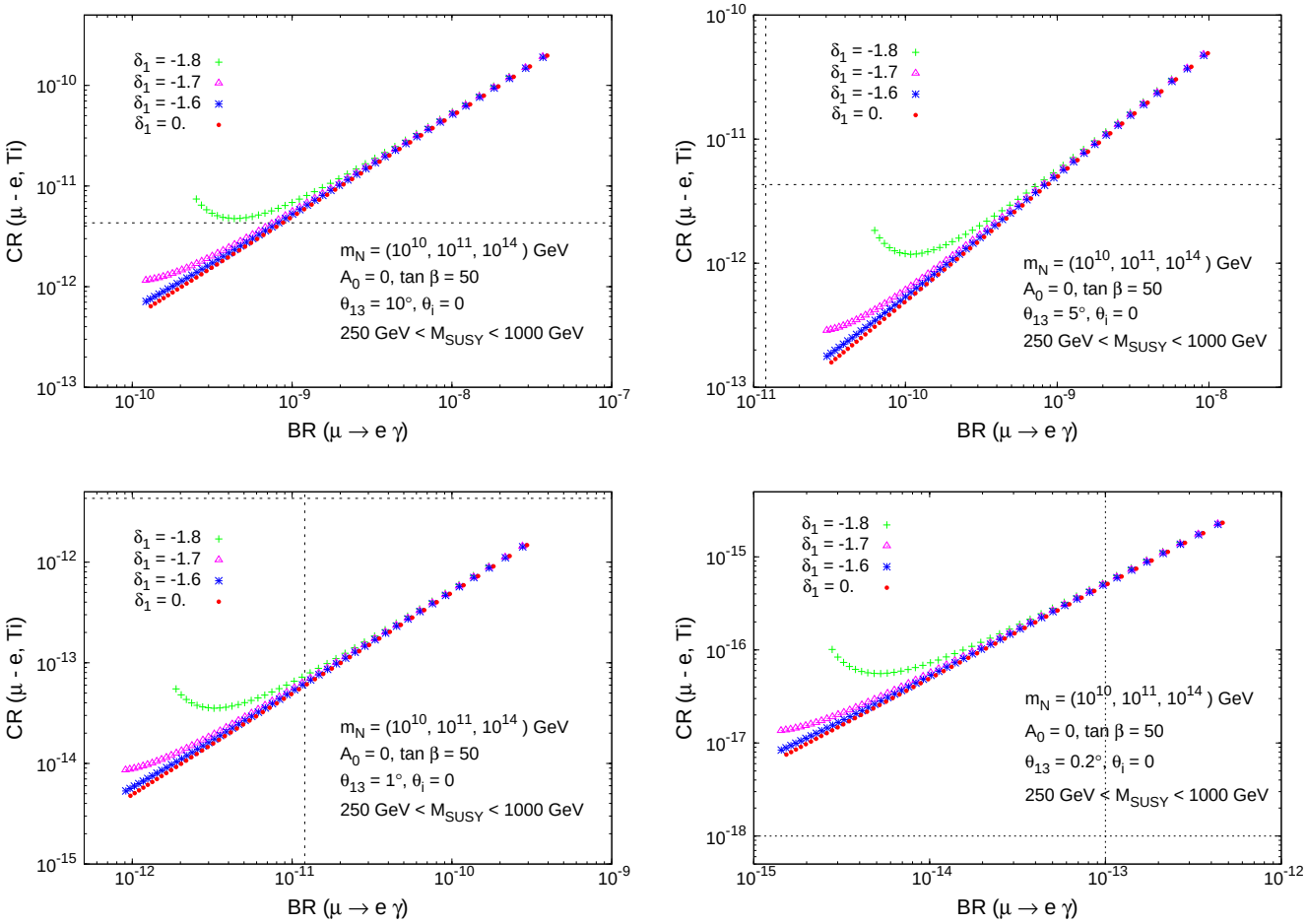

Figure 4.8: CR($\mu - e$, Ti) versus BR($\mu \to e\gamma$) for 250 GeV $\leq M_{\rm SUSY} \leq$ 1000 GeV, and $\delta_1 = -1.8, -1.7, -1.6, 0$ (crosses, triangles, asterisks, dots, respectively). We set $\delta_2 = 0$, and take $m_{N_i} = (10^{10}, 10^{11}, 10^{14})$ GeV, $A_0 = 0$, $\tan\beta = 50$ and $\theta_i = 0$. From left to right and top to bottom, the panels are associated with $\theta_{13} = 10°, 5°, 1°$ and $0.2°$. In each case, the horizontal and vertical dashed (dotted) lines denote the present experimental bounds (future sensitivities) for CR($\mu - e$, Ti) and BR($\mu \to e\gamma$), respectively.

for those high values of $M_{\rm SUSY} \sim 850$ GeV, whose predictions lie at the left end of the curved and straight lines, the predicted BR($\mu \to e\gamma$) is far below the planned 10^{-13} sensitivity. This clearly reflects that $\mu - e$ in nuclei can be a very competitive process to study LFV within the SUSY-seesaw.

Finally, and to summarise the most striking results for these NUHM-seesaw scenarios, we plot in Fig. 4.9 the ratio of the two predicted rates, CR($\mu - e$, Ti)/BR($\mu \to e\gamma$) as a function of m_{H^0}. Since both observables exhibit the same dependence on m_{N_i}, θ_i and θ_{13}, the consideration

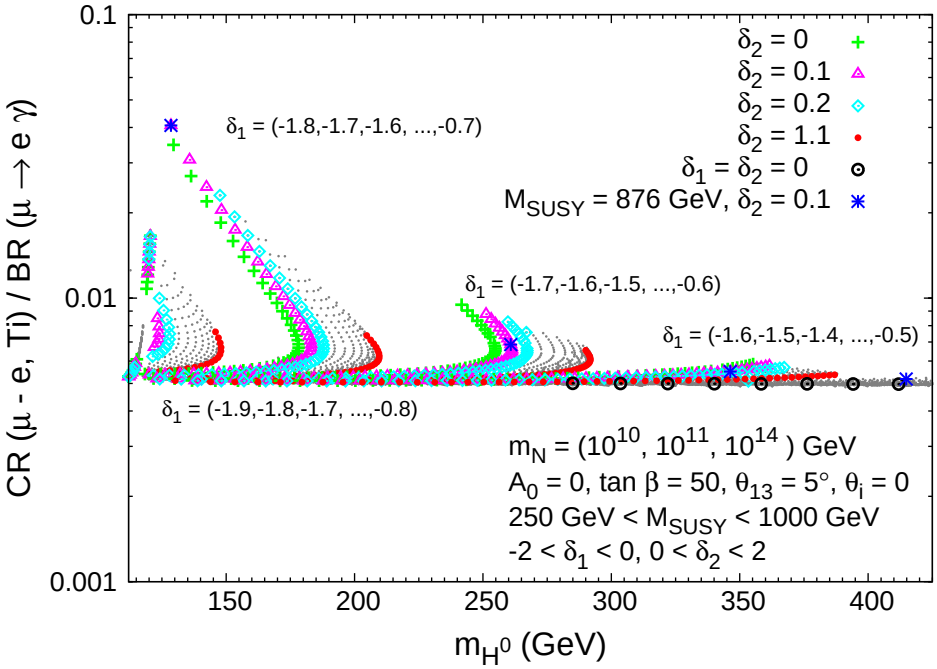

Figure 4.9: Ratio CR($\mu - e$, Ti)/BR($\mu \to e\gamma$) as a function of the Higgs mass, m_{H^0}. We take $m_{N_i} = (10^{10}, 10^{11}, 10^{14})$ GeV, $A_0 = 0$, $\tan\beta = 50$, $\theta_{13} = 5°$ and $\theta_i = 0$, and scan over 250 GeV $\leq M_{\rm SUSY} \leq$ 1000 GeV, $-2 \leq \delta_1 \leq 0$, and $0 \leq \delta_2 \leq 2$ (grey dots). We have highlighted specific choices of $\delta_2 = 0$, 0.1, 0.2, 1.1 (crosses, triangles, diamonds, dots, respectively). In each tilted cluster, we have also indicated the values of δ_1 associated with the δ_2 coloured points. The universality limit ($\delta_1 = \delta_2 = 0$) is denoted by a circle. Asterisks denote points with $M_{\rm SUSY} = 876$ GeV and $\delta_2 = 0.1$.

of this ratio of rates allows to reduce the number of relevant parameters to $\tan\beta$, $M_{\rm SUSY}$ and $\delta_{1,2}$. These last two are clearly the leading ones given that they drive the solutions to the interesting low m_{H^0} values. In this figure, and in order to maximise the Higgs contribution to the total $\mu - e$ conversion rates we have again considered the extreme $\tan\beta = 50$ value. For consistency, we have set the remaining parameters to their reference values, but as we have said, they will not play a relevant role in this study.

Leading to this scatter plot, we have scanned in the intervals $-2 < \delta_1 < 0$, $0 < \delta_2 < 2$ and 250 GeV $< M_{\rm SUSY} <$ 1000 GeV. The most important conclusion from this plot is that the ratio CR($\mu - e$, Ti)/BR($\mu \to e\gamma$) can deviate from the constant prediction of 5×10^{-3} of the universality case by as much as a factor of almost 10. For the scan here conducted, the maximum value of this ratio of rates is found for $\delta_1 = -1.7$, $\delta_2 = 0.1$ and $M_{\rm SUSY} = 876$ GeV, and its size is 0.04.

Considering larger values of $M_{\rm SUSY}$ and identical intervals for $\delta_{1,2}$ leads to somewhat similar results: one finds the same pattern of clusters departing from the constant value of the universal case, but the maximum value of CR($\mu - e$, Ti)/BR($\mu \to e\gamma$) is in general smaller than the 0.04 obtained in the scan of Fig. 4.9. The reason why this ratio is not improved at larger values of $M_{\rm SUSY}$ than 1 TeV is because the acceptable solutions producing the proper $SU(2) \times U(1)$ breaking do not lead to sufficiently light Higgs bosons.

Even without the knowledge of the seesaw parameters, a measurement of CR($\mu - e$, Ti) and BR($\mu \to e\gamma$), together with information on $\tan\beta$ and the SUSY scale, may allow to shed some light into the Higgs sector.

4.3 Summary

In this chapter we have extensively studied the lepton flavour violating process of $\mu - e$ conversion in nuclei, within the context of the SUSY-seesaw. In particular, we considered two distinct scenarios, the CMSSM-seesaw, and the NUHM-seesaw, obtained by partially relaxing the universality conditions of the Higgs boson masses. Throughout our analysis, we compared our theoretical predictions with the present experimental bounds, and with the challenging future sensitivities. In fact, the latter may convert processes like CR($\mu - e$, Ti) into one of the most sensitive probes to new physics.

We have presented here the first full one-loop computation of the $\mu - e$ conversion in nuclei, including the complete set of SUSY-loop diagrams: γ-mediated, Z- and Higgs-boson mediated penguins and box diagrams. We have also provided the full analytical results working in terms of physical eigenstates (for all intervening SUSY and Higgs particles).

For the CMSSM-seesaw, we have considered the dependence of the conversion rates on the several parameters defining the scenario. Choosing the well known SPS benchmark points to specify the CMSSM parameters, we focused on the most relevant parameters in the neutrino sector, namely on the heavy neutrino masses (m_{N_i}), the complex θ_i mixing angles and the still undetermined angle of the $U_{\rm PMNS}$ matrix, θ_{13}. As discussed here, the CRs exhibit a very pronounced dependence on the previous parameters, with variations that can reach up to ten orders of magnitude in the case of m_{N_i} and up to five orders of magnitude in the cases of θ_i and θ_{13}, for the investigated ranges. In turn, this strong dependence implies that a comparison of the theoretical predictions with the present experimental bound allows to derive indirect upper bounds for the unknown seesaw parameters.

We have pointed out that the highest sensitivity is found for the case of hierarchical heavy neutrinos. In this case, the conversion rates are essentially dependent on m_{N_3} and $\theta_{1,2}$, manifesting an extreme sensitivity to θ_{13} (for the case of vanishing θ_i). In fact, the values of these param-

eters in the upper part of their studied intervals, $10^{12}\,\text{GeV} \leq m_{N_3} \leq 10^{15}\,\text{GeV}$, $0 \leq |\theta_{1,2}| < \pi$, $0 \leq \arg\theta_{1,2} \leq \pi/2$ and $0^\circ \leq \theta_{13} \leq 10^\circ$ are already in conflict with the present upper bounds on CR($\mu - e$, Ti) and CR($\mu - e$, Au).

We have put special emphasis on the sensitivity of the CR($\mu - e$,Ti) to θ_{13}, given that either a measurement, or a more stringent bound on this parameter is expected in the near future [90–99]. Therefore, and once θ_{13} is measured, a dedicated study of the $\mu - e$ conversion rates could provide some insight into the potentially unreachable heavy neutrino parameters.

In all the studied examples of the CMSSM-seesaw, the dominant contribution to the $\mu - e$ conversion rates clearly arises from the photon-penguins. Even though we have verified that the Higgs contributions do indeed grow with $\tan^6\beta$, they induce contributions which are several orders of magnitude below those of the photon (which grow as $\tan^2\beta$) for all the studied interval $5 \leq \tan\beta \leq 50$. A very interesting departure from this situation occurs when one relaxes the universality condition for the Higgs soft breaking masses, and this fuelled our interest to consider the NUHM-seesaw.

In the case of the NUHM-seesaw, we explored the influence of the non-universality hypothesis of the soft-SUSY breaking masses $M_{H_{1,2}}$ on the $\mu - e$ conversion rates. The δ_1 and δ_2 parameters which describe the departure from universality in the Higgs sector have an important impact on the predicted Higgs boson masses. In particular, we have found regimes for $\delta_{1,2}$ with very interesting phenomenological implications, namely the possibility of a light Higgs spectrum, even in the limit of large soft SUSY masses. As a concrete example, we recall that for the reference choice of $\delta_1 = -1.8$, $\delta_2 = 0$, we find $m_{H^0} = 113$, 174 and 127 GeV for $M_{\text{SUSY}} = 250, 500, 850$ GeV respectively (in turn associated with moderate, heavy and very heavy SUSY spectra).

The distinctive NUHM-seesaw scenarios associated with light H^0 bosons and a relatively heavy SUSY spectra induce very interesting and unique predictions for the $\mu - e$ conversion rates. Specifically, we have shown that in the large $M_{\text{SUSY}} = M_0 = M_{1/2}$ region (e.g. above 700 GeV), there is a strong enhancement in the Higgs-dominated rates, leading to a remarkable loss of correlation between the CRs in nuclei and the BRs of $\mu \to e\gamma$ decays. As we aimed at illustrating in Fig. 4.8, the departure from the linear correlation of these two observables can be sizable. It is worth stressing that if both these rates and θ_{13} are measured, values of BR($\mu \to e\gamma$) and CR($\mu - e$, Ti) that clearly deviate from the expected SUSY-seesaw ratio in the photon-dominated case, can provide indirect information into the structure of the Higgs sector.

It is also important to remark that with the expected future sensitivities, $\mu - e$ conversion in nuclei may be sensitive to LFV signals that lie beyond the reach of the future sensitivities to $\mu \to e\gamma$ decays. For example, this can occur for a heavy SUSY spectrum, and very small values of θ_{13}.

Finally, we considered the predictions for the ratio CR($\mu - e$, Ti)/BR($\mu \to e\gamma$) as a a function

of m_{H^0} in NUHM-seesaw scenarios, comparing the results with those obtained for the CMSSM-seesaw case. The most important conclusion to be drawn from this study (which is presented in Fig. 4.9) is that in the NUHM-seesaw one can observe a clear deviation from the constant prediction of the CMSSM-seesaw by as much as a factor close to 10. If such deviation is indeed observed, we can obtain some indirect hints regarding the SUSY Higgs sector.

Conclusions

Neutrino physics, in particular neutrino oscillations and the measured neutrino mass differences, strongly manifest that Nature does not conserve the lepton flavour quantum number in the neutrino sector. However, it is not known yet if lepton flavour violation also occurs in the charged lepton sector. If such is the case, one still has to address if LFV in the neutral and charged lepton sectors arises from a common or different origin. It is well known that if the Standard Model of Particle Physics is extended with right-handed neutrinos and the seesaw mechanism is implemented in order to accommodate the present data on neutrino masses and mixings, the corresponding loop induced LFV in the charged lepton sector is extremely tiny and hopeless to be experimentally observed. Therefore, a potential future measurement of LFV in the charged lepton sector will provide a unique insight into the nature of new physics beyond the SM.

Among the various candidates for physics beyond the SM that produce potentially observable effects in LFV processes, one of the most appealing are supersymmetric extensions of the SM, where the seesaw mechanism with three heavy right-handed neutrinos is implemented to generate three light neutrino masses. In these SUSY-seesaw models a new source of LFV appears in the off-diagonal elements of the slepton and sneutrino mass matrices, which can be radiatively generated from the neutrino Yukawa interactions. The size of these elements is governed by the strength of the neutrino Yukawa couplings and, in the case of Majorana neutrinos, the latter can be large, of the order of one. Important LFV effects in the charged lepton processes are then induced by the flavour violating slepton-lepton and sneutrino-neutrino interactions that appear in the contributing SUSY-loop diagrams to these processes.

In this thesis we have been performed a detailed analysis of the most important phenomenological implications of these LFV effects in SUSY-seesaw models, and we have explored the possibility of using a potential measurement of LFV as an indirect test of SUSY and the seesaw mechanism via right-handed neutrinos. Concretely, we have developed an exhaustive study of the following lepton flavour violating processes within constrained SUSY-seesaw scenarios: LFV radiative decays $l_j \to l_i \gamma$, LFV Higgs decays $H \to l_j \bar{l}_i$, LFV leptonic decays into three leptons of equal flavour $l_j \to 3\, l_i$, LFV semileptonic τ decays $\tau \to \mu PP$ and $\tau \to \mu P$ and $\mu - e$ conversion

in nuclei.

We have first studied in Chapter 2 the LFV radiative decays $l_j \to l_i\,\gamma$, the LFV Higgs decays $H \to l_j\,\bar{l}_i$ and the LFV leptonic decays into three leptons of equal flavour $l_j \to 3\,l_i$, within the constrained SUSY-seesaw scenarios introduced in Chapter 1. Our results for $l_j \to 3\,l_i$ decays and LFV Higgs decays are the first ones in the literature that are complete to one-loop order in the context of SUSY-seesaw and are referred to the physical basis for all the particles in the loops. We have indeed corrected some errors of partial results for $l_j \to 3\,l_i$ channels of previous works.

The previous studies have been developed for both scenarios with either degenerate or hierarchical light and heavy neutrinos. We have shown that the case of hierarchical neutrinos with complex θ_i leads in general to much larger LFV rates than the case of degenerate neutrinos. Besides, we have found that the most relevant parameters in the hierarchical case are θ_1, θ_2, the heaviest right-handed neutrino mass m_{N_3} and $\tan\beta$.

We have also analysed in detail the sensitivity of the BRs to θ_{13}. In the simplest case of $\theta_i = 0$, where there are no additional neutrino mixings other than those in the $U_{\rm PMNS}$, we have found a very pronounced sensitivity to θ_{13} in the leptonic decay channels involving $\mu - e$ transitions, concretely in $\mu \to e\,\gamma$ and $\mu \to 3\,e$. Varying θ_{13} from 0° to 10° and for a large region of the SUSY-seesaw parameter space, the branching ratios for these processes increase by up to six orders of magnitude, exceeding in many cases the present experimental bounds. The decay $\mu \to e\,\gamma$ has the most competitive experimental bound and hence it provides the highest sensitivity to θ_{13} at present. The channels involving $\tau - e$ transitions are very sensitive to θ_{13} too, but unfortunately this sensitivity is not experimentally reachable yet.

The case of $\theta_i \neq 0$ reduces the sensitivity of the BRs to θ_{13}, but we have shown in this thesis that it can be still important. From our analysis summarised in Fig. 2.16 of the correlations between ${\rm BR}(\mu \to e\,\gamma)$ and ${\rm BR}(\tau \to \mu\,\gamma)$ and the comparison with their experimental bounds, we have concluded that it is already possible at present to extract θ_{13}-dependent upper bounds on m_{N_3}. With the planned MEG sensitivity to ${\rm BR}(\mu \to e\,\gamma)$ of 10^{-13} these bounds will improve considerably. In consequence, one of the most appealing outcomes of this thesis is that an hypothetical joint measurement of the LFV branching ratios, θ_{13} and the sparticle spectrum will be a powerful tool for giving some hints of the right-handed neutrino masses.

Although the LFV radiative decays are sensitive to the SUSY and right-handed neutrino sectors, they are not sensitive at all to one of the clue pieces of the SM and SUSY models, the Higgs sector. Moreover, we have shown in this thesis that the other two kinds of LFV processes analysed in Chapter 2, LFV Higgs decays and LFV $l_j \to 3\,l_i$ decays, cannot supply information about the Higgs sector at present either. On the one hand, in spite of the large rates obtained here for LFV Higgs decays of about 10^{-5}, they are unfortunately not yet at the reach of the

future experimental sensitivity of 10^{-4} at LHC [191] and e^+e^- and $\mu^+\mu^-$ colliders [192]. On the other hand, LFV leptonic decays $l_j \to 3\, l_i$ do receive contributions from Higgs-mediated diagrams, but in these channels the photon-mediated contributions dominate by far over the rest, even in scenarios with very heavy SUSY spectra and light Higgs bosons. Therefore, in the scenarios considered here it will not be possible to distinguish any kind of Higgs signs from $l_j \to 3\, l_i$ decays.

Fortunately, we have found that some LFV semileptonic τ decays and $\mu - e$ conversion in nuclei are very sensitive to the Higgs sector and, in some cases, the Higgs-mediated contributions can be even the dominant ones. Then, these LFV processes, apart from being useful for indirect SUSY searches and for tests of the heavy neutrino sector, they can provide us some extra information about the Higgs sector.

We have developed a detailed study of LFV semileptonic τ decays in Chapter 3, where we have presented a complete one-loop computation of the branching ratios for the LFV semileptonic τ decays within the CMSSM-seesaw and the NUHM-seesaw scenarios and using a chiral approach to perform the hadronisation of quark bilinears. We have included both analytical and numerical results for the different channels: $\tau \to \mu PP$, with $PP = \pi^+\pi^-, \pi^0\pi^0, K^+K^-, K^0\bar{K}^0$; $\tau \to \mu P$ with $P = \pi, \eta, \eta'$; and $\tau \to \mu\rho$, $\tau \to \mu\phi$. The analysis of the channels $\tau \to \mu PP$, with $PP = \pi^+\pi^-, \pi^0\pi^0, K^0\bar{K}^0$, and $\tau \to \mu\rho$, $\tau \to \mu\phi$ are, to our knowledge, the first ones in the literature within the SUSY-seesaw context. In addition, we have compared our predictions for $\tau \to \mu K^+K^-$ and for $\tau \to \mu P$ with $P = \pi, \eta, \eta'$ with previous predictions in the literature and found some discrepancies. Our overall conclusion from this study is that, for the CMSSM-seesaw scenario, $\tau \to \mu\gamma$ is the most competitive τ decay channel in testing the values of the LFV parameter δ_{32}, but it is not sensitive at all to the Higgs sector. Within the NUHM-seesaw scenario we have found a different and interesting result. Concretely, we have proved that the most competitive channels to explore simultaneously LFV and the Higgs sector are $\tau \to \mu\eta$, $\tau \to \mu\eta'$ and also $\tau \to \mu K^+K^-$. The $\tau \to \mu K^+K^-$ channel is certainly more efficient than $\tau \to 3\,\mu$ as far as the sensitivity to the Higgs sector is concerned. Otherwise, the golden channels to tackle the Higgs sector are undoubtely $\tau \to \mu\eta$ and $\tau \to \mu\eta'$. On the other hand, the rest of the studied semileptonic channels will not provide additional information on LFV with respect to that provided by $\tau \to \mu\gamma$. We have also derived a set of approximate formulae valid at large $\tan\beta$ and large $M_{\rm SUSY}$, which are useful for present and future comparison with data.

We have extensively studied in Chapter 4 the lepton flavour violating process of $\mu - e$ conversion in nuclei, within the context of SUSY-seesaw. Throughout our analysis, we compared our theoretical predictions for several nuclei with the present experimental bounds, and with the challenging future sensitivities for the Titanium nucleus. This last LFV process considered in this thesis becomes very interesting for several reasons. First, in some cases, within the NUHM-

seesaw scenario, the Higgs-mediated contributions to $\mu - e$ conversion in nuclei compete with the γ-mediated ones and we can obtain some information about the Higgs sector. In addition, this process also manifests a strong sensitivity to θ_{13} and given that either a measurement, or a more stringent bound on this parameter is expected in the near future [90–99], a dedicated study of the $\mu - e$ conversion rates could provide some insight into the heavy neutrino parameters like m_{N_3}. Finally, in the future, with the expected sensitivities [64], $\mu - e$ conversion in Titanium can clearly be more competitive for the study of LFV in SUSY-seesaw models than $\mu \to e\gamma$, and certainly provide an important tool for the study of the Higgs sector and the SUSY-seesaw parameters.

To sum up, from the results shown in this thesis, we conclude that, at present, the best channels to test LFV in SUSY-seesaw models are $\mu \to e\,\gamma$ and $\tau \to \mu\,\gamma$ decays which, together with low-energy neutrino data and a potential measurement of θ_{13}, can help to perform indirect searches of SUSY and even provide some insight into the otherwise unreachable heavy neutrino masses. On the other hand, in the future, if the expected sensitivity of PRISM experiment [64] is attained, the most competitive LFV channel will be undoubtely $\mu - e$ conversion in Titanium, since its sensitivity to LFV signals will lie beyond those of $\mu \to e\,\gamma$ and $\tau \to \mu\,\gamma$ decays. In addition, an hypothetical measurement of CR($\mu - e$, Ti) and BR($\mu \to e\,\gamma$), together with information on $\tan\beta$ and the SUSY scale, may allow to shed some light into the Higgs sector.

The overall conclusion of this thesis is that LFV processes constitute an useful and powerful tool for exploring the interesting phenomenology of SUSY-seesaw models and, together with low-energy neutrino data, they can provide some information about the SUSY and Higgs sectors as well as insights into the heavy neutrino sector and the seesaw parameters. Moreover, if we were not able to find LFV in experiments, it is clear from this thesis that the present and future expected bounds on the LFV processes studied here do restrict severely the SUSY and seesaw parameters of these models.

Conclusiones

La física de neutrinos, en particular las oscilaciones de neutrinos y las diferencias medidas entre sus masas, indica fuertemente que la Naturaleza no conserva el número cuántico de sabor leptónico en el sector de los neutrinos. No obstante, todavía no se sabe si la violación del sabor leptónico se da también en el sector de los leptones cargados. Si éste es el caso, todavía tendríamos que averiguar si la violación del sabor leptónico en los sectores de leptones neutros y cargados proviene de un origen común o distinto. Es bien sabido que si el Modelo Estándar de Física de Partículas se extiende con neutrinos dextrógiros y se introduce el mecanismo de seesaw para acomodar los datos experimentales actuales de masas y mezclas de los neutrinos, la LFV en el sector de los leptones cargados, inducida por los correspondientes loops, es extremadamente pequeña y no se espera observarla experimentalmente. Por lo tanto, una potencial medida futura de LFV en el sector de los leptones cargados proporcionará información única acerca de la nueva física más allá del SM.

Entre los varios candidatos de física más allá del SM que producen efectos potencialmente observables en procesos LFV, uno de los más llamativos son las extensiones supersimétricas del SM, en las cuales el mecanismo de seesaw con tres neutrinos dextrógiros se implementa para generar tres masas ligeras de neutrinos. En estos modelos SUSY-seesaw aparece una nueva fuente de LFV en los elementos no diagonales de las matrices de masa de los sleptones y los sneutrinos, que se generan radiativamente a partir de las interacciones de Yukawa de los neutrinos. El tamaño de estos elementos viene gobernado por la fuerza de los acoplamientos de Yukawa de los neutrinos y, en el caso de neutrinos de Majorana, estos últimos pueden ser grandes, de orden uno. Entonces, pueden inducirse efectos LFV importantes en los procesos de leptones cargados por las interacciones sleptón-leptón y sneutrino-neutrino que violan el sabor leptónico, y que aparecen en los diagramas con loops supersimétricos que contribuyen a estos procesos.

En esta tesis hemos desarrollado un análisis detallado de las implicaciones fenomenológicas más importantes de estos efectos LFV en los modelos SUSY-seesaw, y hemos investigado la posibilidad de usar una medida de LFV como un test indirecto de SUSY y del mecanismo de seesaw vía neutrinos dextrógiros. Concretamente, hemos realizado un estudio exhaustivo de los siguientes procesos que violan el sabor leptónico dentro de escenarios SUSY-seesaw restringidos:

desintegraciones radiativas LFV $l_j \to l_i\,\gamma$, desintegraciones LFV de los bosones de Higgs $H \to l_j\,\bar{l}_i$, desintegraciones leptónicas LFV en tres leptones de igual sabor $l_j \to 3\,l_i$, desintegraciones LFV del tau semileptónicas $\tau \to \mu PP$ y $\tau \to \mu P$ y conversión $\mu - e$ en núcleos.

Primero hemos estudiado, en el Capítulo 2, las desintegraciones radiativas LFV $l_j \to l_i\,\gamma$, las desintegraciones LFV de los bosones de Higgs $H \to l_j\,\bar{l}_i$ y las desintegraciones leptónicas LFV en tres leptones de igual sabor $l_j \to 3\,l_i$, dentro de los escenarios SUSY-seesaw restringidos introducidos en el Capítulo 1. Nuestros resultados de las desintegraciones $l_j \to 3\,l_i$ y de las desintegraciones LFV de los bosones de Higgs son los primeros cálculos completos a un loop en la literatura, dentro del contexto SUSY-seesaw, y que se refieren a la base física para todas las partículas en los loops. De hecho, hemos corregido algunos errores de resultados parciales en trabajos previos para los canales $l_j \to 3\,l_i$.

Estos estudios se han desarrollado en escenarios tanto degenerados como jerárquicos para los neutrinos ligeros y pesados. Hemos mostrado que el caso de neutrinos jerárquicos con θ_i complejos conduce en general a tasas LFV mucho más grandes que el caso de neutrinos degenerados. Además, hemos encontrado que los parámetros más relevantes en el caso jerárquico son θ_1, θ_2, la masa del neutrino dextrógiro más pesado m_{N_3} y $\tan\beta$.

También hemos analizado en detalle la sensibilidad de los cocientes de ramificación a θ_{13}. En el caso más simple de $\theta_i = 0$, donde no hay más mezcla de neutrinos que la que proviene de la matriz $U_{\rm PMNS}$, hemos encontrado una sensibilidad muy pronunciada a θ_{13} en los canales de desintegración leptónicos que involucran transiciones $\mu - e$, concretamente en $\mu \to e\,\gamma$ y $\mu \to 3\,e$. Variando θ_{13} de 0° a 10° y para una región grande del espacio de parametros SUSY-seesaw, los cocientes de ramificación de estos procesos se incrementan hasta seis órdenes de magnitud, sobrepasando en algunos casos las cotas experimentales actuales. Los canales que involucran transiciones $\tau - e$ son también muy sensibles a θ_{13}, pero desafortunadamente esta sensibilidad no se puede alcanzar todavía experimentalmente.

El caso de $\theta_i \neq 0$ reduce la sensibilidad de los BRs a θ_{13}, pero en esta tesis hemos mostrado que aún puede ser importante. De nuestro análisis, en Fig. 2.16, de las correlaciones entre BR($\mu \to e\,\gamma$) y BR($\tau \to \mu\,\gamma$) y de la comparación con sus cotas experimentales, hemos concluido que actualmente ya es posible extraer cotas superiores para m_{N_3} dependientes de θ_{13}. Estas cotas mejorarán considerablemente con la sensibilidad de 10^{-13} planeada en MEG para BR($\mu \to e\,\gamma$). En consecuencia, una de las conclusiones más llamativas de esta tesis es que una hipotética medida conjunta de los cocientes de ramificación LFV, de θ_{13} y del espectro supersimétrico, proporcionará una poderosa herramienta para obtener pistas sobre las masas de los neutrinos dextrógiros.

Aunque las desintegraciones radiativas LFV son sensibles a los sectores SUSY y de los neutrinos dextrógiros, no lo son en absoluto a una de las piezas clave del SM y de los modelos

supersimétricos: el sector de Higgs. Más aún, en esta tesis hemos mostrado que los otros dos tipos de procesos LFV analizados en el Capítulo 2, las desintgraciones LFV de los bosones de Higgs y las desintegraciones $l_j \to 3\, l_i$, tampoco pueden suministrar en la actualidad información acerca del sector de Higgs. Por un lado, a pesar de los BRs grandes obtenidos para las desintegraciones LFV de los bosones de Higgs, de alrededor de 10^{-5}, desfortunadamente no están todavía al alcance de las sensibilidades experimentales futuras de 10^{-4} del LHC [191] y de los colisionadores e^+e^- y $\mu^+\mu^-$ [192]. Por otro lado, las desintegraciones LFV leptónicas $l_j \to 3\, l_i$ reciben contribuciones de los diagramas mediados por los bosones de Higgs, pero en estos canales las contribuciones mediadas por el fotón dominan por mucho sobre el resto, incluso en escenarios con espectros SUSY muy pesados y bosones de Higgs ligeros. Por consiguiente, en los escenarios considerados aquí no será posible distinguir ningún tipo de señales del sector de Higgs a partir de las desintegraciones $l_j \to 3\, l_i$.

Afortunadamente, hemos obtenido que algunas desintegraciones LFV semileptónicas del τ y la conversión $\mu - e$ en núcleos son muy sensibles al sector de Higgs y, en algunos casos, las contribuciones mediadas por los bosones de Higgs pueden incluso ser las dominantes. Por tanto, estos procesos LFV, aparte de ser útiles para búsquedas indirectas de SUSY y para sondear el sector de los neutrinos pesados, pueden proporcionarnos información extra sobre el sector de Higgs.

Hemos realizado un estudio detallado de desintegraciones LFV del τ semileptónicas en el Capítulo 3, donde hemos presentado un cálculo completo a un loop de los cocientes de ramificación para estas desintegraciones semileptónicas dentro de los escenarios CMSSM-seesaw y NUHM-seesaw, usando un contexto quiral para los bilineares de quarks. Hemos incluido los resultados tanto analíticos como numéricos para los diferentes canales: $\tau \to \mu PP$, con $PP = \pi^+\pi^-, \pi^0\pi^0, K^+K^-, K^0\bar{K}^0$; $\tau \to \mu P$ con $P = \pi, \eta, \eta'$; y $\tau \to \mu\rho$, $\tau \to \mu\phi$. Nuestro análisis de los canales $\tau \to \mu PP$, con $PP = \pi^+\pi^-, \pi^0\pi^0, K^0\bar{K}^0$, y $\tau \to \mu\rho$, $\tau \to \mu\phi$ son, por lo que sabemos, los primeros en la literatura dentro del contexto SUSY-seesaw. Además, hemos comparado nuestras predicciones para $\tau \to \mu K^+K^-$ y para $\tau \to \mu P$ con $P = \pi, \eta, \eta'$ con predicciones previas en la literatura y encontrado algunas discrepancias. Nuestra conclusión general de este estudio es que, para el escenario CMSSM-seesaw, $\tau \to \mu\gamma$ es el canal de desintegración más competitivo para chequear los valores del parámetro LFV δ_{32}, pero no es sensible al sector de Higgs. En el escenario NUHM-seesaw hemos encontrado un resultado diferente interesante. En particular, hemos visto que los canales más competitivos para explorar simultáneamente la LFV y el sector de Higgs son $\tau \to \mu\eta$, $\tau \to \mu\eta'$ y también $\tau \to \mu K^+K^-$. Este último canal es más eficiente que $\tau \to 3\,\mu$ en lo que se refiere a la sensibilidad al sector de Higgs. Aún así, los mejores canales para sustraer información del sector de Higgs son, indudablemente, $\tau \to \mu\eta$ y $\tau \to \mu\eta'$. Por el contrario, el resto de los canales semileptónicos estudiados no proporcionan información adicional sobre la LFV respecto a la proporcionada por $\tau \to \mu\gamma$. También hemos derivado un

conjunto de fórmulas aproximadas válidas a gran $\tan\beta$ y gran $M_{\rm SUSY}$, que son útiles para la comparación con los datos experimentales actuales y futuros.

En el Capítulo 4 hemos estudiado a fondo el proceso de conversión $\mu - e$ en núcleos, dentro del contexto de SUSY-seesaw. A través de nuestro análisis, hemos comparado nuestras predicciones teóricas para varios núcleos con las cotas experimentales presentes, y con la prometedora sensibilidad futura para el núcleo de Titanio. Este último proceso LFV considerado en esta tesis es muy interesante por varios motivos. Primero, en algunos casos, dentro del escenario NUHM-seesaw, las contribuciones mediadas por el Higgs a la conversión $\mu - e$ en núcleos compiten con las mediadas por el fotón y podemos obtener información adicional sobre el sector de Higgs. Además, este proceso también manifiesta una fuerte sensibilidad a θ_{13} y dado que se espera obtener, en un futuro próximo, una medida o una cota mucho más restrictiva de este ángulo [90–99], un estudio más exhaustivo podría aportar alguna luz sobre los parámetros de los neutrinos pesados como m_{N_3}. Finalmente, en el futuro, con la sensibilidad esperada [64], la conversión $\mu - e$ en Titanio puede claramente ser más competitiva que $\mu \to e\gamma$ para el estudio de la violación del número leptónico en los models SUSY-seesaw, y constituir una importante herramienta para el estudio del sector de Higgs y de los parámetros SUSY-seesaw.

Para resumir, de los resultados mostrados en esta tesis, concluimos que, actualmente, los mejores canales para comprobar la violación del sabor leptónico en los modelos SUSY-seesaw son las desintegraciones $\mu \to e\,\gamma$ y $\tau \to \mu\,\gamma$ que, junto con los datos experimentales de neutrinos a bajas energías y una potencial medida de θ_{13}, pueden ayudar al desarrollo de búsquedas indirectas de SUSY e incluso proporcionar alguna información acerca de las masas de los neutrinos pesados, inalcanzables de otra manera. Por otro lado, en el futuro, si se consigue la sensibilidad esperada del experimento PRISM [64], el canal LFV más competitivo será sin duda la conversión $\mu - e$ en Titanio, ya que su sensibilidad a señales LFV se encontrará más allá de las de $\mu \to e\,\gamma$ y $\tau \to \mu\,\gamma$. Además, una medida hipotética de CR($\mu - e$, Ti) y BR($\mu \to e\,\gamma$), junto con información sobre $\tan\beta$ y la escala SUSY, puede mostrarnos alguna señal del sector de Higgs.

La conclusión general de esta tesis es que los procesos LFV constituyen una herramienta muy útil y poderosa para explorar la interesante fenomenología de los modelos SUSY-seesaw y, junto con los datos experimentales de los neutrinos a bajas energías, pueden suministrar información sobre los sectores de Higgs y SUSY, así como pistas acerca del sector de los neutrinos pesados y los parámetros del seesaw. Más aún, si no fuéramos capaces de encontrar violación del sabor leptónico en los experimentos, está claro, a raíz de esta tesis, que las cotas actuales y futuras de los procesos LFV estudiados restringen severamente los parámetros SUSY y seesaw de estos modelos.

Appendix A

Relevant Feynman rules and couplings for LFV processes

In this appendix we collect the Feynman rules for the interactions and the formulae for the couplings that are relevant in this thesis. The couplings are expressed in the physical eigenstate basis, for all the MSSM sectors involved: sleptons $\tilde{l}_X$ $(X = 1, .., 6)$, sneutrinos $\tilde{\nu}_X$ $(X = 1, 2, 3)$, neutralinos $\tilde{\chi}^0_A$ $(A = 1, .., 4)$, charginos $\tilde{\chi}^-_A$ $(A = 1, 2)$ and the neutral Higgs bosons $H_p\,(p = 1, 2, 3) = h^0, H^0, A^0$.

The notation for the SM parameters that appear in the following couplings is as follows: g is the $SU(2)$ gauge coupling, m_f is the fermion mass, m_W, m_Z are the W-boson and Z-boson masses, respectively, and θ_W is the weak angle. We use sometimes the short notation $s_w = \sin\theta_W$ and $c_w = \cos\theta_W$.

A.1 $\tilde{\chi}^0 f \tilde{f}$ interactions

The Feynman rules for $\tilde{\chi}^0\,\tilde{l}\,l$ interactions are given by

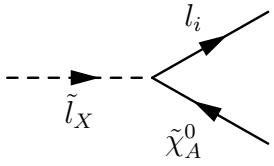

$$i\left(N^{L(l)}_{iAX}P_L + N^{R(l)}_{iAX}P_R\right)$$

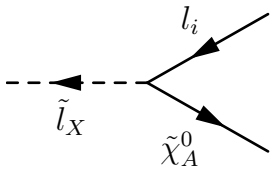

$$i\left(N^{R(l)*}_{iAX}P_L + N^{L(l)*}_{iAX}P_R\right)$$

where the corresponding couplings are the following:

$$N^{L(l)}_{iAX} = -g\sqrt{2}\left\{\frac{m_{l_i}}{2m_W\cos\beta}N^*_{A3}R^{(l)}_{(1,3,5)X} + \tan\theta_W N^*_{A1}R^{(l)}_{(2,4,6)X}\right\}, \quad (A.1)$$

$$N^{R(l)}_{iAX} = -g\sqrt{2}\left\{-\frac{1}{2}\left(\tan\theta_W N_{A1} + N_{A2}\right)R^{(l)}_{(1,3,5)X} + \frac{m_{l_i}}{2m_W\cos\beta}N_{A3}R^{(l)}_{(2,4,6)X}\right\}. \quad (A.2)$$

The Feynman rules for $\chi^0\,\tilde{q}\,q$ interactions are expressed as

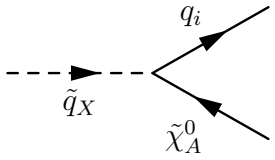

$$i\left(N^{L(q)}_{iAX}P_L + N^{R(q)}_{iAX}P_R\right)$$

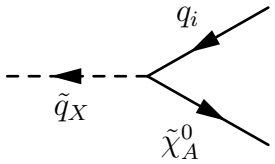

$$i\left(N^{R(q)*}_{iAX}P_L + N^{L(q)*}_{iAX}P_R\right)$$

where

$$N^{L(d)}_{iAX} = -g\sqrt{2}\left\{\frac{m_{d_i}}{2m_W\cos\beta}N^*_{A3}R^{(d)}_{(1,3,5)X} + \frac{1}{3}\tan\theta_W N^*_{A1}R^{(d)}_{(2,4,6)X}\right\}, \quad (A.3)$$

$$N^{R(d)}_{iAX} = -g\sqrt{2}\left\{-\frac{1}{2}\left(-\frac{1}{3}\tan\theta_W N_{A1} + N_{A2}\right)R^{(d)}_{(1,3,5)X} + \frac{m_{d_i}}{2m_W\cos\beta}N_{A3}R^{(d)}_{(2,4,6)X}\right\}, \quad (A.4)$$

$$N^{L(u)}_{iAX} = -g\sqrt{2}\left\{\frac{m_{u_i}}{2m_W\sin\beta}N^*_{A4}R^{(u)}_{(1,3,5)X} - \frac{2}{3}\tan\theta_W N^*_{A1}R^{(u)}_{(2,4,6)X}\right\}, \quad (A.5)$$

$$N^{R(u)}_{iAX} = -g\sqrt{2}\left\{-\frac{1}{2}\left(\frac{2}{3}\tan\theta_W N_{A1} - N_{A2}\right)R^{(u)}_{(1,3,5)X} + \frac{m_{u_i}}{2m_W\sin\beta}N_{A4}R^{(u)}_{(2,4,6)X}\right\}. \quad (A.6)$$

Here, $R^{(l)}, R^{(d)}, R^{(u)}$ are the 6×6 rotation matrices for the charged slepton, down squark and up squark sectors, respectively, and N is the 4×4 rotation matrix for the neutralino sector. For completeness, we have written the full set of couplings, including the three fermion generations. The displayed notation for the sfermion rotation matrices with three entries $R_{(\,,\,,\,)}$ correspond with the three generic possibilities to fermion index i. The fermion masses are correspondingly, $m_{l_i} = m_e, m_\mu, m_\tau$; $m_{d_i} = m_d, m_s, m_b$ and $m_{u_i} = m_u, m_c, m_t$. Notice also that, although we use the same notation for the squark and slepton sectors, and since we have not included mixing in the quark nor squark sectors, the 6×6 rotation matrices $R^{(d)}$ and $R^{(u)}$ are block diagonal in flavour space and only $L-R$ mixing occurs in that case.

A.2 $\tilde{\chi}^{\pm} f \tilde{f}$ interactions

The Feynman rules for $\tilde{\chi}^{\pm}\,\tilde{\nu}\,l$ interactions are given by

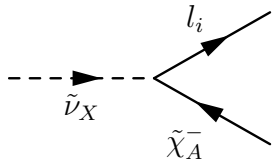

$$i\left(C_{iAX}^{L(l)} P_L + C_{iAX}^{R(l)} P_R\right)$$

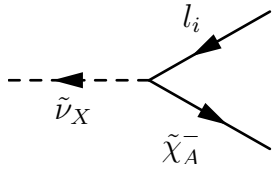

$$i\left(C_{iAX}^{R(l)*} P_L + C_{iAX}^{L(l)*} P_R\right)$$

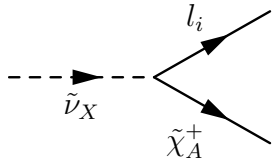

$$i\left(C_{iAX}^{L(l)} P_L + C_{iAX}^{R(l)} P_R\right) C$$

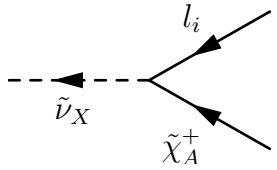

$$-iC^{-1}\left(C_{iAX}^{R(l)*} P_L + C_{iAX}^{L(l)*} P_R\right)$$

where the corresponding couplings are the following:

$$C_{iAX}^{L(l)} = g\frac{m_{l_i}}{\sqrt{2} m_W \cos\beta} U_{A2}^{*} R_{(1,2,3)X}^{(\nu)}\,, \tag{A.7}$$

$$C_{iAX}^{R(l)} = -g V_{A1} R_{(1,2,3)X}^{(\nu)}\,. \tag{A.8}$$

Here $R^{(\nu)}$ is the 3×3 rotation matrix for the sneutrino sector, and U and V are the 2×2 rotation matrices in the chargino sector. The displayed notation for the three entries in the sfermion rotation matrices is as in the previous neutralino couplings. The rotation matrices for neutralinos and charginos can be found in [42] and [43].

The Feynman rules for the $\tilde{\chi}^{\pm}\,\tilde{u}\,d$ interactions are given by

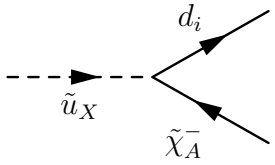

$$i\left(C_{iAX}^{L(d)}P_L + C_{iAX}^{R(d)}P_R\right)$$

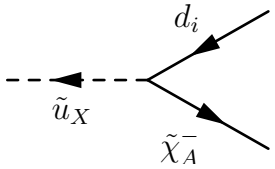

$$i\left(C_{iAX}^{R(d)*}P_L + C_{iAX}^{L(d)*}P_R\right)$$

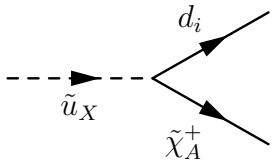

$$i\left(C_{iAX}^{L(d)}P_L + C_{iAX}^{R(d)}P_R\right)C$$

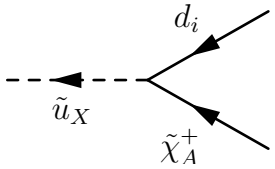

$$-iC^{-1}\left(C_{iAX}^{R(d)*}P_L + C_{iAX}^{L(d)*}P_R\right)$$

where

$$C_{iAX}^{L(d)} = g\frac{m_{d_i}}{\sqrt{2}m_W\cos\beta}U_{A2}^{*}R_{(1,3,5)X}^{(u)}\,, \tag{A.9}$$

$$C_{iAX}^{R(d)} = -gV_{A1}R_{(1,3,5)X}^{(u)} + g\frac{m_{u_i}}{\sqrt{2}m_W\sin\beta}V_{A2}R_{(2,4,6)X}^{(u)}\,. \tag{A.10}$$

The Feynman rules for the $\tilde{\chi}^{\pm}\,\tilde{d}\,u$ interactions are given by

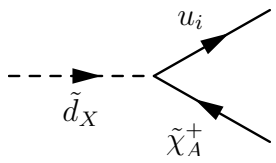

$$i\left(C_{iAX}^{L(u)}P_L + C_{iAX}^{R(u)}P_R\right)$$

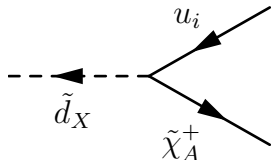

$$i\left(C_{iAX}^{R(u)*}P_L + C_{iAX}^{L(u)*}P_R\right)$$

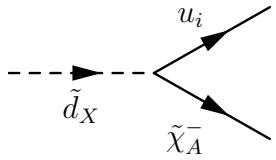

$$i\left(C_{iAX}^{L(u)}P_L + C_{iAX}^{R(u)}P_R\right)C$$

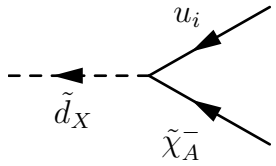

$$-iC^{-1}\left(C_{iAX}^{R(u)*}P_L + C_{iAX}^{L(u)*}P_R\right)$$

where

$$C_{iAX}^{L(u)} = g\frac{m_{u_i}}{\sqrt{2}m_W \sin\beta}V_{A2}^* R_{(1,3,5)X}^{(d)}\,, \tag{A.11}$$

$$C_{iAX}^{R(u)} = -gU_{A1}R_{(1,3,5)X}^{(d)} + g\frac{m_{d_i}}{\sqrt{2}m_W \cos\beta}U_{A2}R_{(2,4,6)X}^{(d)}\,. \tag{A.12}$$

A.3 Photon interactions

The Feynman rules for $\gamma\,\tilde{\chi}^+\,\tilde{\chi}^-$ interactions are given by

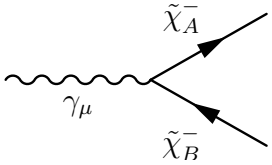

$$ie\,\gamma_\mu\,\delta_{AB}$$

The Feynman rules for $\gamma\,\tilde{l}\,\tilde{l}$ interactions are given by

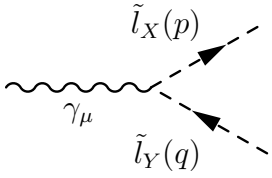

$$ie\,(p_\mu + q_\mu)\,\delta_{XY}$$

The Feynman rules for $\gamma\,\bar{l}\,l$ interactions are given by

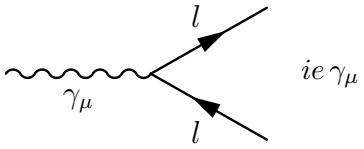

The Feynman rules for $\gamma\,\bar{q}\,q$ interactions are given by

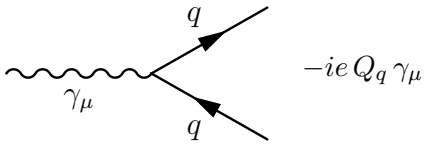

A.4 Z boson interactions

The Feynman rules for $Z\,\tilde{\chi}^0\,\tilde{\chi}^0$ interactions are given by

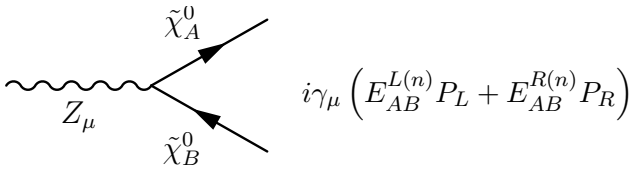

where

$$E^{L(n)}_{AB} = \frac{g}{\cos\theta_W}O''^{L}_{AB} = \frac{g}{c_W}\left(-\frac{1}{2}N_{A3}N^*_{B3} + \frac{1}{2}N_{A4}N^*_{B4}\right), \tag{A.13}$$

$$E^{R(n)}_{AB} = \frac{g}{\cos\theta_W}O''^{R}_{AB} = -\frac{g}{c_W}\left(-\frac{1}{2}N^*_{A3}N_{B3} + \frac{1}{2}N^*_{A4}N_{B4}\right). \tag{A.14}$$

The Feynman rules for $Z\,\tilde{\chi}^+\,\tilde{\chi}^-$ interactions are given by

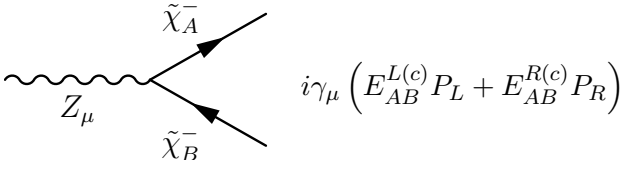

where

$$E^{L(c)}_{AB} = -\frac{g}{\cos\theta_W}O'^{R}_{AB} = -\frac{g}{c_W}\left[-\left(\frac{1}{2} - s^2_W\right)U^*_{A2}U_{B2} - c^2_W U^*_{A1}U_{B1}\right], \tag{A.15}$$

$$E^{R(c)}_{AB} = -\frac{g}{\cos\theta_W}O'^{L}_{AB} = -\frac{g}{c_W}\left[-\left(\frac{1}{2} - s^2_W\right)V_{A2}V^*_{B2} - c^2_W V_{A1}V^*_{B1}\right]. \tag{A.16}$$

The Feynman rules for $Z\,\tilde{l}\,\tilde{l}$ interactions are given by

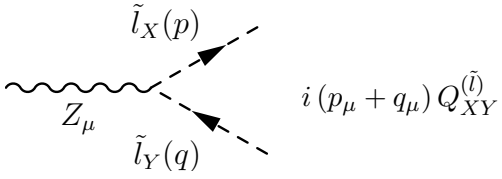

where

$$Q^{(\tilde{l})}_{XY} = -\frac{g}{c_W}\sum_{k=1}^{3}\left[\left(-\frac{1}{2}+s^2_W\right)R^{(l)*}_{2k-1,X}R^{(l)}_{2k-1,Y} + s^2_W R^{(l)*}_{2k,X}R^{(l)}_{2k,Y}\right]. \tag{A.17}$$

The Feynman rules for $Z\,\tilde{\nu}\,\tilde{\nu}$ interactions are given by

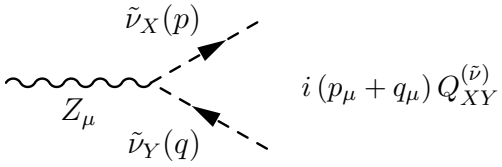

where

$$Q^{(\tilde{\nu})}_{XY} = -\frac{g}{2c_W}\delta_{XY}. \tag{A.18}$$

The Feynman rules for $Z\,\bar{l}\,l$ interactions are given by

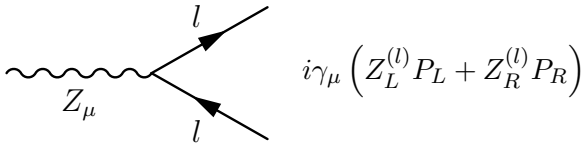

where

$$Z^{(l)}_L = -\frac{g}{c_W}\left[-\frac{1}{2}+s^2_W\right], \tag{A.19}$$

$$Z^{(l)}_R = -\frac{g}{c_W}s^2_W. \tag{A.20}$$

The Feynman rules for $Z\,\bar{q}\,q$ interactions are given by

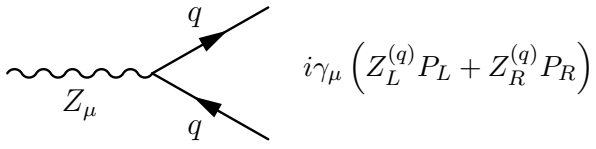

where

$$Z^{(q)}_L = -\frac{g}{c_W}\left[T^q_3 - Q_q s^2_W\right], \tag{A.21}$$

$$Z^{(q)}_R = \frac{g}{c_W}Q_q s^2_W. \tag{A.22}$$

A.5 Higgs boson interactions

The Feynman rules for $H\,\tilde{\chi}^0\,\tilde{\chi}^0$ interactions are given by

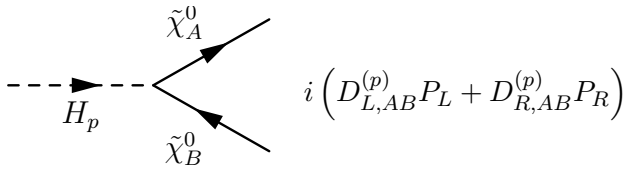

where

$$\begin{aligned} D^{(p)}_{L,AB} &= -\frac{g}{2\cos\theta_W}\Big[(s_W N^*_{B1} - c_W N^*_{B2})\left(\sigma^{(p)}_1 N^*_{A3} + \sigma^{(p)}_2 N^*_{A4}\right) \\ &+ (s_W N^*_{A1} - c_W N^*_{A2})\left(\sigma^{(p)}_1 N^*_{B3} + \sigma^{(p)}_2 N^*_{B4}\right)\Big], \qquad \text{(A.23)} \\ D^{(p)}_{R,AB} &= D^{(p)*}_{L,AB}. \qquad \text{(A.24)} \end{aligned}$$

The Feynman rules for $H\,\tilde{\chi}^+\,\tilde{\chi}^-$ interactions are given by

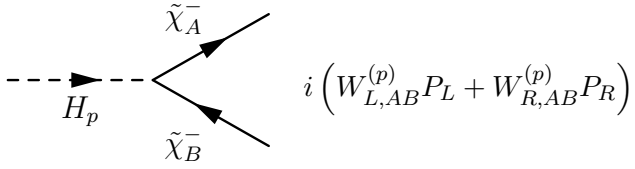

where

$$\begin{aligned} W^{(p)}_{L,AB} &= -\frac{g}{\sqrt{2}}\left[-\sigma^{(p)}_1 U^*_{B2}V^*_{A1} + \sigma^{(p)}_2 U^*_{B1}V^*_{A2}\right], \qquad \text{(A.25)} \\ W^{(p)}_{R,AB} &= -\frac{g}{\sqrt{2}}\left[-\sigma^{(p)*}_1 U_{A2}V_{B1} + \sigma^{(p)*}_2 U_{A1}V_{B2}\right]. \qquad \text{(A.26)} \end{aligned}$$

The Feynman rules for $H\,\tilde{l}\,\tilde{l}$ interactions are given by

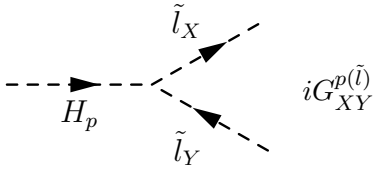

where

$$\begin{aligned} G^{p(\tilde{l})}_{XY} &= -g\Big[g^{(p)}_{LL,e}R^{*(l)}_{1X}R^{(l)}_{1Y} + g^{(p)}_{RR,e}R^{*(l)}_{2X}R^{(l)}_{2Y} + g^{(p)}_{LR,e}R^{*(l)}_{1X}R^{(l)}_{2Y} + g^{(p)}_{RL,e}R^{*(l)}_{2X}R^{(l)}_{1Y} \\ &+ g^{(p)}_{LL,\mu}R^{*(l)}_{3X}R^{(l)}_{3Y} + g^{(p)}_{RR,\mu}R^{*(l)}_{4X}R^{(l)}_{4Y} + g^{(p)}_{LR,\mu}R^{*(l)}_{3X}R^{(l)}_{4Y} + g^{(p)}_{RL,\mu}R^{*(l)}_{4X}R^{(l)}_{3Y} \\ &+ g^{(p)}_{LL,\tau}R^{*(l)}_{5X}R^{(l)}_{5Y} + g^{(p)}_{RR,\tau}R^{*(l)}_{6X}R^{(l)}_{6Y} + g^{(p)}_{LR,\tau}R^{*(l)}_{5X}R^{(l)}_{6Y} + g^{(p)}_{RL,\tau}R^{*(l)}_{6X}R^{(l)}_{5Y}\Big], \qquad \text{(A.27)} \end{aligned}$$

and

$$g^{(p)}_{LL,l} = \frac{m_Z}{\cos\theta_W}\sigma_3^{(p)}\left(\frac{1}{2}-\sin^2\theta_W\right)+\frac{m_l^2}{m_W\cos\beta}\sigma_4^{(p)}, \tag{A.28}$$

$$g^{(p)}_{RR,l} = \frac{m_Z}{\cos\theta_W}\sigma_3^{(p)}\left(\sin^2\theta_W\right)+\frac{m_l^2}{m_W\cos\beta}\sigma_4^{(p)}, \tag{A.29}$$

$$g^{(p)}_{LR,l} = \left(-\sigma_1^{(p)}A_l-\sigma_2^{(p)*}\mu\right)\frac{m_l}{2m_W\cos\beta}, \tag{A.30}$$

$$g^{(p)}_{RL,l} = g^{(p)*}_{LR,l}, \tag{A.31}$$

with $A_l = (A_l)^{ii}/(Y_l)^{ii}$ (at the EW scale), $i = 1,2,3$ for $l = e,\mu,\tau$, respectively.

The Feynman rules for $H\,\tilde{\nu}\,\tilde{\nu}$ interactions are given by

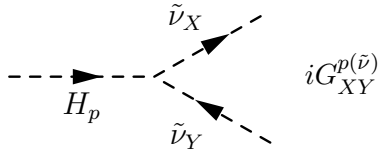

where

$$G^{p(\tilde{\nu})}_{XY} = -g\left[g^{(p)}_{LL,\nu}R^{*(\nu)}_{1X}R^{(\nu)}_{1Y}+g^{(p)}_{LL,\nu}R^{*(\nu)}_{2X}R^{(\nu)}_{2Y}+g^{(p)}_{LL,\nu}R^{*(\nu)}_{3X}R^{(\nu)}_{3Y}\right], \tag{A.32}$$

with

$$g^{(p)}_{LL,\nu} = -\frac{m_Z}{2\cos\theta_W}\sigma_3^{(p)}. \tag{A.33}$$

The Feynman rules for $H\,\bar{l}\,l$ interactions are given by

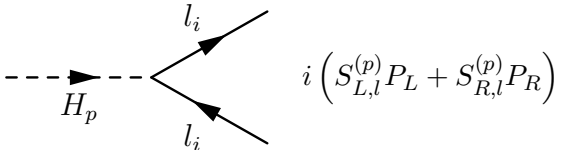

where

$$S^{(p)}_{L,l} = g\frac{m_{l_i}}{2m_W\cos\beta}\sigma_1^{(p)*}, \tag{A.34}$$

$$S^{(p)}_{R,l} = S^{(p)*}_{L,l}. \tag{A.35}$$

The Feynman rules for $H\,\bar{d}\,d$ interactions are given by

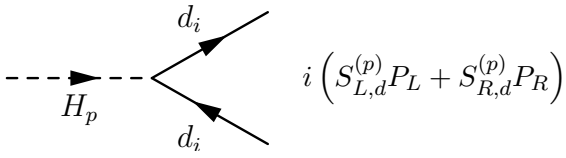

where

$$S^{(p)}_{L,d} = g\frac{m_{d_i}}{2m_W\cos\beta}\sigma_1^{(p)*}, \tag{A.36}$$

$$S^{(p)}_{R,d} = S^{(p)*}_{L,d}. \tag{A.37}$$

The Feynman rules for $H\,\bar{u}\,u$ interactions are given by

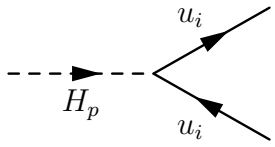

$$i\left(S^{(p)}_{L,u}P_L + S^{(p)}_{R,u}P_R\right)$$

where

$$S^{(p)}_{L,u} = -g\frac{m_{u_i}}{2m_W\sin\beta}\sigma_2^{(p)*}, \tag{A.38}$$

$$S^{(p)}_{R,u} = S^{(p)*}_{L,u}. \tag{A.39}$$

In all the above equations,

$$\sigma_1^{(p)} = \begin{pmatrix} \sin\alpha \\ -\cos\alpha \\ i\sin\beta \end{pmatrix}, \tag{A.40}$$

$$\sigma_2^{(p)} = \begin{pmatrix} \cos\alpha \\ \sin\alpha \\ -i\cos\beta \end{pmatrix}, \tag{A.41}$$

$$\sigma_3^{(p)} = \begin{pmatrix} \sin(\alpha+\beta) \\ -\cos(\alpha+\beta) \\ 0 \end{pmatrix}, \tag{A.42}$$

$$\sigma_4^{(p)} = \begin{pmatrix} -\sin\alpha \\ \cos\alpha \\ 0 \end{pmatrix}. \tag{A.43}$$

and the three entries for index $(p) = 1, 2, 3$ correspond to $H_p = h^0, H^0, A^0$, respectively. We have also used here the standard notation for the low-energy MSSM soft-gaugino-mass parameters $M_{1,2}$ and the μ parameter.

Appendix B

One-loop formulae for LFV processes

In this appendix we collect all the analytical results of the SUSY one-loop diagrams that contribute to the LFV processes considered in this thesis. These are summarised by the photon, Z boson and Higgs boson form factors and box diagrams in Figs. B.1, B.2, B.3, B.4 and B.5, respectively. In the following sections we present the relevant formulae for each separate contribution. All the couplings are presented in Appendix A and the explicit expressions for all the loop functions appearing here are collected in Appendix C.

B.1 Form factors for the $\gamma\, l_j\, l_i$ vertex

Our convention for the form factors $A_{1,2}^{L,R}$ defining the $\gamma l_j l_i$ vertex is as follows:

$$ie\left[q^2\gamma_\alpha(A_1^L P_L + A_1^R P_R) + im_{l_j}\sigma_{\alpha\beta}q^\beta(A_a^L P_L + A_2^R P_R)\right], \tag{B.1}$$

where q is the off-shell photon momentum, $P_{L,R} = (1 \mp \gamma_5)/2$, e is the positron electromagnetic charge and m_{l_j} is the mass of lepton l_j.

In the SUSY-seesaw context the one-loop diagrams that contribute to these form factors are drawn in Fig. B.1. We present the results in terms of the contributions from the chargino and neutralino sectors, separately,

$$A_a^{L,R} = A_a^{(n)L.R} + A_a^{(c)L,R}, \quad a = 1, 2\,. \tag{B.2}$$

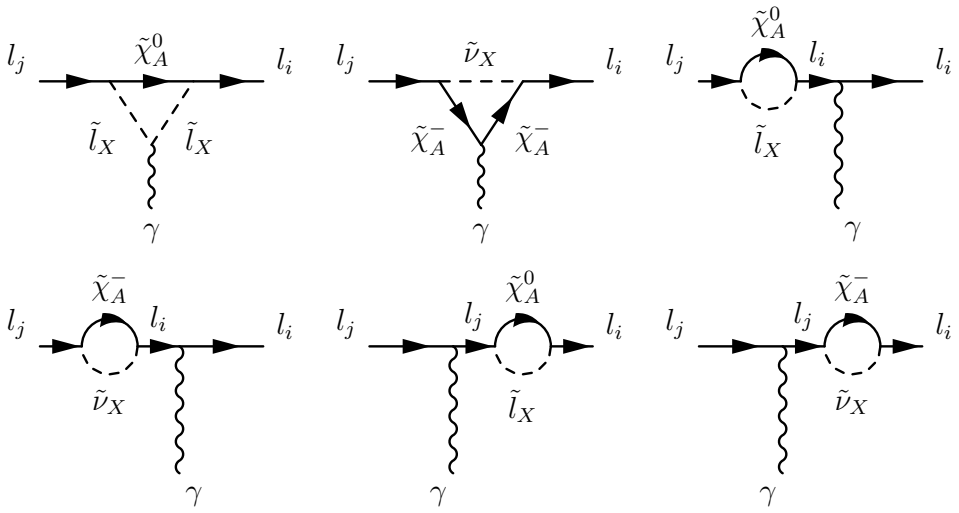

Figure B.1: Relevant SUSY one-loop diagrams for the photon-mediated contributions to LFV processes.

The neutralino contributions are given by

$$A_1^{(n)L} = \frac{1}{576\pi^2} N_{iAX}^R N_{jAX}^{R*} \frac{1}{m_{\tilde{l}_X}^2} \frac{2 - 9x_{AX} + 18x_{AX}^2 - 11x_A^3 + 6x_{AX}^3 \log x_{AX}}{(1 - x_{AX})^4}\,, \tag{B.3}$$

$$\begin{aligned} A_2^{(n)L} &= \frac{1}{32\pi^2} \frac{1}{m_{\tilde{l}_X}^2} \left[N_{iAX}^L N_{jAX}^{L*} \frac{1 - 6x_{AX} + 3x_{AX}^2 + 2x_{AX}^3 - 6x_{AX}^2 \log x_{AX}}{6\,(1 - x_{AX})^4} \right. \\ &+ N_{iAX}^R N_{jAX}^{R*} \frac{m_{l_i}}{m_{l_j}} \frac{1 - 6x_{AX} + 3x_{AX}^2 + 2x_{AX}^3 - 6x_{AX}^2 \log x_{AX}}{6\,(1 - x_{AX})^4} \\ &+ \left. N_{iAX}^L N_{jAX}^{R*} \frac{m_{\tilde{\chi}_A^0}}{m_{l_j}} \frac{1 - x_{AX}^2 + 2x_{AX} \log x_{AX}}{(1 - x_{AX})^3} \right]\,, \end{aligned} \tag{B.4}$$

$$A_a^{(n)R} = A_a^{(n)L}\Big|_{L \leftrightarrow R}\,, \tag{B.5}$$

where $x_{AX} = m_{\tilde{\chi}_A^0}^2 / m_{\tilde{l}_X}^2$ and the indices are $A = 1, .., 4$, $X = 1, .., 6$.

The chargino contributions are given by

$$A_1^{(c)L} = -\frac{1}{576\pi^2} C_{iAX}^R C_{jAX}^{R*} \frac{1}{m_{\tilde{\nu}_X}^2} \frac{16 - 45x_{AX} + 36x_{AX}^2 - 7x_A^3 + 6(2 - 3x_{AX}) \log x_{AX}}{(1 - x_{AX})^4}\,, \tag{B.6}$$

$$
\begin{aligned}
A_2^{(c)L} &= -\frac{1}{32\pi^2}\frac{1}{m^2_{\tilde{\nu}_X}}\left[C^L_{iAX}C^{L*}_{jAX}\frac{2+3x_{AX}-6x^2_{AX}+x^3_{AX}+6x_{AX}\log x_{AX}}{6\,(1-x_{AX})^4}\right.\\
&+ C^R_{iAX}C^{R*}_{jAX}\frac{m_{l_i}}{m_{l_j}}\frac{2+3x_{AX}-6x^2_{AX}+x^3_{AX}+6x_{AX}\log x_{AX}}{6\,(1-x_{AX})^4}\\
&+ \left. C^L_{iAX}C^{R*}_{jAX}\frac{m_{\tilde{\chi}^-_A}}{m_{l_j}}\frac{-3+4x_{AX}-x^2_{AX}-2\log x_{AX}}{(1-x_{AX})^3}\right]\,, \qquad \text{(B.7)}\\
A_a^{(c)R} &= A_a^{(c)L}\Big|_{L\leftrightarrow R}\,, \qquad \text{(B.8)}
\end{aligned}
$$

where in this case $x_{AX} = m^2_{\tilde{\chi}^-_A}/m^2_{\tilde{\nu}_X}$ and the indices are $A = 1,2$, $X = 1,2,3$. Notice that in both neutralino and chargino contributions a summation over the indices A and X is understood. Notice also that we have not neglected the $\mathcal{O}(m_{l_i})$ terms in these formulae.

B.2 Form factors for the $Z\,l_j\,l_i$ vertex

Our convention for the form factors $F_{L,R}$ defining the Zl_jl_i vertex is as follows:

$$-i\gamma_\mu\left[F_L P_L + F_R P_R\right]. \qquad \text{(B.9)}$$

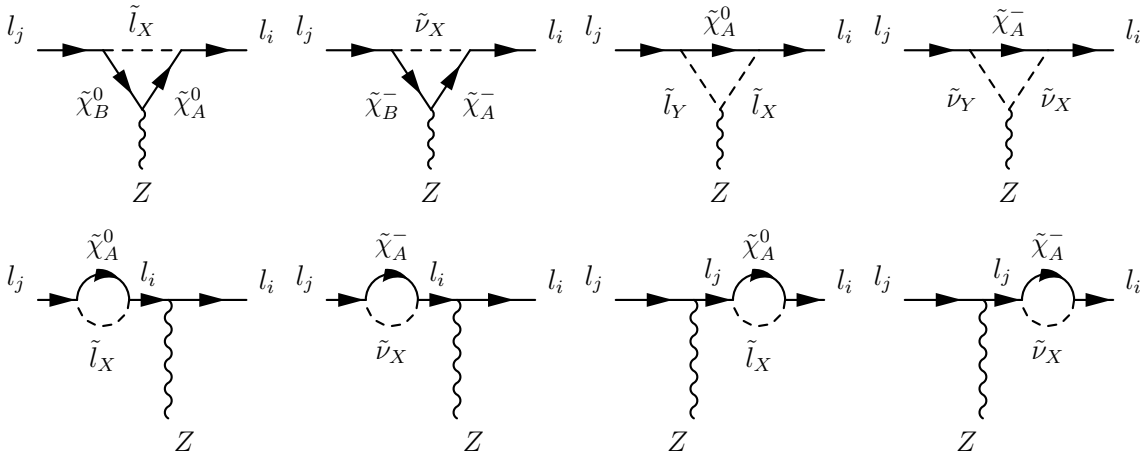

Figure B.2: Relevant SUSY one-loop diagrams for the Z-mediated contributions to LFV processes.

The contributing SUSY one-loop diagrams are collected in Fig. B.2. The Z-boson form factors have also the two kinds of contributions, from neutralinos (n) and charginos (c),

$$F_{L(R)} = F^{(n)}_{L(R)} + F^{(c)}_{L(R)}\,. \qquad \text{(B.10)}$$

The results for the corresponding form factors are the following

$$
\begin{aligned}
F_L^{(n)} &= -\frac{1}{16\pi^2}\Big\{N_{iBX}^R N_{jAX}^{R*}\Big[2E_{BA}^{R(n)} C_{24}(m^2_{\tilde{l}_X}, m^2_{\tilde{\chi}_A^0}, m^2_{\tilde{\chi}_B^0}) - E_{BA}^{L(n)} m_{\tilde{\chi}_A^0} m_{\tilde{\chi}_B^0} C_0(m^2_{\tilde{l}_X}, m^2_{\tilde{\chi}_A^0}, m^2_{\tilde{\chi}_B^0})\Big] \\
&+ N_{iAX}^R N_{jAY}^{R*}\Big[2Q^{\tilde{l}}_{XY} C_{24}(m^2_{\tilde{\chi}_A^0}, m^2_{\tilde{l}_X}, m^2_{\tilde{l}_Y})\Big] + N_{iAX}^R N_{jAX}^{R*}\Big[Z_L^{(l)} B_1(m^2_{\tilde{\chi}_A^0}, m^2_{\tilde{l}_X})\Big]\Big\}\,, \qquad \text{(B.11)} \\
F_R^{(n)} &= F_L^{(n)}\Big|_{L\leftrightarrow R}\,, \qquad \text{(B.12)} \\
F_L^{(c)} &= -\frac{1}{16\pi^2}\Big\{C_{iBX}^R C_{jAX}^{R*}\Big[2E_{BA}^{R(c)} C_{24}(m^2_{\tilde{\nu}_X}, m^2_{\tilde{\chi}_A^-}, m^2_{\tilde{\chi}_B^-}) - E_{BA}^{L(c)} m_{\tilde{\chi}_A^-} m_{\tilde{\chi}_B^-} C_0(m^2_{\tilde{\nu}_X}, m^2_{\tilde{\chi}_A^-}, m^2_{\tilde{\chi}_B^-})\Big] \\
&+ C_{iAX}^R C_{jAY}^{R*}\Big[2Q^{\tilde{\nu}}_{XY} C_{24}(m^2_{\tilde{\chi}_A^-}, m^2_{\tilde{\nu}_X}, m^2_{\tilde{\nu}_Y})\Big] + C_{iAX}^R C_{jAX}^{R*}\Big[Z_L^{(l)} B_1(m^2_{\tilde{\chi}_A^-}, m^2_{\tilde{\nu}_X})\Big]\Big\}\,, \qquad \text{(B.13)} \\
F_R^{(c)} &= F_L^{(c)}\Big|_{L\leftrightarrow R}\,, \qquad \text{(B.14)}
\end{aligned}
$$

where again the indices are $A, B = 1, .., 4$, $X, Y = 1, .., 6$ in the contributions from the neutralino sector and $A, B = 1, 2$, $X, Y = 1, 2, 3$ in the contributions from the chargino sector, and a summation over the various indices is understood.

B.3 Form factors for the $H\, l_j\, l_i$ vertex

Our convention for the form factors $H_{L,R}^{(p)}$ defining the $H_p l_j l_i$ vertex is as follows:

$$
i\left[H_L^{(p)} P_L + H_R^{(p)} P_R\right]. \qquad \text{(B.15)}
$$

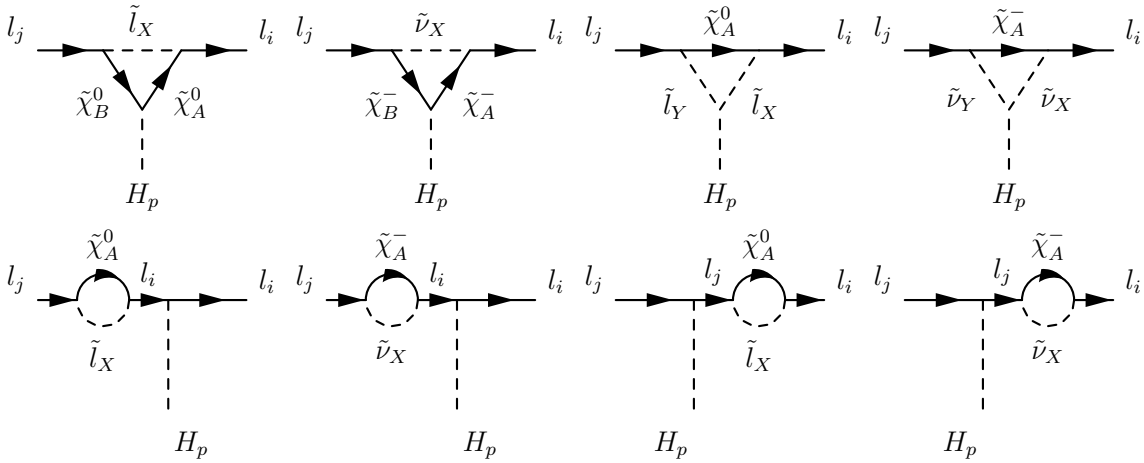

Figure B.3: Relevant SUSY one-loop diagrams for the Higgs-mediated contributions to LFV processes.

The contributing SUSY one-loop diagrams are collected in Fig. B.3. As in the previous cases, we separate the contributions from the neutralino and chargino sectors,

$$H^{(p)}_{L(R)} = H^{(p)}_{L(R),n} + H^{(p)}_{L(R),c}. \tag{B.16}$$

The results for the form factors are the following

$$\begin{aligned}
H^{(p)}_{L,n} &= -\frac{1}{16\pi^2}\Big\{\Big[B_0(m^2_{\tilde\chi^0_A}, m^2_{\tilde\chi^0_B}) + m^2_{\tilde l_X} C_0(m^2_{\tilde l_X}, m^2_{\tilde\chi^0_A}, m^2_{\tilde\chi^0_B}) + m^2_{l_j} C_{12}(m^2_{\tilde l_X}, m^2_{\tilde\chi^0_A}, m^2_{\tilde\chi^0_B}) \\
&+ m^2_{l_i}(C_{11} - C_{12})(m^2_{\tilde l_X}, m^2_{\tilde\chi^0_A}, m^2_{\tilde\chi^0_B})\Big] N^L_{iAX} D^{(p)}_{R,AB} N^{R*}_{jBX} \\
&+ m_{l_i} m_{l_j}(C_{11} + C_0)(m^2_{\tilde l_X}, m^2_{\tilde\chi^0_A}, m^2_{\tilde\chi^0_B}) N^R_{iAX} D^{(p)}_{L,AB} N^{L*}_{jBX} \\
&+ m_{l_i} m_{\tilde\chi^0_B}(C_{11} - C_{12} + C_0)(m^2_{\tilde l_X}, m^2_{\tilde\chi^0_A}, m^2_{\tilde\chi^0_B}) N^R_{iAX} D^{(p)}_{L,AB} N^{R*}_{jBX} \\
&+ m_{l_j} m_{\tilde\chi^0_B} C_{12}(m^2_{\tilde l_X}, m^2_{\tilde\chi^0_A}, m^2_{\tilde\chi^0_B}) N^L_{iAX} D^{(p)}_{R,AB} N^{L*}_{jBX} \\
&+ m_{l_i} m_{\tilde\chi^0_A}(C_{11} - C_{12})(m^2_{\tilde l_X}, m^2_{\tilde\chi^0_A}, m^2_{\tilde\chi^0_B}) N^R_{iAX} D^{(p)}_{R,AB} N^{R*}_{jBX} \\
&+ m_{l_j} m_{\tilde\chi^0_A}(C_{12} + C_0)(m^2_{\tilde l_X}, m^2_{\tilde\chi^0_A}, m^2_{\tilde\chi^0_B}) N^L_{iAX} D^{(p)}_{L,AB} N^{L*}_{jBX} \\
&+ m_{\tilde\chi^0_A} m_{\tilde\chi^0_B} C_0(m^2_{\tilde l_X}, m^2_{\tilde\chi^0_A}, m^2_{\tilde\chi^0_B}) N^L_{iAX} D^{(p)}_{L,AB} N^{R*}_{jBX} \\
&+ G^{(p)\tilde l}_{XY}\Big[-m_{l_i}(C_{11} - C_{12})(m^2_{\tilde\chi^0_A}, m^2_{\tilde l_X}, m^2_{\tilde l_Y}) N^R_{iAX} N^{R*}_{jAY} \\
&- m_{l_j} C_{12}(m^2_{\tilde\chi^0_A}, m^2_{\tilde l_X}, m^2_{\tilde l_Y}) N^L_{iAX} N^{L*}_{jAY} + m_{\tilde\chi^0_A} C_0(m^2_{\tilde\chi^0_A}, m^2_{\tilde l_X}, m^2_{\tilde l_Y}) N^L_{iAX} N^{R*}_{jAY}\Big] \\
&+ \frac{S^{(p)}_{L,j}}{m^2_{l_i} - m^2_{l_j}}\Big[-m^2_{l_i} B_1(m^2_{\tilde\chi^0_A}, m^2_{\tilde l_X}) N^L_{iAX} N^{L*}_{jAX} + m_{l_i} m_{\tilde\chi^0_A} B_0(m^2_{\tilde\chi^0_A}, m^2_{\tilde l_X}) N^R_{iAX} N^{L*}_{jAX} \\
&- m_{l_i} m_{l_j} B_1(m^2_{\tilde\chi^0_A}, m^2_{\tilde l_X}) N^R_{iAX} N^{R*}_{jAX} + m_{l_j} m_{\tilde\chi^0_A} B_0(m^2_{\tilde\chi^0_A}, m^2_{\tilde l_X}) N^L_{iAX} N^{R*}_{jAX}\Big] \\
&+ \frac{S^{(p)}_{L,i}}{m^2_{l_j} - m^2_{l_i}}\Big[-m^2_{l_j} B_1(m^2_{\tilde\chi^0_A}, m^2_{\tilde l_X}) N^R_{iAX} N^{R*}_{jAX} + m_{l_j} m_{\tilde\chi^0_A} B_0(m^2_{\tilde\chi^0_A}, m^2_{\tilde l_X}) N^R_{iAX} N^{L*}_{jAX} \\
&- m_{l_i} m_{l_j} B_1(m^2_{\tilde\chi^0_A}, m^2_{\tilde l_X}) N^L_{iAX} N^{L*}_{jAX} + m_{l_i} m_{\tilde\chi^0_A} B_0(m^2_{\tilde\chi^0_A}, m^2_{\tilde l_X}) N^L_{iAX} N^{R*}_{jAX}\Big]\Big\}\,, \qquad \text{(B.17)} \\
H^{(p)}_{R,n} &= H^{(p)}_{L,n}\Big|_{L\leftrightarrow R} \quad p = 1,2,3\,. \qquad \text{(B.18)}
\end{aligned}$$

Correspondingly, the result for the chargino contribution $H^{(p)}_{L(R),c}$ can be obtained from the previous $H^{(p)}_{L(R),n}$ by replacing everywhere

$$\begin{aligned}
\tilde l &\to \tilde\nu \\
\tilde\chi^0 &\to \tilde\chi^- \\
N^{L(R)} &\to C^{L(R)} \\
D_{L(R)} &\to W_{L(R)}\,.
\end{aligned}$$

In the previous formulae, the index p refers to the each of the Higgs bosons. Concretely, $H_p = h^0, H^0, A^0$ for $p = 1, 2, 3$, respectively. The other indices are again $A, B = 1, .., 4$, $X, Y = 1, .., 6$ in the contributions from the neutralino sector and $A, B = 1, 2$ and $X, Y = 1, 2, 3$ in the contributions from the chargino sector. A summation over all the indices is also understood.

B.4 Contributions from box diagrams

We present in the following the separate contributions from the neutralino and the chargino sectors to the box diagrams which are relevant for $l_j \to 3\, l_i$ decays and $\mu - e$ conversion in nuclei.

B.4.1 Box contributions to $l_j \to 3\, l_i$ decays

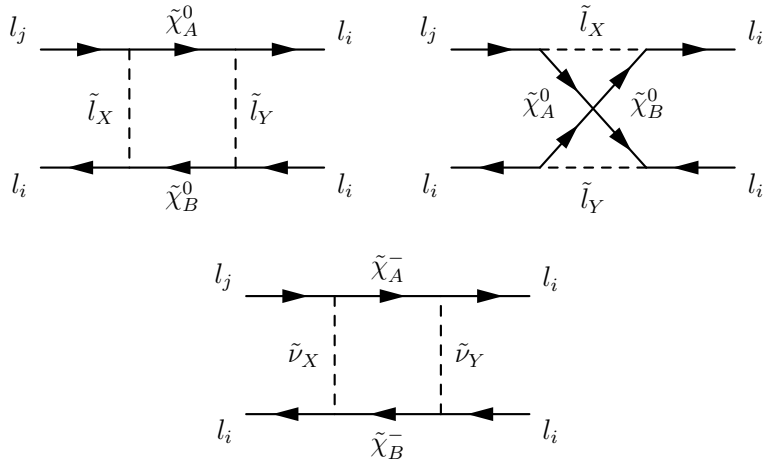

Figure B.4: Box diagrams contributing to $l_j \to 3\, l_i$ decays.

The box diagrams that contribute to $l_j \to 3\, l_i$ decays are displayed in Fig. B.4. Our convention for the box contributions has been derived in Eq. 2.21. We again present separately the contributions from neutralinos and charginos,

$$B_a^{L,R} = B_a^{(n)L,R} + B_a^{(c)L,R} \quad a = 1, ..., 4\,. \tag{B.19}$$

The different neutralino contributions are

$$e^2 B_1^{(n)L} = \frac{1}{16\pi^2}\left[\frac{\tilde{D}_0}{2} N_{iAY}^R N_{jAX}^{R*} N_{iBX}^R N_{iBY}^{R*} + D_0 m_{\tilde{\chi}_A^0} m_{\tilde{\chi}_B^0} N_{iBY}^R N_{iBX}^R N_{jAX}^{R*} N_{iAY}^{R*}\right], \tag{B.20}$$

$$\begin{aligned} e^2 B_2^{(n)L} &= \frac{1}{16\pi^2}\left[\frac{\tilde{D}_0}{4} N_{iAY}^R N_{jAX}^{R*} N_{iBX}^L N_{iBY}^{L*} - \frac{D_0}{2} m_{\tilde{\chi}_A^0} m_{\tilde{\chi}_B^0} N_{iAY}^L N_{jAX}^{R*} N_{iBX}^R N_{iBY}^{L*}\right. \\ &- \left.\frac{\tilde{D}_0}{4} N_{iBY}^L N_{iBX}^R N_{jAX}^{R*} N_{iAY}^{L*} + \frac{\tilde{D}_0}{4} N_{iBY}^R N_{iBX}^L N_{jAX}^{R*} N_{iAY}^{L*}\right], \end{aligned} \tag{B.21}$$

$$e^2 B_3^{(n)L} = \frac{1}{16\pi^2}\left[D_0 m_{\tilde{\chi}_A^0} m_{\tilde{\chi}_B^0} N_{iAY}^L N_{jAX}^{R*} N_{iBX}^L N_{iBY}^{R*} + \frac{D_0}{2} m_{\tilde{\chi}_A^0} m_{\tilde{\chi}_B^0} N_{iBY}^L N_{iBX}^L N_{jAX}^{R*} N_{iAY}^{R*}\right], \tag{B.22}$$

$$e^2 B_4^{(n)L} = \frac{1}{16\pi^2}\left[\frac{D_0}{8} m_{\tilde{\chi}_A^0} m_{\tilde{\chi}_B^0} N_{jAX}^{R*} N_{iAY}^{R*} N_{iBY}^L N_{iBX}^L\right], \tag{B.23}$$

$$B_a^{(n)R} = B_a^{(n)L}\Big|_{L\leftrightarrow R} \quad a = 1, ..., 4\,, \tag{B.24}$$

where

$$D_0 = D_0(m^2_{\tilde{\chi}_A^0}, m^2_{\tilde{\chi}_B^0}, m^2_{\tilde{l}_X}, m^2_{\tilde{l}_Y})\,, \tag{B.25}$$

$$\tilde{D}_0 = \tilde{D}_0(m^2_{\tilde{\chi}_A^0}, m^2_{\tilde{\chi}_B^0}, m^2_{\tilde{l}_X}, m^2_{\tilde{l}_Y})\,. \tag{B.26}$$

The chargino contributions read

$$e^2 B_1^{(c)L} = \frac{1}{16\pi^2}\left[\frac{\tilde{D}_0}{2} C_{iAY}^R C_{jAX}^{R*} C_{iBX}^R C_{iBY}^{R*}\right], \tag{B.27}$$

$$e^2 B_2^{(c)L} = \frac{1}{16\pi^2}\left[\frac{\tilde{D}_0}{4} C_{iAY}^R C_{jAX}^{R*} C_{iBX}^L C_{iBY}^{L*} - \frac{D_0}{2} m_{\tilde{\chi}_A^-} m_{\tilde{\chi}_B^-} C_{iAY}^L C_{jAX}^{R*} C_{iBX}^R C_{iBY}^{L*}\right], \tag{B.28}$$

$$e^2 B_3^{(c)L} = \frac{1}{16\pi^2}\left[D_0 m_{\tilde{\chi}_A^-} m_{\tilde{\chi}_B^-} C_{iAY}^L C_{jAX}^{R*} C_{iBX}^L C_{iBY}^{R*}\right], \tag{B.29}$$

$$e^2 B_4^{(c)L} = 0\,, \tag{B.30}$$

$$B_a^{(c)R} = B_a^{(c)L}\Big|_{L\leftrightarrow R} \quad a = 1, ..., 4\,, \tag{B.31}$$

where

$$D_0 = D_0(m^2_{\tilde{\chi}_A^-}, m^2_{\tilde{\chi}_B^-}, m^2_{\tilde{\nu}_X}, m^2_{\tilde{\nu}_Y})\,, \tag{B.32}$$

$$\tilde{D}_0 = \tilde{D}_0(m^2_{\tilde{\chi}_A^-}, m^2_{\tilde{\chi}_B^-}, m^2_{\tilde{\nu}_X}, m^2_{\tilde{\nu}_Y})\,. \tag{B.33}$$

The indices in the previous formulae are again, $A, B = 1, .., 4$, $X, Y = 1, .., 6$ in the contributions from the neutralino sector and $A, B = 1, 2$, $X, Y = 1, 2, 3$ in the contributions from the chargino sector. A summation over all the indices is also understood.

B.4.2 Box contributions to $\mu - e$ conversion in nuclei

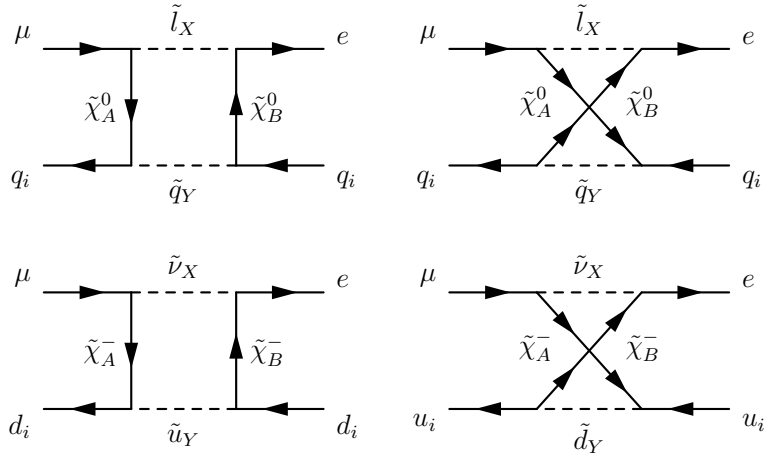

Figure B.5: Box diagrams contributing to $\mu - e$ conversion in nuclei.

The box diagrams that contribute to $\mu - e$ conversion at the quark level are shown in Fig. B.5. Our convention for the box contributions at the quark level is defined in Eqs. (4.6), (4.7) and (4.8). We again present separately the contributions from neutralinos and charginos,

$$B_q^{L,R} = B_q^{(n)L,R} + B_q^{(c)L,R}\,. \tag{B.34}$$

The results for the vector contributions are the following

$$\begin{aligned}
B_q^{(n)LV} &= \frac{1}{16\pi^2}\left\{-\frac{1}{8}\tilde{D}_0(m^2_{\tilde{\chi}^0_A}, m^2_{\tilde{\chi}^0_B}, m^2_{\tilde{l}_X}, m^2_{\tilde{q}_Y}) \times \left[N^{R(l)*}_{\mu AX} N^{R(l)}_{eBX} N^{R(q)*}_{qAY} N^{R(q)}_{qBY}\right.\right. \\
&- \left.\left. N^{R(l)*}_{\mu AX} N^{R(l)}_{eBX} N^{L(q)}_{qAY} N^{L(q)*}_{qBY}\right] + \frac{1}{4} m_{\tilde{\chi}^0_A} m_{\tilde{\chi}^0_B} D_0(m^2_{\tilde{\chi}^0_A}, m^2_{\tilde{\chi}^0_B}, m^2_{\tilde{l}_X}, m^2_{\tilde{q}_Y}) \times \right. \\
&\left. \left[N^{R(l)*}_{\mu AX} N^{R(l)}_{eBX} N^{L(q)}_{qAY} N^{L(q)*}_{qBY} - N^{R(l)*}_{\mu AX} N^{R(l)}_{eBX} N^{L(q)*}_{qAY} N^{R(q)}_{qBY}\right]\right\}\,, \qquad \text{(B.35)} \\
B_q^{(n)RV} &= B_q^{(n)LV}\Big|_{L\leftrightarrow R}\,, \qquad \text{(B.36)} \\
B_d^{(c)LV} &= \frac{1}{16\pi^2}\left\{-\frac{1}{8}\tilde{D}_0(m^2_{\tilde{\chi}^-_A}, m^2_{\tilde{\chi}^-_B}, m^2_{\tilde{\nu}_X}, m^2_{\tilde{u}_Y}) C^{R(l)*}_{\mu AX} C^{R(l)}_{eBX} C^{R(d)}_{dAY} C^{R(d)*}_{dBY}\right. \\
&+ \left.\frac{1}{4} m_{\tilde{\chi}^-_A} m_{\tilde{\chi}^-_B} D_0(m^2_{\tilde{\chi}^-_A}, m^2_{\tilde{\chi}^-_B}, m^2_{\tilde{\nu}_X}, m^2_{\tilde{u}_Y}) C^{R(l)*}_{\mu AX} C^{R(l)}_{eBX} C^{L(d)}_{dAY} C^{L(d)*}_{dBY}\right\}\,, \qquad \text{(B.37)} \\
B_u^{(c)LV} &= \frac{1}{16\pi^2}\left\{\frac{1}{8}\tilde{D}_0(m^2_{\tilde{\chi}^-_A}, m^2_{\tilde{\chi}^-_B}, m^2_{\tilde{\nu}_X}, m^2_{\tilde{d}_Y}) C^{R(l)*}_{\mu AX} C^{R(l)}_{eBX} C^{L(u)*}_{uAY} C^{L(u)}_{uBY}\right. \\
&+ \left.\frac{1}{4} m_{\tilde{\chi}^-_A} m_{\tilde{\chi}^-_B} D_0(m^2_{\tilde{\chi}^-_A}, m^2_{\tilde{\chi}^-_B}, m^2_{\tilde{\nu}_X}, m^2_{\tilde{d}_Y}) C^{R(l)*}_{\mu AX} C^{R(l)}_{eBX} C^{R(u)*}_{uAY} C^{R(u)}_{uBY}\right\}\,, \qquad \text{(B.38)} \\
B_{u,d}^{(c)RV} &= B_{u,d}^{(c)LV}\Big|_{L\leftrightarrow R}\,. \qquad \text{(B.39)}
\end{aligned}$$

The results for the scalar contributions are given by

$$
\begin{aligned}
B_q^{(n)LS} &= \frac{1}{16\pi^2}\left\{\frac{1}{4}\tilde{D}_0(m^2_{\tilde{\chi}^0_A}, m^2_{\tilde{\chi}^0_B}, m^2_{\tilde{l}_X}, m^2_{\tilde{q}_Y}) \times \left[N^{R(l)*}_{\mu AX} N^{L(l)}_{eBX} N^{R(q)}_{qAY} N^{L(q)*}_{qBY}\right.\right. \\
&+ \left.\left. N^{R(l)*}_{\mu AX} N^{L(l)}_{eBX} N^{L(q)*}_{qAY} N^{R(q)}_{qBY}\right] + \frac{1}{4} m_{\tilde{\chi}^0_A} m_{\tilde{\chi}^0_B} D_0(m^2_{\tilde{\chi}^0_A}, m^2_{\tilde{\chi}^0_B}, m^2_{\tilde{l}_X}, m^2_{\tilde{q}_Y}) \times \right. \\
&\left. \left[N^{R(l)*}_{\mu AX} N^{L(l)}_{eBX} N^{L(q)}_{qAY} N^{R(q)*}_{qBY} + N^{R(l)*}_{\mu AX} N^{L(l)}_{eBX} N^{R(q)*}_{qAY} N^{L(q)}_{qBY}\right]\right\}, \qquad \text{(B.40)} \\
B_q^{(n)RS} &= B_q^{(n)LS}\Big|_{L\leftrightarrow R}, \qquad \text{(B.41)} \\
B_d^{(c)LS} &= \frac{1}{16\pi^2}\left\{\frac{1}{4}\tilde{D}_0(m^2_{\tilde{\chi}^-_A}, m^2_{\tilde{\chi}^-_B}, m^2_{\tilde{\nu}_X}, m^2_{\tilde{u}_Y}) C^{R(l)*}_{\mu AX} C^{L(l)}_{eBX} C^{R(d)}_{dAY} C^{L(d)*}_{dBY}\right. \\
&+ \left.\frac{1}{4} m_{\tilde{\chi}^-_A} m_{\tilde{\chi}^-_B} D_0(m^2_{\tilde{\chi}^-_A}, m^2_{\tilde{\chi}^-_B}, m^2_{\tilde{\nu}_X}, m^2_{\tilde{u}_Y}) C^{R(l)*}_{\mu AX} C^{L(l)}_{eBX} C^{L(d)}_{dAY} C^{R(d)*}_{dBY}\right\}, \qquad \text{(B.42)} \\
B_u^{(c)LS} &= \frac{1}{16\pi^2}\left\{\frac{1}{4}\tilde{D}_0(m^2_{\tilde{\chi}^-_A}, m^2_{\tilde{\chi}^-_B}, m^2_{\tilde{\nu}_X}, m^2_{\tilde{d}_Y}) C^{R(l)*}_{\mu AX} C^{L(l)}_{eBX} C^{L(u)*}_{uAY} C^{R(u)}_{uBY}\right. \\
&+ \left.\frac{1}{4} m_{\tilde{\chi}^-_A} m_{\tilde{\chi}^-_B} D_0(m^2_{\tilde{\chi}^-_A}, m^2_{\tilde{\chi}^-_B}, m^2_{\tilde{\nu}_X}, m^2_{\tilde{d}_Y}) C^{R(l)*}_{\mu AX} C^{L(l)}_{eBX} C^{R(u)*}_{uAY} C^{L(u)}_{uBY}\right\}, \qquad \text{(B.43)} \\
B_{u,d}^{(c)RS} &= B_{u,d}^{(c)LS}\Big|_{L\leftrightarrow R}. \qquad \text{(B.44)}
\end{aligned}
$$

The indices in the previous formulae are again, $A, B = 1, .., 4$, $X, Y = 1, .., 6$ in the contributions from the neutralino sector and $A, B = 1, 2$, $X, Y = 1, 2, 3$ in the contributions from the chargino sector. A summation over all the indices is also understood.

Appendix C

Loop functions

In this appendix we present the analytical expressions of the loop functions for the calculations of the LFV leptonic τ and μ decays, LFV semileptonic τ decays and $\mu - e$ conversion in nuclei. In these expressions we neglect the external fermion momenta/masses which for the present computation works extremely well. That is

$$\begin{aligned} B(k^2, m_1^2, m_2^2) &\simeq B(0, m_1^2, m_2^2) = B(m_1^2, m_2^2)\,, & \text{(C.1)} \\ C(k_1^2, k_2^2, m_1^2, m_2^2, m_3^2) &\simeq C(0, 0, m_1^2, m_2^2, m_3^2) = C(m_1^2, m_2^2, m_3^2)\,, & \text{(C.2)} \\ D(k_1^2, k_2^2, k_3^2, m_1^2, m_2^2, m_3^2, m_4^2) &\simeq D(0, 0, 0, m_1^2, m_2^2, m_3^2, m_4^2) \\ &= D(m_1^2, m_2^2, m_3^2, m_4^2)\,. & \text{(C.3)} \end{aligned}$$

Notice that, for the calculation of LFV Higgs decays, to neglect the external Higgs momentum is not a good approximation, and consequently, we do not use these expressions but we compute numerically the full loop functions by means of the public code `SPheno2.2.2`.

C.1 Two-point functions

The analytical expressions for B_0 and B_1 functions are the following

$$\begin{aligned} B_0(m_1^2, m_2^2) &= -\log m_2^2 + \frac{m_2^2 - m_1^2 + m_1^2 \log\left(\frac{m_1^2}{m_2^2}\right)}{m_2^2 - m_1^2}\,, & \text{(C.4)} \\ B_1(m_1^2, m_2^2) &= -\frac{1}{2} + \frac{1}{2}\log m_2^2 - \frac{m_1^4 - m_2^4 + 2m_1^4 \log\left(\frac{m_2^2}{m_1^2}\right)}{4\left(m_1^2 - m_2^2\right)^2}\,. & \text{(C.5)} \end{aligned}$$

C.2 Three-point functions

The expressions for the three-point functions used in this work are given by

$$C_0(m_1^2,m_2^2,m_3^2) = -\frac{1}{m_2^2-m_3^2}\left(\frac{m_1^2\log m_1^2-m_2^2\log m_2^2}{m_1^2-m_2^2}-\frac{m_1^2\log m_1^2-m_3^2\log m_3^2}{m_1^2-m_3^2}\right), \quad \text{(C.6)}$$

$$\tilde{C}_0(m_1^2,m_2^2,m_3^2) = 1-\frac{1}{m_2^2-m_3^2}\left(\frac{m_1^4\log m_1^2-m_2^4\log m_2^2}{m_1^2-m_2^2}-\frac{m_1^4\log m_1^2-m_3^4\log m_3^2}{m_1^2-m_3^2}\right), \quad \text{(C.7)}$$

$$\begin{aligned} C_{11}(m_1^2,m_2^2,m_3^2) &= \frac{1}{2(m_1^2-m_2^2)^2(m_1^2-m_3^2)^2(m_2^2-m_3^2)} \\ &\times \left[-(m_1^2-m_2^2)(m_1^2-m_3^2)(m_2^2-m_3^2)m_1^2+m_1^4m_2^2(2m_1^2-m_2^2)\log\frac{m_1^2}{m_2^2}\right. \\ &+ \left. m_1^4m_3^2(-2m_1^2+m_3^2)\log\frac{m_1^2}{m_3^2}+m_2^2m_3^2(-2m_1^2+m_2^2)(-2m_1^2+m_3^2)\log\frac{m_2^2}{m_3^2}\right], \end{aligned} \quad \text{(C.8)}$$

$$\begin{aligned} C_{12}(m_1^2,m_2^2,m_3^2) &= \frac{1}{2(m_1^2-m_2^2)(m_1^2-m_3^2)^2(m_2^2-m_3^2)^2} \\ &\times \left[(m_1^2-m_2^2)(m_1^2-m_3^2)(m_2^2-m_3^2)m_3^2+m_2^4m_3^2(2m_1^2-m_3^2)\log\frac{m_2^2}{m_3^2}\right. \\ &+ \left. m_1^4\left(m_2^4\log\frac{m_1^2}{m_2^2}+m_3^2(-2m_2^2+m_3^2)\log\frac{m_1^2}{m_3^2}\right)\right], \end{aligned} \quad \text{(C.9)}$$

$$C_{24}(m_1^2,m_2^2,m_3^2) = \frac{1}{4}\tilde{C}_0(0,0,m_1^2,m_2^2,m_3^2)\,. \quad \text{(C.10)}$$

C.3 Four-point functions

Finally, the four-point functions have the following expressions

$$\begin{aligned} D_0(m_1^2,m_2^2,m_3^2,m_4^2) &= -\frac{m_1^2\log m_1^2}{(m_1^2-m_2^2)(m_1^2-m_3^2)(m_1^2-m_4^2)}+\frac{m_2^2\log m_2^2}{(m_1^2-m_2^2)(m_2^2-m_3^2)(m_2^2-m_4^2)} \\ &- \frac{m_3^2\log m_3^2}{(m_1^2-m_3^2)(m_2^2-m_3^2)(m_3^2-m_4^2)}+\frac{m_4^2\log m_4^2}{(m_1^2-m_4^2)(m_2^2-m_4^2)(m_3^2-m_4^2)}, \end{aligned} \quad \text{(C.11)}$$

$$\begin{aligned} \tilde{D}_0(m_1^2,m_2^2,m_3^2,m_4^2) &= -\frac{m_1^4\log m_1^2}{(m_1^2-m_2^2)(m_1^2-m_3^2)(m_1^2-m_4^2)}+\frac{m_2^4\log m_2^2}{(m_1^2-m_2^2)(m_2^2-m_3^2)(m_2^2-m_4^2)} \\ &- \frac{m_3^4\log m_3^2}{(m_1^2-m_3^2)(m_2^2-m_3^2)(m_3^2-m_4^2)}+\frac{m_4^4\log m_4^2}{(m_1^2-m_4^2)(m_2^2-m_4^2)(m_3^2-m_4^2)}. \end{aligned} \quad \text{(C.12)}$$

Appendix D

Hadronic form factors

Our construction of the vector form factors $F_V^{PP}(s)$, defined by Eq. (3.18), follows the idea put forward in [224] that lie on two key points:

1.- At $s \ll M_R^2$ (being M_R a generic resonance mass), the vector form factor should match the $\mathcal{O}(p^4)$ result of χPT. Hence our form factors will satisfy the chiral constraint.

2.- Form factors of QCD currents should behave softly at high transfer of momenta [214], i.e. they should vanish for $s \gg M_R^2$. Accordingly we will demand to our form factors that they satisfy this asymptotic constraint.

In the $N_C \to \infty$ limit resonances have zero-width. However those present in the relevant form factors in tau decays do indeed resonate due to the available phase space. As a consequence we need to include energy-dependent widths for the wider resonances $\rho(770)$ and $\rho(1450)$, or constant for the narrow ones : $\omega(782)$ and $\phi(1020)$. For the $\rho(770)$ we take the definition put forward in [225]

$$\Gamma_\rho(s) = \frac{M_\rho s}{96\pi F^2}\left[\sigma_\pi^3(s)\,\theta(\,s\,-\,4m_\pi^2) \,+\, \frac{1}{2}\,\sigma_K^3(s)\,\theta(\,s\,-\,4m_K^2)\right], \tag{D.1}$$

where $\sigma_P(s) = \sqrt{1-4\frac{m_P^2}{s}}$, while for $\rho(1450)$ we employ a reasonable parameterisation

$$\Gamma_{\rho'}(s) = \Gamma_{\rho'}(M_{\rho'}^2)\,\frac{s}{M_{\rho'}^2}\left(\frac{\sigma_\pi^3(s) \,+\, \frac{1}{2}\,\sigma_K^3(s)\,\theta(\,s\,-\,4m_K^2)}{\sigma_\pi^3(M_{\rho'}^2) \,+\, \frac{1}{2}\,\sigma_K^3(M_{\rho'}^2)\,\theta(\,s\,-\,4m_K^2)}\right)\theta(\,s\,-\,4m_\pi^2)\,. \tag{D.2}$$

The $\mathcal{O}(p^4)$ determination of the vector form factors was done in [209]. Requiring that our expressions match that result at small transfer of momentum we get the following expressions:

$$\begin{aligned}
F_V^{\pi\pi}(s) &= F(s)\ \exp\left[2\,Re\left(\tilde{H}_{\pi\pi}(s)\right)\ +\ Re\left(\tilde{H}_{KK}(s)\right)\right] \\
F(s) &= \frac{M_\rho^2}{M_\rho^2 - s - iM_\rho\Gamma_\rho(s)}\left[1 + \left(\delta\,\frac{M_\omega^2}{M_\rho^2}\ -\ \gamma\,\frac{s}{M_\rho^2}\right)\ \frac{s}{M_\omega^2 - s - iM_\omega\Gamma_\omega}\right] \\
&\quad -\frac{\gamma\,s}{M_{\rho'}^2 - s - iM_{\rho'}\Gamma_{\rho'}(s)}\ ,
\end{aligned}$$

$$\begin{aligned}
F_V^{K^+K^-}(s) &= \frac{1}{2}\,\frac{M_\rho^2}{M_\rho^2 - s - iM_\rho\Gamma_\rho(s)}\,\exp\left[2\,Re\left(\tilde{H}_{\pi\pi}(s)\right)\ +\ Re\left(\tilde{H}_{KK}(s)\right)\right] \\
&\quad +\frac{1}{2}\left[\sin^2\theta_V\,\frac{M_\omega^2}{M_\omega^2 - s - iM_\omega\Gamma_\omega}\ +\ \cos^2\theta_V\,\frac{M_\phi^2}{M_\phi^2 - s - iM_\phi\Gamma_\phi}\right] \\
&\quad \times\exp\left[3\,Re\left(\tilde{H}_{KK}(s)\right)\right]\ ,
\end{aligned}$$

$$\begin{aligned}
F_V^{K^0\bar{K}^0}(s) &= -\frac{1}{2}\,\frac{M_\rho^2}{M_\rho^2 - s - iM_\rho\Gamma_\rho(s)}\,\exp\left[2\,Re\left(\tilde{H}_{\pi\pi}(s)\right)\ +\ Re\left(\tilde{H}_{KK}(s)\right)\right] \\
&\quad +\frac{1}{2}\left[\sin^2\theta_V\,\frac{M_\omega^2}{M_\omega^2 - s - iM_\omega\Gamma_\omega}\ +\ \cos^2\theta_V\,\frac{M_\phi^2}{M_\phi^2 - s - iM_\phi\Gamma_\phi}\right] \\
&\quad \times\exp\left[3\,Re\left(\tilde{H}_{KK}(s)\right)\right]\ , \qquad \text{(D.3)}
\end{aligned}$$

where we have used the definitions

$$\begin{aligned}
\beta &= \frac{\Theta_{\rho\omega}}{3M_\rho^2}\ , \\
\gamma &= \frac{F_V G_V}{F^2}\,(1+\beta) - 1\ , \\
\delta &= \frac{F_V G_V}{F^2} - 1\ , \\
\tilde{H}_{PP}(s) &= \frac{s}{F^2} M_P(s)\ , \\
M_P(s) &= \frac{1}{12}\left(1 - 4\frac{m_P^2}{s}\right)\,J_P(s)\ -\ \frac{k_P(M_\rho)}{6}\ +\ \frac{1}{288\pi^2}\ , \\
J_P(s) &= \frac{1}{16\pi^2}\left[\sigma_P(s)\,\ln\frac{\sigma_P(s)-1}{\sigma_P(s)+1} + 2\right]\ , \\
k_P(\mu) &= \frac{1}{32\pi^2}\left(\ln\frac{m_P^2}{\mu^2} + 1\right)\ . \qquad \text{(D.4)}
\end{aligned}$$

Notice that the β parameter includes the contribution of the isospin breaking $\rho - \omega$ mixing through $\Theta_{\rho\omega} = -3.3 \times 10^{-3}\,\mathrm{GeV}^2$ [226], and F_V and G_V are defined in Eq. (3.11). Moreover the asymptotic constraint on the $N_C \to \infty$ vector form factor indicates $F_V G_V \simeq F^2$ [224]. The mixing between the octet and singlet vector components employed in the construction of the $I = 0$ component of the kaon vector form factors is defined by

$$\begin{pmatrix} \phi \\ \omega \end{pmatrix} = \begin{pmatrix} \cos\theta_V & -\sin\theta_V \\ \sin\theta_V & \cos\theta_V \end{pmatrix} \begin{pmatrix} v_8 \\ v_0 \end{pmatrix}, \tag{D.5}$$

and we will use ideal mixing, i.e. $\theta_V = 35^\circ$.

The values of masses and widths for the various resonances are taken from [10].

Agradecimientos

Llegado a este punto, he de reconocer que ésta es la parte de la tesis que me ha parecido más difícil de desarrollar. Y no porque no sepa qué escribir, sino al contrario, debido a que me gustaría decir tantas cosas y agradecer a tantas personas, que temo que al final parezca que no digo nada. Comencemos y ya veremos al final el resultado...

Empiezo por el principio, y el principio es mi directora de tesis, María José. Me gustaría darle las gracias por estos cinco años de trabajo conjunto, por su natural sinceridad (para bien y para mal...), por su inagotable pasión por la física y sus esfuerzos por intentar transmitírmela, y sobre todo, por la incondicional confianza que ha mostrado tener en mí durante todo este periodo. De una manera más personal, le agradezco las "broncas" casi diarias que hemos mantenido, pues todas aportaban su dosis de reflexión y a su vez han hecho de la tesis algo más divertido y entretenido. Sin ella no habría tenido la oportunidad de vivir esta intensa e irrepetible experiencia que es el doctorado. De todo corazón, muchas gracias.

Seguidamente, querría agradecer y dedicar esta tesis a mis padres, Carmen y Justo, mis referentes espirituales, morales y, ante todo, éticos. Por su cariño, su apoyo y su amor constantes. En estos momentos que hago un pequeño repaso vital, me doy cuenta de que todo lo que soy se lo debo a ellos. Os quiero.

Del mismo modo, nunca dejaré de agradecer a mis hermanitos, Sara e Ignacio, mis dos auténticos compañeros vitales. Sé que siempre estarán a mi lado para ayudarme y tenderme sus manos para levantarme de cualquier caída. Va por vosotros.

A Andrea, por su amor, su sonrisa, su integridad, por su apoyo incondicional tanto en los buenos como en los malos momentos. Por criticarme cuando hace falta, por hacerme sentir feliz cada vez que me da la mano, por tratar de que cada día sea mejor persona. Por todas las experiencias, luchas, viajes y sueños compartidos... ¡Y lo que nos queda! Por ser compañeros dentro y fuera de Casaluche. Y sobre todo, por mirarme como sólo ella sabe...

A mi familia, verdadero refugio nuclear. A mis abuelos, Paquito y Lala, las personas que más me quieren en el mundo; a Ana y a Tito, más que tíos, amigos (y de los buenos buenos); a Jorge, el superprimo (¡nos vas a superar a los tres juntos en todo!). A Ángel, Quico y Ángela,

por quererme tanto en la distancia. A los primos Arganda, por esos encuentros primarios, ¿para cuándo el próximo? A Manuel Yuste, el intelectual integral, gran físico y mejor actor teatral, y a Vicenta. A Esther, mi segunda mami (te debo muchas visitas) y a Rubén.

A mi familia no oficial. Por un lado, a Sergi, "el cuarto hermano", por toda la infancia, adolescencia y madurez peterpanesca conjuntas, no creceremos nunca, pero porque no nos hace falta. Y por otro lado, a mis otros dos hermanos, Sergio y Nico, porque ya irremediablemente, muy a su pesar, son mucho más que amigos. Nunca olvidaré cómo les conocí, a Sergio en la cola para echar la matrícula de primero de Físicas, y a Nico en una reunión de la Manuela Malasaña con Johnny Encuestas de moderador, hace ya la friolera de diez años. Todo este tiempo para darme cuenta de que el verdadero sentido de haber estudiado Físicas no es "descubrir las leyes fundamentales de la Naturaleza" sino haberlos conocido y tener la oportunidad de reirnos a cascoporro cada vez que estamos juntos.

A Amaya y Mario, por su amistad sincera e incondicional, por su manera de afrontar la vida, por todos los sueños que compartimos, por el apoyo mutuo que nunca me faltará.

A los compañeros y amigos del departamento y del IFT. A los compañeros originarios del 504, Ana Curiel, Héctor, Matteo y Fernando, porque hicieron que ese espacio tan reducido fuera como mi segundo hogar, y a los nuevos, Dani, Javi Rubio y Nicolas, que me han aguantado durante el periodo de escritura de tesis y me han ayudado a tirar "palante". A María, Enrique, Jorge Bellorín, Fouad, Matteo, Javi Menéndez, Andrés, África, Ana Fernández, José Oñorbe, Guillermo, Mariluz y Luisfer, que iniciaron el doctorado conmigo y que han hecho de este extraño viaje algo divertido e inolvidable. Os voy a echar de menos. A los de segundo año, Alfonso, Adolfo, Jacobo, Antón, Josemi, Carlitos, Meggy, Fernando e Irene, que siempre me han hecho sentir como uno de los suyos, sobre todo en las salidas nocturnas... A los mayores, David Temes, Natxo, Dani Cremades, Juan Pedro, Juanjo Manjarín, Alicia, Mafer, Pablo, Carlos Hoyos, Edu, Fermín, Irene Hidalgo, Sergio Montañez, y en especial a Tomás, José Delgado y Alberto Ramos, siempre dispuestos a echar un cable sin pedir nada a cambio. A mis hermanos académicos, David Temes, Ana Curiel y Ana Rodríguez, que viene con fuerzas y va a hacer probar a María José de su propia medicina.

A los amigos de toda la vida. A Rubén, Juanjo, Manolo, Jesús y Marian, Diego, Sergio, Sergi, David Carratalá, Davicín, Inés, Tere, Gema, Gilda, Adri, Javier de Lorenzo, Luis y Mauro, por esos parques, por las fiestas de Sanse y Alcobendas, por los torneos de mus, las partidas de rol, los estrenos de Star Wars y El Señor de los Anillos, por los Cretinos!, por tantas cosas... sé que siempre estaréis ahí.

A los compas kandeleros. A Santi, Nati, Óscar, Javi, Álvaro, Pili, Mario, Rafa, Ainara, Heisser, Sol, Sole, Natalia, Ana, Gonza, Rubén, Andrés, Ramiro, Dani, Cris, Nacho, Sergio, Andreita, Bea. Por sus ansias de libertad y justicia social, por las utopías que compartimos,

y sobre todo, por la amistad que me brindaron desde el primer momento, os siento como si fuéramos amigos desde siempre. Kandelismo o barbarie.

A los miembros del Grupo Teórico de SLAC, en especial a Michael Peskin, por la oportunidad que me ofrecieron de disfrutar de dos meses en tan buen ambiente de trabajo y estudio, y de conocer a gente estupenda allí.

A los miembros del Departamento de Física Teórica de la UAM y del IFT, por educarnos científica y académicamente, y tratar de ayudarnos en este campo tan complejo y con difíciles salidas. También me gustaría agradecer la labor de Lola, Juan Carlos y José Valenzuela, sin cuya ayuda seguro que todo habría sido más complicado.

A Ana Teixeira y Jorge Portolés, sin su ayuda y apoyo mucho más allá de lo puramente profesional, gran parte de las publicaciones que han dado lugar a esta tesis no habrían visto la luz. Todo esto también es vuestro.

Finalmente querría pedir disculpas a todas las personas que esperaran más... o menos. Y si alguna quedó satisfecha, es que se lo merecía. Gracias por todo a todos.

Ernesto Arganda Carreras
Madrid, 12 de mayo de 2008

Bibliography

[1] S. L. Glashow. *Partial Symmetries of Weak Interactions. Nucl. Phys.*, **22**:579–588, 1961.

[2] Murray Gell-Mann. *A Schematic Model of Baryons and Mesons. Phys. Lett.*, **8**:214–215, 1964.

[3] G. Zweig. *An SU(3) model for strong interaction symmetry and its breaking. 2.* CERN-TH-412.

[4] Steven Weinberg. *A Model of Leptons. Phys. Rev. Lett.*, **19**:1264–1266, 1967.

[5] Abdus Salam. *Weak and Electromagnetic Interactions.* Originally printed in *Svartholm: Elementary Particle Theory, Proceedings Of The Nobel Symposium Held 1968 At Lerum, Sweden*, Stockholm 1968, 367-377.

[6] Peter W. Higgs. *Broken symmetries, massless particles and gauge fields. Phys. Lett.*, **12**:132–133, 1964.

[7] Peter W. Higgs. *Spontaneous Symmetry Breakdown Without Massless Bosons. Phys. Rev.*, **145**:1156–1163, 1966.

[8] F. Englert and R. Brout. *Broken symmetry and the mass of gauge vector mesons. Phys. Rev. Lett.*, **13**:321–322, 1964.

[9] G. S. Guralnik, C. R. Hagen, and T. W. B. Kibble. *Global conservation laws and massless particles. Phys. Rev. Lett.*, **13**:585–587, 1964.

[10] W. M. Yao et al. *Review of particle physics. J. Phys.*, **G33**:1–1232, 2006.

[11] Y. Fukuda et al. *Atmospheric muon-neutrino / electron-neutrino ratio in the multiGeV energy range. Phys. Lett.*, **B335**:237–245, 1994.

[12] R. Becker-Szendy et al. *Neutrino measurements with the IMB detector. Nucl. Phys. Proc. Suppl.*, **38**:331–336, 1995.

[13] B. T. Cleveland et al. *Measurement of the solar electron neutrino flux with the Homestake chlorine detector. Astrophys. J.*, **496**:505–526, 1998.

[14] W. Hampel et al. *GALLEX solar neutrino observations: Results for GALLEX IV. Phys. Lett.*, **B447**:127–133, 1999.

[15] Q. R. Ahmad et al. *Measurement of the charged current interactions produced by B-8 solar neutrinos at the Sudbury Neutrino Observatory. Phys. Rev. Lett.*, **87**:071301, 2001. `nucl-ex/0106015`.

[16] Q. R. Ahmad et al. *Measurement of day and night neutrino energy spectra at SNO and constraints on neutrino mixing parameters. Phys. Rev. Lett.*, **89**:011302, 2002. `nucl-ex/0204009`.

[17] Y. Ashie et al. *Evidence for an oscillatory signature in atmospheric neutrino oscillation. Phys. Rev. Lett.*, **93**:101801, 2004. `hep-ex/0404034`.

[18] T. Araki et al. *Measurement of neutrino oscillation with KamLAND: Evidence of spectral distortion. Phys. Rev. Lett.*, **94**:081801, 2005. `hep-ex/0406035`.

[19] E. Aliu et al. *Evidence for muon neutrino oscillation in an accelerator- based experiment. Phys. Rev. Lett.*, **94**:081802, 2005. `hep-ex/0411038`.

[20] Z. Maki, M. Nakagawa, and S. Sakata. *Remarks on the unified model of elementary particles. Prog. Theor. Phys.*, **28**:870, 1962.

[21] B. Pontecorvo. *Mesonium and antimesonium. Sov. Phys. JETP*, **6**:429, 1957.

[22] B. Pontecorvo. *Inverse beta processes and nonconservation of lepton charge. Sov. Phys. JETP*, **7**:172–173, 1958.

[23] Peter Minkowski. *mu → e gamma at a Rate of One Out of 1-Billion Muon Decays? Phys. Lett.*, **B67**:421, 1977.

[24] Murray Gell-Mann, Pierre Ramond, and Richard Slansky. *Complex Spinors and Unified Theories.* Print-80-0576 (CERN).

[25] P. Van Nieuwenhuizen and D. Z. Freedman. Supergravity. Proceedings, Workshop at Stony Brook, 27-29 September 1979. Amsterdam, Netherlands: North-holland (1979) 341p.

[26] Tsutomu Yanagida. *Horizontal gauge symmetry and masses of neutrinos.* In Proceedings of the Workshop on the Baryon Number of the Universe and Unified Theories, Tsukuba, Japan, 13-14 Feb 1979.

[27] O. Sawada and A. Sugamoto. *Proceedings of the Workshop on the Unified Theory and the Baryon Number in the Universe, held at National Laboratory for High-Energy Physics (KEK), February 13-14, 1979.* Tsukuba, Japan: Natl.Lab.High Energy Phys.(1979) 109 P.and Japan Natl Lab High Energy - KEK-79-18 (79,REC.JAN 80) 109p.

[28] Sheldon L. Glashow. *Quarks and Leptons.* eds. M. Lévy et al. (Plenum Press, New York, 1980), p.687.

[29] Rabindra N. Mohapatra and Goran Senjanovic. *Neutrino mass and spontaneous parity nonconservation. Phys. Rev. Lett.*, **44**:912, 1980.

[30] Riccardo Barbieri, Dimitri V. Nanopoulos, G. Morchio, and F. Strocchi. *Neutrino Masses in Grand Unified Theories. Phys. Lett.*, **B90**:91, 1980.

[31] R. E. Marshak and Rabindra N. Mohapatra. *Selections rules for baryon number nonconservation in gauge models.* Invited talk given at Orbis Scientiae, Coral Gables, Fla., Jan 14-17, 1980.

[32] T. P. Cheng and Ling-Fong Li. *Neutrino Masses, Mixings and Oscillations in SU(2) x U(1) Models of Electroweak Interactions. Phys. Rev.*, **D22**:2860, 1980.

[33] M. Magg and C. Wetterich. *Neutrino mass problem and gauge hierarchy. Phys. Lett.*, **B94**:61, 1980.

[34] George Lazarides, Q. Shafi, and C. Wetterich. *Proton Lifetime and Fermion Masses in an SO(10) Model. Nucl. Phys.*, **B181**:287, 1981.

[35] J. Schechter and J. W. F. Valle. *Neutrino Masses in SU(2) x U(1) Theories. Phys. Rev.*, **D22**:2227, 1980.

[36] Rabindra N. Mohapatra and Goran Senjanovic. *Neutrino Masses and Mixings in Gauge Models with Spontaneous Parity Violation. Phys. Rev.*, **D23**:165, 1981.

[37] Ernest Ma and Utpal Sarkar. *Neutrino masses and leptogenesis with heavy Higgs triplets. Phys. Rev. Lett.*, **80**:5716–5719, 1998. `hep-ph/9802445`.

[38] M. Fukugita and T. Yanagida. *Baryogenesis Without Grand Unification. Phys. Lett.*, **B174**:45, 1986.

[39] Yu. A. Golfand and E. P. Likhtman. *Extension of the Algebra of Poincare Group Generators and Violation of p Invariance. JETP Lett.*, **13**:323–326, 1971.

[40] D. V. Volkov and V. P. Akulov. *Is the Neutrino a Goldstone Particle? Phys. Lett.*, **B46**:109–110, 1973.

[41] J. Wess and B. Zumino. *Supergauge Transformations in Four-Dimensions. Nucl. Phys.*, **B70**:39–50, 1974.

[42] Howard E. Haber and Gordon L. Kane. *The Search for Supersymmetry: Probing Physics Beyond the Standard Model. Phys. Rept.*, **117**:75–263, 1985.

[43] J. F. Gunion and Howard E. Haber. *Higgs Bosons in Supersymmetric Models. 1. Nucl. Phys.*, **B272**:1, 1986.

[44] J. F. Gunion and Howard E. Haber. *Higgs Bosons in Supersymmetric Models. 2. Implications for Phenomenology. Nucl. Phys.*, **B278**:449, 1986.

[45] Howard E. Haber. *Introductory low-energy supersymmetry*. 1993. `hep-ph/9306207`.

[46] S. Dawson. *SUSY and such. NATO Adv. Study Inst. Ser. B Phys.*, 365:33–80, 1997. `hep-ph/9612229`.

[47] L. Girardello and Marcus T. Grisaru. *Soft Breaking of Supersymmetry. Nucl. Phys.*, **B194**:65, 1982.

[48] Francesca Borzumati and Antonio Masiero. *Large Muon and electron Number Violations in Supergravity Theories. Phys. Rev. Lett.*, **57**:961, 1986.

[49] J. Hisano, T. Moroi, K. Tobe, and Masahiro Yamaguchi. *Lepton-Flavor Violation via Right-Handed Neutrino Yukawa Couplings in Supersymmetric Standard Model. Phys. Rev.*, **D53**:2442–2459, 1996. `hep-ph/9510309`.

[50] J. Hisano, Daisuke Nomura, and T. Yanagida. *Atmospheric neutrino oscillation and large lepton flavour violation in the SUSY SU(5) GUT. Phys. Lett.*, **B437**:351–358, 1998. `hep-ph/9711348`.

[51] J. Hisano and Daisuke Nomura. *Solar and atmospheric neutrino oscillations and lepton flavor violation in supersymmetric models with the right- handed neutrinos. Phys. Rev.*, **D59**:116005, 1999. `hep-ph/9810479`.

[52] Yoshitaka Kuno and Yasuhiro Okada. *Muon decay and physics beyond the standard model. Rev. Mod. Phys.*, **73**:151–202, 2001. `hep-ph/9909265`.

[53] K. S. Babu and Christopher Kolda. *Higgs-mediated tau → 3mu in the supersymmetric seesaw model. Phys. Rev. Lett.*, **89**:241802, 2002. `hep-ph/0206310`.

[54] Marc Sher. *tau → mu eta in supersymmetric models.* *Phys. Rev.*, **D66**:057301, 2002. hep-ph/0207136.

[55] Ryuichiro Kitano, Masafumi Koike, Shinji Komine, and Yasuhiro Okada. *Higgs-mediated muon electron conversion process in supersymmetric seesaw model.* *Phys. Lett.*, **B575**:300–308, 2003. hep-ph/0308021.

[56] Andrea Brignole and Anna Rossi. *Lepton flavour violating decays of supersymmetric Higgs bosons.* *Phys. Lett.*, **B566**:217–225, 2003. hep-ph/0304081.

[57] J. I. Illana and M. Masip. *Lepton flavor violation in Z and lepton decays in supersymmetric models.* *Phys. Rev.*, **D67**:035004, 2003. hep-ph/0207328.

[58] M. L. Brooks et al. *New limit for the family-number non-conserving decay mu+ → e+ gamma.* *Phys. Rev. Lett.*, **83**:1521–1524, 1999. hep-ex/9905013.

[59] U. Bellgardt et al. *Search for the Decay mu+ → e+ e+ e-.* *Nucl. Phys.*, **B299**:1, 1988.

[60] C. Dohmen et al. *Test of lepton flavor conservation in mu - e conversion on titanium.* *Phys. Lett.*, **B317**:631–636, 1993.

[61] W. Bertl et al. *A Search for $\mu - e$ conversion in muonic gold.* *Eur. Phys. J.*, **C47**:337–346, 2006.

[62] S. Ritt. *Status of the MEG expriment mu → e gamma.* *Nucl. Phys. Proc. Suppl.*, **162**:279–282, 2006.

[63] S. Ritt. *Private communication.*

[64] The PRIME working group. *Search for the $\mu - e$ Conversion Process at an Ultimate Sensitivity of the Order of 10^{18} with PRISM.* *Unpublished; LOI to J-PARC 50-GeV PS, LOI-25.* http://psux1.kek.jp/jhf-np/LOIlist/LOIlist.html, **153**:275–315, 2003. hep-ph/0301101.

[65] B. Aubert et al. *Search for lepton flavor violation in the decay $\tau \to \mu\gamma$.* *Phys. Rev. Lett.*, **95**:041802, 2005. hep-ex/0502032.

[66] K. Abe et al. *A new search for tau → mu gamma and tau → e gamma decays at Belle.* 2006. hep-ex/0609049.

[67] K. Hayasaka et al. *New search for tau → mu gamma and tau → e gamma decays at Belle.* 2007. arXiv:0705.0650 [hep-ex].

[68] Swagato Banerjee. *Searches for lepton flavor violating decays tau+- → l+- gamma, tau+- → l+- P0 (where l- = e-, mu-, and P0 = pi0, eta, eta') at B-factories: Status and combinations.* *Nucl. Phys. Proc. Suppl.*, **169**:199–204, 2007. hep-ex/0702017.

[69] Y. Miyazaki et al. *Search for Lepton Flavor Violating tau Decays into Three Leptons.* 2007. arXiv:0711.2189 [hep-ex].

[70] B. Aubert et al. *Improved Limits on the Lepton-Flavor Violating Decays tau- → l-l+l-.* *Phys. Rev. Lett.*, **99**:251803, 2007. arXiv:0708.3650 [hep-ex].

[71] Athanasios Dedes, John R. Ellis, and Martti Raidal. *Higgs mediated B/(s,d)0 → mu tau, e tau and tau → 3mu, e mu mu decays in supersymmetric seesaw models.* *Phys. Lett.*, **B549**:159–169, 2002. hep-ph/0209207.

[72] Y. Yusa et al. *Search for neutrinoless decays tau → l h h and tau → l V0.* *Phys. Lett.*, **B640**:138–144, 2006. hep-ex/0603036.

[73] K. Abe et al. *Search for lepton flavor violating tau- decays into l- eta, l- eta' and l- pi0.* 2006. hep-ex/0609013.

[74] B. Aubert et al. *Search for lepton flavor violating decays tau+- → l+- pi0, l+- eta, l+- eta'. Phys. Rev. Lett.*, **98**:061803, 2007. hep-ex/0610067.

[75] Y. Miyazaki et al. *Search for lepton flavor violating tau- decays into l- eta, l- eta' and l- pi0. Phys. Lett.*, **B648**:341–350, 2007. hep-ex/0703009.

[76] Gordon L. Kane, Christopher F. Kolda, Leszek Roszkowski, and James D. Wells. *Study of constrained minimal supersymmetry. Phys. Rev.*, **D49**:6173–6210, 1994. hep-ph/9312272.

[77] M. Olechowski and S. Pokorski. *Electroweak symmetry breaking with nonuniversal scalar soft terms and large tan beta solutions. Phys. Lett.*, **B344**:201–210, 1995. hep-ph/9407404.

[78] V. Berezinsky et al. *Neutralino dark matter in supersymmetric models with nonuniversal scalar mass terms. Astropart. Phys.*, **5**:1–26, 1996. hep-ph/9508249.

[79] Manuel Drees, Mihoko M. Nojiri, D. P. Roy, and Youichi Yamada. *Light Higgsino dark matter. Phys. Rev.*, **D56**:276–290, 1997. hep-ph/9701219.

[80] Pran Nath and R. Arnowitt. *Non-universal soft SUSY breaking and dark matter. Phys. Rev.*, **D56**:2820–2832, 1997. hep-ph/9701301.

[81] John R. Ellis, Toby Falk, Gerardo Ganis, Keith A. Olive, and Michael Schmitt. *Charginos and neutralinos in the light of radiative corrections: Sealing the fate of Higgsino dark matter. Phys. Rev.*, **D58**:095002, 1998. hep-ph/9801445.

[82] John R. Ellis, Toby Falk, Gerardo Ganis, and Keith A. Olive. *Supersymmetric dark matter in the light of LEP and the Tevatron collider. Phys. Rev.*, **D62**:075010, 2000. hep-ph/0004169.

[83] A. Bottino, F. Donato, N. Fornengo, and S. Scopel. *Probing the supersymmetric parameter space by WIMP direct detection. Phys. Rev.*, **D63**:125003, 2001. hep-ph/0010203.

[84] John R. Ellis, Keith A. Olive, and Yudi Santoso. *The MSSM parameter space with non-universal Higgs masses. Phys. Lett.*, **B539**:107–118, 2002. hep-ph/0204192.

[85] John R. Ellis, Toby Falk, Keith A. Olive, and Yudi Santoso. *Exploration of the MSSM with non-universal Higgs masses. Nucl. Phys.*, **B652**:259–347, 2003. hep-ph/0210205.

[86] Stefano Profumo. *Neutralino dark matter, b - tau Yukawa unification and non-universal sfermion masses. Phys. Rev.*, **D68**:015006, 2003. hep-ph/0304071.

[87] D. G. Cerdeno and C. Munoz. *Neutralino dark matter in supergravity theories with non- universal scalar and gaugino masses. JHEP*, **10**:015, 2004. hep-ph/0405057.

[88] Howard Baer, Azar Mustafayev, Stefano Profumo, Alexander Belyaev, and Xerxes Tata. *Direct, indirect and collider detection of neutralino dark matter in SUSY models with non-universal Higgs masses. JHEP*, **07**:065, 2005. hep-ph/0504001.

[89] John R. Ellis, S. Heinemeyer, K. A. Olive, and G. Weiglein. *Light Heavy MSSM Higgs Bosons at Large tanβ. Phys. Lett.*, **B653**:292–299, 2007. arXiv:0706.0977 [hep-ph].

[90] E. Ables et al. *P-875: A Long baseline neutrino oscillation experiment at Fermilab.* FERMILAB-PROPOSAL-0875.

[91] M. Komatsu, P. Migliozzi, and F. Terranova. *Sensitivity to Theta(13) of the CERN to Gran Sasso neutrino beam. J. Phys.*, **G29**:443, 2003. hep-ph/0210043.

[92] P. Migliozzi and F. Terranova. *Next generation long baseline experiments on the path to leptonic CP violation. Phys. Lett.*, **B563**:73–82, 2003. hep-ph/0302274.

[93] G. S. Tzanakos. *MINOS status and physics goals. AIP Conf. Proc.*, **721**:179–182, 2004.

[94] P. Huber, Joachim Kopp, M. Lindner, M. Rolinec, and W. Winter. *From Double Chooz to Triple Chooz: Neutrino physics at the Chooz reactor complex. JHEP*, **05**:072, 2006. hep-ph/0601266.

[95] Y. Itow et al. *The JHF-Kamioka neutrino project.* 2001. hep-ex/0106019.

[96] A. Blondel et al. *Future neutrino oscillation facilities. Acta Phys. Polon.*, **B37**:2077–2113, 2006. hep-ph/0606111.

[97] P. Huber, M. Lindner, M. Rolinec, and W. Winter. *Optimization of a neutrino factory oscillation experiment. Phys. Rev.*, **D74**:073003, 2006. hep-ph/0606119.

[98] J. Burguet-Castell, D. Casper, E. Couce, J. J. Gomez-Cadenas, and P. Hernandez. *Optimal beta-beam at the CERN-SPS. Nucl. Phys.*, **B725**:306–326, 2005. hep-ph/0503021.

[99] J. E. Campagne, M. Maltoni, M. Mezzetto, and T. Schwetz. *Physics potential of the CERN-MEMPHYS neutrino oscillation project. JHEP*, **04**:003, 2007. hep-ph/0603172.

[100] Pilar Coloma, Andrea Donini, Enrique Fernandez-Martinez, and J. Lopez-Pavon. *θ_{13}, δ and the neutrino mass hierarchy at a $\gamma = 350$ double baseline Li/B β-Beam.* 2007. arXiv:0712.0796 [hep-ph].

[101] Ernesto Arganda, Ana M. Curiel, Maria J. Herrero, and David Temes. *Lepton flavor violating Higgs boson decays from massive seesaw neutrinos. Phys. Rev.*, **D71**:035011, 2005. hep-ph/0407302.

[102] Ernesto Arganda and Maria J. Herrero. *Testing supersymmetry with lepton flavor violating tau and mu decays. Phys. Rev.*, **D73**:055003, 2006. hep-ph/0510405.

[103] S. Antusch, E. Arganda, M. J. Herrero, and A. M. Teixeira. *Impact of theta(13) on lepton flavour violating processes within SUSY seesaw. JHEP*, **11**:090, 2006. hep-ph/0607263.

[104] E. Arganda, M. J. Herrero, and A. M. Teixeira. *$\mu - e$ conversion in nuclei within the CMSSM seesaw: universality versus non-universality. JHEP*, **10**:104, 2007. arXiv:0707.2955 [hep-ph].

[105] E. Arganda, M. J. Herrero, and J. Portoles. *Lepton flavour violating semileptonic tau decays in constrained MSSM-seesaw scenarios.* 2008. arXiv:0803.2039 [hep-ph]. To appear in JHEP(2008).

[106] E. Arganda, A. M. Curiel, M. J. Herrero, and D. Temes. *Lepton flavor violating Higgs boson decays in the MSSM- seesaw.* 2004. hep-ph/0411048.

[107] E. Arganda, A. M. Curiel, M. J. Herrero, and D. Temes. *Lepton flavor changing Higgs boson decays in SUSY with nu(R).* 2005. hep-ph/0506128.

[108] E. Arganda and M. J. Herrero. Lepton flavor violating tau and muon decays. 2006. hep-ph/0605136.

[109] S. Antusch, E. Arganda, M. J. Herrero, and A. M. Teixeira. *LFV in tau and muon decays within SUSY seesaw. Nucl. Phys. Proc. Suppl.*, **169**:155–165, 2007. hep-ph/0610439.

[110] A. M. Teixeira, S. Antusch, E. Arganda, and M. J. Herrero. *Sensitivity to SUSY Seesaw Parameters and Lepton Flavour Violation.* 2007. arXiv:0708.2617 [hep-ph].

[111] Ernesto Arganda and Maria J. Herrero. *Lepton Flavour Violation in SUSY-seesaw: an update*. 2007. `arXiv:0710.4091 [hep-ph]`.

[112] M. Raidal et al. *Flavour physics of leptons and dipole moments*. 2008. `arXiv:0801.1826 [hep-ph]`.

[113] Evgeny Khakimovich Akhmedov. *Neutrino physics*. 1999. `hep-ph/0001264`.

[114] J. A. Casas and A. Ibarra. *Oscillating neutrinos and mu → e, gamma. Nucl. Phys.*, **B618**:171–204, 2001. `hep-ph/0103065`.

[115] M. C. Gonzalez-Garcia and Carlos Pena-Garay. *Three-neutrino mixing after the first results from K2K and KamLAND. Phys. Rev.*, **D68**:093003, 2003. `hep-ph/0306001`.

[116] M. Maltoni, T. Schwetz, M. A. Tortola, and J. W. F. Valle. *Status of global fits to neutrino oscillations. New J. Phys.*, **6**:122, 2004. `hep-ph/0405172`.

[117] G. L. Fogli, E. Lisi, A. Marrone, and A. Palazzo. *Global analysis of three-flavor neutrino masses and mixings. Prog. Part. Nucl. Phys.*, **57**:742–795, 2006. `hep-ph/0506083`.

[118] Manuel Drees. *An introduction to supersymmetry*. 1996. `hep-ph/9611409`.

[119] John F. Gunion and Howard E. Haber. *Two-body decays of neutralinos and charginos. Phys. Rev.*, **D37**:2515, 1988.

[120] M. M. El Kheishen, A. A. Aboshousha, and A. A. Shafik. Analytic formulas for the neutralino masses and the neutralino mixing matrix. *Phys. Rev.*, **D45**:4345–4348, 1992.

[121] Howard E. Haber and Ralf Hempfling. *Can the mass of the lightest Higgs boson of the minimal supersymmetric model be larger than m(Z)? Phys. Rev. Lett.*, **66**:1815–1818, 1991.

[122] Yasuhiro Okada, Masahiro Yamaguchi, and Tsutomu Yanagida. *Upper bound of the lightest Higgs boson mass in the minimal supersymmetric standard model. Prog. Theor. Phys.*, **85**:1–6, 1991.

[123] John R. Ellis, Giovanni Ridolfi, and Fabio Zwirner. *Radiative corrections to the masses of supersymmetric Higgs bosons. Phys. Lett.*, **B257**:83–91, 1991.

[124] Riccardo Barbieri, M. Frigeni, and F. Caravaglios. *The Supersymmetric Higgs for heavy superpartners. Phys. Lett.*, **B258**:167–170, 1991.

[125] Riccardo Barbieri and M. Frigeni. *The Supersymmetric Higgs searches at LEP after radiative corrections. Phys. Lett.*, **B258**:395–398, 1991.

[126] Y. Okada, Masahiro Yamaguchi, and T. Yanagida. *Renormalization group analysis on the Higgs mass in the softly broken supersymmetric standard model. Phys. Lett.*, **B262**:54–58, 1991.

[127] John R. Ellis, Giovanni Ridolfi, and Fabio Zwirner. *On radiative corrections to supersymmetric Higgs boson masses and their implications for LEP searches. Phys. Lett.*, **B262**:477–484, 1991.

[128] Howard E. Haber and Ralf Hempfling. *The Renormalization group improved Higgs sector of the minimal supersymmetric model. Phys. Rev.*, **D48**:4280–4309, 1993. `hep-ph/9307201`.

[129] Damien M. Pierce, Jonathan A. Bagger, Konstantin T. Matchev, and Ren-jie Zhang. *Precision corrections in the minimal supersymmetric standard model. Nucl. Phys.*, **B491**:3–67, 1997. `hep-ph/9606211`.

[130] Jose Ramon Espinosa and Ren-Jie Zhang. *SSM lightest CP-even Higgs boson mass to O(alpha(s) alpha(t)): The effective potential approach. JHEP*, **03**:026, 2000. `hep-ph/9912236`.

[131] Marcela S. Carena et al. *Reconciling the two-loop diagrammatic and effective field theory computations of the mass of the lightest CP-even Higgs boson in the MSSM. Nucl. Phys.*, **B580**:29–57, 2000. hep-ph/0001002.

[132] Jose Ramon Espinosa and Ren-Jie Zhang. *Complete two-loop dominant corrections to the mass of the lightest CP-even Higgs boson in the minimal supersymmetric standard model. Nucl. Phys.*, **B586**:3–38, 2000. hep-ph/0003246.

[133] Yuval Grossman and Howard E. Haber. *Sneutrino mixing phenomena. Phys. Rev. Lett.*, **78**:3438–3441, 1997. hep-ph/9702421.

[134] Athanasios Dedes, Howard E. Haber, and Janusz Rosiek. *Seesaw mechanism in the sneutrino sector and its consequences. JHEP*, **11**:059, 2007. arXiv:0707.3718 [hep-ph].

[135] Werner Porod. *SPheno, a program for calculating supersymmetric spectra, SUSY particle decays and SUSY particle production at e+ e- colliders. Comput. Phys. Commun.*, **153**:275–315, 2003. hep-ph/0301101.

[136] F. Gabbiani, E. Gabrielli, A. Masiero, and L. Silvestrini. *A complete analysis of FCNC and CP constraints in general SUSY extensions of the standard model. Nucl. Phys.*, **B477**:321–352, 1996. hep-ph/9604387.

[137] Piotr H. Chankowski, Oleg Lebedev, and Stefan Pokorski. *Flavour violation in general supergravity. Nucl. Phys.*, **B717**:190–222, 2005. hep-ph/0502076.

[138] Paride Paradisi. *Constraints on SUSY lepton flavour violation by rare processes. JHEP*, **10**:006, 2005. hep-ph/0505046.

[139] S. Pascoli, S. T. Petcov, and C. E. Yaguna. *Quasi-degenerate neutrino mass spectrum, mu $\rightarrow$ e + gamma decay and leptogenesis. Phys. Lett.*, **B564**:241–254, 2003. hep-ph/0301095.

[140] B. C. Allanach et al. *The Snowmass points and slopes: Benchmarks for SUSY searches. Eur. Phys. Rev.*, **C25**:113, 2002. hep-ph/0202233.

[141] M. Passera. *Electron, muon and tau magnetic moments: A theoretical update. Nucl. Phys. Proc. Suppl.*, **169**:213–225, 2007. hep-ph/0702027.

[142] Kazunori Kohri, Takeo Moroi, and Akira Yotsuyanagi. *Big-bang nucleosynthesis with unstable gravitino and upper bound on the reheating temperature. Phys. Rev.*, **D73**:123511, 2006. hep-ph/0507245.

[143] D. N. Spergel et al. *Wilkinson Microwave Anisotropy Probe (WMAP) three year results: Implications for cosmology. Astrophys. J. Suppl.*, **170**:377, 2007. astro-ph/0603449.

[144] G. F. Giudice, A. Notari, M. Raidal, A. Riotto, and A. Strumia. *Towards a complete theory of thermal leptogenesis in the SM and MSSM. Nucl. Phys.*, **B685**:89–149, 2004. hep-ph/0310123.

[145] W. Buchmuller and M. Plumacher. *Neutrino masses and the baryon asymmetry. Int. J. Mod. Phys.*, **A15**:5047–5086, 2000. hep-ph/0007176.

[146] Laura Covi, Esteban Roulet, and Francesco Vissani. *CP violating decays in leptogenesis scenarios. Phys. Lett.*, **B384**:169–174, 1996. hep-ph/9605319.

[147] Sacha Davidson and Alejandro Ibarra. *A lower bound on the right-handed neutrino mass from leptogenesis. Phys. Lett.*, **B535**:25–32, 2002. hep-ph/0202239.

[148] S. T. Petcov, W. Rodejohann, T. Shindou, and Y. Takanishi. *The see-saw mechanism, neutrino Yukawa couplings, LFV decays l(i) → l(j) + gamma and leptogenesis. Nucl. Phys.*, **B739**:208–233, 2006. hep-ph/0510404.

[149] F. Deppisch, H. Pas, A. Redelbach, and R. Ruckl. *Constraints on SUSY seesaw parameters from leptogenesis and lepton flavor violation. Phys. Rev.*, **D73**:033004, 2006. hep-ph/0511062.

[150] Asmaa Abada, Sacha Davidson, Francois-Xavier Josse-Michaux, Marta Losada, and Antonio Riotto. *Flavour issues in leptogenesis. JCAP*, **0604**:004, 2006. hep-ph/0601083.

[151] Enrico Nardi, Yosef Nir, Esteban Roulet, and Juan Racker. *The importance of flavor in leptogenesis. JHEP*, **01**:164, 2006. hep-ph/0601084.

[152] A. Abada et al. *Flavour matters in leptogenesis. JHEP*, **09**:010, 2006. hep-ph/0605281.

[153] S. Antusch and A. M. Teixeira. *Towards constraints on the SUSY seesaw from flavour- dependent leptogenesis. JCAP*, **0702**:024, 2007. hep-ph/0611232.

[154] John R. Ellis, Junji Hisano, Martti Raidal, and Yasuhiro Shimizu. *Lepton electric dipole moments in non-degenerate supersymmetric seesaw models. Phys. Lett.*, **B528**:86–96, 2002. hep-ph/0111324.

[155] John R. Ellis and Martti Raidal. *Leptogenesis and the violation of lepton number and CP at low energies. Nucl. Phys.*, **B643**:229–246, 2002. hep-ph/0206174.

[156] Isabella Masina. *Lepton electric dipole moments from heavy states Yukawa couplings. Nucl. Phys.*, **B671**:432–458, 2003. hep-ph/0304299.

[157] Yasaman Farzan and Michael Edward Peskin. *The contribution from neutrino Yukawa couplings to lepton electric dipole moments. Phys. Rev.*, **D70**:095001, 2004. hep-ph/0405214.

[158] Tarek Ibrahim and Pran Nath. *The neutron and the electron electric dipole moment in $N = 1$ supergravity unification. Phys. Rev.*, **D57**:478–488, 1998. hep-ph/9708456.

[159] S. Abel, S. Khalil, and O. Lebedev. *EDM constraints in supersymmetric theories. Nucl. Phys.*, **B606**:151–182, 2001. hep-ph/0103320.

[160] John R. Ellis, Junji Hisano, Smaragda Lola, and Martti Raidal. *CP violation in the minimal supersymmetric seesaw model. Nucl. Phys.*, **B621**:208–234, 2002. hep-ph/0109125.

[161] G. W. Bennett et al. *Measurement of the negative muon anomalous magnetic moment to 0.7-ppm. Phys. Rev. Lett.*, **92**:161802, 2004. hep-ex/0401008.

[162] G. W. Bennett et al. *Final report of the muon E821 anomalous magnetic moment measurement at BNL. Phys. Rev.*, **D73**:072003, 2006. hep-ex/0602035.

[163] David A. Kosower, Lawrence M. Krauss, and Norisuke Sakai. *Low-Energy Supergravity and the Anomalous Magnetic Moment of the Muon. Phys. Lett.*, **B133**:305, 1983.

[164] T. C. Yuan, R. Arnowitt, Ali H. Chamseddine, and Pran Nath. *Supersymmetric Electroweak Effects on G-2 (mu). Zeit. Phys.*, **C26**:407, 1984.

[165] Jorge L. Lopez, Dimitri V. Nanopoulos, and Xu Wang. *Large (g-2)-mu in SU(5) x U(1) supergravity models. Phys. Rev.*, **D49**:366–372, 1994. hep-ph/9308336.

[166] U. Chattopadhyay and Pran Nath. *Probing supergravity grand unification in the Brookhaven g-2 experiment. Phys. Rev.*, **D53**:1648–1657, 1996. hep-ph/9507386.

[167] Takeo Moroi. *The Muon Anomalous Magnetic Dipole Moment in the Minimal Supersymmetric Standard Model. Phys. Rev.*, **D53**:6565–6575, 1996. hep-ph/9512396.

[168] Marcela S. Carena, G. F. Giudice, and C. E. M. Wagner. *Constraints on supersymmetric models from the muon anomalous magnetic moment. Phys. Lett.*, **B390**:234–242, 1997. hep-ph/9610233.

[169] Tarek Ibrahim and Pran Nath. *CP violation and the muon anomaly in N = 1 supergravity. Phys. Rev.*, **D61**:095008, 2000. hep-ph/9907555.

[170] Lisa L. Everett, Gordon L. Kane, Stefano Rigolin, and Lian-Tao Wang. Implications of muon g-2 for supersymmetry and for discovering superpartners directly. *Phys. Rev. Lett.*, **86**:3484–3487, 2001. hep-ph/0102145.

[171] S. Schael et al. *Search for neutral MSSM Higgs bosons at LEP. Eur. Phys. J.*, **C47**:547–587, 2006. hep-ex/0602042.

[172] *Search for charged Higgs bosons: Preliminary combined results using LEP data collected at energies up to 209- GeV.* 2001. hep-ex/0107031.

[173] B. Abbott et al. *Search for squarks and gluinos in events containing jets and a large imbalance in transverse energy. Phys. Rev. Lett.*, **83**:4937–4942, 1999. hep-ex/9902013.

[174] J. Abdallah et al. *Photon events with missing energy in e+ e- collisions at s**(1/2) = 130-GeV to 209-GeV. Eur. Phys. J.*, **C38**:395–411, 2005. hep-ex/0406019.

[175] P. Abreu et al. *Search for neutralino pair production at s**(1/2) = 189- GeV. Eur. Phys. J.*, **C19**:201–212, 2001. hep-ex/0102034.

[176] A. Heister et al. *Absolute lower limits on the masses of selectrons and sneutrinos in the MSSM. Phys. Lett.*, **B544**:73–88, 2002. hep-ex/0207056.

[177] B. Aubert et al. *Search for lepton flavor violation in the decay $\tau^{\pm} \to e^{\pm}\gamma$. Phys. Rev. Lett.*, **96**:041801, 2006. hep-ex/0508012.

[178] B. Aubert et al. *Search for lepton flavor violation in the decay $\tau^- \to \ell^-\ell^+\ell^-$. Phys. Rev. Lett.*, **92**:121801, 2004. hep-ex/0312027.

[179] Paride Paradisi. *Higgs-mediated tau → mu and tau → e transitions in II Higgs doublet model and supersymmetry. JHEP*, **02**:050, 2006. hep-ph/0508054.

[180] S. T. Petcov and T. Shindou. *Charged lepton decays l(i) → l(j) + gamma, leptogenesis CP-violating parameters and Majorana phases. Phys. Rev.*, **D74**:073006, 2006. hep-ph/0605151.

[181] Antonio Masiero, Sudhir K. Vempati, and Oscar Vives. *Massive neutrinos and flavour violation. New J. Phys.*, **6**:202, 2004. hep-ph/0407325.

[182] F. Deppisch, H. Pas, A. Redelbach, R. Ruckl, and Y. Shimizu. *Probing the Majorana mass scale of right-handed neutrinos in mSUGRA. Eur. Phys. J.*, **C28**:365–374, 2003. hep-ph/0206122.

[183] Stefan Antusch, Joern Kersten, Manfred Lindner, and Michael Ratz. *Running neutrino masses, mixings and CP phases: Analytical results and phenomenological consequences. Nucl. Phys.*, **B674**:401–433, 2003. hep-ph/0305273.

[184] Stefan Ritt. *[MEGA Collaboration], on the web page* http://meg.web.psi.ch/docs/talks/s_ritt/mar06_novosibirsk/ritt.ppt.

[185] J. I. Illana and M. Masip. *Quasi-degenerate neutrinos and lepton flavor violation in supersymmetric models. Eur. Phys. J.*, **C35**:365–372, 2004. hep-ph/0307393.

[186] S. T. Petcov, S. Profumo, Y. Takanishi, and C. E. Yaguna. *Charged lepton flavor violating decays: Leading logarithmic approximation versus full RG results. Nucl. Phys.*, **B676**:453–480, 2004. hep-ph/0306195.

[187] Piotr H. Chankowski, John R. Ellis, Stefan Pokorski, Martti Raidal, and Krzysztof Turzynski. *Patterns of lepton flavor violation motivated by decoupling and sneutrino inflation. Nucl. Phys.*, **B690**:279–301, 2004. hep-ph/0403180.

[188] J. Lorenzo Diaz-Cruz and J. J. Toscano. *Probing lepton flavour violation with the Higgs boson decays H → l/i+ l/j-. Phys. Rev.*, **D62**:116005, 2000. hep-ph/9910233.

[189] W. Hollik. *Precision Tests of the Standard Electroweak Model. P. Langacker ed., World Scientific, Singapore*, pages 37–116, 1995.

[190] A. M. Curiel, M. J. Herrero, W. Hollik, F. Merz, and S. Penaranda. *SUSY - electroweak one-loop contributions to flavour- changing Higgs-boson decays. Phys. Rev.*, **D69**:075009, 2004. hep-ph/0312135.

[191] U. Cotti, L. Diaz-Cruz, C. Pagliarone, and E. Vataga. *Search for the lepton flavor violating Higgs decay H → tau mu at hadron colliders.* 2001. hep-ph/0111236.

[192] Shinya Kanemura et al. *Search for lepton flavor violation in the Higgs boson decay at a linear collider. Phys. Lett.*, **B599**:83–91, 2004. hep-ph/0406316.

[193] Wilfried Buchmuller, David Delepine, and Francesco Vissani. *Neutrino mixing and the pattern of supersymmetry breaking. Phys. Lett.*, **B459**:171–178, 1999. hep-ph/9904219.

[194] John R. Ellis, M. E. Gomez, G. K. Leontaris, S. Lola, and Dimitri V. Nanopoulos. *Charged lepton flavour violation in the light of the Super-Kamiokande data. Eur. Phys. J.*, **C14**:319–334, 2000. hep-ph/9911459.

[195] Xiao-Jun Bi, Yuan-Ben Dai, and Xiao-Yuan Qi. *Lepton flavor violation in supersymmetric SO(10) grand unified models. Phys. Rev.*, **D63**:096008, 2001. hep-ph/0010270.

[196] Junji Hisano and Kazuhiro Tobe. *Neutrino masses, muon g-2, and lepton-flavour violation in the supersymmetric see-saw model. Phys. Lett.*, **B510**:197–204, 2001. hep-ph/0102315.

[197] Stephane Lavignac, Isabella Masina, and Carlos A. Savoy. *tau → mu gamma and mu → e gamma as probes of neutrino mass models. Phys. Lett.*, **B520**:269–278, 2001. hep-ph/0106245.

[198] Xiao-Jun Bi and Yuan-Ben Dai. *Lepton flavor violation and its constraints on the neutrino mass models. Phys. Rev.*, **D66**:076006, 2002. hep-ph/0112077.

[199] D. F. Carvalho, John R. Ellis, M. E. Gomez, S. Lola, and J. C. Romao. *Tau flavour violation in sparticle decays at the LHC. Phys. Lett.*, **B618**:162–170, 2005. hep-ph/0206148.

[200] John R. Ellis, Junji Hisano, Martti Raidal, and Yasuhiro Shimizu. *A new parametrization of the seesaw mechanism and applications in supersymmetric models. Phys. Rev.*, **D66**:115013, 2002. hep-ph/0206110.

[201] Junji Hisano. *Lepton-flavor violating decay of tau lepton in the supersymmetric seesaw model.* 2002. hep-ph/0209005.

[202] Takeshi Fukuyama, Tatsuru Kikuchi, and Nobuchika Okada. *Lepton flavor violating processes and muon g-2 in minimal supersymmetric SO(10) model.* *Phys. Rev.*, **D68**:033012, 2003. hep-ph/0304190.

[203] Andrea Brignole and Anna Rossi. *Anatomy and phenomenology of mu tau lepton flavour violation in the MSSM.* *Nucl. Phys.*, **B701**:3–53, 2004. hep-ph/0404211.

[204] K. Abe et al. *Search for lepton flavor violating $\tau \to \ell V^0$ decays at Belle.* 2007. arXiv:0708.3276 [hep-ex].

[205] Gerard 't Hooft. *A Planar Diagram Theory for Strong Interactions.* *Nucl. Phys.*, **B72**:461, 1974.

[206] Santiago Peris, Michel Perrottet, and Eduardo de Rafael. *Matching long and short distances in large-N(c) QCD.* *JHEP*, **05**:011, 1998. hep-ph/9805442.

[207] Johan Bijnens, Elvira Gamiz, Edisher Lipartia, and Joaquim Prades. *QCD short-distance constraints and hadronic approximations.* *JHEP*, **04**:055, 2003. hep-ph/0304222.

[208] Steven Weinberg. *Phenomenological Lagrangians.* *Physica*, **A96**:327, 1979.

[209] J. Gasser and H. Leutwyler. *Chiral Perturbation Theory: Expansions in the Mass of the Strange Quark.* *Nucl. Phys.*, **B250**:465, 1985.

[210] G. Ecker, J. Gasser, A. Pich, and E. de Rafael. *The Role of Resonances in Chiral Perturbation Theory.* *Nucl. Phys.*, **B321**:311, 1989.

[211] P. Herrera-Siklody, J. I. Latorre, P. Pascual, and J. Taron. *Chiral effective Lagrangian in the large-N/c limit: The nonet case.* *Nucl. Phys.*, **B497**:345–386, 1997. hep-ph/9610549.

[212] Roland Kaiser and H. Leutwyler. *Pseudoscalar decay constants at large N(c).* 1998. hep-ph/9806336.

[213] Chuan-Hung Chen and Chao-Qiang Geng. *Lepton flavor violation in tau decays.* *Phys. Rev.*, **D74**:035010, 2006. hep-ph/0605299.

[214] G. Peter Lepage and Stanley J. Brodsky. *Exclusive Processes in Perturbative Quantum Chromodynamics.* *Phys. Rev.*, **D22**:2157, 1980.

[215] J. D. Vergados. *The Neutrino Mass and Family, Lepton and Baryon Nonconservation in Gauge Theories.* *Phys. Rept.*, **133**:1, 1986.

[216] J. Bernabeu, E. Nardi, and D. Tommasini. *mu - e conversion in nuclei and Z-prime physics.* *Nucl. Phys.*, **B409**:69–86, 1993. hep-ph/9306251.

[217] Amand Faessler, T. S. Kosmas, Sergey Kovalenko, and J. D. Vergados. *Constraints on R-parity violating supersymmetry from mu- e- nuclear conversion.* 1999. hep-ph/9904335.

[218] T. S. Kosmas, Sergey Kovalenko, and Ivan Schmidt. *mu- - e- conversion in strange quark sea.* *Phys. Lett.*, **B511**:203, 2001. hep-ph/0102101.

[219] H. C. Chiang, E. Oset, T. S. Kosmas, A. Faessler, and J. D. Vergados. *Coherent and incoherent (mu-, e-) conversion in nuclei.* *Nucl. Phys.*, **A559**:526–542, 1993.

[220] Ryuichiro Kitano, Masafumi Koike, and Yasuhiro Okada. *Detailed calculation of lepton flavor violating muon electron conversion rate for various nuclei.* *Phys. Rev.*, **D66**:096002, 2002. hep-ph/0203110.

[221] L. Calibbi, A. Faccia, A. Masiero, and S. K. Vempati. *Lepton flavour violation from SUSY-GUTs: Where do we stand for MEG, PRISM / PRIME and a super flavour factory. Phys. Rev.*, **D74**:116002, 2006. `hep-ph/0605139`.

[222] F. Deppisch, T. S. Kosmas, and J. W. F. Valle. *Enhanced mu- e- conversion in nuclei in the inverse seesaw model. Nucl. Phys.*, **B752**:80–92, 2006. `hep-ph/0512360`.

[223] Monika Blanke, Andrzej J. Buras, Bjoern Duling, Anton Poschenrieder, and Cecilia Tarantino. *Charged Lepton Flavour Violation and $(g-2)_m u$ in the Littlest Higgs Model with T-Parity: a clear Distinction from Supersymmetry. JHEP*, **05**:013, 2007. `hep-ph/0702136`.

[224] G. Ecker, J. Gasser, H. Leutwyler, A. Pich, and E. de Rafael. *Chiral Lagrangians for Massive Spin 1 Fields. Phys. Lett.*, **B223**:425, 1989.

[225] D. Gomez Dumm, A. Pich, and J. Portoles. *The hadronic off-shell width of meson resonances. Phys. Rev.*, **D62**:054014, 2000. `hep-ph/0003320`.

[226] A. Pich and J. Portoles. *Vector form factor of the pion: A model-independent approach. Nucl. Phys. Proc. Suppl.*, **121**:179–182, 2003. `hep-ph/0209224`.